Année 2017 № d'ordre: 42474

UNIVERSITÉ DE LILLE
ÉCOLE DOCTORALE BIOLOGIE ET SANTÉ

THÈSE
Présentée pour obtenir le grade de : Docteur de l'Université de Lille
Discipline : Aspects moléculaires et cellulaires de la Biologie

Présentée et soutenue publiquement par
OKSANA IAMSHANOVA

ROLE OF NALCN CHANNEL IN PROSTATE CANCER METASTATIC BEHAVIOURS

Thèse dirigée par Professeur Natalia Prevarskaya

Soutenue le 14 Decembre 2017

Jury :

Prof. Corinne Abbadie, Institut de Biologie de Lille (Lille, France)	President
Dr. Arnaud Monteil, Institut de Génomique Fonctionelle (Montpellier, France)	Rapporteur
Dr. Sebastien Roger, Université de Francois-Rabelais (Tours, France)	Rapporteur
Prof. Gaëlle Fromont-Hankard, Université de Francois-Rabelais (Tours, France)	Examinateur
Prof. Mustafa Djamgoz, Imperial College London (London, United Kingdom)	Examinateur
Dr. Dmytro Gordienko, Université de Lille (Lille, France)	Examinateur
Prof. Natalia Prevarskaya, Université de Lille (Lille, France)	Examinateur

Thèse realisée au sein du Laboratoire de Physiologie Cellulaire INSERM U1003
Université de Lille
Villeneuve d'Ascq France

Acknowledgements

First, I would like to acknowledge all the members of my thesis committee for agreeing to evaluate my PhD work.

I would like to thank Prof Corinne Abbadie for accepting the responsibility of a president of the jury, despite her highly busy schedule at the time of my defense. Moreover, I would like to express my gratitude to Prof Corinne Abbadie for her guidance and suggestions throughout the whole PhD project as one of the examiners of my 'comité de suivi individuel' (CSI).

I would like to thank Dr Arnaud Monteil for accepting to be the reporter of my thesis. I greatly appreciate all the NALCN constructs he provided and also our discussions on the project. Contribution of Dr Arnaud Monteil is indispensable for this study.

I would like to express my gratitude to Dr Sebastien Roger for accepting to be the reporter of my thesis. I am very grateful to Dr Sebastien Roger for his ideas and suggestions for this study about relationship between Na^+ signalling and pH.

I would like to thank Prof Gaëlle Fromont-Hankard for accepting to be examiner of my thesis. I greatly value contribution of Prof Gaëlle Fromont-Hankard for this study. In particular, immunohistochemical analysis of NALCN in human prostate biopsies and its correlation with other proteins.

I would like to express my gratitude to Prof Mustafa Djamgoz for accepting to be external examiner of my thesis. Thanks to support and encouragement of Prof Mustafa Djamgoz I have pursued my dream of doing PhD in the field of ion channels and cancer disease. I would also like to acknowledge Prof Mustafa Djamgoz for his suggestion to investigate relationship between Na^+ signalling and cytosolic Ca^{2+} oscillations in cancer cells, that became one of the highlights of the current study.

I would like to thank to Dr Dmitri Gordienko for accepting to be internal examiner of my thesis and for his priceless contribution into this study. In particular, for Dr Dmitri Gordienko's ideas, suggestions, experimental procedures using confocal microscopy, analysis, precise figure design and for his highly valuable critical approach.

Especially, I would like to thank to Prof Natalia Prevarskaya for accepting me as a PhD student in her laboratory. I would like to express my gratitude to Prof Natalia Prevarskaya for believing in me and for mentoring me over the years. In particular, for her bright ideas, guidance and support throughout this study.

I would also like to thank to Dr François Foulquier for being examiner of my CSI throughout this PhD. For his helpful ideas and suggestions, as well as for his understanding of the project-associated challenges and receptiveness in the process of problem solving.

Second, I would like to acknowledge all the external collaborators on this study.

I would like to express my appreciation to Dr Corentin Spriet for his work on cellular motility and wound-healing.

I am thanking to Dr Martin Figeac and Dr Frederic Lepretre for their work on genomic sequencing.

I would like to thank to Dr Severine Marionneau-Lambot and Dr Thibauld Oullier for their highly valuable *in vivo* work.

I would like to express my gratitude to Prof Philippe Clezardin and Dr Sandra Geraci for their greatly appreciated bone metastasis study.

I would like to thank to Prof Pierre Gosset and Dr Adriana Mihalache for their contribution into immunohistochemical analysis of human biopsies.

I am also thanking to Prof Daniel Metzger for providing *PTEN*$^{-/-}$ mice samples.

I am greatly grateful to Dr Nathalie Jouy for the wonderful introduction into FACS technique and cell sorting assistance.

I would like to express my gratitude to Dr Chann Lagadec and Prof Robert-Allain Toillon for kindly letting me using their FACS machine and helping with the analysis.

I would like to express my appreciation to Dr Lucie Brisson for her work on pH and ion channel expression profile.

I am also thanking to Dr Malik Bouasse and Alexandre Milman for their discussions about NALCN.

Third, I would like to thank the members of the laboratory where I have been working for the last 4 years.

I would like to express my appreciation to Dr Christian Slomianny for all his support and kindness throughout all the ups and downs of my PhD journey.

I am very grateful to Dr Etienne Dewailly for his positivity, patience and sincerity. Especially, for the whole-year Christmas spirit in the office.

I am also expressing my gratitude to Elodie Richard and Anne-Sophie Lacoste for their cordiality and work in microscopy.

I would like to express my appreciation to MOVI team, in particular to Dr Emanuelle Germain, Dr Ingrid Fliniaux and Dr Valerio Farfariello for our discussions and meetings on the senescence project.

I would like to thank to Dr Mehdi Hammadi for his collaboration on nanoparticles.

I would like to express my appreciation to Dr George Shapovalov for the electrophysiological recordings and his advices on the project.

I am very grateful to Dr Pascal Mariot for everything that he taught me on Ca^{2+} and Na^{+} imaging, for his electrophysiological recordings and overall contribution into the project.

I would like to thank to Dr Artem Kondratskyi and Dr Kateryna Kondratskaya for being kind, helpful and genuine people.

I would like to express my gratitude to Dr Loic Lemonnier for being very responsive to every little question I might have and for being a nice friend.

I had a great pleasure to work with Prof Alessandra Fiorio Pla on the review and overall I would like to thank her for the everyday cheerful spirit.

I would like to thank to Emilie Desruelles for her help with experiments and also for her much appreciated friendship.

I would like to thank to Dr Dimitra Gkika for trusting me the responsibility of performing all those qPCRs on the highly valuable patients' samples. It was a great pleasure to collaborate.

I would like to express my gratitude to Prof Morad Roudbaraki for all his advices and enthusiastic scientific discussions.

I am grateful to Prof Roman Skryma for the introduction into laboratory rules and his philosophic life approach.

I would like to thank to Dr Christophe Tastet for his friendly and pleasant temperament.

I would like to acknowledge Laurent Allart for his help with experiments and minipreps.

I would like to thank to Dr Fabien Vanden-Abeele for his help in evaluation of the channel mechanosensitivity.

I would like to acknowledge Prof Yaroslav Shuba for his amiability and interesting lab talk on the bladder contractility.

I would like to thank to Abigaël Ritaine, Lucile Noyer, Guillaume Grolez and Aurelien Rock for their hospitality, support and understanding of the daily PhD-associated challenges.

I have much appreciated working with Antoine Folcher thanks to his meticulous work approach. I am confident he has a great potential in scientific research.

I also would like to acknowledge Dr V'yacheslav Lehen'kyi and his student Aurelien Haustrate for teaching me being more vigilant with my data.

I am very grateful to Pauline Jezraoui and Brigitte Macquart for their kindness, sympathy and professionalism, especially with my visas applications and organization of PhD defense.

I would like to express my gratitude to Andrée Menin for keeping our working environment clean and tidy.

Fourth, I would like to thank the previous members of our laboratory who I had a pleasure to meet during my PhD.

I would like to express my gratitude to Dr Eric Vancauwenberghe, Dr Michela Bernardini, Dr Marine Warnier, Dr Maylis Raphaël, Dr Charlotte Dubois and Dr Angela Morabito for their help during my integration into the lab and also for setting up an example of successful PhD defense.

I would like to thank to Dr Gabriel Bidaux and Dr Anne-Sophie Borowiec for their sympathy and support.

I was very glad to work with Raquel Diez. I have much appreciated her diligence and enthusiasm.

I would like to acknowledge Philippe Delcourt for his goodwill and kindness.

I would like to thank to Woodys Lenga, Quentin Plumereau, Andrea De Rosa and Andrea Stacchetti for their friendship.

Fifth, I would like to express my appreciation to my friends from Lille who I met during my PhD studies.

I would like to thank to Gulzar Seidamatova, Marc-Antoine Louchez, Alex Laguta, Anastasia Penkina, Andrey Suchkov, Valentin, Andrii and Yulia Bovchaluk. I greatly appreciate your kindness, support, and encouragement. You are wonderful friends and I was very lucky to have you around me throughout all this time.

Sixth, I would like to thank to my colleagues from Imperial College London.

I am grateful to Dr Scott Fraser for his support and assistance throughout my work at ICL.

I would like to express my gratitude to Dr Mine Güzel and Dr Selin Özkan for their continuous support, encouragement and much appreciated friendship.

I would like to thank to Dr Hussein Taha for everything that he taught me while being a PhD student himself and also for his friendliness.

And last, but not the least, I would like to express my endless gratitude to the closest people around me.

I am very grateful to Alexandre Bokhobza for his enormous everyday support, for all his love, warmth and care. I would not have managed it without help and support of Alex.

I would like to thank the family of Alex for their support as well. Annick, Samuel, Laurane, Josiane, Nathalie, Helena, Guy, Valentin, and Stephanie – thank you so much for being around all this time.

I am extremely thankful to my dad Yurii for being my true inspiration and role model in life. I am so grateful to my mom Viktoriia for being my hero in my life, for all the love and care she gave me. I am very lucky to have such an amazing, thoughtful, warm-hearted and highly talented brother Andrii. I am very grateful to Luda, Sasha, Vika and Yulia for being by my side, for their support and sensibility. Overall, I am very grateful to my family for believing in me, for supporting me on my scientific path, for encouraging me to always achieve high and never giving up my dreams.

TITRE DE LA THÈSE EN FRANÇAIS:

Rôle du canal ionique NALCN dans le processus de formation des métastases du cancer de la prostate.

RESUMÉ DE LA THÈSE EN FRANÇAIS:

L'homéostasie sodique joue un rôle prépondérant lors de la carcinogénèse prostatique. Cependant, le rôle du canal de fuite sodique NALCN lors de la carcinogénèse prostatique était totalement inconnu. L'objectif principal de cette étude était d'étudier le rôle de NALCN dans la dérégulation de l'homéostasie sodique lors de la tumorigenèse prostatique.

Tout d'abord, nous avons montré sur des coupes de tissus prostatiques que l'expression de NALCN est augmentée dans les cancers. De plus, NALCN est surexprimé dans les lignées cancéreuses prostatiques les plus agressives. Nous avons vérifié la fonctionnalité du canal NALCN et de ses protéines associées via des expériences d'imagerie sodique dans ces lignées. Grâce à notre étude, nous montrons que NALCN n'est pas impliqué dans le cycle cellulaire, la viabilité cellulaire, l'apoptose ni la prolifération. En revanche, nous avons démontré que ce canal affecte grandement la motilité, la migration et l'invasion de nos lignées cellulaires cancéreuses prostatiques. Nous avons montré que NALCN et le protooncogène Src sont co-localisées dans le cancer de la prostate, notamment au niveau de structures appelées invadopodes. Enfin, nous avons prouvé par des études *in vivo* que la croissance tumorale et la formation de métastases sont inhibées lorsque l'expression du canal NALCN est diminuée.

En conclusion, nos données mettent en évidence que le canal NALCN est un acteur important dans l'augmentation du potentiel métastatique des cellules cancéreuses de prostate à la fois *in vitro* et *in vivo*. NALCN peut donc être considéré comme une nouvelle cible thérapeutique permettant de diminuer l'agressivité des cancers de la prostate.

TITLE OF THE THESIS IN ENGLISH:

Role of NALCN channel in prostate cancer metastatic behaviours.

ABSTRACT OF THE THESIS IN ENGLISH:

Importantly, altered Na^+ homeostasis was implemented in prostate carcinogenesis. However, until now nothing was known about a newly discovered Na^+ leak channel, NALCN, and its role in prostate malignancy. Therefore, the main objective of this study was to investigate the involvement of NALCN as a potential candidate of the deregulated Na^+-dependent signalling mechanisms in prostate cancer.

Interestingly, NALCN represented distinctly different localization patterns and levels of expression between human healthy and cancer prostate tissues. Indeed, NALCN was expressed preferentially in highly aggressive prostate cancer cell lines. Na^+ imaging results verified on functionality of NALCN channelosome in these cells. Our study also revealed that NALCN was not involved in cell cycle, viability, apoptosis and proliferation, but significantly affected motility, migration and invasiveness of the prostate cancer cells. Interestingly, it was already reported that protooncogene Src family kinase is recruited to the NALCN complex. In this study, we confirmed that NALCN and Src kinase are co-localized in human prostate cancer cells, particularly in the structures that represent invadopodia formation sites. Furthermore, *in vivo* studies confirmed that NALCN downregulation inhibits tumour growth and metastasis formation.

Overall, these data provide evidence on NALCN contribution to the increased metastatic potential of human prostate cancer cells both *in vitro* and *in vivo*. Therefore, NALCN could provide new perspective molecular target for the disease suppression, in particular at its advanced stages.

Author contributions

Publications:

1. Iamshanova O., Fiorio Pla A., Prevarskaya N. **Molecular mechanisms of tumour invasion: regulation by calcium signals.** J Physiol. 2017 May 15;595(10):3063-3075. doi: 10.1113/JP272844. Epub 2017 Apr 21.
2. Iamshanova O., Mariot P., Lehen'kyi V., Prevarskaya N. **Comparison of fluorescence probes for intracellular sodium imaging in prostate cancer cell lines.** Eur Biophys J. 2016 Sep 22.
3. Burgess S. J., Taha H., Yeoman J. A., Iamshanova O., Chan K. X., Boehm M., Behrends V., Bundy J. G., Bialek W., Murray J. W., Nixon P. J. **Identification of the Elusive Pyruvate Reductase of Chlamydomonas reinhardtii Chloroplasts.** Plant Cell Physiol. 2016 Jan;57(1):82-94. doi: 10.1093/pcp/pcv167.
4. Farfariello V, Iamshanova O, Germain E, Fliniaux I, Prevarskaya N. **Calcium homeostasis in cancer: A focus on senescence.** Biochim Biophys Acta. 2015 Sep;1853(9):1974-9. doi: 10.1016/j.bbamcr.2015.03.005.

Conferences:

Oral presentations

- 2nd LabEx ICST Young Researchers Meeting, 1st prize (2016, Nice, France)
- 27th Ion Channel Meeting (2016, Sete, France)
- Laboratory of Excellence in Ion Channel Science and Therapeutics (2015, Montpellier, France)

Poster presentations

- 2nd Ion Channel Modulation Symposium (2017, Cambridge, United Kingdom)
- An International Meeting on Ion Channels, Transporters & Cancer (2015, London, United Kingdom)
- XV Edition of the Journée André Verbert (2015, Lille, France)
- Laboratory of Excellence in Ion Channel Science and Therapeutics, ICST young researchers meeting (2014, Lille, France)

Other activities:

- XVII Edition of the Journée André Verbert (2017, Lille, France)
- Formation 'Fondamentaux en statistiques et tests d'hypothèses' (2017, Lille, France)
- Scientific meeting on ion channels in cancer 06/06/17 (2017, Lille, France)
- XVI Edition of the Journée André Verbert (2016, Lille, France)
- Cours de Français Langue Etrangère 2015/2016 Semestre 2 (Lille, France)
- Cours de Français Langue Etrangère 2015/2016 Semestre 1 (Lille, France)
- Cours de Français Langue Etrangère 2014/2015 Semestre 2 (Lille, France)
- XIV Edition of the Journée André Verbert (2014, Lille, France)
- Course 'Easily manage your bibliography with ZOTERO' (2014, Lille, France)
- Cours de Français Langue Etrangère 2014/2015 Semestre 1 (Lille, France)
- Cancer Stem Cell meeting (2014, Lille, France)
- Formation théorique aux risques biologiques (2014, Lille, France)
- Cours de Français Langue Etrangère 2013/2014 Semestre 1 (Lille, France)

Teaching experience:

- April 2015 – 2 hour lecture 'Calcium and aging' for Master students, University of Lille
- April 2016 – 2 hour lecture 'Calcium and aging' for Master students, University of Lille
- April 2017 – 2 hour lecture 'Calcium and tumour spread' for Master students, University of Lille

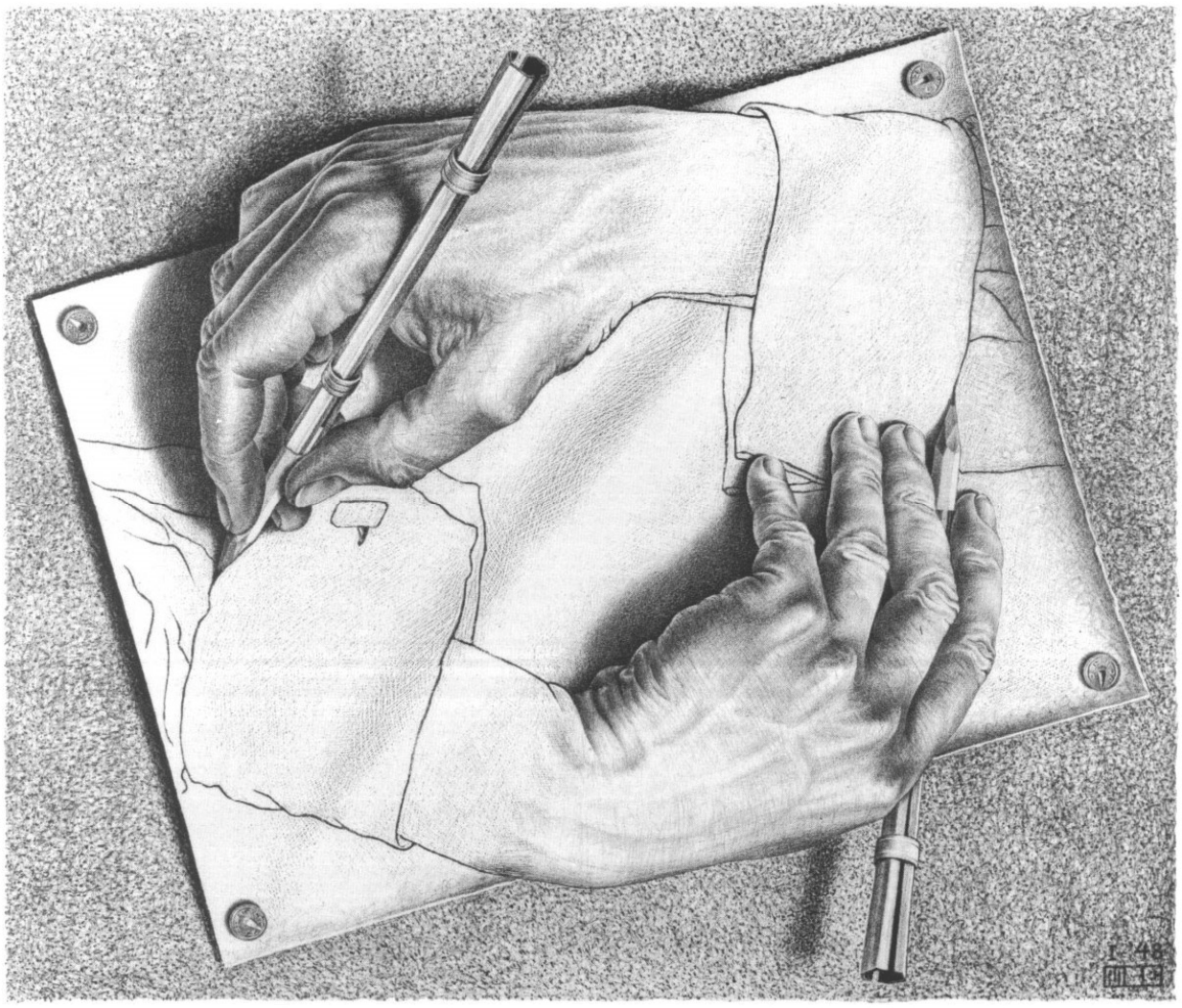

“He who wonders discovers that this in itself is wonder.”

Maurits Cornelis Escher

Table of contents

List of abbreviations

$[Ca^{2+}]_i$ − intracellular Na^+ concentration
$[Na^+]_i$ − intracellular Ca^{2+} concentration
ACh − acetylcholine
AM − acetoxymethyl ester
Amp − ampicillin
APS − ammonium persulfate
BD − bipolar disorder
bp − base pair
BSA − bovine serum albumin
Ca^{2+} − calcium ion
Carb − carbenicillin
CaSR − Ca^{2+}-sensing receptor
Cav − voltage-gated Ca^{2+} channel
CCh − carbachol
cDNA − complementary deoxyribonucleic acid
CHX − cycloheximide
CLIFAHDD − syndrome of congenital contractures of the limbs and face with hypotonia and developmental delay
CLK − CLOCK
CPA − cyclopiazonic acid
cPCR − conventional PCR
CROP − cisplatin resistance-associated overexpressed protein
CS − cisplatin
Cs^+ − cesium ion
CT − cycle threshold (relating to qRT-PCR)
CTRL − control
CTS − cardiotonic steroids
DAG − diacylglycerol
$Dbx1^+$ − developing brain homeobox protein 1
dH_2O − distilled water
DMEM − Dulbecco's Modified Eagle's Medium
DMSO − dimethyl sulfoxide
DNA − deoxyribonucleic acid

dNTP − deoxynucleotide triphosphate
DPBS − Dulbecco's Phosphate Buffered Saline
ds − double stranded
ECL − enhancer of chemiluminescence
ECM − extracellular matrix
EDTA − ethylenediaminetetraacetic acid
EGF − epidermal growth factor
ER − endoplasmic reticulum
EtOH − ethanol
FAK − focal adhesion kinase
FBS − fetal bovine serum
FW − forward
G418 − geneticin
GABA − gamma-aminobutyric acid
GAPDH − glyceraldehyde 3-phosphate dehydrogenase
GFP − green fluorescent protein
GPCR − G-protein coupled receptor
H^+ − hydrogen ion
HBSS − Hank's Balanced Salt Solution
IgG − immunoglubulin G
IHPRF − syndrome of infantile hypotonia with psychomotor retardation and characteristic facies
I_{NALCN} − NALCN-mediated current
I_{NaP} − persistent Na^+ current
I_{NaT} − transient Na^+ current
IP_3 − inositol triphosphate
IP_3R − inositol triphosphate receptor
$iPLA_2$ − Ca^{2+}-independent phospholipase A2
K^+ − potassium ion
K_2P − two-pore domain K^+ channel
Kan − kanamycin
kb − kilobases
KB-R − KB-R7943
kDa − kilo Daltons

LB − Lysogeny Broth
Lwt − lightweight
Lys − Lysine
M_3R − muscarinic receptor 3
MetOH − methanol
MMP − matrix metalloproteinase
mRNA − messenger RNA
MTS − 3-(4,5-dimethylthiazol-2-yl)-5-(3-carboxymethoxyphenyl)-2-(4-sulfophenyl)-2H-tetrazolium
Mya − millions of years ago
NA − narrow abdomen ion channel
Na^+ − sodium ion
NALCN − Na^+ leak channel non-selective
Nav − voltage-gated Na^+ channel
NaVI2.1 − voltage independent Na^+ channel 2.1
NCLX − mitochondrial Na^+/Ca^{2+} exchanger
NCX − Na^+/Ca^{2+} exchanger
NHE1 − Na^+/H^+ exchanger
NK1R − neurokinin 1 receptor
NKA − Na^+/K^+-ATPase
NLF-1 − NCA-localization factor 1
NREMS − non-rapid eye movement sleep
nt − nucleotide
NT − neurotensin
OD − optical density
p − p-value
PAGE − polyacrylamide gel electrophoresis
PBS − phosphate buffer saline
PCa − prostate cancer
PCR − polymerase chain reaction
PDF − pigment-dispersing factor
PER − PERIOD
pH − potential of H^+
pH_e − extracellular pH

pH_i	− intracellular pH
PIP_2	− phosphatidylinositol 4,5-bisphosphate
PMS	− phenazine methosulfate
preBötC	− preBötzinger complex
PTEN	− phosphatase and tensin homolog
Puro	− puromycin
Pyk2	− proline-rich tyrosine kinase 2
qPCR	− quantitative real time PCR
REMS	− rapid eye movement sleep
RIPA	− radioimmunoprecipitation assay buffer
RNA	− ribonucleic acid
RNA-seq	− RNA sequencing
ROS	− reactive oxygen species
rpm	− rotations per minute
RPMI	− Roswell Park Memorial Institute
RT	− reverse transcription
RTN	− retrotrapezoid nucleus
RV	− reverse
SBFI	− sodium-binding benzofuran isophthalate
SCZ	− schizophrenia
SD	− standard deviation
SDS	− sodium dodecyl sulfate
SDS-PAGE	− SDS-polyacrylamide gel electrophoresis
SEM	− standard error of mean
SERCA	− sarco/endoplasmic reticulum Ca^{2+}-ATPase
SFK	− Src-family kinases
SFRB	− sulforhodamine B
shRNA	− short hairpin RNA
siRNA	− small interfering RNA
SNP	− single nucleotide polymorphism
SOC	− Super Optimal broth with Catabolic repression
SOCE	− store-operated Ca^{2+} entry
SP	− substance P
ss	− single stranded

STIM	− stromal interaction molecule
TAE	− Tris-acetate EDTA
TB	− terrific broth
TBE	− Tris-borate EDTA
TBP	− TATA-binding protein
TBS	− Tris buffered saline
TBS-T	− Tris buffered saline Tween 20
TEA	− tetramethylammonium
TEMED	− N-N-N'-N'-tetramethylethylenediamine
TG	− thapsigargin
TNF-α	− tumour necrosis factor α
Tris	− 2-amino-2hydroxy-methylpropane-1,3-diol
TRPC	− transient receptor potential canonical channel
TTX	− tetrodotoxin
UNC	− uncoordinated
UTR	− untranslated region
UV	− ultraviolet
VGCNL1	− voltage-gated channel like protein 1
w/m	− weight per mass
w/v	− weight per volume
WT	− wild type

1. Introduction

1.1 Ion channels

1.1.1 The minds behind ion channel discovery

"**Dr. Henry Frankenstein:**	Look! It's moving. It's alive. It's alive... It's alive, it's moving, it's alive, it's alive, it's alive, it's alive, IT'S ALIVE!
Victor Moritz:	Henry - in the name of God!
Dr. Henry Frankenstein:	Oh, in the name of God! Now I know what it feels like to BE God!"

This quote is taken from the movie "Frankenstein" (1931), based on the original novel of Mary Shelley (1797-1851) written in 1818. Indeed, in 18th century electricity was thought of as a kind of 'vital fluid' that could have been used to bring back life into organisms. Accordingly, 'galvanism' was gaining popularity within both public and scientific communities. The term was named after Italian physicist Luigi Galvani (1737-1798) thanks to his remarkable experiment in 1791 when he made a dead frog's leg to twitch by using electrical current. Later, encouraged by Galvani's work Alessandro Volta (1745-1827) repeated his experiment and found that the frog's leg by itself did not produce electricity but rather served as an indicator of the electricity presence. Moreover, he was the first to build voltaic pile, an early electric battery, after imitating the electric organ of fish. In 1825, Italian physicist Leopoldo Nobili (1784-1835) invented 'astatic galvanometer', one that did not use Earth's magnetic field, which much facilitated measurements of electrical current in frog. In 1835, German physiologist Johannes Peter Müller (1801-1858) proposed his theory of 'the specific nerve energies', which were transmitted by different nerves (e.g. optical, auditive) and identified by brain. Following up on Nobili's work, in 1838 Carlo Matteucci (1811-1868) developed 'rheoscopic frog', consisted of skinned frog's leg with electrical connections to a nerve, and discovered that muscle cells after stimulation by a nerve, produced a current of their own. In 1848, Emil Henrich du Bois-Reymond (1818-1896) noted some 'negative variation' in metallic electrodes connecting the nerve to galvanometer only during nerve stimulation (mechanical or electrical), shown that the frog's nerve exhibit 'action current'. In 1852, Hermann von Helmholtz (1821-1894) determined the velocity of electrical signal on a nerve cell (27 meters/second), which was much slower than conduction in a metal wire. Thus, Hermholtz concluded that nerves carried electrical signal in a different manner than a wire. Overall, little by little scientific discoveries of 19th century were indicating onto underlying chemical processes in nerve and muscle tissues conducting the electrical signals. Subsequently, common at that time

belief into existence of some supernatural living forces, or so called 'vitalism', was progressively rejected.

In 1885, British physiologist Sydney Ringer (1835-1910) discovered that in order to keep the heart beating it had to stay in a saline solution with specific concentrations of Na^+, Ca^{2+} and K^+. Shortly after, German chemist Walther Hermann Nernst (1864-1941) postulated equation of the reduction potential of an electrochemical reaction. In 1912, his student Julius Bernstein (1839-1917) further developed Nernst equation and postulated the ionic theory. According to it, the inactive nerve or muscle fibre is normally electrically polarized, with the external surface positive in relation to the internal one, and that the action potential is a self-propagated depolarization of the membrane. In 1937, British zoologist John Zachary Young (1907-1997) discovered the squid giant axon and the corresponding squid giant synapse. Since squid neuron's diameter is approximately 100 to 1000 times larger than in other animals, it became ultimately convenient model for the electrophysiological studies. In 1939 Alan Lloyd Hodgkin (1914-1998) and Sir Andrew Fielding Huxley (1917-2012), for the first time performed intracellular recording of the squid giant axon potential. In 1949 thanks to work of Ralph Waldo Gerard (1900-1974), Judith Graham Pool (1919-1975), Gilbert Ning Ling (1919-) the glass microelectrode was developed, that enabled researchers to investigate ionic gradients more directly and precisely. Not long after this, Hodgkin with David Goldman (1910–1998) and Sir Bernard Katz (1911-2003) reported on the importance of Na^+ ions to form the action potential. In essence, they found a simple linear relationship between the amount of Na^+ outside the neuron and the amplitude of the action potential. Overall, it was elucidated that neurons conduct messages along their length due to Na^+ influx and K^+ efflux, which is generating travelling change in the membrane potential that can be then detected by another cell and thus transmit the signal further.

The next instrumental improvement performed by Kenneth Stewart Cole (1900-1984) and George Marmont (n/a) in 1949, involved placing a second glass electrode inside the cell in order to 'voltage clamp' the cell. This discovery enabled researchers to distinguish the voltage changes induced by the actual plasmalemmal ion passage from those made deliberately by the experimenter. In 1952, Hodgkin and Huxley described the first mathematical theory that proposed existence of the ion channels. Indeed, the discovery of specific pore blockers, like tetrodotoxin (TTX) for Na^+ and tetramethylammonium (TEA) for K^+, proved the simultaneous presence of differently controlled membraner pores. In addition, thanks to the radioactive tracers, the movements of ions in nerve axons were successfully monitored. Overall, the observed results indicated onto existence of specific 'single narrow pores', or so called channels, letting the ions to pass. In 1971, American biophysicist Bertil Hille (1940-) proposed that ion channel consists of the

specific structure part, named ‘filter’, which controls ion movements and is about 3-5 Å in size. In 1976, Erwin Neher (1944-) and Bert Sakmann (1942-) invented the ‘patch clamp’ method. Since then, it became possible to detect currents smaller than 10^{-12} Amperes (A), sensitive enough to measure ion flow though the single channel molecule. It was through this technique that the presence of ion channels was confirmed with sufficient physical evidence and the processes that take place within a single ion channel were uncovered

Noteworthy, in 1970, there were only 3 scientific publications with the term ‘channel’. By 1980 the number raise over 300, and by 1990 over 1000. By 2017, PubMed offers more than 240,000 scientific articles using ‘ion channel’ in their titles. The main highlights of the events leading towards such broad acceptance of the ion channel concept by the scientific community are presented in the chronological manner in Figure 1.

18th century - Galvanism

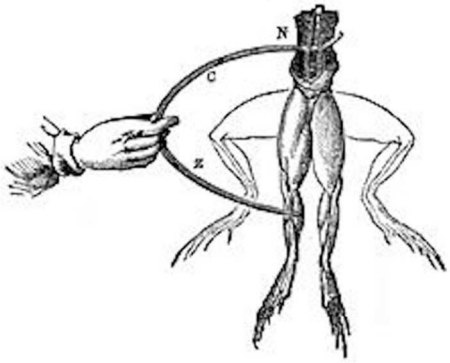

1912 - Nernst equation

$$E = \frac{RT}{zF} \ln \frac{[ion]_e}{[ion]_i}$$

1939 – recording of an action potential in squid giant axon

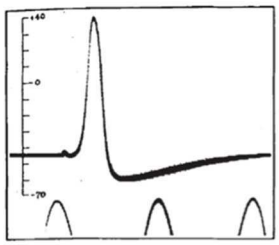

Fig. 2.

ACTION POTENTIAL RECORDED BETWEEN INSIDE AND OUTSIDE OF AXON. TIME MARKER, 500 CYCLES/SEC. THE VERTICAL SCALE INDICATES THE POTENTIAL OF THE INTERNAL ELECTRODE IN MILLIVOLTS, THE SEA WATER OUTSIDE BEING TAKEN AT ZERO POTENTIAL.

1971 – selectivity filter in cell membrane

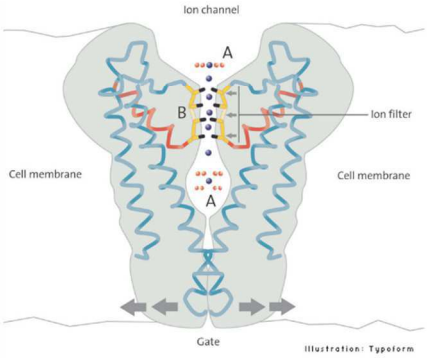

1976 – patch clamp technique

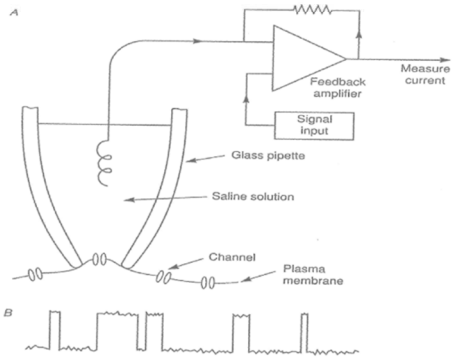

Figure 1. Scientific discoveries that led to acceptance of the ion channel concept.
In 1791, Luigi Galvani made a dead frog's leg to twitch by using electrical current. In 1912, Julius Bernstein developed the equation proposed by Walther Nernst. According to it, the inactive nerve or muscle fibre is normally electrically polarized, with the external surface positive in relation to the internal one, and that the action potential is a self-propagated depolarization of the membrane. In 1939, Hodgkin and Huxley for the first time recorded the action potential in squid giant axon. In 1971, Hille reported on existence of a specific structure in cell membrane, named 'filter', which controls ion movements and is about 3-5 Å in size. In 1976, Neher and Sakmann invented the 'patch clamp' method, sensitive enough to measure the ion conductance of a single ion channel.

1.1.2 Diversity and structural properties

The ion transporting proteins are integral membrane molecules (whether plasmalemmal or organellal) that can be functionally classified into pumps, transporters and channels (Figure 2). The main difference is that pumps and transporters are using so called 'active transport', whereas ion channels – exclusively 'passive transport', which is the diffusion of ions along their electrochemical gradient. Pumps utilize metabolic energy (e.g. ATP hydrolysis) and can transport limited amount of ions against the electrochemical gradient. Ion transporters work by the mean of 'secondary active transport', that relies on electrochemical potential difference. Transporters move ions down the electrochemical gradient, but possibly against the concentration gradient. Importantly, the charge of transported ions determines whether the transport is 'electroneutral' (does not generate electrical current), or 'electrogenic'.

Of note, the most distinctive features of ion channels that differentiate them from other types of ion transporting proteins are as follows:

- high rate of ion diffusion - around 10^6-10^8 ions/second;
- the filter pore is around 3-5 Å in diameter; and
- their functioning allows ion to pass through the pore down the electrochemical gradient, hence it creates electric current and is intrinsically electrogenic.

Ion channels greatly differ in their structure (Figure 3). Typically, they are consisted of two or more transmembrane segments that are organized in a pore-forming subunit. Ion channels can be represented whether as an individual large polypeptide (monomer) or as the assemblies of several proteins (multimer). The latter may be formed by the identical proteins (homomeric ion channel) or by the products of the different genes expression (heteromeric ion channel).

1.1.3 Classification by gating

The term 'gating' refers to the opening (activation) or closing (by deactivation or inactivation) of ion channel. They could be distinguished following major classes of the ion channels depending on their mode of activation (Figure 4):

- Mechano-operated ion channels – activated due to the membrane stretch. For example, the application of phospholipids drives plasma membrane perturbations, which in turn are detected by C-terminal of $K_{2P}2.1$, that activates the channel and hence leads to K^+ efflux (Patel *et al.*, 1998).

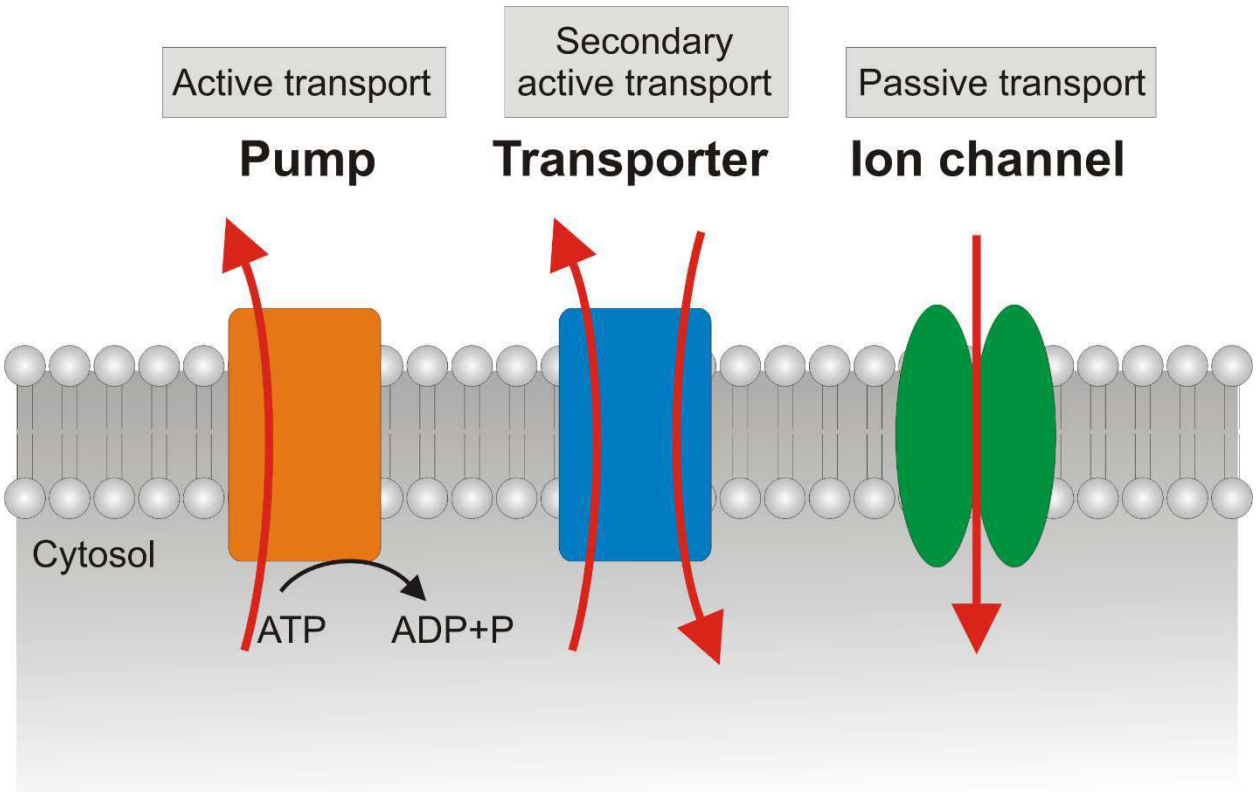

Figure 2. Ion transporting proteins.
Ion transporting proteins are membrane-embedded proteins or protein complexes that span the lipid bilayer several times to create an ion translocation pathway. Functionally, ion transporting proteins can be classified into pumps, transporters and channels. Modified from (Jentsch, 2016).

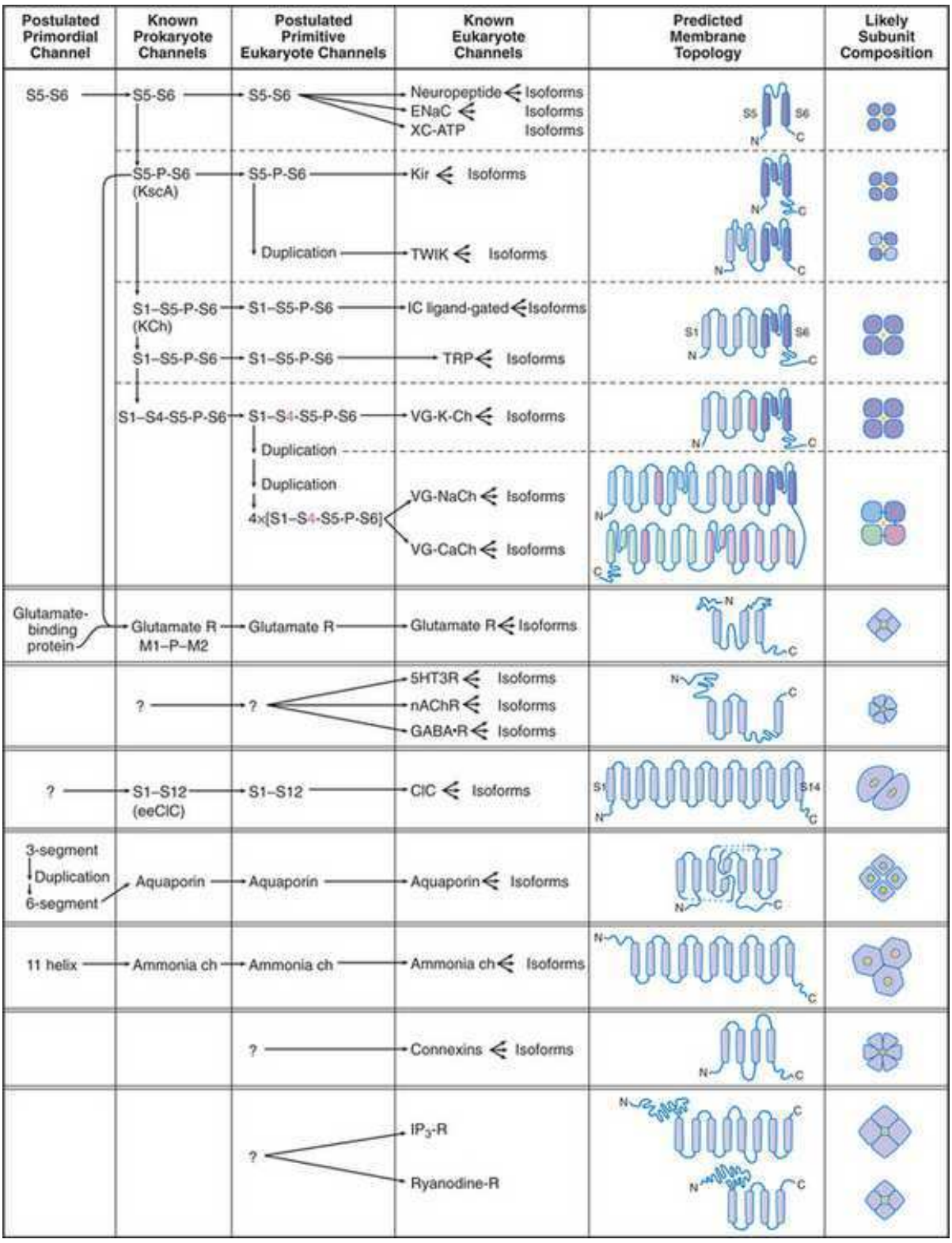

Figure 3. Diversity of ion channel proteins.
This scheme is based on primary structure, atomic structures (where known), and postulated evolutionary origins. The predicted transmembrane topology has the extracellular side at the top and uses rectangles to indicate helices labeled "S." P loops are shown as a short helix and loop between two transmembrane helices. The last column shows the known (or likely) subunit compositions. Adapted from (Pollard & Earnshaw, 2008)

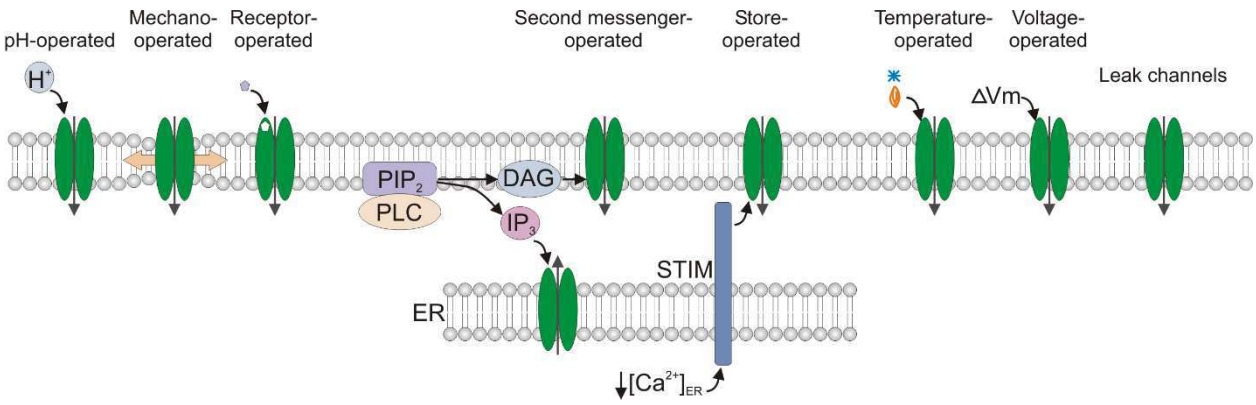

Figure 4. Ion channels classification by the gating properties.

- pH-operated ion channels – activated by the changes in pH. For example, acid-sensing ion channels, ASICs, are activated by the presence of extracellular protons (H^+) and permeate Na^+ entry (Gründer & Pusch, 2015).
- Receptor-operated ion channels – activated by extra- or intracellular ligands. For example, the binding of glutamate and glycine activates N-methyl-D-aspartate receptors and thus modulates flow of positively charged ions though the membrane channel (Furukawa *et al.*, 2005).
- Second messenger-operated ion channels – activated by the second messengers. Phospholipase C degrades plasmalemmal phosphatidylinositol 4,5-bisphosphate (PIP_2) into inositol triphosphate (IP_3) and diacylglycerol (DAG). Both second messenger molecules stimulate activation of various ion channels. For example, IP3 activates endoplasmic reticulum (ER) residing IP3 receptor (IP3R) and thus leads to the release of Ca^{2+} from intracellular stores (Ross et al., 1989).
- Store-operated ion channels – activated due to the Ca^{2+} store depletion. For example, decreased Ca^{2+} level in ER is detected by the stromal molecule interaction protein (STIM), which in turn via clustering under plasma membrane activate ORAI1 channel and thus trigger significant intracellular Ca^{2+} entry (Gonzalez *et al.*, 2014).
- Temperature-operated ion channels – activated by changes in temperature. For example, TRPM8 channel is activated by cold temperatures and cooling agents, such as menthol and icilin, and as a result permeates Na^+ and Ca^{2+} ions.
- Voltage-operated ion channels – activated by changes in the resting membrane potential. For example, voltage sensing S4 segment of Nav1.5 channel responds to the level of membrane potential, which leads to the changes in protein conformation and pore opening for Na^+ influx (Catterall, 2012).

It is important to note, that another class of ion channels exists. In contrast to others, it does not exhibit any specific gating properties and hence was suggested to represent the ion channels that are constitutively open or possess high basal activation. For this reason, they were named as 'leak channels'. It is generally considered that leak ion channels are required to set up the resting membrane potential. Indeed, two-pore domain (K_2P), or so called 'leak K^+ channels' give rise to background K^+ currents that are responsible for the resting membrane potential and input resistance (Renigunta *et al.*, 2015). Interestingly, even channels from other families were suggested to possess some background/leak currents. For example, the current generated by

voltage-operated Na^+ channels exhibits two distinct components: fast-inactivating current with high amplitude, named as transient current (I_{NaT}), and persistent current component with low amplitude (I_{NaP}). Importantly, I_{NaP} manifests itself significantly under a variety of pathophysiological conditions, including cancer (Kiss, 2008; Djamgoz & Onkal, 2013) (Figure 5). Thus, in addition to being already applied for a range of coronary conditions (e.g. angina, arrthymia) I_{NaP} blockers were suggested as the highly promising potential candidates for cancer treatment (Djamgoz & Onkal, 2013). Overall, it highlights the importance of background Na^+ leak in various physio- and pathological processes.

Importantly, another channel that provides background Na^+ current was recently discovered (Snutch & Monteil, 2007). In fact, the main function of this channel is to provide basal Na^+ and to lower extent K^+ and Ca^{2+} leak, hence the name – Na^+ leak channel non-selective (NALCN) (Lu *et al.*, 2007). Although NALCN was shown to maintain the resting membrane potential and thus was already associated with neuronal physiology, very little is yet known about its implication in other tissues and pathologies (Lee *et al.*, 1999; Lu *et al.*, 2007). Therefore, this PhD project is devoted to widen our understanding on Na^+ leak provided through NALCN with particular focus on cancer pathophysiology.

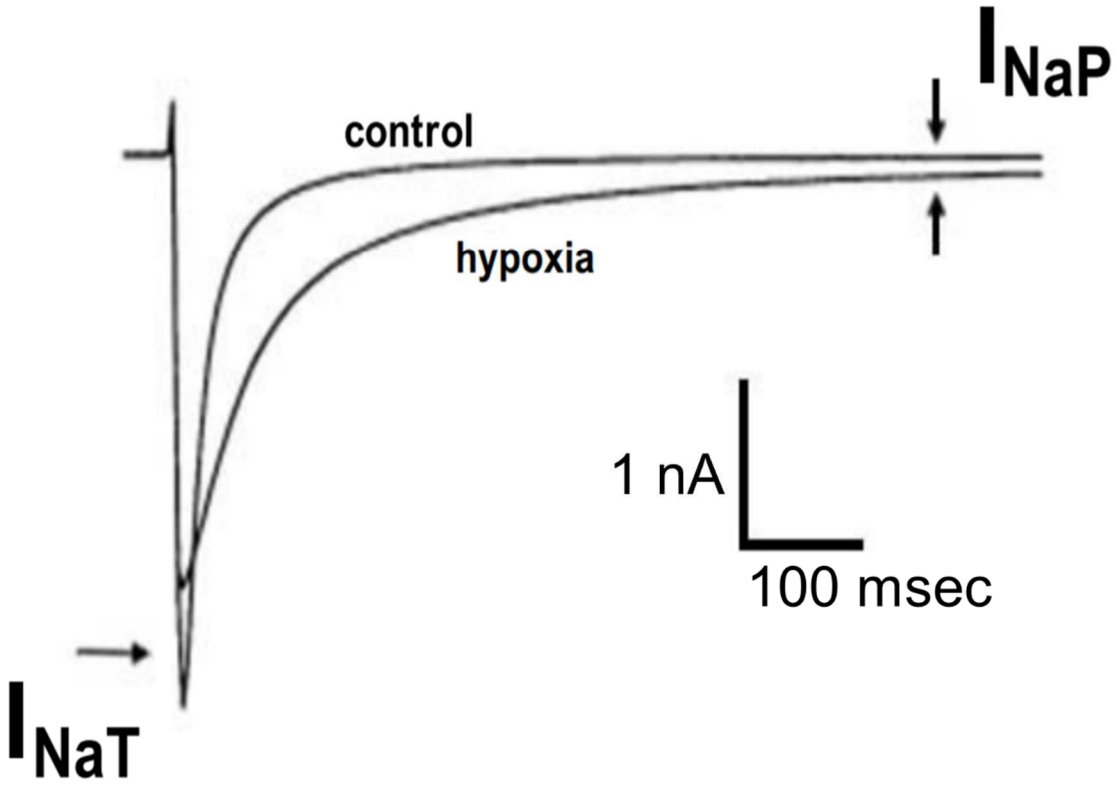

Figure 5. Activity of voltage-operated Na^+ channels.
Importantly, the membrane current generated by voltage-operated Na^+ channels has two distinct components: classic 'transient' component (I_{NaT}) lasting a miliseconds and a 'persistent' phase (I_{NaP}) which is only <1 % of the corresponding I_{NaT} but can outlast it by hundreds of miliseconds - seconds, even at positive membrane potentials. Interestingly, the condition of oxygen deprivation, named hypoxia, that often occurs during tumourigenesis, was shown to preferentially enhance I_{NaP}. Therefore, background Na^+ leak plays remarkable role in various physio- and pathological conditions. Adapted from (Djamgoz & Onkal, 2013)

1.2 Sodium leak channel non-selective, NALCN

1.2.1 Discovery and structure

In 1999, Perez-Reyes and colleagues cloned a novel protein from rat brain (Lee *et al.*, 1999). Based on its sequence and structure similarities with voltage-gated Ca^{2+} (Cav) and Na^+ channels (Nav), novel protein was proposed to be the 21st member of the voltage-gated cation channel family and hence named Rb21 (Lee *et al.*, 1999) (Figure 6). Despite multiple attempts, the current for this putative channel was not detected at that time. However, Rb21 was found to be highly expressed in human brain, moderately in heart, and weakly in pancreas (Lee *et al.*, 1999). Later, it was discovered that Rb21 is voltage-insensitive nonselective cation channel, responsible for the TTX- and cesium (Cs^+)-resistant background Na^+ leak current (Lu *et al.*, 2007). Since then, it was renamed onto Na^+ leak channel non-selective, or NALCN. Of note, it might be also referred to as voltage independent Na^+ channel 2.1 ($Na_VI2.1$) or voltage-gated channel like protein 1 (VGCNL1) in mammals, narrow abdomen ion channel (NA) in fruit fly *Drosophila melanogaster* and NCA-1/2 in nematode *Caenorhabditis elegans* (Nash *et al.*, 2002; Yu & Catterall, 2004; Humphrey *et al.*, 2007).

Interestingly, in almost all organisms (except of nematode, cnidarian and sponge) NALCN is encoded only by one gene (Liebeskind *et al.*, 2012; Senatore *et al.*, 2013). Noteworthy, the phylogenetic analysis indicates onto evolutionary transformation of NALCN selectivity filter from Ca^{2+} (EEEE) towards Na^+ (EKEE or EEKE) (Senatore & Spafford, 2013; Senatore *et al.*, 2013) (Figure 7). This adaptation may be explained by the requirement for organism conversion from Ca^{2+}-dependent to Na^+-dependent depolarization (discussed in 1.1.1.1 section 'Hypothetical point of view on the evolution of ion channels'). As a result, the speed of conduction considerably accelerated: unlike Ca^{2+} ions, Na^+ ions do not interfere with any of the cellular processes, and hence the quantity of plasmalemmal Na^+ channels as well as the density of generated inward current, could be greatly elevated (Franciolini & Petris, 1989). Indeed, the simplest and oldest animals and their eukaryote relatives (e.g choanoflgellates, sponges, protists, poriferans, and placozoans), which lack nervous systems, possess only Ca^{2+}-selective channels. Accordingly, it was suggested that Ca^{2+}-permeable channels, including some Cav and NALCN with EEEE selectivity filter, evolved earlier than Nav, possibly from the common predecessor (Figure 8). Importantly, the inclusion of amino-acid residue Lysine (Lys) into the channel pore switched the preference of filter selectivity over Ca^{2+} towards Na^+ ions (Dudev & Lim, 2014). Therefore, the co-appearance of channels with Lys residue in the pore (EKEE and EEKE for NALCN, and DEKA for Nav) is consistent with the evolution of Na^+ to generate membrane excitability, and simultaneously to avoid redundancy of signalling crossover introduced by Ca^{2+} influx (Figure 9).

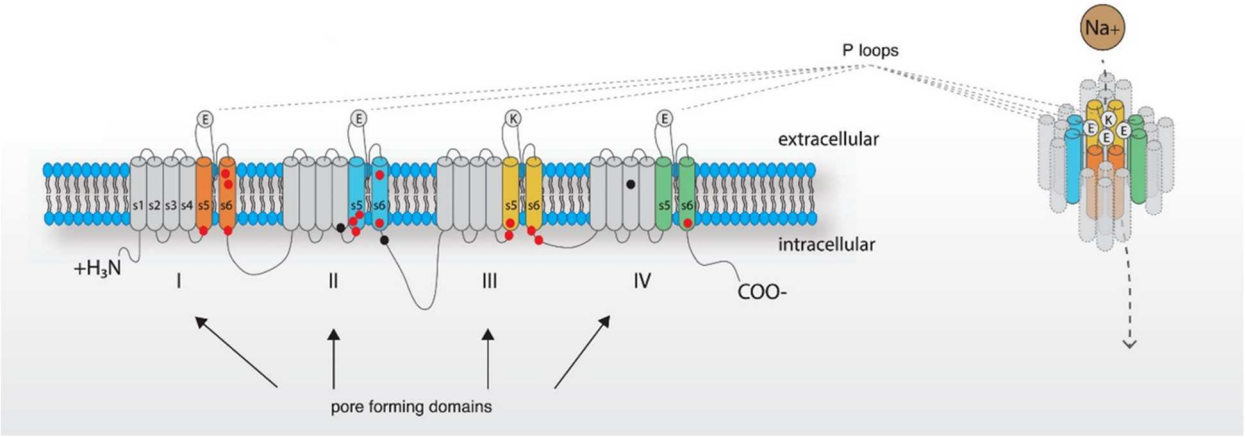

Figure 6. NALCN protein structure.
NALCN consists of 4 domains (I-IV), each of which possess 6 transmembrane segments (S1-S6). N- and C-terminals are intracellular. The ion channel filter is formed due to the conformational proximity of S5, p-loop and S6 elements from each domain. The sequence of amino-acid residues of each p-loop element predetermines the filter selectivity, which in humans is represented by EEKE motif. S4 segments lack positively charged amino-acid residues, and hence precondition voltage-insensitivity of NALCN. Adapted from (Chong *et al.*, 2015).

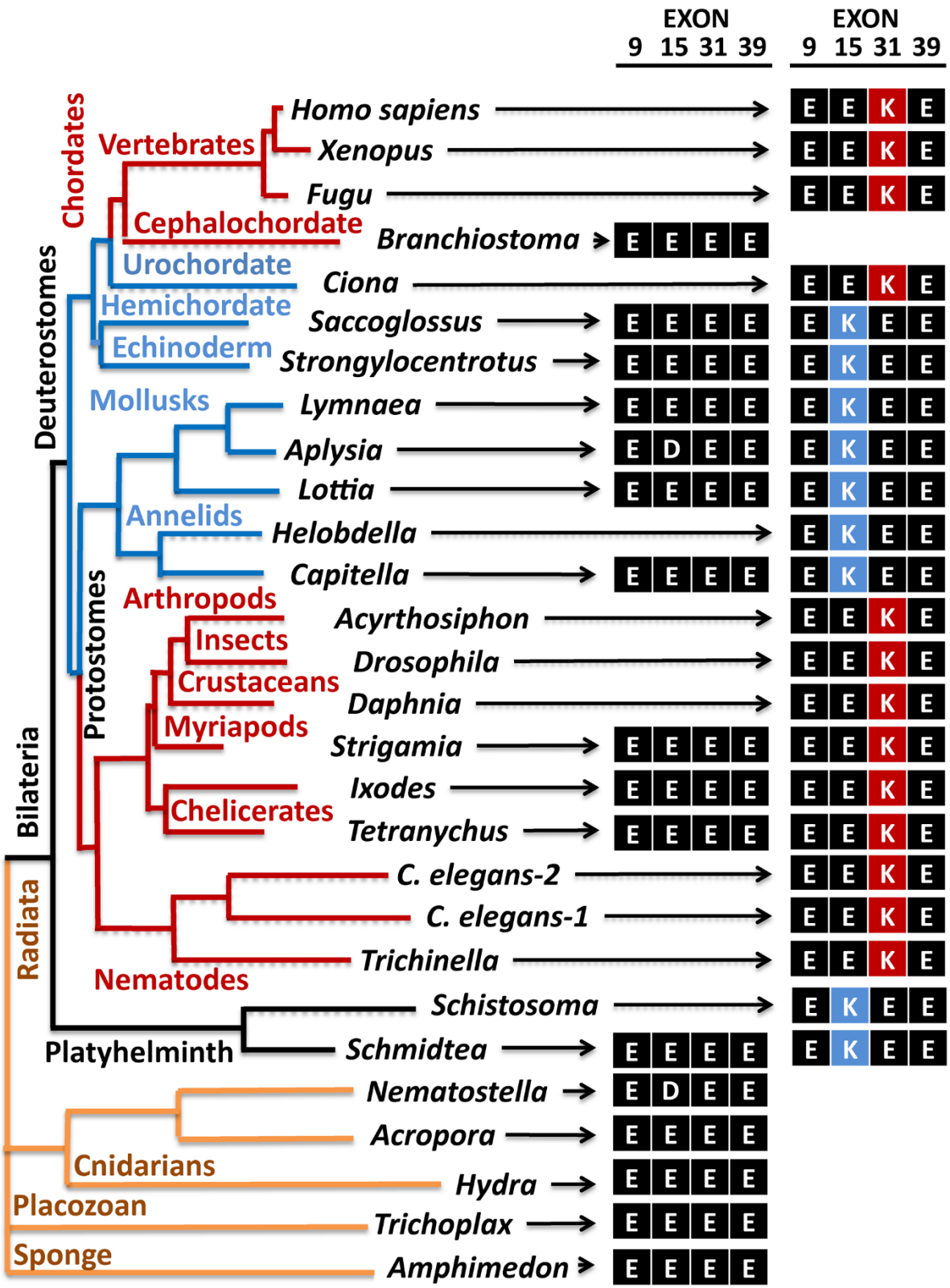

Figure 7. Illustration of the NALCN selectivity filter evolution.
Metazoan genomes represent alternative selectivity filters of NALCN. First, it appears to possess Ca^{2+}-selective pore (EEEE or EDEE). Later, the appearance of Lysine amino-acid residue in the pore, switches it selectivity towards Na^{+} (EKEE or EEKE). Adapted from (Senatore *et al.*, 2013).

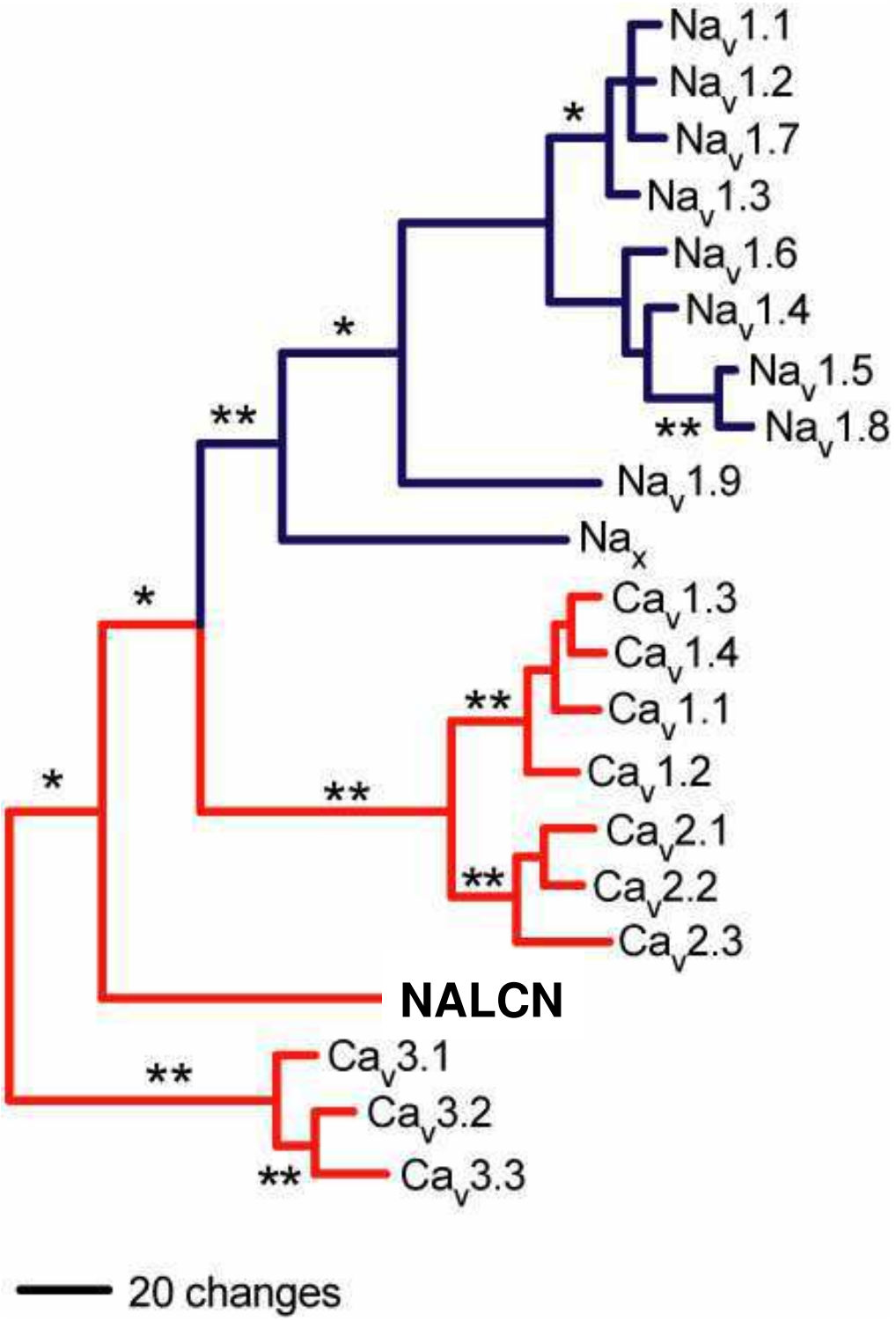

Figure 8. Phylogenetic tree of 4x6TM protein family.
Tree was rooted to the bacterial sodium channel (NachBac), but this branch is not shown in the figure. Bootstrap values of 50 to 74% are depicted by an asterisk (*); values of 75 to 100% are depicted by **; and those that are <49% are not shown. The scale bar corresponds to the number of changes needed to explain the differences in the protein sequences. Vertical branch length is not significant. Adapted from (Yu & Catterall, 2004).

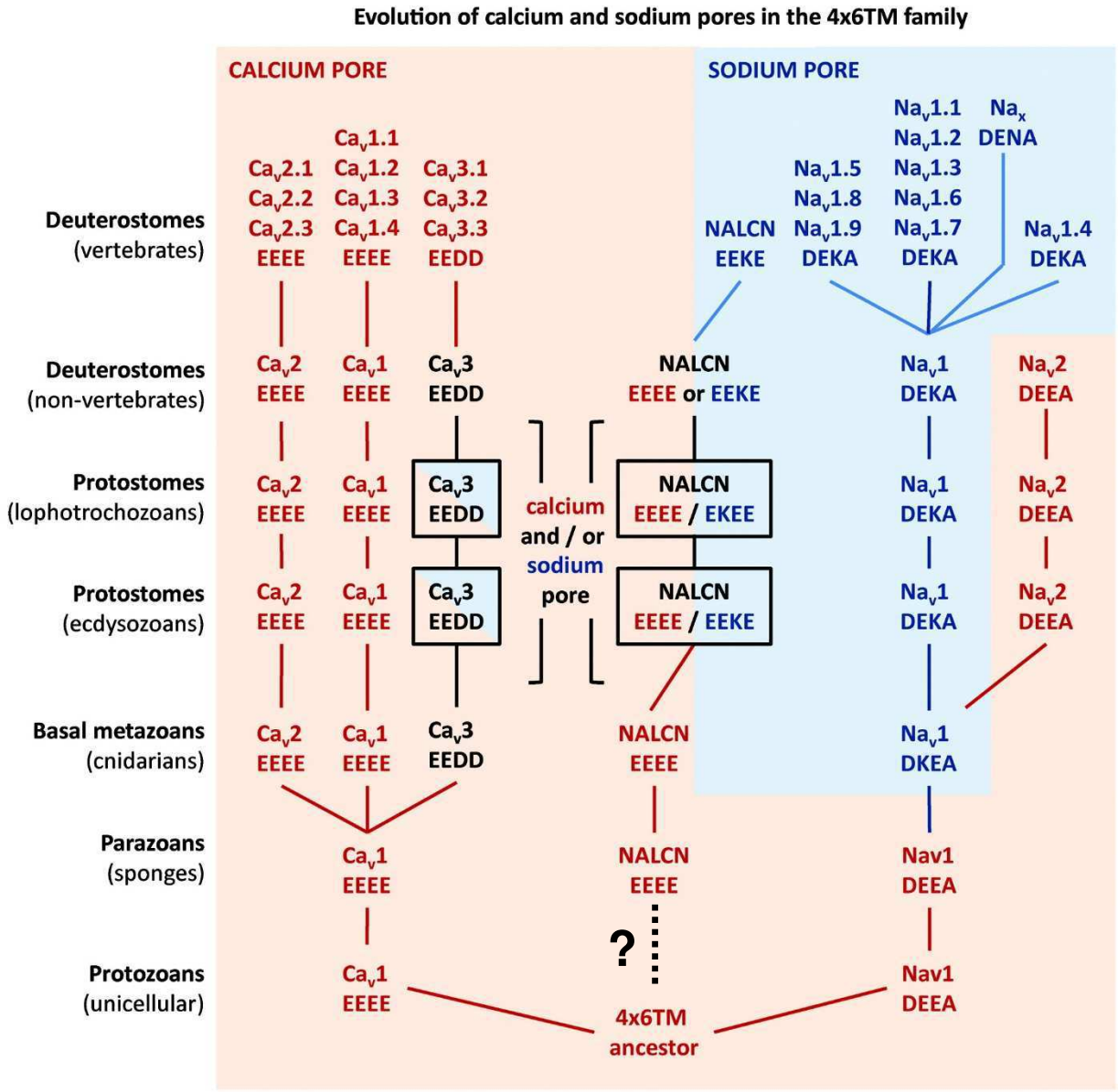

Figure 9. Evolutionary conversion of 4x6TM ion channel family from Ca^{2+}- to Na^{+}-permeability.
The simplest and oldest animals and their eukaryote relatives (choanoflgellates, sponges, protists, poriferans, and placozoans), which lack nervous systems, possess only Ca^{2+}-selective channels. The co-appearance of NALCN (EKEE and EEKE) and Nav (DEKA) channels with a Lysine residue in the pore is consistent with the evolution of Na^{+} ions to generate membrane excitability in nervous systems, circumventing the toxicity that intracellular Ca^{2+} ions have as agents for membrane depolarization. Adapted from (Senatore & Spafford, 2013)

In mammals, *NALCN* is a highly conserved gene (99% identity between human and mouse) (Lu & Feng, 2012) (Figure 10). In humans, the gene encoding *NALCN* is located on chromosome 13 and comprises at least 44 exons (43 coding exons) (Figure 11). On the protein level, it consists of 1738 amino-acid residues and has a predicted topology similar to Nav and Cav channels (Snutch & Monteil, 2007). However, unlike in Nav and Cav channels, the S4 transmembrane segments of NALCN possess fewer amino acid residues with positive charge (e.g. Arginine and Lysine), especially in domains II and IV, and thus lack voltage sensitivity in NALCN (Senatore *et al.*, 2013). Several splice variants of NALCN were identified, however, there is still not much known about their functioning and physiological role (Figure 12).

1.2.2 Functional properties

The very first functional characterization of NALCN as a Na^+ leak channel was performed only 10 years ago (Lu *et al.*, 2007; Snutch & Monteil, 2007). At that time it was discovered that NALCN is one of the few channels in the 4x6TM channel family required for the neonatal survival (Lu *et al.*, 2007). Although the newborns of $NALCN^{-/-}$ mice did not exhibit apparent abnormalities, they did not survive beyond 24 hours after birth (Lu *et al.*, 2007). Importantly, regular rhythmic respiratory activities of null mice were significantly disrupted, more likely due to the defects in electrical signaling of the nervous system, conditioned by *NALCN* deletion (Lu *et al.*, 2007). Furthermore, the hippocampal neurons of null mice were hyperpolarized by around 10 mV, when compared to the wild-type mice (Lu *et al.*, 2007). Moreover, the frequency of continuous firing was significantly reduced in NALCN knock-out neurons, indicating onto the channel importance for neuronal excitability (Lu *et al.*, 2007). Overall, it was concluded that NALCN contributes to the resting membrane potential by providing a depolarizing current that assists in counterbalance of the hyperpolarizing current induced by K_{2P} channels (Ren, 2011; Lu & Feng, 2012). Indeed, TTX-insensitive background Na^+ leak current was absent in NALCN mutant neurons and was restored by transient expression of NALCN using cDNA transfection (Lu *et al.*, 2007). In addition, it was suggested that together with Na^+ NALCN permeates other ions ($Na^+ > K^+ > Cs^+ > Ca^{2+}$), and thus it lacks the ion selectivity (Lu *et al.*, 2007). Taken together, widely expressed in neurons voltage-independent, non-selective NALCN current (I_{NALCN}) provides around 70% of the total basal Na^+ leak, with reverse potential approximately at 0 mV (Figure 13).

Identity to Homo sapiens	Genes	Alternate names	Accession no.		Phylum	Species
			mRNA	Protein		
100 %	*NALCN*	VGCNL1	XM_001149573	XP_001149573	Chordata	*Pan troglodytes*
99 %	*NALCN*	VGCNL1	NM_177393	NP_796367	Chordata	*Mus musculus*
99 %	*NALCN*	VGCNL1	XM_542654	XP_542654	Chordata	*Canis lupus familiaris*
99 %	*NALCN*		XM_001492809	XP_001492859	Chordata	*Equus caballus*
99 %	*NALCN*		XM_003270152	XP_003270200	Chordata	*Nomascus leucogenys*
99 %	*NALCN*		XM_002713013	XP_002713059	Chordata	*Oryctolagus cuniculus*
98 %	*NALCN*		XM_001513615	XP_001513665	Chordata	*Ornithorhynchus anatinus*
98 %	*NALCN*	VGCNL1	XM_416967	XP_416967	Chordata	*Gallus gallus*
98 %	*NALCN*		XM_001366005	XP_001366042	Chordata	*Monodelphis domestica*
98 %	*NALCN*		XM_002914851	XP_002914897	Chordata	*Ailuropoda melanoleuca*
96 %	*NALCN*	VGCNL1	XM_002691980	XP_002692026	Chordata	*Bos taurus*
96 %	*NALCN*	VGCNL1	NM_153630	NP_705894	Chordata	*Rattus norvegicus*
96 %	*NALCN*		XM_003218712	XP_003218760	Chordata	*Anolis carolinensis*
92 %	*NALCN*		XM_003451547	XP_003451595	Chordata	*Oreochromis niloticus*
90 %	*NALCN*		NM_001017549	NP_001017549	Chordata	*Danio rerio*
79 %	*NALCN*		XM_003482928	XP_003482976	Chordata	*Sus scrofa*
57 %	*na*	alpha1U, Dmα1U	NM_001103511	NP_001096981	Arthropoda	*D. melanogaster*
55 %	*U*-type		AF484086	AAO84496	Mollusca	*Lymnaea stagnalis*
48 %	*nca-1*		NM_171352	NP_741413	Nematoda	*Caenorhabditis elegans*
48 %	*nca-2*		NM_065653	NP_498054	Nematoda	*Caenorhabditis elegans*

Figure 10. Homology of NALCN between *Homo sapiens* and other species.
Adapted from (Lu & Feng, 2012).

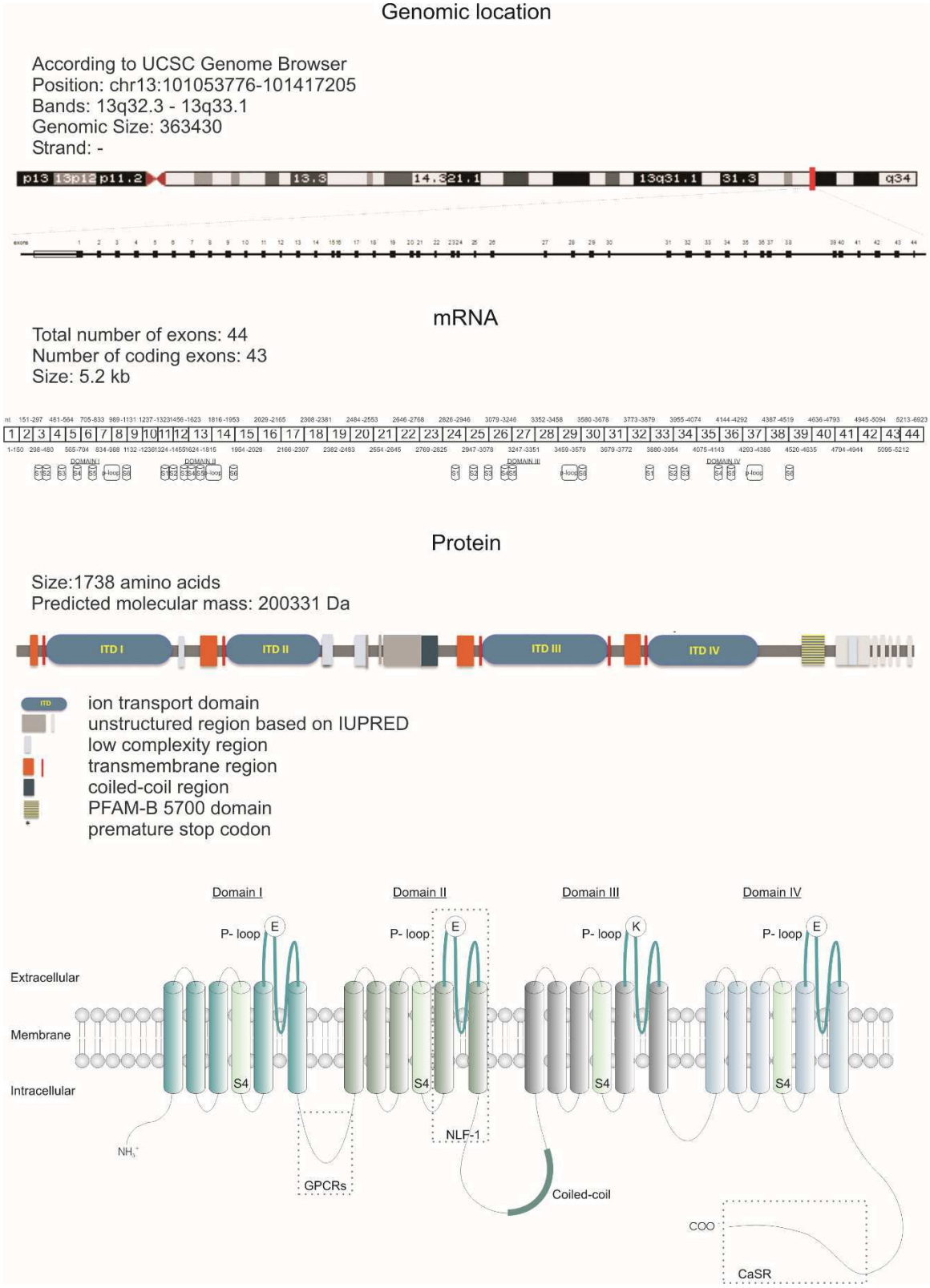

Figure 11. Human NALCN.
The gene encoding *NALCN* is located on chromosome 13 and comprises at least 44 exons. NALCN is a 1738 amino-acids protein that forms the channel similar to Nav and Cav. The selectivity filter is represented by EEKE motif. The putative interaction sites with other molecules are indicated.

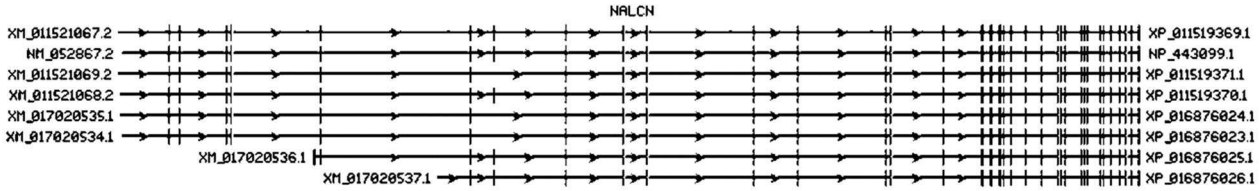

Figure 12. Alternative splice variants of NALCN.
According to the NCBI database by September 2017.

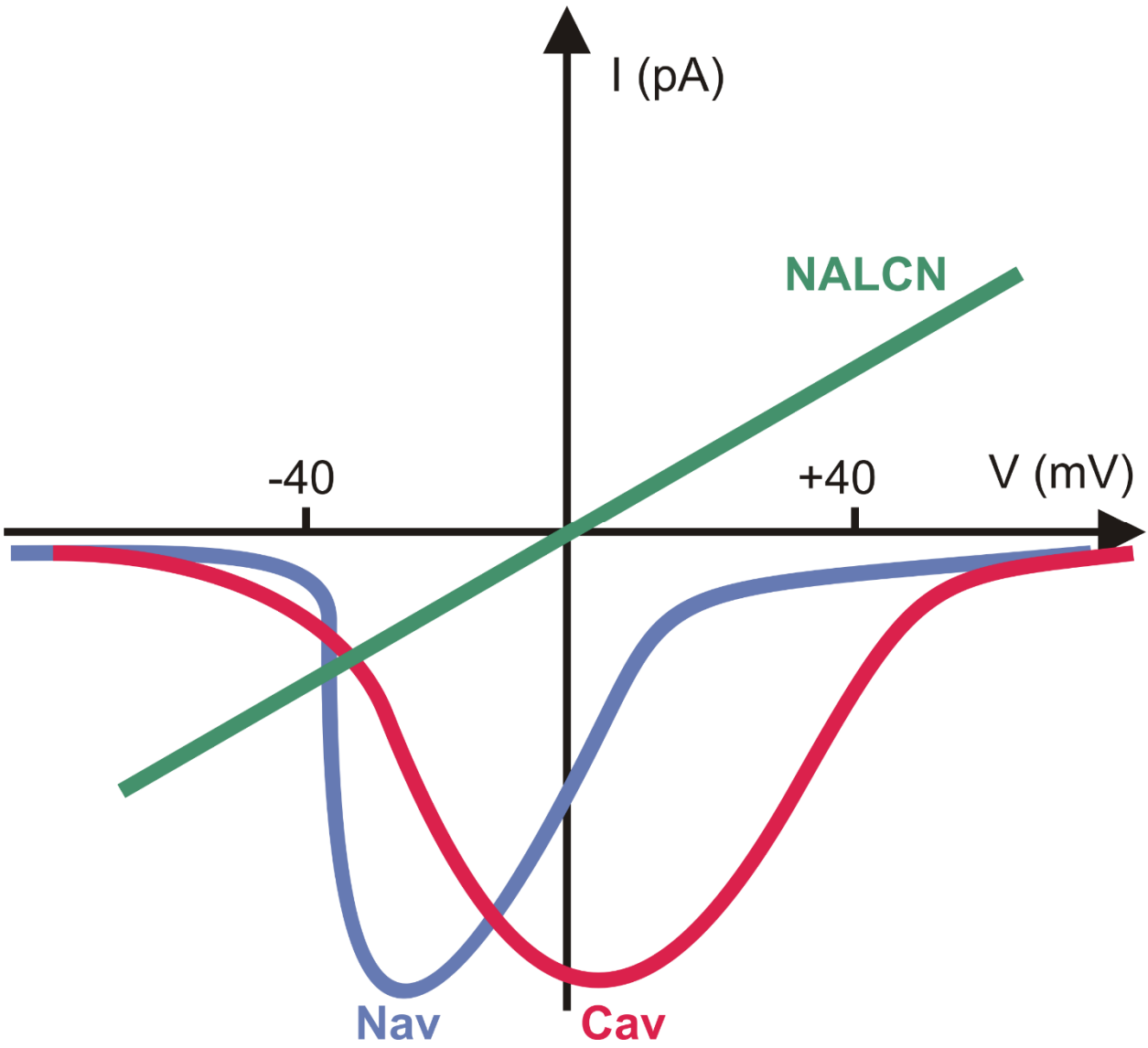

Figure 13. Illustrative current-voltage relationships of the 4x6TM ion channel family. Modified from (Ren, 2011).

In contrast to the evidence that NALCN provides constitutive background current, another study in pancreatic cancer cells reported on activation of NALCN-mediated Na^+ current through M3 muscarinic receptor (M3R) (Swayne *et al.*, 2009). Similarly, in mouse hippocampal and ventral tegmental area neurons NALCN current was found to be activated by neuropeptides such as substance P (SP) and neurotensin (NT), more likely through its coupling with neurokinin 1 receptor (NK1R) (Lu *et al.*, 2009). Interestingly, both G protein-coupled receptor (GPCR) pathways (mediated though M3R and NK1R) exhibited G protein-independent signalling mostly relying on the activity of Src family of tyrosine kinases (SFK) (Lu *et al.*, 2009; Swayne *et al.*, 2009). On contrary, another GPCR, the Ca^{2+}-sensing receptor (CaSR), was found to act through G-protein-dependent and SFK-independent pathway leading to inhibition of NALCN-mediated current (Lu *et al.*, 2010). Taken together, these studies provided first evidence that in addition to its basal Na^+ leak function, NALCN might being regulated by GPCRs, possibly with some tissue-dependent mode of operation. Nevertheless, much still remains to be determined about functional properties and regulation of NALCN.

1.2.3 Channelosome complex

Like many ion channels, NALCN is associated with several proteins to form a larger channel complex, named as NALCN channelosome (Figure 14). These auxiliary subunits were shown to play role in the folding, stabilization, cellular localization, and to some extent function of the channel complex. The main members of NALCN channelosome are described below.

1.2.3.1 UNC-80

Homolog of *C. elegans* uncoordinated locomotion protein 80, UNC-80, (alternatively KIAA1843, C2orf21) was first cloned from human cDNA library in 2001 (Nagase *et al.*, 2001). It is located on chromosome 2, cytoband q34, on the (+) strand with genomic size around 230 kb. UNC-80 mRNA is comprised of presumably 64 exons, around 13.5 kb in length. UNC-80 is a large protein of about 3,300 amino-acid residues, with predicted size around 360 kDa. Any transmembrane segments or particular functional domains of UNC-80 were not yet identified. According to NCBI database, several splice variants of human UNC-80 exist (Figure 15A).

UNC-80 is a central ‘connector’ of NALCN channelosome. Indeed, major members of the channel complex, in particular, UNC-79, SFK, and NALCN itself, all directly interact with UNC-80, but not with each other (Lu *et al.*, 2010). In particular, UNC-80 acts as scaffold protein for SFK and UNC-79 (Wang & Ren, 2009). Such cooperation with UNC-80 was found being important for NALCN activation, specifically, by the means of unique mechanism:

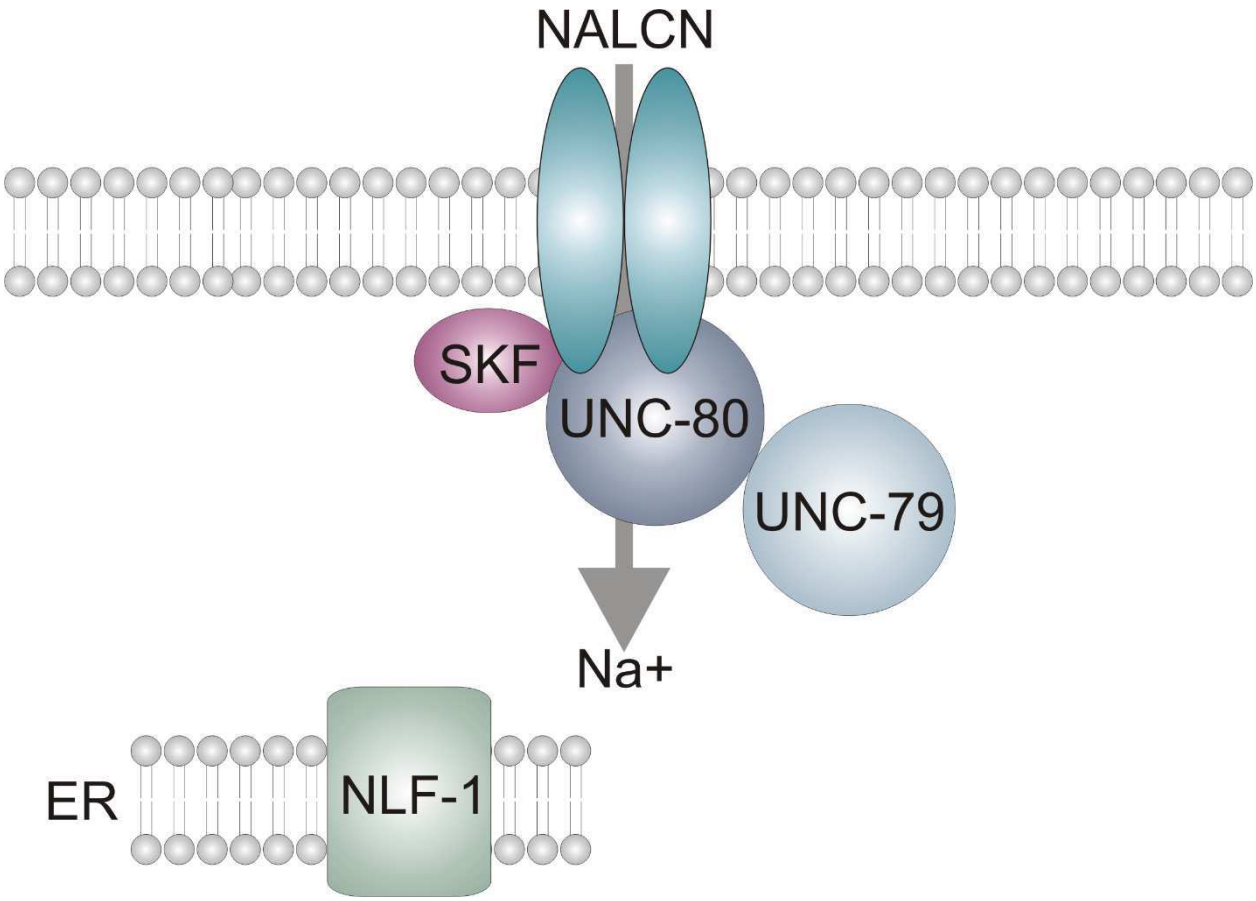

Figure 14. Schematic representation of NALCN channelosome.
UNC79 and UNC80 represent auxiliary subunits of the NALCN channel: UNC80 directly physically interacts with UNC79 on one hand and with NALCN on the other; UNC79 affects UNC80 protein levels. UNC-80 interacts with NALCN and SFKs and acts as a scaffolding protein. UNC-79 interacts with UNC-80 but not NALCN and is involved in the expression levels and the neuronal localization of NALCN and UNC-80. NLF-1, an endoplasmic reticulum-resident protein that interacts with NALCN and is possibly involved in its folding is shown apart. Overall, regulation of the NALCN channel complex is extremely important for controlling neuronal excitability. Modified from (Senatore *et al.*, 2013).

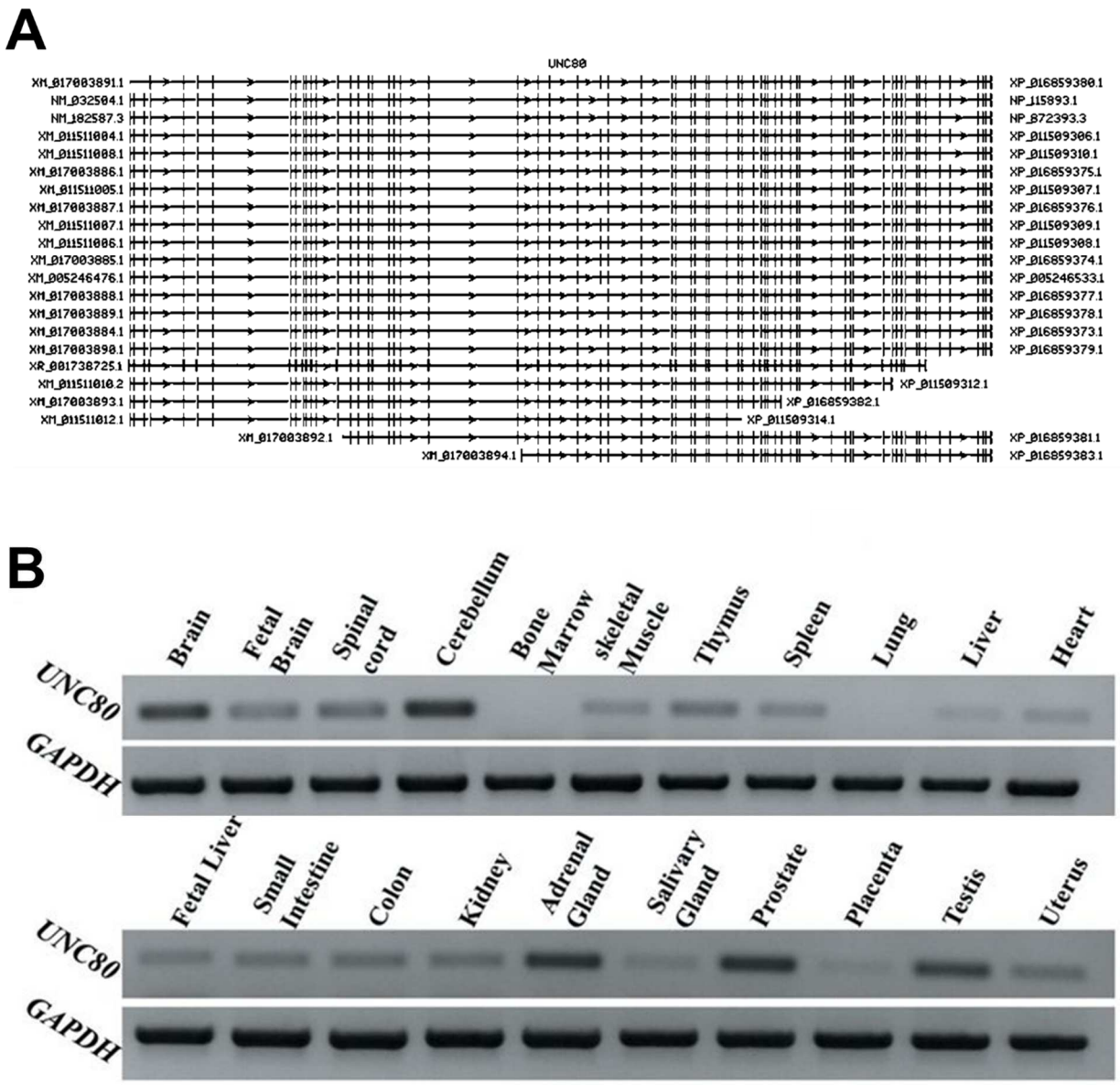

Figure 15. Human UNC-80.
A, Alternative splice variants according to the NCBI database by September 2017. **B**, Reverse transcription PCR of 21 normal human tissues demonstrating the expression pattern of UNC-80. Adapted from (Perez *et al.*, 2016).

switching on GPCRs, which in turn resulted in SFK activation, omitting G protein-dependent pathway, and led to the subsequent I_{NALCN} (Lu *et al.*, 2009). Moreover, I_{NALCN} was suggested being extracellular Ca^{2+}-sensitive depending on the presence of UNC-80 (Lu *et al.*, 2010). Overall, UNC-80 contributes to the neuronal localization of NALCN channelosome (Jospin *et al.*, 2007; Yeh *et al.*, 2008; Lear *et al.*, 2013).

Human and mouse UNC-80 orthologues exhibit 97% homology (Lu *et al.*, 2009). Recently, the expression pattern of UNC-80 in various normal human tissues was investigated (Figure 15B) (Perez *et al.*, 2016). Nevertheless, despite its widespread expression in the mammalian brain, the *in vivo* function of UNC-80 is still largely unknown. Of note, the deletion of 2q33.3-q34 was reported for patient with autistic and Rett-like features (Jang *et al.*, 2015). In addition, several UNC-80 mutations were identified in patients with infantile hypotonia with psychomotor retardation and characterisis facies (Perez *et al.*, 2016; Shamseldin *et al.*, 2016; Stray-Pedersen *et al.*, 2016). To date, UNC-80 mutations were mostly associated with severe intellectual disabilities, encephalopathy, persistent hypotonia and growth retardation, reminiscent of the phenotype related to NALCN mutations.

1.2.3.2 UNC-79

Homolog of *C. elegans* uncoordinated locomotion protein 79, UNC-79 (alternative names KIAA1409, FLJ4333) was first cloned from human cDNA library in 2000 (Nagase *et al.*, 2001). It is located on chromosome 14, cytoband q32.12, on the (+) strand with genomic size around 380 kb. UNC-79 mRNA is comprised of presumably 59 exons, and 9.2 kb in length. UNC-79 is a large protein of about 2,800 amino-acid residues, with predicted size of around 300 kDa. Of note, any transmembrane segments or particular functional domains of UNC-79 were not yet identified. According to NCBI database, several splice variants of human UNC-79 exist (Figure 16).

UNC-79 could be called as a ‘stabilizer’ of NALCN channelosome. Indeed, it interacts with UNC-80 and regulates its level of expression, and consequently the level of NALCN expression, more likely though the posttranslational mechanism (Humphrey *et al.*, 2007; Yeh *et al.*, 2008). Interestingly, absence of UNC-79 in null mice considerably suppressed UNC-80 protein level, without any substantial effect on I_{NALCN} (Lu *et al.*, 2010; Speca *et al.*, 2010). Accordingly, UNC-79 stabilizes UNC-80 and thus regulates neuronal localization of NALCN channelosome (Humphrey *et al.*, 2007; Yeh *et al.*, 2008; Lear *et al.*, 2013).

In vivo studies revealed the importance of UNC-79 in neonatal survival, as well as its involvement in breathing rhythms and nursing (Lu *et al.*, 2010; Speca *et al.*, 2010). Furthermore, mutation that conditioned premature stop codon in the middle of UNC-79, in heterozygous mice

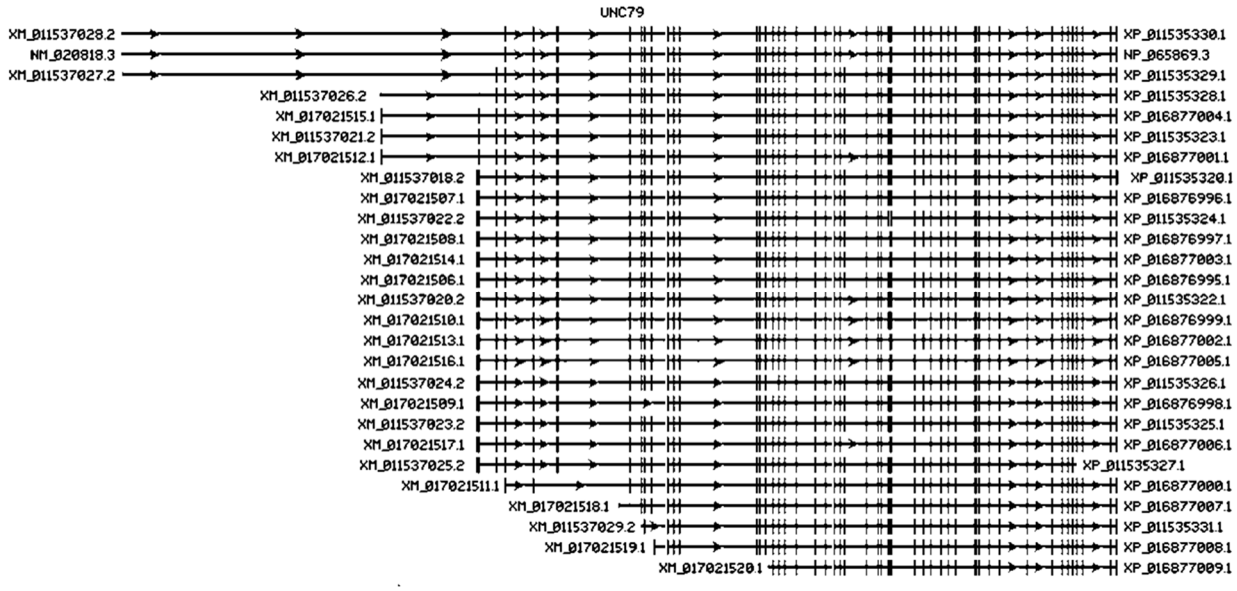

Figure 16. Alternative splicing forms of human UNC-79.
Alternative splice variants according to the NCBI database by September 2017.

showed reduced body weight, modest hyperactivity, increased ethanol consumption, increased food and water intake, preference for saccharin, and resistance to isoflurane (Speca *et al.*, 2010).

1.2.3.3 NLF-1

NCA localization factor 1, NLF-1 (alternative names FAM155A, B1AL88, mid1) is located on chromosome 13, cytoband q33.3, on the (-) strand with genomic size around 700 kb. NLF-1 mRNA is comprised of 4 exons, around 3.8 kb in length. NLF-1 is an ER-residing protein of around 460 amino-acid residues, with predicted size of approximately 52 kDa. NLF-1 is predicted to have one single transmembrane domain, and putative ER retention motif at the N-terminal. In addition, NLF-1 has a cysteine-rich domain, that could be involved in signal transduction (Pei & Grishin, 2012). According to NCBI database, few splice variants of human NLF-1 exist (Figure 17).

NLF-1 is proposed being a chaperone protein that facilitates folding and assembly of NALCN channel. Accordingly, this ER resident protein promotes membrane trafficking of NALCN, and thus through mediated I_{NALCN} maintains the resting membrane potential (Xie *et al.*, 2013; Flourakis *et al.*, 2015; Moose *et al.*, 2017). Indeed, NLF-1 physically interacts with NALCN and its knockdown effectively reduces basal Na^+ leak (Xie *et al.*, 2013). Importantly, NLF-1 is rhythmically expressed in clock neurons, suggesting on its involvement in circadian behaviour (Flourakis *et al.*, 2015; Moose *et al.*, 2017). Interestingly, in NLF-1 mutants the endogenous level of UNC-79 is significantly decreased. However, *vice versa*, the absence of UNC-79 and UNC-80 does not affect NLF-1 expression level (Xie *et al.*, 2013). Furthermore, it was suggested that NLF-1 expression correlates with channelosome production and is developmentally regulated (Moose *et al.*, 2017).

Figure 17. Alternative splicing forms of human NLF-1.
Alternative splice variants according to the NCBI database by September 2017.

1.2.3.4 G protein-coupled receptors

In addition to its baseline activity, NALCN current was also suggested of being modulated by several GPCRs. For example, in neurons from NALCN$^{-/-}$ mice the previously observed neuropeptide-activated currents, in particular, mediated by substance P and neurotensin through NK1R, were absent (Lu *et al.*, 2009). Furthermore, another member of GPCRs, M3R was reported to directly interact with NALCN and support acetylcholine-induced I_{NALCN} in pancreatic β-cells (Swayne *et al.*, 2009). Interestingly, NK1R- and M3R-dependent mechanisms did not require G-protein stimulation, but rather were comprised of unconventional pathway, mediated through SFK activity (Lu *et al.*, 2009). Surprisingly, another GPCR, CaSR, was found to inhibit NALCN (Lu *et al.*, 2010). This regulation was reported to be G-protein-dependent and SFK-independent, to require UNC-80 and to involve molecular determinants in the C-terminal portion of NALCN (Lu *et al.*, 2010). However, recent study in *C. elegans*, provided contrasting evidence, indicating that G_q signalling involves stimulation of Rho GTPases and leads to the activation of NALCN orthologs, NCA-1/NCA-2 (Topalidou *et al.*, 2017). Since it is known that G_o inhibits G_q (Hajdu-Cronin et al. 1999), one can suggest that G-protein-dependent activation/inhibition of NALCN channelosome would be highly restrained to the type of upstream GPCRs. Indeed, CaSR is GPCR coupled with G_o-protein, whereas NK1R and M3R – with G_q proteins (Figure 18).

1.2.3.5 Src Family Kinase

As described above, it was reported that some GPCRs mediate I_{NALCN} through SFK activation (Lu *et al.*, 2009). Indeed, SFK-generated currents were lacking in NALCN$^{-/-}$ neurons, and thus implying on NALCN as their major cation channel target (Lu *et al.*, 2009). Of note, UNC-80 directly interacts with proto-oncogene tyrosine protein kinase, c-Src (Wang & Ren, 2009). Importantly, this interaction was shown for both wild-type and constitutively active Src, but not for inactive mutant (Figure 18) (Wang & Ren, 2009).

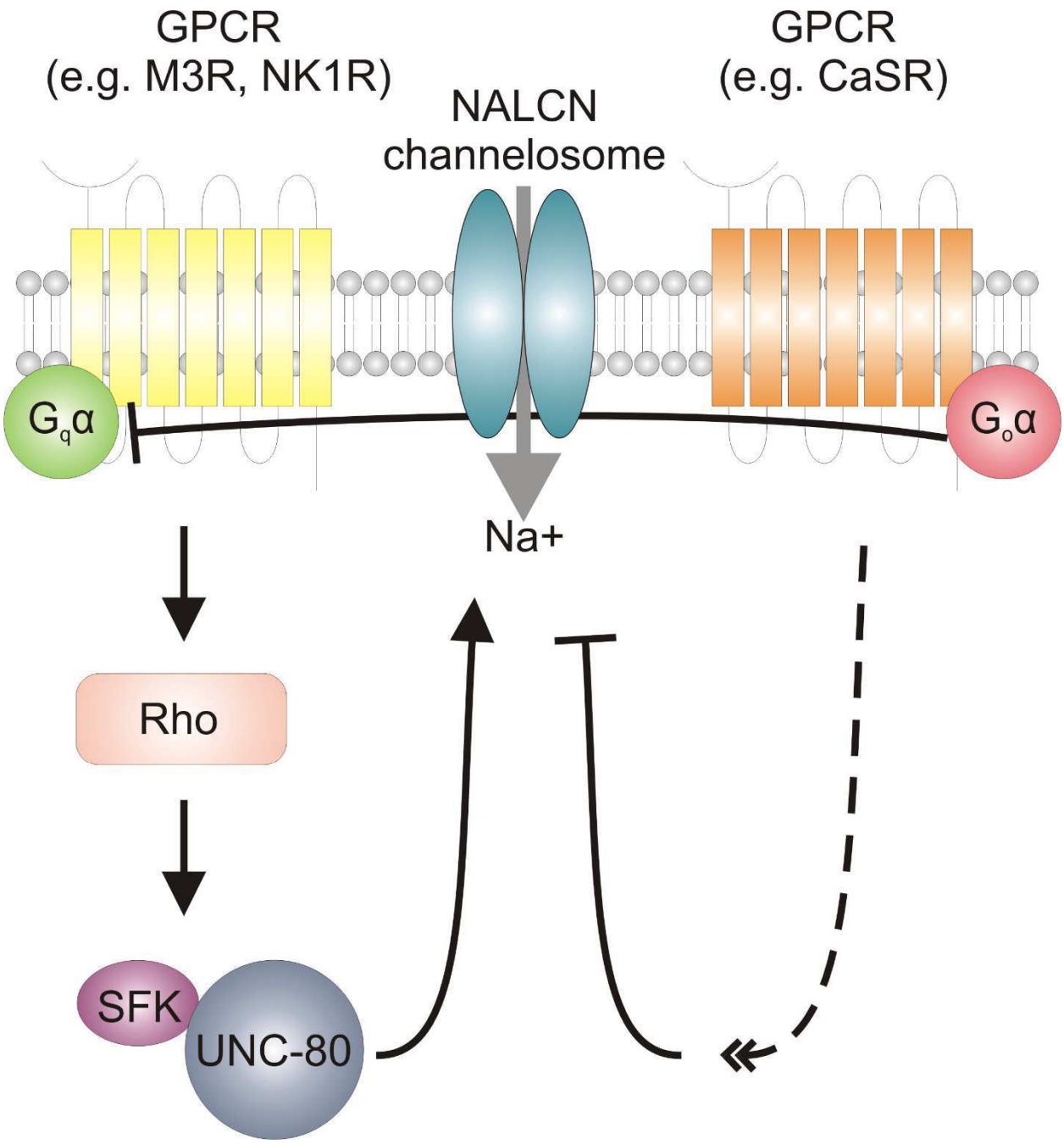

Figure 18. Schematic illustration of GPCRs involvement in the functioning of NALCN channelosome.
GPCRs may affect NALCN channelosome functioning by the means of different mechanisms: SFK-dependent pathway was reported to activate I_{NALCN}, whereas G-protein-dependent pathway was thought to inhibit I_{NALCN}. However, recent evidence suggests that NALCN modulation is more likely determined by the particular type of G-protein coupled to GPCR: G_q proteins would activate Rho GTPases, involve SFK-dependent signalling, and lead to NALCN activation; whereas G_o proteins would inhibit G_q stimulation and decrease NALCN functioning.

1.2.4 Physiological role

Investigations of NALCN channelosome-associated phenotypes were mostly conducted on mammals and invertebrates. Accordingly, in this chapter the physiological role of NALCN channel complex will be described based on the evidence collected from animal model studies.

1.2.4.1 Abdominal morphology

The orthologue of human *NALCN* in *D. melanogaster* was identified due to particular changes in the mutants morphology: thinner and more elongated abdomens with no obvious deformities, hence the name - narrow abdomen (NA) ion channel (Krishnan & Nash, 1990; Mir *et al.*, 1997; Nash *et al.*, 2002). Additionally, *UNC-79* mutants fruit flies also exhibited cylindrically shaped abdomen (Humphrey *et al.*, 2007). On contrary, *NALCN* null mice did not display striking morphological abnormalities (Lu *et al.*, 2007).

1.2.4.2 Cardiovascular pathologies

Interestingly, different minerals, vitamins and trace elements considerably affected cardiac gene expression pattern in rat, in particular, NALCN was found significantly downregulated (Sárközy *et al.*, 2015).

1.2.4.3 Circadian rhythm and sleep

Various studies performed with *D. melanogaster*, and later with mice, highlighted the importance of NALCN in rhythmical behaviours. Importantly, *NA* null mutants of *D. melanogaster* displayed impaired circadian rhythm: typically diurnal animals exhibited suppressed daylight activity (Nash *et al.*, 2002). Indeed, *NA* expression was found in circadian pacemaker neurons of *D.melanogaster*, acting there as an essential component of neuronal output (Lear *et al.*, 2005). Accordingly, in *NA* mutants the accumulation of pigment-dispersing factor (PDF), essential protein for robust circadian behaviour, was associated with attenuated neuropeptide release, whilst oscillations of the clock protein PERIOD (PER) were intact (Lear *et al.*, 2005). Furthermore, loss-of-function mutations introduced into auxiliary subunit genes *UNC-79* and *UNC-80* displayed severe defects in circadian locomotor rhythmicity of *D. melanogaster* (Lear *et al.*, 2013). Although *NA*, *UNC-79*, and *UNC-80* mutants exhibited indistinguishable phenotypes, none of these channelosome members were able to substitute for each other (Lear *et al.*, 2013). Additionally, *NLF-1* suppression in *D. melanogaster* also led to disrupted diurnal control of locomotor behaviour, indicating on its importance in circadian regulation (Ghezzi *et al.*, 2014). Indeed, it is particularly NLF-1 that was found to link NA channelosome with molecular clock in pacemaker neurons of *D.*

melanogaster. Importantly, *NLF-1*, but not *NA*, *UNC-79*, *UNC-80*, or *Src*, exhibited rhythmic expression in both 12 hour light/ 12 hour dark and constant dark conditions (Flourakis *et al.*, 2015). Furthermore, *NLF-1* was found to be highly enriched in the clock neurons of fruit fly when compared with the whole head (Flourakis *et al.*, 2015). Indeed, the major circadian clock transcription factor, CLOCK (CLK), was found to bind *NLF-1* genomic locus, already suggesting on a direct biochemical link between the two (Abruzzi *et al.*, 2011). Surprisingly, in *NLF-1* knockdown flies NA-mediated current and protein level were dramatically reduced, whereas NA transcript level was unchanged (Flourakis *et al.*, 2015). *Vice versa*, NLF-1 overexpression increased NA current at a time when membrane potential, firing rates and cellular excitability are near their daily through in wild-type flies (Flourakis *et al.*, 2015). Therefore, NLF-1 was proposed being a key mediator of NA rhythms that couples the transcriptional oscillator to membrane potential rhythms. This 'bicycle' mechanism is conserved in master clock neurons between fruit flies and mice (Flourakis *et al.*, 2015). Moreover, it was reported that much of the NA channel complex that functions in adult circadian neurons is normally produced during development, and that the channel complex is very stable in the most neurons of *Drosophila* brain (Moose *et al.*, 2017). Therefore, it was proposed that it is particularly developmental expression of NLF-1 which promotes adult rhythmicity, whereas circadian regulation of NA channel function in adult pacemaker neurons is mediated primarily by post-translational mechanisms which are NLF-1-independent (Moose *et al.*, 2017). Interestingly, the role of NLF-1 also extends to neurons expressing PDF. Accordingly, *NLF-1* knockdown technically compelled into PDF neurons, considerably reduced free running rhythms (Flourakis *et al.*, 2015).

Sleep is an animal behaviour ubiquitously conserved from vertebrates to invertebrates, including flies and nematodes and is tightly regulated by circadian rhythms. In mammals it exhibits the cycles of rapid eye movement sleep (REMS) and non-rapid eye movement sleep (NREMS). Interestingly, ethylnitrosourea-mutagenized mice with REMS abnormality, named as *Dreamless*, exhibited heterozygous missense gain-of-function *NALCN* mutation (Funato *et al.*, 2016). Furthermore, when the very same mutation was introduced into wild-type mice by using gene editing technique CRISPR/Cas9, it exhibited short REMS episode duration, similar to the original *Dreamless* pedigree (Funato *et al.*, 2016). Additionally, when compared to the wild-type channel NALCN with *Dreamless*-associated mutation produced current with considerably higher ion conductance (Funato *et al.*, 2016). Thus, a missense, gain-of-function NALCN mutation reduced the total amount and episode duration of REMS, apparently by increasing the excitability of REMS-inhibiting neurons. Indeed, the deep mesencephalic nucleus neurons from brain slices of *Dreamless* mice exhibited significant depolarization and higher spontaneous firing rates than in

wild-type mice (Funato *et al.*, 2016). Taken these data together, NALCN was suggested to work in the REMS regulating neuronal groups and hence controlling various oscillatory behaviours in mammalian brain.

1.2.4.4 Ethanol sensitivity and consumption

Interestingly, the mutations of *UNC-79* gene were shown to regulate ethanol sensitivity in *C. elegans* (Morgan & Sedensky, 1995). Indeed, *UNC-79*, *UNC-80*, and *NCA-1/NCA-2* nematode mutants demonstrated ethanol hypersensitivity (Speca *et al.*, 2010). Furthermore, *UNC-79* mice heterozygotes exhibited enhanced voluntary consumption of ethanol and increased sensitivity to its acute sedative effects (Speca *et al.*, 2010). Nonetheless, the precise relationship between ethanol and NALCN channelosome remains elusive.

1.2.4.5 Enteric nervous system

Analysis of mouse enteric system revealed that the loss of *Ret*, Hirschsprung disease susceptibility gene, leads to significant changes in the intestine transcriptome (around 300 genes) (Kapoor *et al.*, 2017). Of note, downregulated *NALCN* was found within top 50 differentially expressed genes in *Ret* null mice (Kapoor *et al.*, 2017). Indeed, NALCN was shown to mediate SP-induced depolarization of pacemaking activity in the interstitial cells of Cajal, already implying on the channel involvement in the functioning of enteric nervous system (Kim *et al.*, 2012).

1.2.4.6 Locomotor activity

The locomotion of nematodes, particularly *C.elegans*, is produced by interior pressure and excitation of certain sets of muscles that enables continuous body propagation/retraction accompanied by typical sinusoidal movements. Importantly, loss of *NCA-1/NCA-2*, *UNC-79*, *UNC-80* and *NLF-1* in *C. elegans* led to so called 'fainting', a unique motor deficit characterized by periodic halting during movement (Sedensky & Meneely, 1987; Morgan *et al.*, 1988; Rajaram *et al.*, 1999; Humphrey *et al.*, 2007; Jospin *et al.*, 2007; Xie *et al.*, 2013). Moreover, *NCA*, *UNC-79* and *UNC-80* mutants were found to be paralyzed upon immersion in liquid, suggesting onto defective transition between crawling and swimming behaviours (Pierce-Shimomura *et al.*, 2008). Indeed, NALCN channelosome was reported to provide Na^+ leak current in premotor interneurons and hence suggested to maintain rhythmic locomotion of *C.elegans* (Xie *et al.*, 2013). Similarly, in *D. melanogaster* inactivated mutants of *NA* and *UNC-79* genes displayed pause-interrupted walking behaviour (Krishnan & Nash, 1990; Mir *et al.*, 1997; Nash *et al.*, 2002; Humphrey *et al.*, 2007). *Vice versa*, nematodes with gain-of-function *NCA* mutation demonstrated phenotype with

elevated body bending and coiling, and exhibited larger Ca^{2+} transients at synaptic sites (Yeh *et al.*, 2008; Aoyagi *et al.*, 2015). Accordingly, *NCA* depletion reduced synaptic transmission at neuromuscular junctions, subserving into halted locomotion (Yeh *et al.*, 2008). Interestingly, the loss of NALCN channelosome functioning led to a relative cationic concentration shift and hyperpolarization of key neurons in *C. elegans* (Xie *et al.*, 2013; Kasap *et al.*, 2017). Accordingly, pharmacological agents that selectively blocked K^+ channels and gap junction, or activated Ca^{2+} channels significantly improved the movement of NCA-deficient nematodes (Kasap *et al.*, 2017). Of note, *UNC-80* mutant strains were less responsive to K^+ channel inhibitors than worms with *NCA-1/NCA-2* and *UNC-79*, especially in the touch-freeze assay (Kasap *et al.*, 2017).

Small GTPase family Rho was reported to act in multiple classes of neurons to promote locomotion in adult *C. elegans* (Topalidou *et al.*, 2017). Importantly, NALCN channel complex was proposed to act downstream of Rho after the G_q protein activation. Indeed, *UNC-80* and *NCA-1/NCA-2* mutants suppressed the locomotion and body posture phenotypes of an activated Rho mutant (Topalidou *et al.*, 2017). Of note, particularly NCA-1 was suggested being a primary target of G protein regulation (Topalidou *et al.*, 2017). Overall, the G_q-Rho-NCA pathway was shown to regulate two different classes of neurons and thus to control locomotion rate, waveform, and fainting in *C. elegans*.

The substantia nigra neurons are main output of the basal ganglia motor circuit in mammals. Interestingly, it was discovered that spontaneous firing of the mice substantia nigra neurons was maintained by the depolarizing current provided through NALCN, but not by the transient receptor potential canonical (TRPC) channels as it was suggested previously (Lutas *et al.*, 2016). Indeed, NALCN exhibited the highest level of expression within all non-selective cation channels in substantia nigra neurons (Lutas *et al.*, 2016). Additionally, *UNC-79*, *UNC-80*, and *NLF-1* were also found in substantia nigra neurons, indicating on the functionality of the channel complex (Lutas *et al.*, 2016). Of note, *UNC-79* null newborns exhibited differential movements when compared with their heterozygote littermates (Nakayama *et al.*, 2006). Interestingly, the spontaneous firing rate of NALCN knockdown was significantly lower than in control substantia nigra neurons (Lutas *et al.*, 2016). Furthermore, NALCN was shown to modulate the excitability of substantia nigra neurons by changes in glycolysis and by activation of muscarinic acetylcholine receptors (Lutas *et al.*, 2016). Therefore, deficient functioning of NALCN complex in basal ganglia circuit was suggested as one of the potential causes of severe motor and cognitive deficits.

1.2.4.7 Metabolism

Importantly, mice with *UNC-79* depletion lacked ability to nurse and died within several days after birth (Nakayama *et al.*, 2006). Accordingly, unlike their heterozygote and wild-type littermates,

UNC-79 null pups failed to gain weight and drastically weakened (Nakayama *et al.*, 2006). Interestingly, heterozygous *UNC-79* disruption also significantly reduced mice body weight, and hence was named as 'Lightweight mutation' (Lwt) (Speca *et al.*, 2010). Indeed, Lwt heterozygotes displayed shorter body length, lower mass, enlarged lean tissue, decreased body fat, and enhanced food uptake when comparing with wild-type mice of the same body weight (Speca *et al.*, 2010). Furthermore, in mice pancreatic β-cell line, NALCN was reported to encode an inward cationic current mediated through the activation of muscarinic receptors (Swayne *et al.*, 2009). Therefore, it was hypothesized that NALCN plays important role for glucose-stimulated insulin secretion in pancreatic β-cells, which represent the so called 'metabolic hub', connecting nutrient metabolism and the endocrine system (Swayne *et al.*, 2010; Fridlyand *et al.*, 2013).

1.2.4.8 Osmoregulation

Interestingly, within the total of five genomic loci associated with osmoregulation in mice, *NALCN* was identified as the gene that most significantly correlated with serum Na^+ concentration (Sinke *et al.*, 2011). Indeed, heterozygous *NALCN* knockout mice exhibited hypernatremia, highlighting the importance of this Na^+ leak channel in osmobalance (Sinke *et al.*, 2011). Although the exact mechanism of NALCN implication in osmoregulation is not known yet, it was hypothesized that decreased channel expression would lead to the hyperpolarization of osmosensitive neurons and thus reduce the frequency of their action potentials (Sinke & Deen, 2011).

1.2.4.9 Pacemaker activity

Resting membrane potential is a key intracellular prerequisite that defines spontaneous rhythmic activity of pacemaker neurons. Since typically it is highly depolarized, the well-established K^+ leak mechanism by itself is not sufficient to maintain the resting membrane potential, and hence it requires additional current components. Indeed, NALCN was reported to provide such background Na^+ leak and thus contribute to the neuronal depolarization (Lu *et al.*, 2007). Furthermore, NALCN maintained the resting membrane potential and bursting activity of respiratory pacemaker neuron in pond snail, *Lymnaea stagnalis* (Lu & Feng, 2011). Importantly, in *D. melanogaster* NA is endogenously expressed in a set of circadian pacemaker neurons and functions downstream of the core oscillator to regulate diurnal behaviour (Lear *et al.*, 2005). Specifically, NA was shown to effect expression of PDF, an important molecule of pacemaker neurons (Lear *et al.*, 2005). In addition, pacemaker neurons of *D. melanogaster* exhibited functional requirement for UNC-79 UNC-80 and NLF-1 in order to promote the rhythmic behaviours (Lear *et al.*, 2013; Flourakis *et*

al., 2015; Moose *et al.*, 2017). Therefore, NALCN-provided Na^+ background current was considered as an essential component of pacemaker neuron activity.

Furthremore, NALCN and UNC-80 were found in mice interstitial cells of Cajal, the main generators of pacemaker currents during rhythmic bowel contractions (Kim *et al.*, 2012). Albeit the lack of apparent involvement in basal intestinal pacemaking activity, NALCN was accounted for around 75% of SP-induced depolarization in the interstitial cells of Cajal, and hence highly suggested to modulate their pacemaking activity (Kim *et al.*, 2012).

1.2.4.10 Reproduction and offspring survival

Deletion or loss-of-function mutations introduced into NALCN channelosome genes produced fewer, but still viable offspring in *C. elegans* and *D. melanogaster* (Krishnan & Nash, 1990; Speca *et al.*, 2010). Of note, the depletion of *NCA-1/NCA-2*, *UNC-79* or *UNC-80* in *C. elegans* did not display striking defects of the nervous system development (Pierce-Shimomura *et al.*, 2008).

Similarly, no apparent abnormalities of embryonic development in *NALCN* and *UNC-79* knock-out mice were detected (Nakayama *et al.*, 2006; Lu *et al.*, 2007). However, these pups did not survive beyond several days after birth (Nakayama *et al.*, 2006; Lu *et al.*, 2007). Whilst lethality of *UNC-79* knock-outs was presumed due to their inability to consume milk, fatal *NALCN* depletion was largely attributed to the disrupted respiratory rhythm (Nakayama *et al.*, 2006; Lu *et al.*, 2007). Recently, it was discovered that the critical determinant for NALCN-dependent viability is channelosome functioning in the particular subpopulation of brainstem neurons. Specifically, glutamatergic preBötzinger complex (preBötC) neurons expressing the developing brain homeobox protein 1 ($Dbx1^+$) are crucial for NALCN-controlled survival (Yeh *et al.*, 2017). Of note, NALCN knockout in $Dbx1^+$ preBötC neurons led to around 30% of neonatal lethality (Yeh *et al.*, 2017). Furthermore, *NALCN* null GABAergic neurons led to around 15% of lethality in mice within 24 hours of birth, whereas cholinergic, serotonergic, glycinergic and glutamatergic retrotrapezoid nucleus (RTN) neurons with *NALCN* elimination resulted in survival of all animals (Yeh *et al.*, 2017).

1.2.4.11 Respiratory rhythm

Interestingly, *NALCN* knockdown in pond snail *Lymnaea stagnalis* reduced total breathing time of the animal (Lu & Feng, 2011). Specifically, the resting membrane potential of the right pedal dorsal 1 neuron that initiates the respiratory rhythm was found to be hyperpolarized by around 15mV and its rhythmic firing was abolished (Lu & Feng, 2011). Therefore, NALCN was suggested

to maintain activity of respiratory pacemaker neurons, and hence regulate respiratory behaviour in snails.

Similarly, *NALCN* knockouts mice exhibited remarkably distinct breathing pattern in comparison to the wild-type animals: sporadic respiration accompanied by apnea with the bursts of deep breathing lasting around 5-10 seconds (Lu *et al.*, 2007). Of note, such breathing pattern is highly reminiscent of Cheyne-Stokes respiration found in humans with hyponatremia, heart failure, strokes, brain pathologies, including cancer, and near-to-death patients (Strohl, 2003). Importantly, the electrical activities of cervical nerve root, C4, that controls breathing due to diaphragm innervation, were largely absent in *NALCN* null mice (Lu *et al.*, 2007). Therefore, it was hypothesized that respiratory rhythm is highly dependent on NALCN particularly due to its pivotal input into central nervous system. Indeed, recent studies demonstrated that NALCN plays important role in mice neuronal groups that control respiratory rhythmogenesis, specifically in preBötC and RTN neurons (Shi *et al.*, 2016; Yeh *et al.*, 2017). Accordingly, in these neurons NALCN, UNC-79 and UNC-80 were found to be co-localized, suggesting onto functionality of the channel complex (Yeh *et al.*, 2017). Of note, approximately 30% of mice newborn population with *NALCN* knockout in $Dbx1^+$ preBötC neurons showed increased frequency of apnea and longer inspiratory time, consistent with the rate of lethality (Yeh *et al.*, 2017). These results indicated that NALCN expression in the preBötC is critical for neonatal respiration in both awake and sleep states. Furthermore, NALCN regulated CO_2-evoked, independent of direct pH sensing neuronal activation and breathing in RTN neurons (Shi *et al.*, 2016). In addition, Na^+ leak provided through NALCN was shown to influence resting membrane potential and thus neuronal excitability of the oscillatory populations within the RTN and the preBötC (Shi *et al.*, 2016; Yeh *et al.*, 2017). Moreover, in these neurons NALCN also contributed to the maintenance of stable network activity and mediated modulatory responses to the neuropeptide substance P (Shi *et al.*, 2016; Yeh *et al.*, 2017). Overall, NALCN contributes to the biophysical properties of glutamatergic preBötC and RTN neurons and hence plays an important role in sustaining the respiratory activity in adult mammals.

1.2.4.12 Sensitivity to general anaesthetics

Amongst multiple downstream molecular targets, ion channels are considered being predominant subjects of general anaesthetics action. Importantly, NCA channelosome mutants in *C. elegans* exhibited remarkable profile of sensitivity to general anaesthetics: striking hypersensitivity to ethanol, halothane, thiomethoxuflurane, methoxyflurane, toluene and chloroform, modest sensitivity to diethylether, lack of sensitivity to fluroxene and isoflurane, and increased resistance

to flurothyl and enflurane (Sedensky & Meneely, 1987; Morgan *et al.*, 1988, 1990, 2000; Minto *et al.*, 1997; Humphrey *et al.*, 2007; Singaram *et al.*, 2011; Davies *et al.*, 2012). Interestingly, in *D. melanogaster* mutants this profile was somewhat different: hypersensitivity to isoflurane, lack of sensitivity to enflurane, and resistance to methoxyflurane, chloroform and trichloroethylene (Krishnan & Nash, 1990; NASH *et al.*, 1991; Campbell & Nash, 1994; Mir *et al.*, 1997; Guan *et al.*, 2000; Van Swinderen, 2006; Humphrey *et al.*, 2007). Of note, some discrepancy in response of *D. melanogaster* NA mutants to halothane was reported: primarily described as halothane-resistant, and later discovered as halothane hypersensitive (Krishnan & Nash, 1990; Nishikawa & Kidokoro, 1999; Humphrey *et al.*, 2007; Burg *et al.*, 2013).

Furthermore, mice with heterozygote Lwt mutation (UNC-79 disruption) became extensively hypersensitive to acute sedative effects of ethanol, despite the same level of blood ethanol concentration (Speca *et al.*, 2010). Of note, in Lwt heterozygotes no alterations of minimum alveolar concentration in response to halothane, cyclopropane, and sevoflurane were detected. However, a significant resistance to isoflurane-induced anaesthesia was detected in this model of Lwt mice (Speca *et al.*, 2010).

1.2.4.13 Social clustering

Selectively advantageous strategy of local enhancement led to the evolution of a specific animal behaviour type – social clustering. Interestingly, in *D. melanogaster NA* and *NLF-1* deficient mutants exhibited significantly suppressed social clustering behaviour (Burg *et al.*, 2013; Ghezzi *et al.*, 2014). Of note, rescue of NA in cholinergic neurons completely restored behavioural defects of fruit flies, whilst only partial reversion was achieved by NA reexpression in glutamergic neurons (Burg *et al.*, 2013).

1.2.4.14 Synaptic transmission

Communication between neurons is achieved due to the synaptic transmission, a process which is mediated by repeated cycles of exocytotis-dependent neurotransmitters release. Interestingly, NALCN was found to be preferentially localized at the synaptic regions of *D. melanogaster* neurons, implying on the channel importance in postsynaptic response or neurotransmitter release (Nash *et al.*, 2002). Indeed, PDF accumulation in *NALCN* deficient pacemaker neurons of fruit flies indicated onto abolished neuropeptide release (Lear *et al.*, 2005).

Retrieval of synaptic vesicles after neurotransmitter release is an important stage for presynaptic cell restoration with new neurotransmitter, that allows it to sustain repeated cycles of exocytosis. Synaptojanin is an essential protein of vesicle recovery at the synapse. Interestingly,

synaptojanin mutants in *C. elegans* demonstrated defects in recycling of synaptic vesicles, and disruption of NCA channelosome suppressed this uncoordination (Jospin *et al.*, 2007). Indeed, the highly conserved UNC-80 and UNC-79 proteins in *C. elegans* were reported being essential for proper NCA-1 and NCA-2 localization (Jospin *et al.*, 2007; Yeh *et al.*, 2008). Furthermore, NCA, UNC-79 and UNC-80 were found highly enriched at nonsynaptic regions along axons in *C. elegans* and to play critical role in transmission of depolarizing signals from neuronal cell bodies to synapses (Yeh *et al.*, 2008). Specifically, synaptic calcium transients were strongly correlated with the functional activity of NCA (Yeh *et al.*, 2008). Accordingly, NCA loss considerably reduced the synaptic transmission at neuromuscular junctions and thus halted nematode locomotion (Yeh *et al.*, 2008). Importantly, due to presynaptic depression halothane was reported to suppress the synaptic transmission in wild-type *D. melanogaster*, but not in hypomorphic NA mutants (Nishikawa & Kidokoro, 1999).

In addition, NALCN depletion in *L. stagnalis* hyperpolarized the resting membrane potential of pacemaker neurons, favouring the attenuation of excitatory synaptic input into respiratory network (Lu & Feng, 2011).

1.2.5 Human channelopathies

To date, a number of congenital and acquired human pathologies were associated with deregulated NALCN channelosome (Cochet-Bissuel *et al.*, 2014).

1.2.5.1 13q deletion syndrome

The 13q deletion syndrome is a rare genetic disease caused by absence (deletion or monosomy) of a portion of the long arm in chromosome 13, that causes intellectual disability and affects many organ systems (LELE *et al.*, 1963). Importantly, deletion of 13q33.1-13q34 region, that comprises *NALCN* and *NLF-1* genes, was reported in female with congenital heart defects, facial anomalies, developmental delay, and intellectual disability (Huang *et al.*, 2012). Furthermore, genotype of 13q chromosomal deletions was linked to the patients' phenotype, and accordingly *NALCN* and *NLF-1* containing regions were related to microcephaly, cortical development malformations, Dandy-Walker malformation, corpus callosum agenesis, meningocele/ encephalocele, neural tube defects, ano-/microphthalmia, cleft lip/palate, lung hypoplasia, thumb a-/hypoplasia, growth retardation, facial dysmorphism, and seizures (Kirchhoff *et al.*, 2009; Lalani *et al.*, 2013).

1.2.5.2 Alcoholism

Although alcohol dependence is not a hereditary health problem, some studies suggest on genetic influence predisposing alcoholism development (Mayfield *et al.*, 2008; Morozova *et al.*, 2012). Interestingly, single-nucleotide mutation (SNP) located in *NALCN* was significantly correlated with high-risk alcohol dependence screened within 2322 individuals (Wetherill *et al.*, 2014). Furthermore, SNP found in *UNC-79* gene was associated with alcohol/nicotine dependence (Lind *et al.*, 2010). Moreover, locus located on chromosome 2, near *UNC-80* gene, was presumably related with alcohol tolerance and comorbidity of alcoholism and depression (Nurnberger *et al.*, 2001; Schuckit *et al.*, 2001).

1.2.5.3 Alzheimer's disease

Alzheimer's disease is a chronic polygenic neurodegenerative disease, frequently leading to dementia. Interestingly, several Alzheimer's susceptibility loci might be linked to NALCN channelosome: D2S2944 marker located in 2q34 (*UNC-80*); D14S617 marker and SNP rs11622883 in 14q32.12 (*UNC-79*) (Scott *et al.*, 2003; Grupe *et al.*, 2007; Lee *et al.*, 2008).

1.2.5.4 Autism

Autism spectrum disorder refers to a group of complex neurodevelopmental disorders characterized by repetitive and characteristic patterns of behaviour, frequently accompanied by hardship in socialization. Importantly, *UNC-80* truncation was discovered as one of the gene-disrupting *de novo* mutations linked with the likelihood of autistic spectrum analyzed within 343 families (Iossifov *et al.*, 2012).

1.2.5.5 Congenital syndromes with coding mutations for the channelosome genes

The first coding *NALCN* mutations for inherited disorders were found in patients with an autosomal-recessive syndrome characterized by subtle facial dysmorphism, variable degrees of hypotonia, speech impairment, chronic constipation, and cognitive delay from two unrelated consanguineous families (Al-Sayed *et al.*, 2013). Thus, it was named as infantile hypotonia with psychomotor retardation and characteristic facies (IHPRF) syndrome. Noteworthy, recessive mutations for *NALCN* are now classified as IHPRF1, whereas recessive mutations for *UNC-80* are now being referred to as IHPRF2. Accordingly, the loss-of-function NALCN mutations were reported for 3 male patients due to homozygous single nucleotide deletion c.1489delT (Y497Tfs*21), whereas for 3 female patients due to homozygous missense mutation c.3860G>T (W1287L) (Al-Sayed *et al.*, 2013). Infantile neuroaxonal dystrophy (INAD), which is also now classified as IHPRF1 is an extremely rare, inherited (in an autosomal recessive fashion) degenerative disorder of the nervous system caused by lipid storage defects, mostly aroused due to the mutations in *PLA2G6* gene, which encodes Ca^{2+}-independent phospholipase A2β (iPLA2β). It is usually diagnosed in infancy and characterized by progressive motor, mental and visual deterioration. Homozygous truncating *NALCN* mutation (Q642X) was identified in INAD patients with facial dysmorphism (Köroğlu *et al.*, 2013). Importantly, despite severe growth and neuromotor retardation these patients lived to adulthood (Köroğlu *et al.*, 2013). Of note, the fact that *PLA2G6* and *NALCN* mutations lead to similar disorders suggest on substantial relationship between iPLA2β and NALCN functioning.

Interestingly, another exome sequencing study identified 14 *de novo* missense *NALCN* mutations in individuals with congenital contractures of the limbs and face with hypotonia and developmental delay (CLIFAHDD) syndrome: c.530A>C (G177P), c.934C>A (L312I), c.938T>G (V313G), c.979G>A (Q327K), c.1526T>C (L509S), c.1534T>G (F512V), c.1538C>A (T513N), c.1733A>C (Y578S), c.1768C>T (L590F), c.3017T>C (V1006A), c.3050T>C (I1017T), c.3493A>C (T1165P), c.3542G>A (R1181Q), c.4338T>G (I1446M) (Chong *et al.*, 2015). Additionally, the same *de novo* missense *NALCN* mutation c.1768C>T (L590F) was reported in

an infant with a severe neonatal lethal form of CLIFAHDD syndrome (Bend *et al.*, 2016). Moreover, other three novel *de novo* missense *NALCN* mutations were found in four unrelated patients with intellectual disability, seizures, arthrogryposis and dysmorphic facial features (Vivero *et al.*, 2017). Furthermore, another *de novo* heterozygous mutation in *NALCN* (R1181Q) was found in the girl with episodic and persistent ataxia, arthrogryposis, and intellectual disability (Aoyagi *et al.*, 2015). In addition to this mutation (R1181Q), two novel (L312V and V1020F) mutations occurring *de novo* in *NALCN* were found in three patients with neurodevelopmental disease and hypotonia (Fukai *et al.*, 2016). Moreover, another *de novo NALCN* mutation c.1789G>A (V597I) was considered responsible for cerebellar ataxia associated with intellectual instability and arthrogryposis in an adult individual (Wang *et al.*, 2016). Furthermore, 3-year-old girl with reversed circadian rhythm, frequent episodes of disrupted respiratory rhythms, central and obstructive sleep apneas with recurrent hypoxia, and sensitivity to sevoflurane, exhibited *de novo* missense mutation in *NALCN*: c.956C>T (A319V) (Lozic *et al.*, 2016). Additional *de novo NALCN* mutations (F317C and V595F) were reported for two patients with distal arthrogryposis and central hypertonicity (Karakaya *et al.*, 2016). Interestingly, the muscle biopsy in 3-year-old boy with congenital arthrogryposis, hypotonia and developmental delay that possessed heterozygous *de novo NALCN* mutation c.965T>C (p.1332T) suggested on the possible mitochondrial bioenergetics dysfunction (Sivaraman *et al.*, 2016). Furthermore, three siblings born to consanguineous parents exhibited severe intellectual disability, cachexia, strabismus, seizures and episodes of abnormal respiratory rhythm, reminiscent of previously described homozygous NALCN knockout mice (Lu *et al.*, 2007), and presented novel homozygous splice site *NALCN* mutations c.G3390A (IVS29-1G>A) (Gal *et al.*, 2016). Of note, dominant mutations for *NALCN* are now referred to as CLIFAHDD syndrome.

Interestingly, homozygous nonsense *UNC-80* mutation c.151C>T (R51*) was detected in siblings from two remotely related consanguineous Bedouin Israeli families that exhibited hypotonia, severe intellectual disability, dyskinesia and mild dysmorphism (Perez *et al.*, 2016). Furthermore, homozygous missense or compound heterozygous truncating *UNC-80* mutations were found in four individuals characterized by persistent hypotonia, encephalopathy, growth failure, and severe intellectual disability: c.5098C>T (P1700S), c.7607G>C (R2536T, predicted to cause aberrant splicing), c.7757T>A (L2586*), and c.2033delA (N678Tfs*15) (Stray-Pedersen *et al.*, 2016). Of note, one of these mutations c.5098C>T (P1700S) exhibited significantly inhibited NALCN channel currents, when it was expressed in HEK293T cells (Stray-Pedersen *et al.*, 2016). Moreover, in individuals with infantile encephalopathy whole-exome sequencing revealed homozygous *UNC-80* mutations: c.565G>A (p.V189M), c.1078C>T (p.R360*), and c.3793C>T

(p.R1265*) (Shamseldin *et al.*, 2016). Additional biallelic *UNC-80* mutations were reported in two female siblings with spastic paraplegia, global developmental delay, and failure to thrive: paternally inherited c.3983-33994delinsA (S1328Rfs*19) and maternally inherited c.2431C>T (R811*) (Valkanas *et al.*, 2016).

Overall, mutations either loss-of-function or gain-of-function in the encoding part of NALCN channelosome might cause recessive or dominant conditions characterized by neurodevelopmental phenotypic features.

1.2.5.6 Cardiovascular pathologies

Interestingly, analysis of human cardiomyopathy signature revealed significant upregulation of *NALCN* mRNA, suggesting onto involvement of Na^+ leak channel in the cardiovascular pathology (Matkovich *et al.*, 2009).

1.2.5.7 Cervical dystonia

Cervical dystonia, also named as spasmodic torticollis, is a rare chronic neurological movement disorder, comprised of involuntarily contraction of neck muscles. Of note, a genome-wide association study in 212 British patients reported on 2 SNPs located in *NALCN* region as putative genetic risk factors for cervical dystonia (Mok *et al.*, 2014). However, these results were not confirmed for 252 Spanish and 201 Chinese patients, indicating that NALCN was not associated with cervical dystonia in these populations (Gómez-Garre *et al.*, 2014; Zhou *et al.*, 2016).

1.2.5.8 Hepatic and biliary disorders

One of the most common types of liver diseases is nonalcoholic fatty liver disease. Its main problematics is associated with poor diagnosis, especially before the disease progression into symptomatic cirrhosis or liver cancer. Interestingly, *NALCN* was identified as one of 64 genes that were reproducibly associated with severe nonalcoholic fatty liver disease, when compared to the mild form of disorder, and hence could potentially facilitate disease prognostics (Moylan *et al.*, 2014). Furthermore, analysis of DNA integration sites for chronic hepatitis B revealed 2 intronic regions within chromosome 13 related to *NALCN* gene (Mason *et al.*, 2016).

Primary biliary cirrhosis is a chronic autoimmune disease of the liver, characterized by slow, progressive destruction of bile ducts. Interestingly, a genome wide association study in 2072 North-American individuals exhibited strong correlation between this disease and human leukocyte antigen-related genes, and also significant correlation with SNP in *NLF-1* gene (Hirschfield *et al.*, 2009).

1.2.5.9 Hypertension

Hypertension is a long-term medical condition characterized by persistently elevated blood pressure. Interestingly, a significant relationship between systolic blood pressure and SNP located within *NLF-1* region was reported due to examination of 1017 African-American individuals (Adeyemo *et al.*, 2009).

1.2.5.10 Kidney stones

Although the precise mechanism of its implementation was not established, NALCN was suggested to play role in osmoregulation (Sinke & Deen, 2011). Interestingly, NALCN expression was found in renal papillary tissue, specifically in epithelial, tubular and interstitial cells (Taguchi *et al.*, 2017). Importantly, mRNA and protein levels of NALCN were significantly downregulated in tissues from Randall plaques stone patients, suggesting onto renal cell damage that might prone formation of idiopathic Ca^{2+} oxalate kidney stones (Taguchi *et al.*, 2017).

1.2.5.11 Trinucleotide repeat disorders

Trinucleotide repeat disorders are a set of neurodegenerative diseases caused by trinucleotide repeat expansion. Today, trinucleotide repeat disorders are categorized as follows: Category I – includes Huntington's disease and spinocerebellar ataxias, mainly caused by cytosine-adenine-guanine (CAG) repeat expansion in protein-coding portions of specific genes; Category II – more phenotypically diverse with heterogeneous expansions that are generally small in magnitude, but also found in the exons of genes; Category III – includes fragile X syndrome, myotonic dystrophy, two of the spinocerebellar ataxias, juvenile myoclonic epilepsy, and Friedreich's ataxia.

Of note, bovine NLF-1 displayed polymorphic polyglutamine repeat-associated tract, which is conserved in other species, including human (Whan *et al.*, 2010).

1.2.5.12 Psychiatric disorders

Bipolar disorder and schizophrenia

Bipolar disorder (BD) and schizophrenia (SCZ) are mental health illnesses that are characterized by abnormal perception of reality and series of severe manic-depressive mood shifts, respectively. Although the precise cause of these diseases occurrence is not established yet, growing evidence indicates on their close relationship as well as strong genetic predisposition. Interestingly, *NALCN* lies within a region on chromosome 13q that was found susceptible for BD and SCZ (Detera-Wadleigh & McMahon, 2006). Importantly, NALCN mRNA expression was found to correlate with SCZ-associated *GABRB2* gene in human brain (Kang *et al.*, 2011). Furthermore, SNP

(rs9513877) found in *NALCN* was significantly associated with BD (Baum *et al.*, 2008). Additionally, another SNP (rs2044117) in *NALCN* was linked with both SCZ and BD in cohorts of European-American patients (Wang *et al.*, 2010). In contrast, other studies did not reveal association between NALCN and these mental illnesses in other cohorts of patients (Ollila *et al.*, 2009; Souza *et al.*, 2011; Teo *et al.*, 2012). Moreover, several findings reported on linkage between these diseases and auxiliary channelosome subunits, UNC-79 and UNC-80 (Askland *et al.*, 2009; Mead *et al.*, 2010).

Depression and attention-deficit/ hyperactivity disorders

Interestingly, a genome-wide association study in major depressive disorder patients revealed possible but not significant association between this condition and several *NLF-1* SNPs (rs9634463, rs7329003, rs713548, rs9301191, and rs1924397) (Terracciano *et al.*, 2010). Additionally, SNPs (rs10492664 and rs8002852) located in the vicinity to *NLF-1* represented the strongest, however, again not significant, association with attention-deficit/hyperactivity disorder (Anney *et al.*, 2008).

Epilepsy

Epilepsy is a set of neurological disorders characterized by the occurrence of unprovoked epileptic seizures. Importantly, seizures were reported for patients with various neurodevelopmental disorders, that exhibited altered NALCN channelosome profile (Kirchhoff *et al.*, 2009; Al-Sayed *et al.*, 2013; Köroğlu *et al.*, 2013; Lalani *et al.*, 2013; Gal *et al.*, 2016; Perez *et al.*, 2016; Shamseldin *et al.*, 2016; Stray-Pedersen *et al.*, 2016; Valkanas *et al.*, 2016). Furthermore, a whole genome analysis performed in multiple related individuals with remarkable family history of juvenile myoclinic epilepsy revealed critical *UNC-80* comprised genetic interval within 2q33-q36 region (Ratnapriya *et al.*, 2010).

1.2.5.13 Restless legs syndrome

Restless legs syndrome is a sensorimotor disorder characterized by abnormal urge for legs movement, especially at rest (e.g. sleep). Interestingly, analysis of 11 individuals revealed locus on chromosome 13q, where *NALCN* is located, susceptible for the condition development (Balaban *et al.*, 2012).

1.2.5.14 Cancer

To date, NALCN channelosome was associated with cancer disease exclusively due to the results of genomic sequencing analysis that reported onto significant genes alterations. Importantly, the mutant allele frequency of *NALCN* somatic mutation (D468E) was reported to be significantly enriched in metastases of basal-like breast cancer, when compared with the primary tumours (Ding *et al.*, 2010). Furthermore, exome sequencing analysis of pancreatic ductal adenocarcinoma patients revealed mutations in the axon guidance pathway genes, including 5 somatic SNPs in *NALCN* (Biankin *et al.*, 2012). Moreover, advanced-stage non-small cell lung carcinoma patients also exhibited SNP in *NALCN* that was significantly associated with taxane sensitivity, smoking history, and poor prognosis in the additive genetic model (Lee *et al.*, 2013). Additionally, another nonsense *NALCN* mutation (c.1114C>T) was found in colorectal tumour (Sottoriva *et al.*, 2015). Furthermore, 1 silent, 3 non-silent and 3 non-coding *NALCN* mutations that represented 3.9% of its genetic abberations were found in gallbladder cancer (Li *et al.*, 2014; Valle *et al.*, 2017).

Interestingly, the same study that reported NALCN mutation in advanced-stage non-small cell lung carcinoma indicated onto possible disease association with *UNC-80* (Lee *et al.*, 2013). Additionally, analysis on Ewing sarcoma samples revealed *UNC-80* as a recurrently mutated gene with significant nonsynonymous mutation frequency at around 8% (Agelopoulos *et al.*, 2015). Nonetheless, such low mutation frequency suggested onto involvement of *UNC-80* in tumour pathology, but more likely is not sufficient enough for the disease initiation (Agelopoulos *et al.*, 2015). Further linking the channelosome to cancer, elevated *NLF-1* copy number was reported for tumour-derived endothelial cells that are resistant to anti-angiogenic cancer therapies (McGuire *et al.*, 2012). Moreover, high correlation between the malignant state and decreased copy number of *NALCN* and *NLF-1* regions was reported for human glioblastoma patients (De Las Rivas *et al.*, 2012).

Overall, several studies found significantly altered *NALCN*, *UNC-80* and *NLF-1* genes in tumours of various origins, suggesting onto involvement of NALCN channelosome in the disease development. However, nothing is yet known about its functioning in cancer.

1.3 Sodium influx in cancer

To date, most of the studies on the role of Na^+ influx in cancer cells were investigated due to the activity of voltage-operated Na^+ channels. Accordingly, multiple studies demonstrated that Na^+ current generated through pore-forming subunit of voltage-operated Na^+ channels, Navα, is involved in controlling particularly metastatis-associated cancer cell behaviours. Indeed, usage of Na^+-free extracellular medium, pharmacological openers and blockers of Navα indicated on the importance of Na^+ influx for voltage-operated Na^+ channel-dependent migration and invasiveness (Roger *et al.*, 2003; Onkal *et al.*, 2008; Carrithers *et al.*, 2009; Besson *et al.*, 2015). In addition, other Na^+-permeable channels were also demonstrated to possess similar Na^+-dependent regulatory mechanisms involved in tumour promoting properties. For example, family of epithelial Na^+ channels ENaC/ASIC, purinergic receptor P_2X_7 and transient receptor potential canonical channel TRPC1 were all suggested to regulate metastatic cancer cell behaviours particularly due to provided Na^+ influx (Kapoor *et al.*, 2009; Dong *et al.*, 2010; Jelassi *et al.*, 2011). Therefore, one can hypothesize that elevated intracellular Na^+ concentration ($[Na^+]_i$) by itself plays an important role in cancer progression, whereas the channel type preference is rather determined as a tissue specific tool of Na^+ delivery. Noteworthy, elevated tissue Na^+ concentration was even proposed as a highly specific *in vivo* indicator of malignant lesions in human cancer patients (Ouwerkerk *et al.*, 2007; Jacobs *et al.*, 2011). However, little is yet known about the underlying mechanisms of Na^+-signalling that control aggressiveness of cancer cells.

Of note, Na^+ influx induces reverse mode of Na^+-Ca^{2+} exchanger (NCX) and thus leads to increased $[Ca^{2+}]_i$. Interestingly, functioning of NCX in reverse mode was associated with enhanced motility and invasiveness in various cell types, including cancer (Ifuku *et al.*, 2007; Raizman *et al.*, 2007; Dong *et al.*, 2010; Andrikopoulos *et al.*, 2011; Balasubramaniam *et al.*, 2015; Wen *et al.*, 2016). Therefore, inward Na^+ current might be required by cancer cells in order to acquire high migratory activity through the same molecular pathway which is regulated by the reverse mode of NCX. In addition, Navα activity was shown to fuel proton extrusion through Na^+-H^+ exchanger NHE1 and hence to lower pH of the pericellular microenvironment (Busco *et al.*, 2010; Brisson *et al.*, 2011, 2013; Xia *et al.*, 2016). Extracellular acidification activates extracellular matrix (ECM) degrading enzymes and thus promotes cancer cell dissemination (Cardone *et al.*, 2005; Gillet *et al.*, 2009). Indeed, Na^+/H^+ exchanger 1 (NHE1) was found to be localized in invadopodia and to modulate both their formation and proteolytic activity (Busco *et al.*, 2010). Therefore, Na^+ permeation was suggested to be the key parameter controlling signalling pathways of invasion, through the regulation of other proteins such as NHE1 and NCX (Roger *et al.*, 2015).

Furthermore, binding of cardiotonic steroids such as ouabain to the Na^+/K^+-ATPase (NKA) inhibits the ion pumping function of enzyme and thus leads to $[Na^+]_i$ increase. At the same time, it was shown to activate proto-oncogene kinase Src, leading to the subsequent protein tyrosine phosphorylation (Li & Xie, 2009). Of note, epithelial cells contain two functionally distinct pools of the pump, and it is particularly reduction of α1 NKA that preferentially depletes the NKA/Src complex, leading to the activation of Src signalling (Liang et al., 2006, 2007; Chen et al., 2009). Indeed, it was shown, that in human prostate cancer *in vitro* and *in vivo*, the raise in phenotype aggressiveness was associated with reduced expression of α1 NKA protein and elevated Src activity (Li et al., 2011). Therefore, the link between Na^+ signalling and activation of the substantial promoter of cancer progression Src kinase, was proposed (Vlaeminck-Guillem *et al.*, 2014). Nonetheless, it still not clear whether Src activation actually rely on the $[Na^+]_i/[K^+]_i$ disbalance caused by NKA inhibition. For example, initial studies suggested that direct interaction with NKA constrains Src activity in $[Na^+]_i$, $[K^+]_i$, and $[Ca^{2+}]_i$-independent manner, whereas upon ouabain binding Src dissociates and gets activated (Xie & Askari, 2002; Liu & Xie, 2010). However, later on, using purified NKA, it was shown that Src phosphorylation was suppressed by elevated K^+ and attenuated Na^+ (Ye *et al.*, 2011). Indeed, any other stimuli (e.g. ouabain) that triggered the E1-E2 conformational transition of NKA were sufficient to release and activate Src kinase (Ye *et al.*, 2011). Taken together, it was strongly suggested that at least in some cell types the elevated $[Na^+]_i/[K^+]_i$ ratio contributes to the Src-mediated signalling (Orlov *et al.*, 2017). Noteworthy, *vice versa* Src kinase was shown to modulate the activity of Nav, more likely to increase the rate of channel recovery from fast inactivated states, and thus to provide enhanced Na^+ influx (Ahern *et al.*, 2005; Scheuer, 2011). Therefore, it was suggested that interrelationship between Na^+ signalling and proto-oncogene tyrosine kinase Src could subserve in the establishment of more aggressive phenotype in cancer cells (Figure 19).

Overall, Na^+ ions were proposed being an important second messengers with fine spatiotemporal regulation, which is deregulated in cancer disease (Roger *et al.*, 2015). In this regard, due to its Na^+ leak and association with Src kinase NALCN channelosome could provide interesting anti-cancer target. Of note, all current studies that reported on deregulation of NALCN complex in cancer were based only on the genome sequencing analysis (Biankin *et al.*, 2012; De Las Rivas *et al.*, 2012; Lee *et al.*, 2013; Agelopoulos *et al.*, 2015). Accordingly, nothing yet is known about its particular functioning in tumourigenesis. Therefore, this PhD project is a pioneer study that would provide first evidence on the role of NALCN in the disease progression.

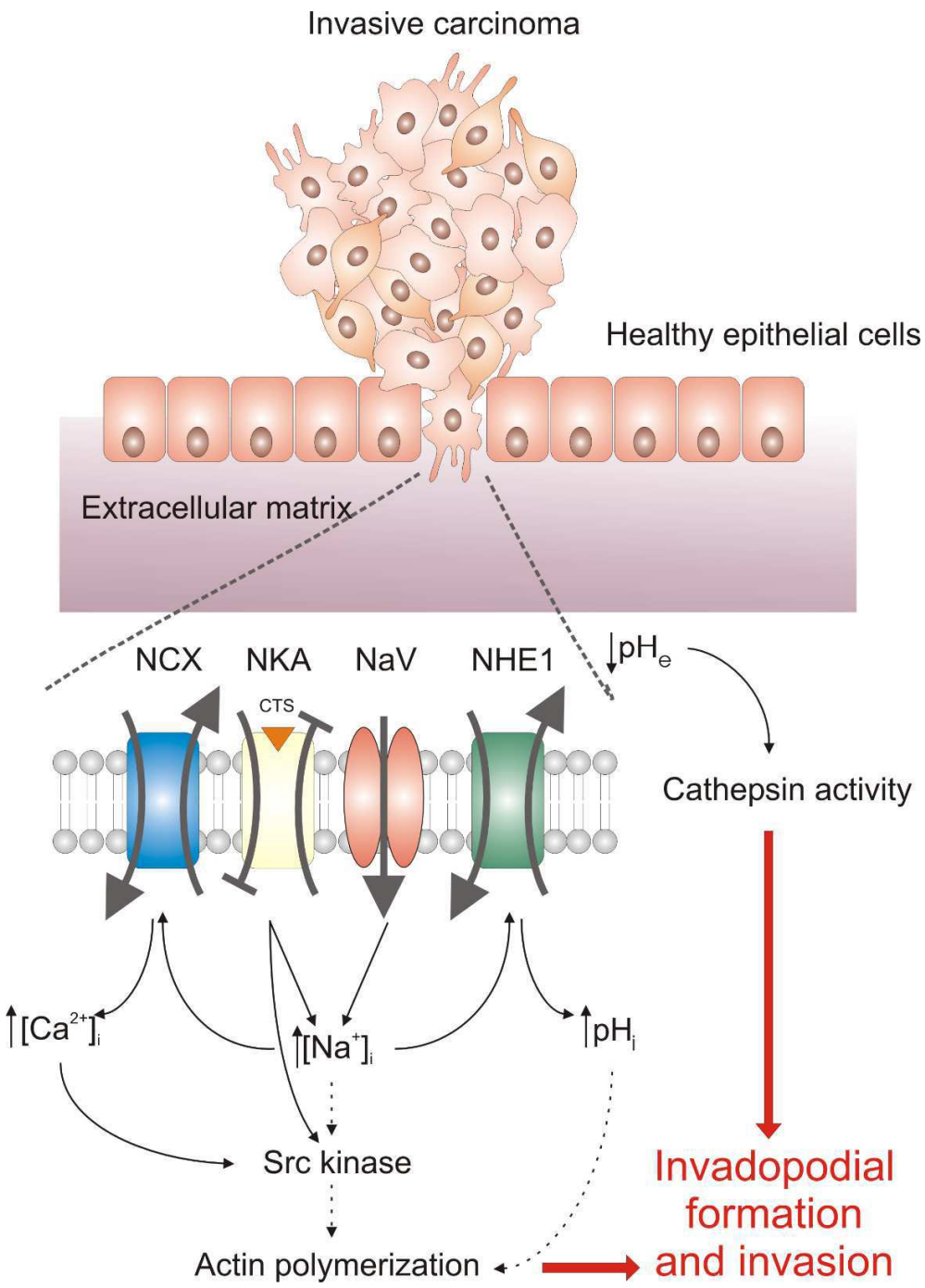

Figure 19. Na^+ influx in cancer progression.
Cancer cells degrade extracellular matrix (ECM) due to activity of protrusive structures, enriched in F-actin, called invadopodia. Voltage-operated Na^+ channels, in particular NaVα proteins, are overexpressed in highly invasive cancer cells, and are found in invadopodia. They provide Na^+ influx and thus enhance H^+ extrusion through activity of Na^+-H^+ exchanger type 1 (NHE1). It leads to acidification of nearby environment and subsequent activation of ECM degrading enzymes, cathepsins. Elevated intracellular Na^+ concentration ($[Na^+]_i$) was also proposed to increase the intracellular Ca^{2+} concentration ($[Ca^{2+}]_i$) due to reverse mode of Na^+-Ca^{2+} exchangers (NCX). Moreover, the elevated $[Na^+]_i/[K^+]_i$ ratio caused by Na^+/K^+-ATPAse (NKA) blockage with cardiotonic steroids (CTS) might contribute to the Src-mediated signalling. Altogether, this suggests that elevated Na^+ influx in cancer cells enhances both the formation and the ECM degradative activity of invadopodia.Modified from (Roger *et al.*, 2015).

1.4 Link between calcium signalling and metastatic disease

Ca^{2+} as a second messenger was shown to participate in manifold cellular processes, including carcinogenesis (Monteith *et al.*, 2017). For example, one of the primary responses to cancer initiation, senescence, was proposed being an intrinsic anti-tumour protective mechanism regulated by Ca^{2+} signalling (Farfariello *et al.*, 2015). Furthermore, proto-oncogene Src kinase was also demonstrated to be activated through Ca^{2+}-dependent mechanisms (Gudermann & Roelle, 2006). Specifically, a particular feature of Ca^{2+} signal – cytosolic oscillations –was recently associated with the metastatic phenotype in cancer cells (Sun *et al.*, 2014). Noteworthy, Ca^{2+} oscillations, but not the sustained elevated intracellular Ca^{2+} levels, are defined as substantial signalling trigger for the vesicle secretion (Wollman & Meyer, 2012). Indeed, in cancer cells abolished Ca^{2+} oscillations revoked fusion of matrix-metalloproteinases-containing vesicles with the plasma membrane and resulted in constrained ECM degradation (Sun *et al.*, 2014). Noteworthy, the loss of background Na^+ leak is associated with defective rhythmically oscillating activities in neurons and cancer cells, as well as with abrogated secretion especially in cells with fast or continuous vesicle turnover (Lear *et al.*, 2005; Jospin *et al.*, 2007; Lu *et al.*, 2007; Pierce-Shimomura *et al.*, 2008; Yeh *et al.*, 2008; Bouhours *et al.*, 2011; Rizaner *et al.*, 2016). Indeed, ouabain-NKA complex was shown to induce Src activation with simultaneous evocation of cytosolic Ca^{2+} oscillations (Fontana et al., 2013). Moreover, coupling of NHE1-integrin-NCX by lipid rafts was shown to initiate integrin ligand interactions and hence trigger Ca^{2+} oscillations (Yi *et al.*, 2009). Furthermore, in highly aggressive breast cancer cells cytosolic Ca^{2+} oscillations were inhibited by the Navα blocker, tetrodotoxin (Rizaner *et al.*, 2016). Taken together, this data implies on the importance of Na^+ influx provided through various mechanisms as a governor of Ca^{2+} oscillations and invasiveness (Rizaner *et al.*, 2016).

Therefore, one of the objectives of this PhD project was devoted to investigate NALCN involvement in controlling the cytosolic Ca^{2+} oscillations as the part of mechanisms assisting in cancer progression.

Of note, potential role of Ca^{2+} involvement in regulation of senescence-associated characteristics is discussed in the review "Calcium homeostasis in cancer: A focus on senescence" (Farfariello *et al.*, 2015).

In addition, the role of Ca^{2+} signalling as a substantial intracellular tool that regulates dynamicity and complexity of the metastatic cascade is discussed in the review "Molecular mechanisms of tumour invasion: regulation by calcium signals" (Iamshanova *et al.*, 2017).

Review 1:

“Calcium homeostasis in cancer: A focus on senescence.”

Farfariello V., Iamshanova O., Germain E., Fliniaux I., Prevarskaya N.

Biochim Biophys Acta. 2015 Sep;1853(9):1974-9. doi: 10.1016/j.bbamcr.2015.03.005.

Calcium homeostasis in cancer: a focus on senescence

Valerio Farfariello, Oksana Iamshanova, Emmanuelle Germain, Ingrid Fliniaux and Natalia Prevarskaya*

Inserm U1003, Laboratory of Excellence, Ion Channels Science and Therapeutics, Equipe Labellisée par la Ligue Nationale Contre le Cancer, SIRIC ONCOLille, Université des Sciences et Technologies de Lille, Villeneuve d'Ascq 59656, France

Corresponding author :

Prof. Natalia Prevarskaya

Laboratory of Cell Physiology, INSERM U1003

Université des Sciences et Technologies de Lille

Avenue Paul Langevin,

59655 Villeneuve d'Ascq

FRANCE

e-mail: natacha.prevarskaya@univ-lille1.fr

tel.(33) 3 20 33 60 18

fax.(33) 3 20 43 40 66

Abstract

Senescence is one of the primary responses to the activation of oncoproteins or down-regulation of tumor suppressors in normal cells and is therefore considered as being anti-tumorigenic but the mechanisms controlling this process are still much unknown. Calcium (Ca^{2+}) plays a major role in many cellular processes and calcium channels control many of the "hallmarks of cancer" but their involvement in tumor initiation is poorly understood and remains unclear.

Therefore, in this article we review some striking senescence-associated characteristics and their potential regulation by Ca^{2+}. The main aim is to produce plausible hypothesis on how calcium homeostasis may participate in cancer-related senescence.

Highlights:

- Senescence is a major cellular response during cancer initiation
- Calcium controls many hallmarks of cancer and can regulate senescence
- Calcium can prime the senescence escape during tumor initiation

Keywords: senescence, cancer, calcium homeostasis, calcium channels

1. Introduction

Cell division is an essential tool used by multicellular organisms to survive and, where necessary, to renew or repair damaged tissues. However, genomes are continually damaged by environmental and oxidative stresses and, in dividing cells, by errors in DNA replication and mitosis. In fact, dividing cells can sometimes undergo genomic mutations that, if occur in cell cycle-controlling genes, put the organism at risk to develop cancer [1]. To counteract this phenomenon, complex organisms have developed some mechanisms in the attempt to repair the damage, if possible, or to block proliferation in cells susceptible of oncogenic transformation. The most common way for cells to limit uncontrolled proliferation is to die by apoptosis (or programmed cell death), but cells have developed alternative mechanisms to block proliferation avoiding death.

The concept of cellular senescence was formally postulated five decades ago when Hayflick and colleagues showed that normal cells had a limited ability to proliferate in culture [2]. Further experiments demonstrated that the loss of the proliferative potential was due to the telomere shortening. Indeed, when the length of one or more telomeres falls below a certain threshold, the exposed DNA end is recognized as a DNA doublestrand break by the DNA damage response machinery and triggers the canonical DNA damage checkpoint. As a general mechanism, DNA damage signals contribute to activation of the p53 and pRB tumor suppressor pathways, key regulators of much of the senescence program. Activation of p53 contributes to senescence-associated proliferation arrest through one of its target genes, CDKN1a, encoding the cyclin/cdk inhibitor $p21^{CIP1}$. By inhibiting cyclin/cdk2 or cyclin/cdk4 complexes, $p21^{CIP1}$ activates the pRB tumor suppressor pathway, which inhibits cell proliferation through numerous downstream targets, including the E2F family of transcription factors, whose response genes are necessary for progression through S phase [3,4]. Senescent cells are characterized by specific features such as irreversible proliferation arrest, resistance to apoptotic cell death and altered differentiated

functions, such as morphological modifications, changes in gene expression and production of secreted proteins like metalloproteases, inflammatory cytokines and growth factors. In the context of cancer, senescence would represent an obstacle to overcome for the cells to become fully tumorigenic in that it irreversibly arrests cell growth. As a matter of fact, cells with cellular and molecular characteristics of senescence are found in benign precancerous neoplasms associated with oncogene activation in both humans and mice. For example, human nevi or moles are benign clonal neoplasms containing melanocytes made senescent by a mutated Ras or B-Raf [5]. Evidence for the tumour suppressor role of senescence has been obtained also with mouse models of cancer triggered by ablation of the tumour suppressor *Pten* in the prostate [6] or oncogenic N-Ras expression in the haematopoietic system [7], in which the oncogenic initiating event led to the development of senescent premalignant lesions with little evidence of apoptosis. However, even if cells attempts to block uncontrolled proliferation by triggering senescence, cancer still occurs. Many evidence indicate that at one point, some cells lose the senescent phenotype and re-enter in the cell cycle progression, the so-called senescence escape. It is thus not surprising that the main effectors of senescence, such as p53 and pRB, are the most commonly lost functions in mammalian cancers. Indeed, in experimental models of cancer, the progression to cancerous neoplasms instead of benign ones occurs when the oncogenic event is combined with simultaneous deletion of mediators of the senescence response [6,8]. Calcium controls many aspects of the cellular lifecycle and it is conceivable that senescent cells are characterized by a specific calcium signature that could be responsible in part for the senescent "phenotype". Moreover, since the prominent role of Ca^{2+} in cancer progression [9], particular perturbations of Ca^{2+} equilibrium could allow cells to bypass the proliferation arrest and become tumorigenic.

Therefore, the aim of this review is to provide new hypothesis on how Ca^{2+} signaling could participate in senescence during tumor initiation. However, since on the one hand senescence is the

tight cellular balance between proliferation, apoptosis and autophagy and on the other hand Ca^{2+} is a key controller of all these processes, we will recapitulate first the current knowledge of how it governs the "cellular life".

2. Ca^{2+} and the regulation of the cellular fates

2.1 Proliferation

Typically quiescent cells exhibit localized short-term Ca^{2+} fluctuations, which represent native Ca^{2+} signaling pathways, required to maintain basic cellular physiological activity. However, as a second messenger, it is able to regulate a plethora of intracellular pathways. This "versatility" mostly depends on spatial and temporal localization of Ca^{2+} in the so-called nanodomains that activate specific pathways in specific circumstances.

In cancer cells, the enhanced proliferation is usually associated with increased cytosolic Ca^{2+} concentration [10]. Indeed, multiple transcription factors responsible for cell cycle propagation highly depend on Ca^{2+} ions. Among the most common regulators of those are calmodulin, Ca^{2+}/calmodulin-dependent protein kinases, calcineurin and protein kinase C (PKC) [11].

For instance, Nuclear Factor of Activated T-cells (NFAT) signaling pathway has been implemented in multiple features of cellular cycle, including proliferation. As a general mechanism, following phospholipase Cγ (PLCγ) activation the phosphatidyl-inositol-1,4,5-trisphosphate (InsP3) is produced and binds to the InsP3 receptor (InsP3R) on the endoplasmic reticulum (ER) membrane, inducing the efflux of Ca^{2+}. Stromal interaction molecule 1 (STIM1) and STIM2 subsequently detect the decrease of ER Ca^{2+} stores, form small clusters and communicate with Orai channel protein at the plasma membrane to trigger Store-Operated Calcium Entry (SOCE). Ca^{2+} binds to the Ca^{2+} sensor protein calmodulin, resulting in activation of calcineurin, which assists in dephosphorylation of NFAT, its nuclear localization and subsequent target genes expression.

Interestingly, it has been recently shown that Orai1 detects local Ca^{2+} by N-terminal domain in specific nanodomains thus effectively coupling Ca^{2+} entry to NFAT activation explaining such selective activation of a fundamental downstream response by Orai1 [12]. Nevertheless, there is evidence that the same proliferation-promoting Ca^{2+}/calmodulin/calcineurin/NFAT pathway can be also activated by the store-independent Ca^{2+} entry (e.g. through transient receptor potential (TRP) channels, Orai heteromers) [13–15].

Another ubiquitous regulator of genes that control cell proliferation and survival is Nuclear Factor Kappa-light-chain-enhancer of activated B cells (NF-κB). It has been shown to be constitutively activated in some types of cancer cell and can control the expression of genes that are involved in the stimulation of cell proliferation, inhibition of apoptosis and increase of metastatic and angiogenic potential [16]. Ca^{2+} seems to play a crucial role in the activity of NF-kB: using primary cultures of neonatal cerebellar granule neurons, Lilienbaum and Israël found that opening of Ca^{2+} channels at the plasma membrane and at intracellular stores is indispensable for the basal NF-κB activity [17]. They demonstrated that calmodulin, protein kinases C (PKCs), and the $p21^{CIP1}$/Ras/phosphatidylinositol 3-kinase (PI3K)/Akt pathways are simultaneously involved in the steps linking the Ca^{2+} signal to NF-κB activity. Of note, there are studies that found NFAT and NF-κB transcription factors or their upstream activators acting as tumor suppressors and hence inhibit cellular proliferative rate [16,18]. Therefore, Ca^{2+}-dependent signaling pathways realized through NFAT and NF-κB provide a peculiar tool for balancing between proliferation and cell cycle arrest. (Fig. 1; point 2.1).

2.2 Apoptosis

The involvement of Ca^{2+} and Ca^{2+} channels in extrinsic and intrinsic apoptosis is a widely investigated topic (for review, see [19]). Both during extrinsic and intrinsic apoptosis induction, mitochondria eventually become overloaded with Ca^{2+}, causing mitochondrial depolarization,

leading to the opening of the mitochondrial permeability transition pore (mPTP) and the release of the cytochrome C in the cytosol, allowing apoptosome formation and the well-described caspase cascade.

The paradigm of apoptosis regulation by calcium resides in B-cell lymphoma-2 (Bcl-2) activity. First, Bcl-2 ensures a balance between Bcl-2 pro-apoptotic family members at the mitochondrion for the BAK/BAX (Bcl-2 homologous antagonist killer/Bcl-2 associated X protein) pore formation [20]. Additionally, they were proposed to affect different Ca^{2+}- handling proteins at the ER (inactivation of Sarco/Endoplasmic Reticulum Ca^{2+}-ATPase (SERCA), interaction with IP3R), leading to Ca^{2+} release from the ER, mitochondrial calcium uptake and cytosolic calcium elevation. Of note, increased levels of IP3R are usually associated with promotion of cell death, whereas reduction of SERCA levels is a common feature of cancer cells that avoid apoptosis [21,22]. Overall, Ca^{2+} movement mechanism from ER to mitochondrion seems to be complex, and elucidation of molecular complexes located in ER/mitochondrion juxtaposition contacts is of primordial interest. In parallel, intracellular Ca^{2+} elevation causes calcineurin-dependent dephosphorylation and activation of Bcl-2 associated death promoter (Bad), a pro-apoptotic Bcl-2 family member, as well as the activation of the Ca^{2+}-dependent cystein protease calpain. This latter mediates cleavage of several members of Bcl-2 family and activates caspase-12, promoting apoptotic cell death induced by oxygen and glucose deprivation [23].

2.3 Autophagy

Autophagy is a self-digestive process that provides breakdown and recycling of damaged or unused cellular components. In this way cell preserves its energy levels and at the same time provides additional self-repairing mechanism. Hence, increased autophagy might be triggered by various stress-factors, such as rise in free cytosolic Ca^{2+}. However, depending on its spatial and temporal organization, Ca^{2+} has been demonstrated to both stimulate and prevent autophagy [24].

Interestingly, most studies report ER-residing IP3R as a prominent inhibitor of autophagy [25]. However, in starvation-induced autophagy IP3R has also been demonstrated as a stimulator [26]. There is some evidence on involvement of TRPV1 and L-type calcium channels in autophagy regulation [27,28]. However, their direct implication is further to be confirmed by using more specific effectors. Interestingly, autophagolysosome formation is much facilitated due to luminal Ca^{2+} release performed via TRPML1, also known as mucolipin-1. Moreover, expressions of TRPML3 also localized in endo-lysosome compartments, directly correlate with autophagy induction [29].

Channels expressed in mitochondria have been also demonstrated to regulate autophagy. Among them are Mitochondrial Calcium Uniporter (MCU) and its regulator MCUR1, proteins responsible for mitochondrial Ca^{2+} uptake, which have been shown to induce autophagy when in downregulated state [30].

3. Ca^{2+} and the senescent phenotype

3.1 Increase of cell volume

Modifications of the cell volume is one of the most prominent feature of senescent cells. In many cells, swelling is rapidly followed by Ca^{2+} entry and the so-called regulatory volume decrease (RVD) during which cells extrude ions to counteract the cell volume increase. The activation of ion release during RVD is paralleled by inhibition of ion uptake mechanisms.

The transport systems most often activated by cell swelling are separate K^+ and anion channels and in many cells, swelling leads to the activation of nonselective cation channels [31].

A possible participant in RVD is the non-selective cation channel Transient Receptor Potential Vanilloid 4 (TRPV4), a member of the Transient Receptor Potential (TRP) superfamily that has been shown to react to hypotonic stimuli with a conductance for Ca^{2+}. Indeed, cells lacking TRPV4

are not able to undergo RDV, property that is re-established in TRPV4-transfected cells [32]. As for TRPV4, also TRPM7 is proposed to be activated by osmotic swelling and its knockdown attenuates RVD [33]. Piezo proteins have recently been identified as non selective cation channels mediating mechanosensory transduction in mammalian cells. A recent paper shed new light on the role of Piezo-1 in the regulation and maintenance of cell volume homeostasis, in that its knockdown leads to zebrafish erythrocyte swelling [34].

In addition, inhibition of Ca^{2+}/calmodulin-dependent kinases has been shown to inhibit RVD or activation of cell volume regulatory ion channels [35], and it has been concluded that calmodulin/Ca^{2+} complexes are important for activation of RVD.

In senescent cells, this control mechanism is apparently modified because after senescence stimulus, cells increase their volume that remains unchanged with time. It is thus conceivable that senescent cells regulate differentially calcium-permeable channels and the associated downstream signaling pathways to trigger and maintain the specifics morphological features (Figure 1, 3.1).

3.2 Changes in membrane potential

Membrane potential (V_m), is the voltage across the plasma membrane provided due to differences in ions (e.g. Na^+, K^+, Ca^{2+}) concentration between extra- and intra-cellular regions. Accordingly, activity of ion permeable channels/transporters provokes changes in V_m. Typically, in excitable cells, changes in V_m are required for propagation of action potential, driving force of cell-to-cell communication, whereas in other types of cells, V_m is a biophysical activator of intracellular signaling. Indeed, V_m has been shown to play key roles in multiple cellular activities such as proliferation and differentiation [9]. Recently, Lallet-Daher and colleagues have suggested on association of V_m with another feature of cellular physiology in senescence [36]. They have demonstrated that oncogenic stress triggers an increase of potassium channel KCNA1 expression and its relocation from the cytoplasm to the membrane responsible for changes in V_m and leading to

cellular senescence. In similar manner, Ca^{2+} channels have been known to modulate V_m, however no direct evidence on their involvement in senescence initiation is yet known. In addition, V_m regulates activity of voltage-gated channels that provide another significant trail of Ca^{2+} influx affecting subsequent downstream signaling [37]. Nevertheless, this aspect has not been investigated in the work of Lallet-Daher. Therefore, since changes in V_m has been implemented in oncogene-induced senescence, it would be reasonable to investigate whether similar effects could be potentiated by remodeling of Ca^{2+}-channels as wells as to affect downstream Ca^{2+}-signalling (Figure 1, 3.2).

3.3 Inhibition of telomerase activity

Expression of telomerase is the most common mechanism by which cancer cells stabilize their telomeres and hence avoid replicative senescence [38]. Telomerase activity can be modulated by Ca^{2+} homeostasis. In HaCaT human epidermal keratinocytes, the levels of telomerase activity were reduced in response to ER Ca^{2+} release even without the downregulation of hTERT human Telomerase Reverse Transcriptase (hTERT) expression, suggesting that Ca^{2+} release can directly modulate the activity of the telomerase complex [39]. This modulation was postulated to occur via the S100A8 Ca^{2+}-binding protein, which inhibits the telomerase complex (Figure 1, 3.2). Ca^{2+} can also exert the opposite effect, in that elevated extracellular Ca^{2+} levels can enhance telomerase activity likely by L-type voltage-operated Ca^{2+} channels [40].

3.4 Mitochondria-endoplasmic reticulum interactions

Mitochondria and ER are well-recognized nodes where significant remodeling of Ca^{2+} signaling occurs in cancer cells to sustain proliferation and avoid cell death [41]. In a recent study conducted with a loss of function approach, ER-to-mitochondria Ca^{2+} transmission is proposed as a potent senescence-inducing signal. Indeed, senescent cells exhibit an altered calcium homeostasis. During oncogene and replicative senescence induction, ITPR2 triggers calcium release from the ER

followed with by mitochondrial calcium accumulation through MCU channel. This Ca^{2+} remodeling causes a drop in mitochondrial membrane potential and an accumulation of oxygen species [42]. Knockdown of *MCU* or *MICU1* modulator prior to oncogenic stress application leads to a strong decrease in mitochondrial accumulation correlated to loss of mitochondrial depolarization and senescence escape. Although the precise mechanism underlying ER-to-mitochondria Ca^{2+} transfer during senescence is still unclear, it is tempting to speculate a link between mitochondrial Ca^{2+} modulation, mitochondrial respiration and eventually metabolic crisis such as autophagy [19,43] (Figure 1, 3.4). Mitochondria and ER networks are interconnected in punctuate microdomains called Mitochondria-Associated Endoplasmic Reticulum Membrane (MAM) sharing structural and functional interactions essential for Ca^{2+} signaling, lipid transport, energy metabolism, and cell death [44]. In mammalian, these MAMs are composed of the Voltage-Dependent Anion Channel (VDAC) located at the outer mitochondrial membrane interacting with the IP3R at the ER membrane through the molecular chaperone glucose-regulated protein 75 (Grp75), allowing Ca^{2+} transfer from the ER to mitochondria [45] (Figure 1, 3.4). These 'hotspots' of calcium transfer are now considered as crosstalk platforms in response to various stresses associated with specific proteins recruitment. Altogether, it appears that Ca^{2+} signals regulating cell death, autophagy and metabolism depend on spatially and dynamically restricted domains. Under this prespective, the subcellular localization of all calcium permeable channels appears of great significance.

3.5 Transcriptional reprogramming

In paragraph 2.1 we reported some of the potential effects of Ca^{2+} in the regulation of transcription factors responsible for cell proliferation. As a key regulator of senescence, p53 is the first that should be taken into account. A direct link between Ca^{2+} and p53 activity was provided by Lu et al., showing that siRNA-mediated silencing of Cav3.1 channels expressed in certain esophageal carcinoma cell lines can reduce cell proliferation via the p53 tumor-suppressing transcription factor-

dependent pathway, leading to the upregulation of cell-cycle arrest protein $p21^{CIP1}$ [46]. Moreover, calcium can indirectly modulate the expression and function of p53 by regulating the activity of the large conductance Ca^{2+}-dependent K^+ channel (BKCa). Indeed, the pharmacological blockade of BKCa channels in human HeLa cervical and A2780 ovarian cancer cell lines has been reported to induce the increased expression of p53 and cell-cycle arrest in the G1 phase [47], suggesting that BKCa channel activity is required to keep p53 under negative control to prevent its antitumor actions. Additionally, Ca^{2+} can regulate the ability of partner proteins to bind and modulate p53 activity. Mueller and colleagues have in fact demonstrated that the S100A2, a member of the subfamily of S100 Ca^{2+}-binding proteins, is able to interact with p53 in a Ca^{2+}-dependent manner, and that this interaction facilitates binding of p53 to its responsive element [48]. By contrast, the S100B Ca^{2+}-binding protein exerts the opposite role, by decreasing p53 DNA binding and transcriptional activity [49]. Moreover, Delphin et al. demonstrated that *in vitro*, Ca^{2+}-dependent PKC is able to phosphorylate recombinant murine p53 protein on several residues contained within a conserved basic region of 25 amino acids, located in the C-terminal part of the protein, thus increasing the stability of p53 protein tetramers and oligomers [50].

Ca^{2+} is the major regulator of NFAT, however no data are available on its role in cancer-related senescence. However, dysregulation of NFAT is now known to be associated with malignant transformation and the development of cancer. For example, it is expressed and transcriptionally active in human metastatic melanoma cell lines, in which it is activated by oncogenic $B\text{-}Raf^{V600E}$ via the canonical MEK/ERK pathway [51]. Moreover, this specific pathway is also known to induce senescent-like cycle arrest of human naevi, suggesting that the additional NFAT activation is required for cells to become tumorigenic. As a matter of fact, recently Unemura et colleagues [52] showed that STIM1 and Orai1 are expressed in metastatic human melanoma cell lines, while the melanocyte cell line, HEMA-LP, displayed only a low level of Orai1 expression

that could explain partially the increased activation of NFAT in malignant cells. It is thus conceivable that the activation of NFAT occurs in part as the result of changes in Ca^{2+} homeostasis due to channels expression and function remodeling that can occur in cells during the tumorigenic process, allowing cells to pass from a senescent-like to a more aggressive phenotype.

Little is known about the role of NF-kB cancer-associated senescence. It has been shown that chronic NF-κB activation delays H-Ras^{V12}-induced premature senescence in IMR-90 normal human diploid fibroblasts [53]. Accordingly, inhibition of p53 or p65 expression alone had no overt effect on the growth arrest phenotype induced by oncogenic H-Ras^{V12} in IMR-90 cells, but inhibiting both p53 and p65 simultaneously promoted cell growth and reversed the senescent phenotype [54]. In the same paper, the authors found that NF-κB acts as a master regulator of the Senescence-Associated Secretory Phenotype (SASP), influencing the expression of several genes, including interleukin 6 (IL-6), IL-8, CXCL1 chemokine, InterCellular Adhesion Molecule 1(ICAM1), matrix metalloproteinases and noninflammatory response genes. Indeed, oncogene-induced senescence has been associated with secretion of multiple CXCR2-binding chemokines in NF-κB-dependent manner [55] (Figure 1, 3.5).

3.6 Senescence-associated secretory phenotype (SASP)

It is well known that senescent cells are able to secrete a large number of soluble factors (the so-called SASP) like growth factors, cytokines, extracellular matrix, and degradative enzymes, all of which can alter tissue microenvironments and affect nearby epithelial cells [56,57]. Calcium channels are well known regulators of secretion. Indeed, Cav3.2 T-type calcium channels were found to be involved in calcium-dependent secretion of neuroendocrine prostate cancer cells probably by stimulating intracellular trafficking and exocytosis [58]. Moreover, Ca^{2+} influx via store-dependent TRPs (TRPC1, TRPC4, aids the enhanced secretion of angiogenic factors and TRPM8 is in part responsible for the secretion of mitogenic factors in prostate cancer cells [9].

Indeed, modulation of the expression of calcium channels in senescent cells could contribute to regulate the secretory phenotype acting either directly on the exocytic pathway or indirectly by promoting the activity of transcription factors such as NF-κB (Figure 1, 3.6).

3.7 Autophagic flux

Autophagy has been linked with aging and indeed found in senescence transition phase (reviewed in [59]). Actually, the significant switch of protein degradation from proteosomal onto autophagosomal pathway has been reported to take place during senescence [60]. Indeed, autophagy has been suggested to mediate acquisition of oncogene-induced senescence, whereas its inhibition delays senescence-associated processes, including specific secretion phenotype [61]. In fact, the main result of autophagy functioning is the production of particular vesicles that assist in degradation of a required material after their fusion with lysosomes. Indeed, previously it has been shown that lysosomal membrane permeabilization induces autophagy and triggers stress-induced premature senescence, which is reversible by autophagy inhibition [62]. In fact, one of the most spread assays for determination of senescent cells is enhanced lysosomal enzyme β-galactosidase activity. In consistence with this, during Ras-induced-senescence the kinetics of β-galactosidase activity and autophagy activation have been tightly correlated [61].

Indeed, the evidence of a profound relationship between the autophagy process and oncogene-induced senescence strengthen the potential role of Ca^{2+} signaling as one of the main actors in the acquisition of the senescent phenotype (Figure 1, 3.7).

4. Concluding remarks

Senescence is a critical step through which “oncogene-stressed” cells pass to limit the proliferation, the consequent accumulation of genomic mutations and finally the tumor progression.

Over these last few years, the importance of Ca^{2+} channels in regulating few hallmarks of cancer is

emerging. Indeed, they have been demonstrated to play important roles in 1) self-sufficiency in growth signals and aberrant cell proliferation, 2) insensitivity to antigrowth signals, 3) evasion of programmed cell death (apoptosis), and 4) tissue invasion and metastasis. Some of these channels have a specific profile of expression depending on the cancer cell phenotype thereby pointing on the possibility to use them as diagnostic/prognostic markers for cancer development.

Proliferating tumor cells show very distinct patterns of expression and function of Ca^{2+} channels if compared to their normal counterparts. It is therefore highly probable that some of the features of this "intermediate" phenotype are regulated by Ca^{2+} homeostasis, through the modulation of ion fluxes caused by differential expression and/or remodeling of channels activities. However, senescence is often bypassed and cells re-acquire features of proliferating cells allowing cancer to arise and progress but little is known about the molecular mechanisms involved in this phenomenon. Thus, unveiling their role in senescence could be of help for the development of new more conscious therapeutic strategies targeting Ca^{2+} channels, or to identify new early diagnostic markers.

Acknowledgements

This work was supported in part by a fellowship from the Fondation pour la Recherche Médicale (FRM) n. SPF20130526749.

References

[1] J. Campisi, Cellular senescence as a tumor-suppressor mechanism, Trends Cell Biol. 11 (2001) S27–31.

[2] L. Hayflick, THE LIMITED IN VITRO LIFETIME OF HUMAN DIPLOID CELL STRAINS, Exp. Cell Res. 37 (1965) 614–636.

[3] U. Herbig, W.A. Jobling, B.P.C. Chen, D.J. Chen, J.M. Sedivy, Telomere shortening triggers senescence of human cells through a pathway involving ATM, p53, and p21(CIP1), but not p16(INK4a), Mol. Cell. 14 (2004) 501–513.

[4] F. d' Adda di Fagagna, Living on a break: cellular senescence as a DNA-damage response, Nat. Rev. Cancer. 8 (2008) 512–522. doi:10.1038/nrc2440.

[5] C. Michaloglou, L.C.W. Vredeveld, M.S. Soengas, C. Denoyelle, T. Kuilman, C.M.A.M. van der Horst, et al., BRAFE600-associated senescence-like cell cycle arrest of human naevi, Nature. 436 (2005) 720–724. doi:10.1038/nature03890.

[6] Z. Chen, L.C. Trotman, D. Shaffer, H.-K. Lin, Z.A. Dotan, M. Niki, et al., Crucial role of p53-dependent cellular senescence in suppression of Pten-deficient tumorigenesis, Nature. 436 (2005) 725–730. doi:10.1038/nature03918.

[7] M. Braig, S. Lee, C. Loddenkemper, C. Rudolph, A.H.F.M. Peters, B. Schlegelberger, et al., Oncogene-induced senescence as an initial barrier in lymphoma development, Nature. 436 (2005) 660–665. doi:10.1038/nature03841.

[8] P. Sun, N. Yoshizuka, L. New, B.A. Moser, Y. Li, R. Liao, et al., PRAK is essential for ras-induced senescence and tumor suppression, Cell. 128 (2007) 295–308. doi:10.1016/j.cell.2006.11.050.

[9] N. Prevarskaya, R. Skryma, Y. Shuba, Ion channels and the hallmarks of cancer, Trends Mol. Med. 16 (2010) 107–121. doi:10.1016/j.molmed.2010.01.005.

[10] T. Capiod, The need for calcium channels in cell proliferation, Recent Patents Anticancer Drug Discov. 8 (2013) 4–17.

[11] H.L. Roderick, S.J. Cook, Ca2+ signalling checkpoints in cancer: remodelling Ca2+ for cancer cell proliferation and survival, Nat. Rev. Cancer. 8 (2008) 361–375. doi:10.1038/nrc2374.

[12] P. Kar, C. Nelson, A.B. Parekh, Selective activation of the transcription factor NFAT1 by calcium microdomains near Ca2+ release-activated Ca2+ (CRAC) channels, J. Biol. Chem. 286 (2011) 14795–14803. doi:10.1074/jbc.M111.220582.

[13] V. Lehen'kyi, M. Flourakis, R. Skryma, N. Prevarskaya, TRPV6 channel controls prostate cancer cell proliferation via Ca(2+)/NFAT-dependent pathways, Oncogene. 26 (2007) 7380–7385. doi:10.1038/sj.onc.1210545.

[14] S. Thebault, M. Flourakis, K. Vanoverberghe, F. Vandermoere, M. Roudbaraki, V. Lehen'kyi, et al., Differential role of transient receptor potential channels in Ca2+ entry and proliferation of prostate cancer epithelial cells, Cancer Res. 66 (2006) 2038–2047. doi:10.1158/0008-5472.CAN-05-0376.

[15] C. Dubois, F. Vanden Abeele, V. Lehen'kyi, D. Gkika, B. Guarmit, G. Lepage, et al., Remodeling of channel-forming ORAI proteins determines an oncogenic switch in prostate cancer, Cancer Cell. 26 (2014) 19–32. doi:10.1016/j.ccr.2014.04.025.

[16] M. Karin, Y. Cao, F.R. Greten, Z.-W. Li, NF-kappaB in cancer: from innocent bystander to major culprit, Nat. Rev. Cancer. 2 (2002) 301–310. doi:10.1038/nrc780.

[17] A. Lilienbaum, A. Israël, From calcium to NF-kappa B signaling pathways in neurons, Mol. Cell. Biol. 23 (2003) 2680–2698.

[18] B.K. Robbs, A.L.S. Cruz, M.B.F. Werneck, G.P. Mognol, J.P.B. Viola, Dual roles for NFAT transcription factor genes as oncogenes and tumor suppressors, Mol. Cell. Biol. 28 (2008) 7168–7181. doi:10.1128/MCB.00256-08.

[19] A. Kondratskyi, K. Kondratska, R. Skryma, N. Prevarskaya, Ion channels in the regulation of apoptosis, Biochim. Biophys. Acta. (2014). doi:10.1016/j.bbamem.2014.10.030.

[20] B. Bonneau, J. Prudent, N. Popgeorgiev, G. Gillet, Non-apoptotic roles of Bcl-2 family: the calcium connection, Biochim. Biophys. Acta. 1833 (2013) 1755–1765. doi:10.1016/j.bbamcr.2013.01.021.

[21] B. Korosec, D. Glavac, M. Volavsek, M. Ravnik-Glavac, Alterations in genes encoding sarcoplasmic-endoplasmic reticulum Ca(2+) pumps in association with head and neck squamous cell carcinoma, Cancer Genet. Cytogenet. 181 (2008) 112–118. doi:10.1016/j.cancergencyto.2007.12.003.

[22] D. Boehning, R.L. Patterson, S.H. Snyder, Apoptosis and calcium: new roles for cytochrome c and inositol 1,4,5-trisphosphate, Cell Cycle Georget. Tex. 3 (2004) 252–254.

[23] T. Nakagawa, J. Yuan, Cross-talk between two cysteine protease families. Activation of caspase-12 by calpain in apoptosis, J. Cell Biol. 150 (2000) 887–894.

[24] A. Kondratskyi, M. Yassine, K. Kondratska, R. Skryma, C. Slomianny, N. Prevarskaya, Calcium-permeable ion channels in control of autophagy and cancer, Front. Physiol. 4 (2013) 272. doi:10.3389/fphys.2013.00272.

[25] D. Lam, A. Kosta, M.-F. Luciani, P. Golstein, The inositol 1,4,5-trisphosphate receptor is required to signal autophagic cell death, Mol. Biol. Cell. 19 (2008) 691–700. doi:10.1091/mbc.E07-08-0823.

[26] J.-P. Decuypere, K. Welkenhuyzen, T. Luyten, R. Ponsaerts, M. Dewaele, J. Molgó, et al., Ins(1,4,5)P3 receptor-mediated Ca2+ signaling and autophagy induction are interrelated, Autophagy. 7 (2011) 1472–1489.

[27] V. Farfariello, C. Amantini, G. Santoni, Transient receptor potential vanilloid 1 activation induces autophagy in thymocytes through ROS-regulated AMPK and Atg4C pathways, J. Leukoc. Biol. 92 (2012) 421–431. doi:10.1189/jlb.0312123.

[28] A. Williams, S. Sarkar, P. Cuddon, E.K. Ttofi, S. Saiki, F.H. Siddiqi, et al., Novel targets for Huntington's disease in an mTOR-independent autophagy pathway, Nat. Chem. Biol. 4 (2008) 295–305. doi:10.1038/nchembio.79.

[29] X. Cheng, D. Shen, M. Samie, H. Xu, Mucolipins: Intracellular TRPML1-3 channels, FEBS Lett. 584 (2010) 2013–2021. doi:10.1016/j.febslet.2009.12.056.

[30] K. Mallilankaraman, C. Cárdenas, P.J. Doonan, H.C. Chandramoorthy, K.M. Irrinki, T. Golenár, et al., MCUR1 is an essential component of mitochondrial Ca2+ uptake that regulates cellular metabolism, Nat. Cell Biol. 14 (2012) 1336–1343. doi:10.1038/ncb2622.

[31] F. Lang, G.L. Busch, M. Ritter, H. Völkl, S. Waldegger, E. Gulbins, et al., Functional significance of cell volume regulatory mechanisms, Physiol. Rev. 78 (1998) 247–306.

[32] D. Becker, C. Blase, J. Bereiter-Hahn, M. Jendrach, TRPV4 exhibits a functional role in cell-volume regulation, J. Cell Sci. 118 (2005) 2435–2440. doi:10.1242/jcs.02372.

[33] T. Numata, T. Shimizu, Y. Okada, Direct mechano-stress sensitivity of TRPM7 channel, Cell. Physiol. Biochem. Int. J. Exp. Cell. Physiol. Biochem. Pharmacol. 19 (2007) 1–8. doi:10.1159/000099187.

[34] A. Faucherre, K. Kissa, J. Nargeot, M.E. Mangoni, C. Jopling, Piezo1 plays a role in erythrocyte volume homeostasis, Haematologica. 99 (2014) 70–75. doi:10.3324/haematol.2013.086090.

[35] A.S. Bender, J.T. Neary, J. Blicharska, L.O. Norenberg, M.D. Norenberg, Role of calmodulin and protein kinase C in astrocytic cell volume regulation, J. Neurochem. 58 (1992) 1874–1882.

[36] H. Lallet-Daher, C. Wiel, D. Gitenay, N. Navaratnam, A. Augert, B. Le Calvé, et al., Potassium channel KCNA1 modulates oncogene-induced senescence and transformation, Cancer Res. 73 (2013) 5253–5265. doi:10.1158/0008-5472.CAN-12-3690.

[37] W.A. Catterall, Voltage-gated calcium channels, Cold Spring Harb. Perspect. Biol. 3 (2011) a003947. doi:10.1101/cshperspect.a003947.

[38] C.P. Chiu, C.B. Harley, Replicative senescence and cell immortality: the role of telomeres and telomerase, Proc. Soc. Exp. Biol. Med. Soc. Exp. Biol. Med. N. Y. N. 214 (1997) 99–106.

[39] S. Rosenberger, I.S. Thorey, S. Werner, P. Boukamp, A novel regulator of telomerase. S100A8 mediates differentiation-dependent and calcium-induced inhibition of telomerase activity in the human epidermal keratinocyte line HaCaT, J. Biol. Chem. 282 (2007) 6126–6135. doi:10.1074/jbc.M610529200.

[40] M.Y. Alfonso-De Matte, H. Moses-Soto, P.A. Kruk, Calcium-mediated telomerase activity in ovarian epithelial cells, Arch. Biochem. Biophys. 399 (2002) 239–244. doi:10.1006/abbi.2002.2762.

[41] P. Pinton, C. Giorgi, R. Siviero, E. Zecchini, R. Rizzuto, Calcium and apoptosis: ER-mitochondria Ca2+ transfer in the control of apoptosis, Oncogene. 27 (2008) 6407–6418. doi:10.1038/onc.2008.308.

[42] C. Wiel, H. Lallet-Daher, D. Gitenay, B. Gras, B. Le Calvé, A. Augert, et al., Endoplasmic reticulum calcium release through ITPR2 channels leads to mitochondrial calcium accumulation and senescence, Nat. Commun. 5 (2014) 3792. doi:10.1038/ncomms4792.

[43] D. Gitenay, C. Wiel, H. Lallet-Daher, D. Vindrieux, S. Aubert, L. Payen, et al., Glucose metabolism and hexosamine pathway regulate oncogene-induced senescence, Cell Death Dis. 5 (2014) e1089. doi:10.1038/cddis.2014.63.

[44] G.-H. Lee, H.-Y. Lee, B. Li, H.-R. Kim, H.-J. Chae, Bax inhibitor-1-mediated inhibition of mitochondrial Ca2+ intake regulates mitochondrial permeability transition pore opening and cell death, Sci. Rep. 4 (2014) 5194. doi:10.1038/srep05194.

[45] G. Szabadkai, K. Bianchi, P. Várnai, D. De Stefani, M.R. Wieckowski, D. Cavagna, et al., Chaperone-mediated coupling of endoplasmic reticulum and mitochondrial Ca2+ channels, J. Cell Biol. 175 (2006) 901–911. doi:10.1083/jcb.200608073.

[46] F. Lu, H. Chen, C. Zhou, S. Liu, M. Guo, P. Chen, et al., T-type Ca2+ channel expression in human esophageal carcinomas: a functional role in proliferation, Cell Calcium. 43 (2008) 49–58. doi:10.1016/j.ceca.2007.03.006.

[47] X. Han, F. Wang, W. Yao, H. Xing, D. Weng, X. Song, et al., Heat shock proteins and p53 play a critical role in K+ channel-mediated tumor cell proliferation and apoptosis, Apoptosis Int. J. Program. Cell Death. 12 (2007) 1837–1846. doi:10.1007/s10495-007-0101-9.

[48] A. Mueller, B.W. Schäfer, S. Ferrari, M. Weibel, M. Makek, M. Höchli, et al., The calcium-binding protein S100A2 interacts with p53 and modulates its transcriptional activity, J. Biol. Chem. 280 (2005) 29186–29193. doi:10.1074/jbc.M505000200.

[49] J. Lin, M. Blake, C. Tang, D. Zimmer, R.R. Rustandi, D.J. Weber, et al., Inhibition of p53 transcriptional activity by the S100B calcium-binding protein, J. Biol. Chem. 276 (2001) 35037–35041. doi:10.1074/jbc.M104379200.

[50] C. Delphin, K.P. Huang, C. Scotto, A. Chapel, M. Vincon, E. Chambaz, et al., The in vitro phosphorylation of p53 by calcium-dependent protein kinase C--characterization of a protein-kinase-C-binding site on p53, Eur. J. Biochem. FEBS. 245 (1997) 684–692.

[51] R.J. Flockhart, J.L. Armstrong, N.J. Reynolds, P.E. Lovat, NFAT signalling is a novel target of oncogenic BRAF in metastatic melanoma, Br. J. Cancer. 101 (2009) 1448–1455. doi:10.1038/sj.bjc.6605277.

[52] M. Umemura, E. Baljinnyam, S. Feske, M.S. De Lorenzo, L.-H. Xie, X. Feng, et al., Store-operated Ca2+ entry (SOCE) regulates melanoma proliferation and cell migration, PloS One. 9 (2014) e89292. doi:10.1371/journal.pone.0089292.

[53] C. Batsi, S. Markopoulou, G. Vartholomatos, I. Georgiou, P. Kanavaros, V.G. Gorgoulis, et al., Chronic NF-kappaB activation delays RasV12-induced premature senescence of human fibroblasts by suppressing the DNA damage checkpoint response, Mech. Ageing Dev. 130 (2009) 409–419. doi:10.1016/j.mad.2009.04.002.

[54] Y. Chien, C. Scuoppo, X. Wang, X. Fang, B. Balgley, J.E. Bolden, et al., Control of the senescence-associated secretory phenotype by NF-κB promotes senescence and enhances chemosensitivity, Genes Dev. 25 (2011) 2125–2136. doi:10.1101/gad.17276711.

[55] J.C. Acosta, A. O'Loghlen, A. Banito, M.V. Guijarro, A. Augert, S. Raguz, et al., Chemokine signaling via the CXCR2 receptor reinforces senescence, Cell. 133 (2008) 1006–1018. doi:10.1016/j.cell.2008.03.038.

[56] A. Krtolica, S. Parrinello, S. Lockett, P.Y. Desprez, J. Campisi, Senescent fibroblasts promote epithelial cell growth and tumorigenesis: a link between cancer and aging, Proc. Natl. Acad. Sci. U. S. A. 98 (2001) 12072–12077. doi:10.1073/pnas.211053698.

[57] J.-P. Coppé, K. Kauser, J. Campisi, C.M. Beauséjour, Secretion of vascular endothelial growth factor by primary human fibroblasts at senescence, J. Biol. Chem. 281 (2006) 29568–29574. doi:10.1074/jbc.M603307200.

[58] F. Gackière, G. Bidaux, P. Delcourt, F. Van Coppenolle, M. Katsogiannou, E. Dewailly, et al., CaV3.2 T-type calcium channels are involved in calcium-dependent secretion of

neuroendocrine prostate cancer cells, J. Biol. Chem. 283 (2008) 10162–10173. doi:10.1074/jbc.M707159200.

[59] D. Grasso, M.I. Vaccaro, Macroautophagy and the oncogene-induced senescence, Front. Endocrinol. 5 (2014) 157. doi:10.3389/fendo.2014.00157.

[60] M. Gamerdinger, P. Hajieva, A.M. Kaya, U. Wolfrum, F.U. Hartl, C. Behl, Protein quality control during aging involves recruitment of the macroautophagy pathway by BAG3, EMBO J. 28 (2009) 889–901. doi:10.1038/emboj.2009.29.

[61] A.R.J. Young, M. Narita, M. Ferreira, K. Kirschner, M. Sadaie, J.F.J. Darot, et al., Autophagy mediates the mitotic senescence transition, Genes Dev. 23 (2009) 798–803. doi:10.1101/gad.519709.

[62] S. Patschan, J. Chen, A. Polotskaia, N. Mendelev, J. Cheng, D. Patschan, et al., Lipid mediators of autophagy in stress-induced premature senescence of endothelial cells, Am. J. Physiol. Heart Circ. Physiol. 294 (2008) H1119–1129. doi:10.1152/ajpheart.00713.2007.

Figure 1

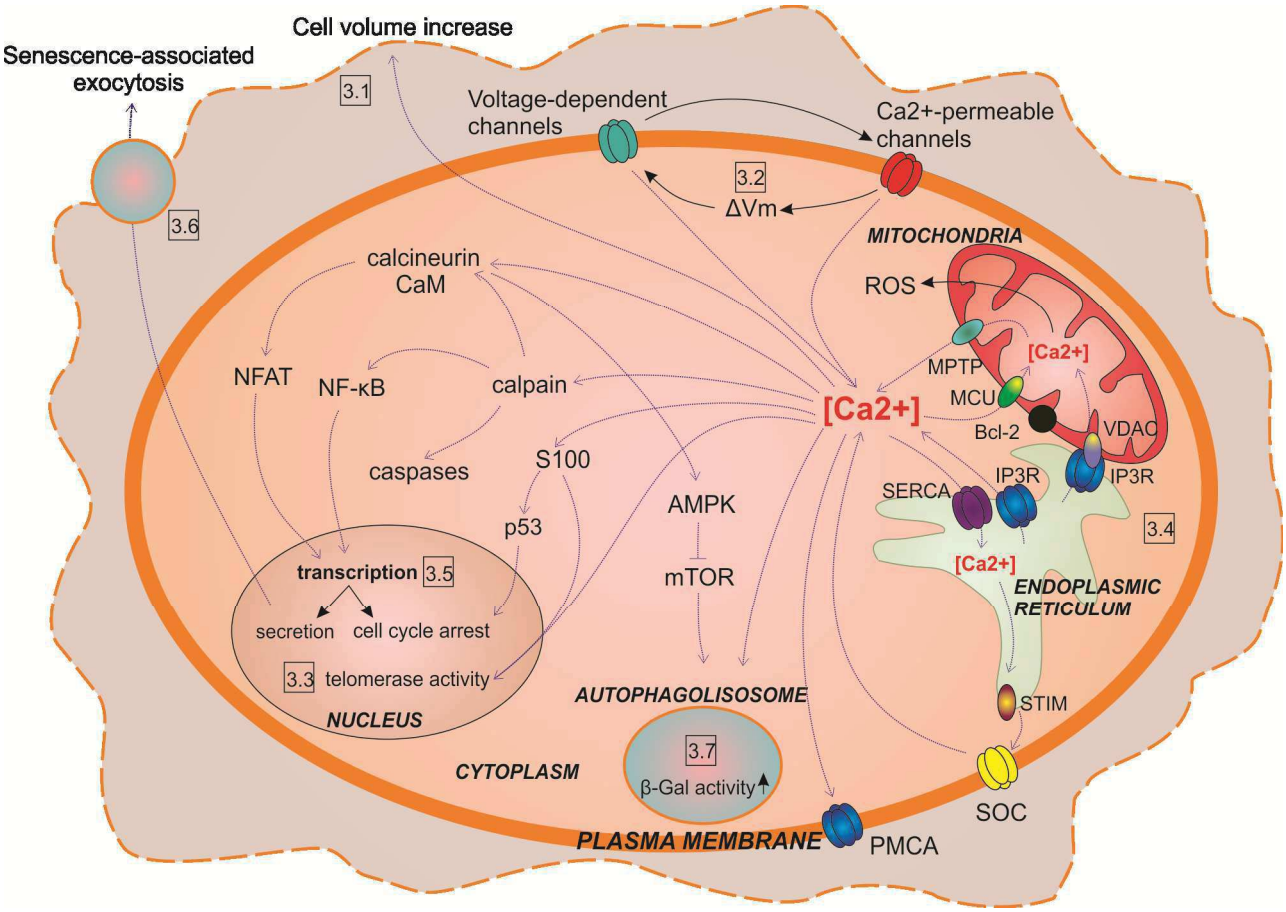

Calcium and calcium-permeable channels in the control of senescence. The potential pathways by which Ca^{2+} could regulate senescence are depicted. Numbers indicate the relative paragraph in the text.

Review 2:

"Molecular mechanisms of tumour invasion: regulation by calcium signals."

Iamshanova O, Fiorio Pla A, Prevarskaya N.

J Physiol. 2017 May 15;595(10):3063-3075. doi: 10.1113/JP272844.

Comparison of Three Sodium-Sensitive Fluorescent Dyes and Their Suitability for *in vitro* Intracellular Sodium Imaging in Cancer Cells

Oksana Iamshanova, Pascal Mariot, V'yacheslav Lehen'kyi & Natalia Prevarskaya[#]

University of Lille, Inserm, U-1003 – PHYCELL – Physiology Cellulaire, F-59000 Lille, France; Inserm, U1003, F-59000 Lille, France

[#] Corresponding author: Prof. Natalia Prevarskaya,

Laboratory of Cell Physiology,

Inserm U1003, Bâtiment SN3, USTL,

59650 Villeneuve d'Ascq, France;

Tel: +33 3 20 33 64 23

Fax : +33 3 20 43 40 66

Email: natacha.prevarskaya@univ-lille1.fr

http://www.phycell.univ-lille1.fr

Abstract

Na^+ ions are known to regulate many signalling pathways involved in both physiological and pathological conditions. Though the functionality of Na^+ channels and the corresponding Na^+ currents can be investigated using the patch-clamp technique, the latter does not provide the fast and dynamic method to study $[Na^+]_i$ transients as do Na^+ fluorescence indicator dyes. Despite the fact that Na^+ signalling is considered as an important controller of cancer progression, only few data using Na^+ imaging technique are available so far, suggesting the persisting challenge within the scientific community. In this study, we have performed the comparison of three Na^+ specific fluorescent dyes – Na^+-binding benzofuran isophthalate (SBFI), CoroNa^{TM} Green (Corona) and Asante NaTRIUM Green-2 (ANG-2) in prostate cancer cells. These dyes have been assessed for optimal loading conditions, working range, $[Na^+]_i$ sensitivity, *etc*, in order to determine which probe can be considered as the most reliable to visualize Na^+ fluctuations *in vitro*. This is the first study to report on Na^+ fluorescence imaging in prostate cancer cells. Moreover, it addresses many technical issues associated with different Na^+ specific probes and provides better understanding on their proper application *in vitro*.

Key words: sodium-imaging, fluorescent dye, prostate cancer cells

Introduction

Virtually all living organisms could be unified in their feature to possess sodium (Na^+) concentration gradient across plasma membrane. It is reached due to the great difference in ionic composition between interior and exterior regions of the cell. Intracellular Na^+ concentration $[Na^+]_i$ is ten to twenty times lower than extracellular concentration in every organisms. Typically, $[Na^+]_i$ varies around 5-15 mM depending on the cell type in mammals, whereas its extracellular amount is much higher, around 120-150 mM. Such concentration gradient is established through activity of ion channels/transporters and pumps and is required for maintenance of resting membrane potential. Thus, ion movement across plasma membrane might initiate electrical excitation as well as local cytoplasmic responses. Therefore, Na^+ ion has been proposed as a second messenger that could regulate many signalling pathways involved in both physiological and pathological cellular properties (Besson et al. 2015; Roger et al. 2015). Despite being important in functioning of excitable and non-excitable tissues (e.g. nerve conduction and organogenesis, accordingly), Na^+ signalling has also been associated with cancer cell behaviours (Fraser et al. 2014). Indeed, Na^+ signalling has been shown to play a significant role in cell polarity, motility, migration, invasiveness and extracellular matrix remodelling. Importantly, elevated total tissue Na^+ concentration has been proposed as a highly specific *in vivo* indicator of malignant lesions in human cancer patients (Jacobs et al. 2011; Ouwerkerk et al. 2003; Ouwerkerk et al. 2007). Therefore, investigation of Na^+ signalling dynamics at a cellular level could give us a better understanding on how variety of carcinogenic processes are being regulated.

Various experimental approaches have been developed to study changes in $[Na^+]_i$. For example, ^{23}Na nuclear magnetic resonance spectroscopy offers a reliable method for non-invasive quantification of $[Na^+]_i$ in perfused cancer cells and tissues(Hansen et al. 1993). Flow cytometry also provides feasible $[Na^+]_i$ measurements (Amorino and Fox 1995). However,

due to the heterogeneity of cancer cell populations, only large differences could be accurately discriminated by these methods. Functionality of Na^+ channels and hence their active Na^+ currents can be investigated by usage of the patch-clamp technique (Armstrong 1981; Roden and George 1997). However, all these options do not provide fast and dynamic method to quantify $[Na^+]_i$ variations as Na^+ fluorescence indicator dyes do. Indeed, some studies have reported on successful Na^+ imaging in various types of cells (Baquero and Gilbertson 2011; Komlosi et al. 2003; Lahn et al. 2011; Miyazaki and Ross 2015). Regarding the fact that Na^+ signalling is considered as an important controller of cancer progression, it is highly surprising that only few research groups have published their Na^+ imaging results using cancer cell lines (Gao et al. 2009b; Roger et al. 2007). Therefore, it can be suggested that realization of this technique is still imposing many challenges within the scientific community. In addition, existing variety of the commercially available Na^+ dyes makes unclear which one can be considered as the most reliable probe to visualize Na^+ fluctuations *in vitro*.

In this study, we have performed the comparison of three Na^+ specific fluorescent dyes – Na^+-binding benzofuran isophthalate (SBFI), CoroNa^{TM} Green (Corona) and Asante NaTRIUM Green-2 (ANG-2) in prostate cancer cells. The dyes have been evaluated by their various parameters (e.g. time for loading, working range, and sensitivity). Throughout this study, increases in free $[Na^+]_i$ have been reached *via* diverse pathways – ubiquitous and cell type-specific (Fig.1). For example, various types of human cancer cells, including prostate, have been reported to express voltage-gated sodium channels (Fraser et al. 2014; Shan et al. 2014). Thus, application of sodium channel activator, veratridine, would lead to $[Na^+]_i$ increase only in cells where functional sodium channels are expressed on plasma membrane. On the contrary, Na^+/K^+-ATPase, protein that transports three Na^+ out of the cell against two K^+ inside, is found in plasma membrane of all animal cells (Dlouha et al. 1979; Quinton and

Tormey 1976; Robinson 1975). Hence, the application of ouabain, a specific inhibitor of Na^+/K^+-ATPase, would result in omnipresent $[Na^+]_i$ increase. Similarly, ionomycin is an ionophore that acts on any kind of cell where it enables calcium (Ca^{2+}) entry through plasma membrane and its release from the endoplasmic reticulum (Moskowitz and Hruska 1992; Nilsson et al. 1987). Elevated cytosolic $Ca^{2+}$are thus expected to affect the activity of Na^+/Ca^{2+} exchanger that imports Na^+ and hence to increase $[Na^+]_i$. In addition, Na^+ entry can be provided *via* ion diffusion down the electrochemical gradient through Na^+-specific leak channels (Pajor and Wright 1992; Parent et al. 1992; Wright et al. 1992). However, very little is yet known on the mode of operation of these channels. In this study, the function of Na^+-leak channels has been investigated due to the alteration of extracellular Na^+ concentration.

Overall, this is the first study to report on Na^+ fluorescence imaging in prostate cancer cells. Moreover, it addresses many technical issues associated with the different Na^+ specific probes and provides a better understanding on their proper application *in vitro*.

Materials and Methods

Cell culture

In this study, human prostate cancer cell lines of epithelial origin have been used. DU 145 and PC-3 have been purchased from the American Type Culture Collection (ATCC®), whereas – PC-3M have been kindly provided by Prof Mustafa Djamgoz (Imperial College London, UK). These cancer cell lines derive from various metastatic sites and are relatively classified by their tumorigenic potential as follows: DU 145 – issue from brain, moderately metastatic (Stone et al. 1978); PC-3 – issue from bone, highly metastatic (Kaighn et al. 1979); and PC-3M – issue from liver, more aggressive derivative of PC-3(Kozlowski et al. 1984). Cells were routinely cultured at 37ºC in a humidified atmosphere with 5% CO_2 in RPMI 1640 medium (Gibco^{TM}, Thermo Fischer Scientific) containing a final concentration of 10% fetal bovine serum (Gibco^{TM}) and 2 mM L-Glutamine (Gibco^{TM}, Thermo Fischer Scientific). Twice a week, cultures were split by treatment with 0.25% trypsin-EDTA (Gibco^{TM}, Thermo Fischer Scientific) for 5 min at 37ºC.

Solutions

The Hank's buffer saline solution (HBSS) comprised as follows (mM): NaCl 150, KCl 5, $MgCl_2$ 1, $CaCl_2$ 2, D-Glucose 10, and HEPES 10, adjusted to pH 7.4 with 1 M NaOH. Na^+-free solution contained the following components (in mM): Choline chloride 150, $MgCl_2$ 1, KCl 5, $CaCl_2$ 2, D-Glucose 5.6, and HEPES 10, adjusted to pH 7.4 with 1 M KOH. Extracellular solution with high Na^+ concentration consisted of (mM): NaCl 150, KCl 5, $MgCl_2$ 1, $CaCl_2$ 2, D-Glucose 5.6, and HEPES 10, adjusted to pH 7.4 with 1 M NaOH. For calibration purposes, Na^+ dilutions (ranged from 0 to 140 mM) containing 20 µM gramicidin and monensin have been prepared. Ouabain-, ionomycin- and veratridine-containing solutions

were prepared in HBSS. All reagents have been purchased from Sigma-Aldrich, unless otherwise specified.

Sodium fluorescent imaging

All probes were purchased in a form of cell-permeant acetoxymethyl esters: Na^+-binding benzofuran isophthalate (SBFI) from Interchim (Cat. №FP-82902B), whereas CoroNa™ Green (CoroNa) and Asante NaTRIUM Green-2 (ANG-2) – from Life Technologies (Cat. № C36676) and TEFlabs (Cat. № 3512), accordingly. Dyes were reconstituted in dimethyl sulfoxide (DMSO) and diluted in HBSS containing 0.02% of Pluronic® F127 to the final concentrations of 7 µM for SBFI, 10 µM for CoroNa, and 5 µM for ANG-2.

Cells were plated onto 30 mm glass coverslips and grown in standard conditions for three days. During this time, cells properly attached to the coverslips and had time to divide at least once. In such a way, we reassured that cells were exhibiting healthy phenotype prior to experimental procedure. Then coverslips were washed with HBSS and loaded with 1 ml of the dye solution as follows: for SBFI – 5 hours in the incubator at 37ºC, for CoroNa – 1 hour in the incubator at 37ºC, and for ANG-2 – 1 hour at room temperature. Afterwards, coverslips were gently rinsed with HBSS, fixed on the imaging platform and left in the appropriate experimental solution. All recordings, including calibrations, were performed at room temperature. About 50 cells per field of view were selected for fluorescence measurements. Background fluorescence was selected as an area with no cells and subtracted from each data point obtained during experiment.

Fluorescence was excited using an illumination DG4 system (Sutter) fitted with a xenon lamp 300W. All recordings of Na^+ fluorescence have been acquired using objective 20x Superfluor Nikon Eclipse T*i*- series inverted microscope coupled to EMCCD camera Rolera EM-C^2 (Qimaging) and processed using Metafluor 7.7.5.0 software. The excitation

filters represented following parameters in terms of wavelength and bandwidth: 340 nm / 26 nm and 387 nm / 11 nm for SBFI; 482 nm / 35 nm for CoroNa; and for ANG-2. The emission filters were as follows: 510 nm / 84 nm for SBFI, 536 nm / 40 nm for CoroNa and for ANG-2.

Results

Basics of sodium imaging and ion-specific indicators

The Na^+-imaging technique is based on the recordings of signals produced by fluorescent Na^+ indicator dyes. These molecules are typically composed of an ion-binding site and a fluorophore unit (Fig. 2). Thus, the principle is built on dye conformational changes upon Na^+ binding which are followed by spectral changes. This can be assessed by exciting dyes' fluorescence using specific wavelengths and measuring the emitted light, which can be registered and visualized by the software. The variety of commercially available Na^+ probes is still relatively small, when comparing to the wide range of Ca^{2+} indicator dyes (Rose 2012). Nevertheless, there is still a significant contrast between general chemical properties of the molecules (e.g. fluorescence, ion specificity, affinity, *etc*). Therefore, these differences have to be accurately considered prior to the dye employment. Importantly, a reliable Na^+ indicator should be highly specific for Na^+ over other ions. Hence, Na^+ binding (or unbinding) should result in a significant change in the fluorescence emission. Furthermore, high dye concentrations and long-term exposure times are not advised for elimination of the possible cytotoxic effects. Thus, emission efficacy of the fluorophore should be as high as possible. To date, Na^+ indicator dyes are available in the modified form of acetoxymethyl esters. In this form, the passage of the dye across cell membrane is facilitated. Once inside, the acetoxymethyl groups are removed by cellular esterases and uniformly dispersed in the cytoplasm.

Despite new developments, the most commonly used Na^+ indicator dye is still SBFI, first described in 1989 (Minta and Tsien 1989). As a ratiometric dye, it can be excited at two separate wavelengths (340 nm and 380 nm) and the emitted fluorescence reaches a maximum of intensity at 500 nm. The excitation spectra is shifted upon Na^+ binding onto SBFI, the Na-bound SBFI and the Na-free SBFI displaying excitation peak at 340 and 380 nm, respectively. The ratio of emitted fluorescence obtained at each wavelength (F_{340nm}/ F_{380nm}) thus directly correlates with $[Na^+]_{i,}$ whereas the SBFI emission spectra does not depend on changes in $[Na^+]_i$. The properties of CoroNa have been described in detail by earlier studies (Martin et al. 2005; Meier et al. 2006). It is excited by visible light and exhibits an increase in fluorescence emission intensity upon binding of Na^+ with just little shift in wavelength. The excitation and emission maxima of CoroNa are at 492 nm and 516 nm, accordingly, whereas for absorbance it is near 488 nm. The selectivity of CoroNa is 4 times higher to Na^+ than to K^+ binding (Martin et al. 2005). Moreover, CoroNa exhibits relatively high dissociation constant K_d, making it well suitable for measuring large $[Na^+]_i$ transients (Martin et al. 2005). Lately, a novel Na^+ indicator, Asante NaTrium Green 1 has been described (Kim et al. 2010; Lamy and Chatton 2011). According to the manufacturer (TEFLabs Inc., Austin, TX), another derivative, ANG-2, does even show improved fluorescence properties, but up to now, no data with this dye have been published. The excitation and emission maxima of ANG-2 are around 532 nm and 550 nm, and sodium binding induces an increase in fluorescence intensity.

Loading of the cells with sodium indicator dyes

Within the existing variety of methods for the dye delivery inside of the cell (e.g. microinjection, electroporation, patch-pipette administration, etc.), the usage of esterified compounds is the most practical. The membrane-permeable ester reaches cytoplasm due to hydrolytic reaction and hence no special facilities are required. However, the disadvantage of

esters is their ability to accumulate inside intracellular compartments making indicator insensitive to the cytosolic levels of Na^+. It can be avoided by decreasing the loading temperature, which usually implies longer incubation time. Therefore, the loading conditions of each Na^+ indicator have to be accurately adjusted.

In this study, we optimized loading conditions of esterified SBFI, CoroNa and ANG-2 indicator dyes when using human prostate cancer cell lines DU 145, PC-3 and PC-3M. The loading conditions were mostly comparable to the manufacturer indications and changed if necessary. It has been reported that the loading time for SBFI may vary depending on the cell type. In our study, the loading times for SBFI and CoroNa were prolonged for 5 hours and 1 hour, respectively. Furthermore, the working concentrations of CoroNa were step-wise increased from 0.5 µM to 10 µM. Nevertheless, even with high concentrations of CoroNa (10 µM), a gradual fluorescence signal loss was observed, more likely due to the dye leakage out of the cell. Alterations of the loading temperatures did not improve the procedure and hence were not modified.

Calibration of the dyes

When employing Na^+ indicator dyes, $[Na^+]_i$ is not measured directly. Therefore, calibration is required in order to convert fluorescence signals into defined changes in $[Na^+]_i$. Of note, constructed calibration curves are crucial for estimating multiple working parameters. For example, the dissociation constant K_d, indicative of the indicator dye affinity for Na^+, should be within the expected physiological range of $[Na^+]_i$ in the biological sample. Furthermore, efficient measurements of $[Na^+]_i$ changes could be recorded under condition where the working range of the dye varies between 0.1 to 10 times of its K_d value. Therefore, these parameters have to be taken into account during the experimental design. Here we describe *in vitro* calibration procedures of SBFI, CoroNa and ANG-2 Na^+ indicator dyes using PC-3 cells

that have been sequentially exposed to solutions with different Na^+ values (ranged from 0 to 120 mM) containing 10 µg/ml of monensin and gramicidin.

Calibration of ratiometric dye SBFI:

Typical changes in fluorescence emitted during excitation at 340 nm (F_{340nm}) and 380 nm (F_{380nm}) have been obtained after calibration and are illustrated as F_{340nm} and F_{380nm}, respectively, in Fig. 3A. As it has been expected, F_{380nm} inversely correlates with the changes in $[Na^+]_i$, whereas F_{340nm} remains essentially unaffected. Accordingly, the fluorescence ratio F_{340nm}/F_{380nm} directly corresponds to the alterations in $[Na^+]_i$ (Fig. 3B). Nevertheless, it is still required to convert F_{340nm}/F_{380nm} recordings into $[Na^+]$ values. Typically for ratiometric dyes as SBFI, it is done by using standard equation (Grynkiewicz et al. 1985):

$$[Na^+] = \beta \times K_d [(R_n - R_{n(min)}) / (R_{n(max)} - R_n)] \quad (1)$$

where $\beta = F_{380nm(max)}/F_{380nm(min)}$; K_d – dissociation constant; $R_n = F_{340nm}/F_{380nm}$ at each data point recorded; $R_{n(min)}$ and $R_{n(max)}$ are the fluorescence ratios F_{340nm}/F_{380nm} at the lowest and highest $[Na^+]$concentration applied during calibration. Thus, R_n, $R_{n(min)}$ and $R_{n(max)}$ are known, and β can be estimated from the values illustrated in Fig. 3A. In order to calculate K_d, the fluorescence ratio F_{340nm}/F_{380nm} has been plotted versus $\log_{10}$ of known $[Na^+]$ values used for the calibration (Fig. 3C). The derived curve was fitted by using Logistic function.

$$R_n = R_{n(max)} + [R_{n(min)} - R_{n(max)}) / (1 + ([Na^+] / K_d) \wedge p] \quad (2)$$

where p = is the power which represents the slope of the linear part of the curve.The EC_{50} (K_d value) was computed and found to be 5.3 mM. We propose that the optimal working range of SBFI varies between 0.5 mM and 30 mM $[Na^+]$ *in vitro*. This range has been also confirmed on Fig. 3B, where alterations of $[Na^+]_i$ have initiated the most apparent changes in ratio F_{340nm}/F_{380nm} intensity. Overall, the identification of all parameters required in *Eq.1* has enabled us to evaluate $[Na^+]_i$ throughout all recordings performed with SBFI in this study.

Calibration of non-ratiometric dyes CoroNa and ANG-2:

The calibration for single wavelengths dyes as CoroNa and ANG-2 is relatively simple. The fluorescence intensities obtained after administration of various extracellular Na^+ levels are illustrated in Fig. 4A and 5A. Afterwards, the intensity values have been plotted versus $\log_{10}$ of [Na^+] applied (Fig. 4B and 5B). The Logistic function has been used for curve fitting (see *Eq.2*), where K_d value has been derived as EC_{50}. In this study for CoroNa dye K_d = 10.5 mM, whereas for ANG-2 dye K_d = 3.4 mM. Accordingly, the working range of the dyes is suggested as follows: 1mM to 60 mM for CoroNa, and 0.5 mM to 30 mM for ANG-2.

Response to changes in extracellular sodium concentration

The passive transport of many ions including Na^+ is carried out across the plasma membrane down the electrochemical gradient. Thus, in order to investigate the correlation of $[Na^+]_i$ variations with changes in extracellular [Na^+], we performed a so called "Na^+ switch". First, cells were washed in Na^+-free media to eliminate residual Na^+ ion presence. After an initial recording carried out in Na^+-free solution, extracellular [Na^+]was switched to 75 mM and 110 mM. As indicated in Fig. 6A, PC-3 cells responded to the sodium switch with a two-fold larger Na^+ entry than PC-3M, whereas DU 145 exhibited relatively stable levels of $[Na^+]_i$ whatever the extracellular Na^+ concentration was. Although Na^+ diffusion at resting membrane potential is generally accepted as a well-known phenomenon, very little is known about its precise mechanisms. From our results, it is obvious that DU 145 cells are more resistant to extracellular [Na^+] changes than PC-3 or PC-3M. Thus, it can be suggested that $[Na^+]_i$ in DU 145 cells has reached some limit or saturation point, and hence no more Na^+ can enter inside or that DU145 have efficient Na^+ buffering mechanisms which allow its rapid extrusion upon Na^+ entry. In addition, it can be hypothesized that passive Na^+ transports might be mediated through some ion-specific channels, which are absent/non-functional in

DU 145 cells. Nevertheless, these pathways are still scarcely described overall and have to be identified for prostate cancer cells in particular.

Response to increase in cytosolic calcium concentration

Ionomycin is an ionophore which is often used as a tool for investigating Ca^{2+}-associated mechanisms (Moskowitz and Hruska 1992; Nilsson et al. 1987). Of note, it creates pores in the lipid membrane layer that permits intracellular Ca^{2+} entry. Moreover, after application, ionomycin itself easily penetrates inside of the cell and reaches endoplasmic reticulum. Consequently, the rise of $[Ca^{2+}]_i$ is augmented due to endoplasmic reticulum depletion. In this study, we have used ionomycin in order to elevate $[Ca^{2+}]_i$ and hence affect Na^+/Ca^{2+} exchanger as the predominant cellular mechanism of Ca^{2+} efflux. Accordingly, in conditions where $[Ca^{2+}]_i$ is high, the Na^+/Ca^{2+} exchanger allows Na^+ entry and as a result $[Na^+]_i$ increases. Here, we have observed a similar raise in $[Na^+]_i$ within all prostate cancer cell lines tested (Fig. 7). It might be explained due to the nature of ionomycin, which is not cell type-dependent reagent. Hence, its application leads to equal intracellular Ca^{2+} release regardless of the cell line. Consequently, the activity of Na^+/Ca^{2+} exchanger has been similarly affected and provoked comparable changes in $[Na^+]_i$ in all cell lines. Of note, ANG-2 was slightly less sensitive than SBFI, whereas CoroNa exhibited only partial $[Na^+]_i$ fluctuations after ionomycin administration (Fig. 7).

Response to sodium/potassium pump inhibition

Na^+/K^+ ATPase participates in active ion transport by pumping Na^+ and K^+ against their concentration gradients. The enzyme is present in all higher eukaryotes and hence its functioning has been investigated in galore. In particular it has been attributed to the maintenance of the membrane resting potential, cell volume regulation, signal transduction,

etc (Dlouha et al. 1979; Quinton and Tormey 1976; Robinson 1975). Besides controlling intrinsic cellular activities, multiple studies have reported on Na^+/K^+ ATPase differential expression in cancer cells and its involvement in cell survival, proliferation, adhesion, migration and invasiveness (Mijatovic et al. 2012; Mijatovic et al. 2008; Weidemann 2005). Overall, Na^+/K^+ ATPase may be considered as one of the most important players of intracellular Na^+ signalling with its prominent role in cellular (patho)-physiology. Therefore, Na^+-imaging is an essential technique for visualization of Na^+/K^+ ATPase functioning *in vitro*. In the present study, the activity of Na^+/K^+ ATPase was examined by the application of a pump-specific inhibitor, ouabain, at a concentration of 250 μM. As expected, all cell lines tested have responded with a progressive accumulation of $[Na^+]_i$ (Fig. 8). Interestingly, DU 145 and PC-3 cells exhibited higher $[Na^+]_i$ elevations than PC-3M cells (Fig. 8). This could imply various expression levels of this enzyme among different prostate cancer cell lines. Noteworthy, all three Na^+ indicator dyes were able to detect $[Na^+]_i$ increase in DU 145 and PC-3 cells (Fig 8A, B). However, CoroNa exhibited lower sensitivity for $[Na^+]_i$ elevation in these cells and was not sufficiently effective to uncover lower response in PC-3M cells (Fig. 8A, B).

Response to voltage-gated sodium channel agonist

Voltage-gated Na^+ channels are known for their involvement in allowing action potential triggering and propagation in nerve and muscle tissues (Denac et al. 2000). However, there is growing evidence on the implementation of these channels in “non-excitable” epithelial cells (Barshack et al. 2008; Gao et al. 2009a). Especially voltage-gated Na^+ channels have been found upregulated in many carcinomas, and in particular associated with their metastatic potential (Patel and Brackenbury 2015; Roger et al. 2015). Therefore, in our study we have used DU 145, PC-3 and PC-3M cells which are considered as highly aggressive model of

human prostate cancer. Indeed, these cell lines have been reported to express voltage-gated Na^+ channels (Nakajima et al. 2009; Shan et al. 2014). Thus, we have investigated their functioning using a channel-specific agonist, veratridine. Surprisingly, as measured using SBFI and ANG-2, voltage-gated Na^+ channel "opener" provoked a minor $[Na^+]_i$ increase in DU 145 cells and had no effect on PC-3 and PC-3M (Fig. 9A, B). On the one hand, it can be suggested that voltage-gated Na^+ channels are simply not functionally active or localized in intracellular compartments rather than on the plasma membrane in the cell lines tested. On the other hand, it can be explained due to the lack of the effect of veratridine itself, which has already been reported for rat prostate cancer cells (Fraser et al. 2000). Interestingly, veratridine was found to affect only differentiated cells (Imanishi et al. 2006). Thus, it can explain poor performance of this agonist on advanced cancer cells that are considered to possess undifferentiated cell phenotype. Furthermore, the value of veratridine as a chemical activator of voltage-gated Na^+ channels has been undermined since it was shown to have only a slight influence on the tetrodotoxin-resistant channel in non-voltage-clamped cells (Farrag et al. 2008). Overall, it has been previously suggested that veratridine may interact with other ion channels and hence its mode of action may be rather complex (Fraser et al. 2003; Romey and Lazdunski 1982; Verheugen et al. 1994).

Discussion

Technical aspects

Occasionally, technical limitations may become decisive for awhole experimental design. Thus, some major aspects of SBFI, CoroNa and ANG-2 applications have to be taken into account (Table 1) for intracellular Na^+ measurements. For example, employment of such a ratiometric dye as SBFI eliminates experimental variables as cell thickness or size, photobleaching and dye concentration. However, it is sensitive to changes in intracellular pH (Diarra et al. 2001). Therefore, Na^+ recordings involving significant pH alterations should be reconsidered using an alternative Na^+ indicator dye. However, a ratiometric dye enables direct comparison between different experiments and quantitative measurement of signals. And, if precise $[Na^+]_i$ estimation is required while using single-excitation wavelength dye, the calibration procedure has to be performed on each sample tested. The employment of the latter becomes markedly inconvenient for Na^+-imaging in multiple samples, that is often required to reach statistical significance, especially when the response is transient and/or of a low magnitude. Interestingly, the calibration of all three Na^+ indicator dyes has shown that CoroNa is more suitable for detecting $[Na^+]_i$ variations in a wider range of concentrations. Its working range and K_d are at least twice larger than for SBFI or ANG-2. Indeed, CoroNa has been previously reported to discriminate substantial $[Na^+]_i$ changes at high background $[Na^+]$ (Meier et al. 2006). SBFI, CoroNa and ANG-2 are not toxic *per se* and there have not been any pharmacological effects of the indicators demonstrated yet. However, short exposure times and low indicator concentrations are favourable to minimize cellular stress. In this case, the disadvantage of SBFI is its slow cellular transfusion even after addition of special dispersion agent Pluronic® F127. For example, in this study it took 5 hours to charge human prostate cancer cells DU 145, PC-3 and PC-3M. Nevertheless, it has been reported that SBFI

loading strongly depends on the cell type and hence it is possible that for some other *in vitro* models this issue will not occur (Diarra et al. 2001; Minta and Tsien 1989).

Suitability for sodium-imaging in vitro

This study has been conducted to compare three different Na^+ specific fluorescent dyes and their feasibility for *in vitro* Na^+-imaging. After the working parameters were derived from calibration curves, it was necessary to examine the dyes utilities within experimental conditions. Therefore, changes in $[Na^+]I$ were initiated through various pathways (Fig 1). Of note, CoroNa has exhibited lower signal intensities than SBFI or ANG-2 throughout all experiments. This could be interpreted due to the elevated K_d and working range of CoroNa, which means that the dye may work more accurately for higher $[Na^+]$ alterations (Table 1). Another explanation could be attributed to the leakage of CoroNa out of the cells with time which has been observed in this study. Indeed, previous reports indicate that CoroNa may be lost quickly from intracellular medium due to its relatively small size. This can be alleviated with a constant delivery of the dye through a patch-pipette during whole-cell path clamp recordings which enables stable intracellular CoroNa concentrations (Meier et al. 2006). In a promising novel approach, Lamy and coworkers encapsulated CoroNa Green in a PAMAM dendrimer-nanocontainer to counteract permanent dye extrusion (Lamy et al. 2012). SBFI and ANG-2 have exhibited comparable levels of signal intensities after various $[Na^+]_i$ alterations. However, it has to be kept in mind that Na^+-imaging conducted with the SBFI dye enables a reliable and quantitative determination of the real $[Na^+]_i$, whereas loading conditions for ANG-2 are more practical.

In conclusion, this study presents *in vitro* Na^+-imaging in human prostate cancer cells. According to our data, CoroNa is not suitable for detection of relatively low $[Na^+]_i$ changes in the prostate cancer cell model studied here, whereas SBFI and ANG-2 can provide efficient recordings.

Acknowledgement

Ms Oksana Iamshanova was funded by the “Ligue Contre le Cancer”, France.

Figure legends

Fig. 1. Schematic representation of the molecular pathways used in this study to induce alterations of the intracellular sodium concentrations ($[Na^+]_i$). Typical Na^+ concentrations of the mammalian cells are 5 to 15 mM for cytosol ($[Na^+]_{int}$) and 120 to 150 mM for extracellular ($[Na^+]_{ext}$) medium. The extracellular concentration has been switched from 0 to 110 mM for investigating ion diffusion down the electrochemical gradient through Na^+ leak channels. Ouabain inhibits the activity of Na^+/K^+ ATPase and hence restrains constant expulsion of the intracellular Na^+. The application of voltage-gated sodium channels (VGSCs) opener, veratridine, should also result in a $[Na^+]_i$ increase. Ionomycin as an ionophore promotes calcium entry through the plasma membrane and the depletion of endoplasmic reticulum (ER) Ca^{2+}storesand hence boosts the activity of Na^+/Ca^{2+} exchanger (NCX).

Fig. 2. Chemical structures of the different Na^+ indicator dyes used in this study in the form of acetoxymethyl esters (AM): Na^+-binding benzofuran isophthalate (SBFI), CoroNa^{TM} Green (CoroNa) and Asante NaTriumGreen 2 (ANG-2).

Fig. 3. Calibration of SBFI in human prostate cancer PC-3cells. The real-time extracellular concentrations of Na^+(0 to 120 mM) are indicated. **A,** changes in emitted fluorescence intensities during excitation at 340 nm and 380 nm. **B,** fluorescence ratio 340 nm/ 380 nm derived from signals shown in A. **C,** data from **B** plotted versus $\log_{10}$ of the known Na^+ concentrations and fitted using a Logistic function; the derived EC_{50} value has been attributed to K_d = 5.3 mM. The working range is proposed to lie within the linear scale of the curve, i.e. 0.5 to 30 mM. Data is represented as mean±SD.

Fig. 4. Calibration of CoroNa in human prostate cancer PC-3cells. The real-time extracellular concentrations of Na^+ (0 to 120 mM) are indicated. **A,** emitted fluorescence intensities at 488 nm. **B,** data from **A** plotted versus log_{10} of the known Na^+ concentrations and fitted using a Logistic function; the derived EC_{50} value has been attributed to K_d of 10.5mM.The working range is proposed to lie within the linear scale of the curve, i.e. 1 to 60 mM. Data is represented as mean±SD.

Fig. 5. Calibration of ANG-2 in human prostate cancer PC-3cells. The real-time extracellular concentrations of Na^+ (0 to 120 mM) are indicated. **A,** emitted fluorescence intensities at 540 nm. **B,** data from **A** plotted versus log_{10} of the known Na^+ concentrations and fitted using a Logistic function; the derived EC_{50} value has been attributed to K_d = 3.4mM.The working range is proposed to lie within the linear scale of the curve, i.e. 0.5 to 30 mM. Data is represented as mean±SD.

Fig. 6.$[Na^+]_i$ levels during Na^+ switch from 0 to 75 mM and 110 mM concentrations. **A,** fluorescence intensities normalized to the initial values (F/F_0). **B,** SBFI fluorescence ratios 340 nm/380 nm and corresponding calibrated levels of $[Na^+]_i$. Data is represented as mean±SD.

Fig. 7.$[Na^+]_i$ levels after Na^+/K^+-ATPase inhibition induced by an application of 250 µM ouabain. **A,** fluorescence intensities normalized to the initial values (F/F_0). **B,** SBFI fluorescence ratios 340 nm/ 380 nm and corresponding calibrated levels of $[Na^+]_i$. Data is represented as mean±SD.

Fig. 8.$[Na^+]_i$ levels after cytosolic Ca^{2+} increase induced by an application of 1 µM ionomycin. **A,** fluorescence intensities normalized to the initial values (F/F_0). **B,** SBFI fluorescence ratios 340 nm/ 380 nm and corresponding calibrated levels of $[Na^+]_i$. Data is represented as mean±SD.

Fig. 9. $[Na^+]_i$ levels after voltage-gated sodium channels opening induced by an application of 50 µM veratridine. **A,** fluorescence intensities normalized to the initial values (F/F_0). **B,** SBFI fluorescence ratios 340 nm/ 380 nm and corresponding calibrated levels of $[Na^+]_i$. Data is represented as mean±SD.

References

Amorino GP, Fox MH (1995) Intracellular Na+ measurements using sodium green tetraacetate with flow cytometry Cytometry 21:248-256 doi:10.1002/cyto.990210305

Armstrong CM (1981) Sodium channels and gating currents Physiol Rev 61:644-683

Baquero AF, Gilbertson TA (2011) Insulin activates epithelial sodium channel (ENaC) via phosphoinositide 3-kinase in mammalian taste receptor cells Am J Physiol Cell Physiol 300:C860-871 doi:ajpcell.00318.2010 [pii]10.1152/ajpcell.00318.2010

Barshack I, Levite M, Lang A, Fudim E, Picard O, Ben Horin S, Chowers Y (2008) Functional voltage-gated sodium channels are expressed in human intestinal epithelial cells Digestion 77:108-117 doi:000123840 [pii]10.1159/000123840

Besson P, Driffort V, Bon E, Gradek F, Chevalier S, Roger S (2015) How do voltage-gated sodium channels enhance migration and invasiveness in cancer cells? Biochim Biophys Acta 1848:2493-2501 doi:S0005-2736(15)00136-4 [pii]10.1016/j.bbamem.2015.04.013

Denac H, Mevissen M, Scholtysik G (2000) Structure, function and pharmacology of voltage-gated sodium channels Naunyn Schmiedebergs Arch Pharmacol 362:453-479

Diarra A, Sheldon C, Church J (2001) In situ calibration and [H+] sensitivity of the fluorescent Na+ indicator SBFI Am J Physiol Cell Physiol 280:C1623-1633

Dlouha H, Teisinger J, Vyskocil F (1979) Activation of membrane Na+/K+-ATPase of mouse skeletal muscle by acetylcholine and its inhibition by alpha-bungarotoxin, curare and atropine Pflugers Arch 380:101-104

Farrag KJ, Bhattacharjee A, Docherty RJ (2008) A comparison of the effects of veratridine on tetrodotoxin-sensitive and tetrodotoxin-resistant sodium channels in isolated rat dorsal root ganglion neurons Pflugers Arch 455:929-938 doi:10.1007/s00424-007-0365-5

Fraser SP, Grimes JA, Djamgoz MB (2000) Effects of voltage-gated ion channel modulators on rat prostatic cancer cell proliferation: comparison of strongly and weakly metastatic cell lines Prostate 44:61-76 doi:10.1002/1097-0045(20000615)44:1<61::AID-PROS9>3.0.CO;2-3 [pii]

Fraser SP, Ozerlat-Gunduz I, Brackenbury WJ, Fitzgerald EM, Campbell TM, Coombes RC, Djamgoz MB (2014) Regulation of voltage-gated sodium channel expression in cancer: hormones, growth factors and auto-regulation Philos Trans R Soc Lond B Biol Sci 369:20130105 doi:rstb.2013.0105 [pii]10.1098/rstb.2013.0105

Fraser SP et al. (2003) Contribution of functional voltage-gated Na+ channel expression to cell behaviors involved in the metastatic cascade in rat prostate cancer: I. Lateral motility J Cell Physiol 195:479-487 doi:10.1002/jcp.10312

Gao N et al. (2009a) Voltage-gated sodium channels in taste bud cells BMC Neurosci 10:20 doi:1471-2202-10-20 [pii]10.1186/1471-2202-10-20

Gao R, Wang J, Shen Y, Lei M, Wang Z (2009b) Functional expression of voltage-gated sodium channels Nav1.5 in human breast cancer cell line MDA-MB-231 J Huazhong Univ Sci Technolog Med Sci 29:64-67 doi:10.1007/s11596-009-0113-5

Grynkiewicz G, Poenie M, Tsien RY (1985) A new generation of Ca2+ indicators with greatly improved fluorescence properties J Biol Chem 260:3440-3450

Hansen LL, Rasmussen J, Friche E, Jaroszewski JW (1993) Method for determination of intracellular sodium in perfused cancer cells by 23Na nuclear magnetic resonance spectroscopy Anal Biochem 214:506-510 doi:S0003-2697(83)71530-7 [pii]10.1006/abio.1993.1530

Imanishi T, Matsushima K, Kawaguchi A, Wada T, Masuko T, Yoshida S, Ichida S (2006) Enhancement of veratridine-induced sodium dynamics in NG108-15 cells during differentiation Biol Pharm Bull 29:701-704 doi:JST.JSTAGE/bpb/29.701 [pii]

Jacobs MA et al. (2011) Monitoring of neoadjuvant chemotherapy using multiparametric, (2)(3)Na sodium MR, and multimodality (PET/CT/MRI) imaging in locally advanced breast cancer Breast Cancer Res Treat 128:119-126 doi:10.1007/s10549-011-1442-1

Kaighn ME, Narayan KS, Ohnuki Y, Lechner JF, Jones LW (1979) Establishment and characterization of a human prostatic carcinoma cell line (PC-3) Invest Urol 17:16-23

Kim MK, Lim CS, Hong JT, Han JH, Jang HY, Kim HM, Cho BR (2010) Sodium-ion-selective two-photon fluorescent probe for in vivo imaging Angew Chem Int Ed Engl 49:364-367 doi:10.1002/anie.200904835

Komlosi P, Fuson AL, Fintha A, Peti-Peterdi J, Rosivall L, Warnock DG, Bell PD (2003) Angiotensin I conversion to angiotensin II stimulates cortical collecting duct sodium transport Hypertension 42:195-199 doi:10.1161/01.HYP.0000081221.36703.0101.HYP.0000081221.36703.01 [pii]

Kozlowski JM, Fidler IJ, Campbell D, Xu ZL, Kaighn ME, Hart IR (1984) Metastatic behavior of human tumor cell lines grown in the nude mouse Cancer Res 44:3522-3529

Lahn M, Dosche C, Hille C (2011) Two-photon microscopy and fluorescence lifetime imaging reveal stimulus-induced intracellular Na+ and Cl- changes in cockroach salivary acinar cells Am J Physiol Cell Physiol 300:C1323-1336 doi:ajpcell.00320.2010 [pii]10.1152/ajpcell.00320.2010

Lamy CM, Chatton JY (2011) Optical probing of sodium dynamics in neurons and astrocytes Neuroimage 58:572-578 doi:S1053-8119(11)00720-8 [pii]10.1016/j.neuroimage.2011.06.074

Lamy CM, Sallin O, Loussert C, Chatton JY (2012) Sodium sensing in neurons with a dendrimer-based nanoprobe ACS Nano 6:1176-1187 doi:10.1021/nn203822t

Martin VV, Rothe A, Gee KR (2005) Fluorescent metal ion indicators based on benzoannelated crown systems: a green fluorescent indicator for intracellular sodium ions Bioorg Med Chem Lett 15:1851-1855 doi:S0960-894X(05)00186-1 [pii]10.1016/j.bmcl.2005.02.017

Meier SD, Kovalchuk Y, Rose CR (2006) Properties of the new fluorescent Na+ indicator CoroNa Green: comparison with SBFI and confocal Na+ imaging J Neurosci Methods 155:251-259 doi:S0165-0270(06)00046-X [pii]10.1016/j.jneumeth.2006.01.009

Mijatovic T, Dufrasne F, Kiss R (2012) Na+/K+-ATPase and cancer Pharm Pat Anal 1:91-106 doi:10.4155/ppa.12.3

Mijatovic T, Ingrassia L, Facchini V, Kiss R (2008) Na+/K+-ATPase alpha subunits as new targets in anticancer therapy Expert Opin Ther Targets 12:1403-1417 doi:10.1517/14728222.12.11.1403

Minta A, Tsien RY (1989) Fluorescent indicators for cytosolic sodium J Biol Chem 264:19449-19457

Miyazaki K, Ross WN (2015) Simultaneous Sodium and Calcium Imaging from Dendrites and Axons(1,2,3) eNeuro 2 doi:10.1523/ENEURO.0092-15.2015eN-MNT-0092-15 [pii]

Moskowitz DW, Hruska KA (1992) Ca2+ uptake by endoplasmic reticulum of renal cortex. I. Ionic requirements and regulation in vitro Calcif Tissue Int 51:35-41

Nakajima T et al. (2009) Eicosapentaenoic acid inhibits voltage-gated sodium channels and invasiveness in prostate cancer cells Br J Pharmacol 156:420-431 doi:BPH059 [pii]10.1111/j.1476-5381.2008.00059.x

Nilsson T, Arkhammar P, Hallberg A, Hellman B, Berggren PO (1987) Characterization of the inositol 1,4,5-trisphosphate-induced Ca2+ release in pancreatic beta-cells Biochem J 248:329-336

Ouwerkerk R, Bleich KB, Gillen JS, Pomper MG, Bottomley PA (2003) Tissue sodium concentration in human brain tumors as measured with 23Na MR imaging Radiology 227:529-537 doi:10.1148/radiol.2272020483 [pii]

Ouwerkerk R et al. (2007) Elevated tissue sodium concentration in malignant breast lesions detected with non-invasive 23Na MRI Breast Cancer Res Treat 106:151-160 doi:10.1007/s10549-006-9485-4

Pajor AM, Wright EM (1992) Cloning and functional expression of a mammalian Na+/nucleoside cotransporter. A member of the SGLT family J Biol Chem 267:3557-3560

Parent L, Supplisson S, Loo DD, Wright EM (1992) Electrogenic properties of the cloned Na+/glucose cotransporter: I. Voltage-clamp studies J Membr Biol 125:49-62

Patel F, Brackenbury WJ (2015) Dual roles of voltage-gated sodium channels in development and cancer Int J Dev Biol 59:357-366 doi:150171wb [pii]10.1387/ijdb.150171wb

Quinton PM, Tormey JM (1976) Localization of Na/K-ATPase sites in the secretory and reabsorptive epithelia of perfused eccrine sweat glands: a question to the role of the enzyme in secretion J Membr Biol 29:383-399

Robinson JD (1975) Mechanisms by which Li+ stimulates the (Na+ and K+)-dependent ATPase Biochim Biophys Acta 413:459-471

Roden DM, George AL, Jr. (1997) Structure and function of cardiac sodium and potassium channels Am J Physiol 273:H511-525

Roger S, Gillet L, Le Guennec JY, Besson P (2015) Voltage-gated sodium channels and cancer: is excitability their primary role? Front Pharmacol 6:152 doi:10.3389/fphar.2015.00152

Roger S et al. (2007) Voltage-gated sodium channels potentiate the invasive capacities of human non-small-cell lung cancer cell lines Int J Biochem Cell Biol 39:774-786 doi:S1357-2725(07)00018-0 [pii]10.1016/j.biocel.2006.12.007

Romey G, Lazdunski M (1982) Lipid-soluble toxins thought to be specific for Na+ channels block Ca2+ channels in neuronal cells Nature 297:79-78

Rose CR (2012) Two-photon sodium imaging in dendritic spines Cold Spring Harb Protoc 2012:1161-1165 doi:2012/11/pdb.prot072074 [pii]10.1101/pdb.prot072074

Shan B et al. (2014) Voltage-gated sodium channels were differentially expressed in human normal prostate, benign prostatic hyperplasia and prostate cancer cells Oncol Lett 8:345-350 doi:10.3892/ol.2014.2110ol-08-01-0345 [pii]

Stone KR, Mickey DD, Wunderli H, Mickey GH, Paulson DF (1978) Isolation of a human prostate carcinoma cell line (DU 145) Int J Cancer 21:274-281

Verheugen JA, Oortgiesen M, Vijverberg HP (1994) Veratridine blocks voltage-gated potassium current in human T lymphocytes and in mouse neuroblastoma cells J Membr Biol 137:205-214

Weidemann H (2005) Na/K-ATPase, endogenous digitalis like compounds and cancer development -- a hypothesis Front Biosci 10:2165-2176 doi:1688 [pii]

Wright EM, Hager KM, Turk E (1992) Sodium cotransport proteins Curr Opin Cell Biol 4:696-702

Table 1. Comparison of three Na^+ indicator fluorescent dyes used in this study.

Characteristics of Na^+ indicator dye	**SBFI**	**CoroNa**	**ANG-2**
As indicated by the manufacturer:			
Molecular weight, g/mol	1127.09	657.62	1084
λ_{ex}, nm	340 / 380	492	517
λ_{em}, nm	505	516	540
Ratiometric	yes	no	no
K_d, mM	3.8	80	20
Concentration, µM	5-10	0.5-10	3-10
Loading time	40 mins – 4 hours	10-45 mins	1 hour
Loading conditions	37ºC, 5% CO_2, humidified	37ºC, 5% CO_2, humidified	room conditions
As used/ obtained in this study:			
Concentration, µM	7	10	5
Loading time, hours	5	1	1
K_d *in vitro*, mM	5.3	10.5	3.4
Working range, mM	0.5 - 30	1 - 60	0.5 - 30

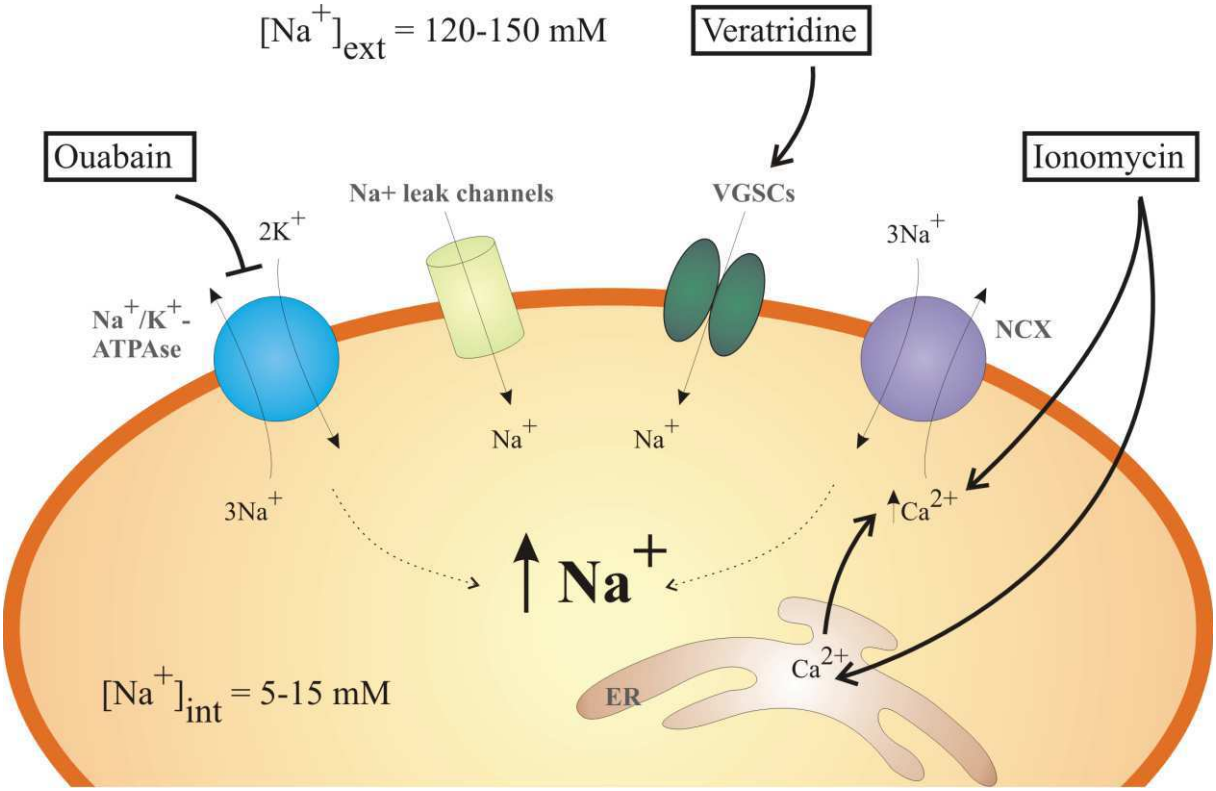

Figure 1

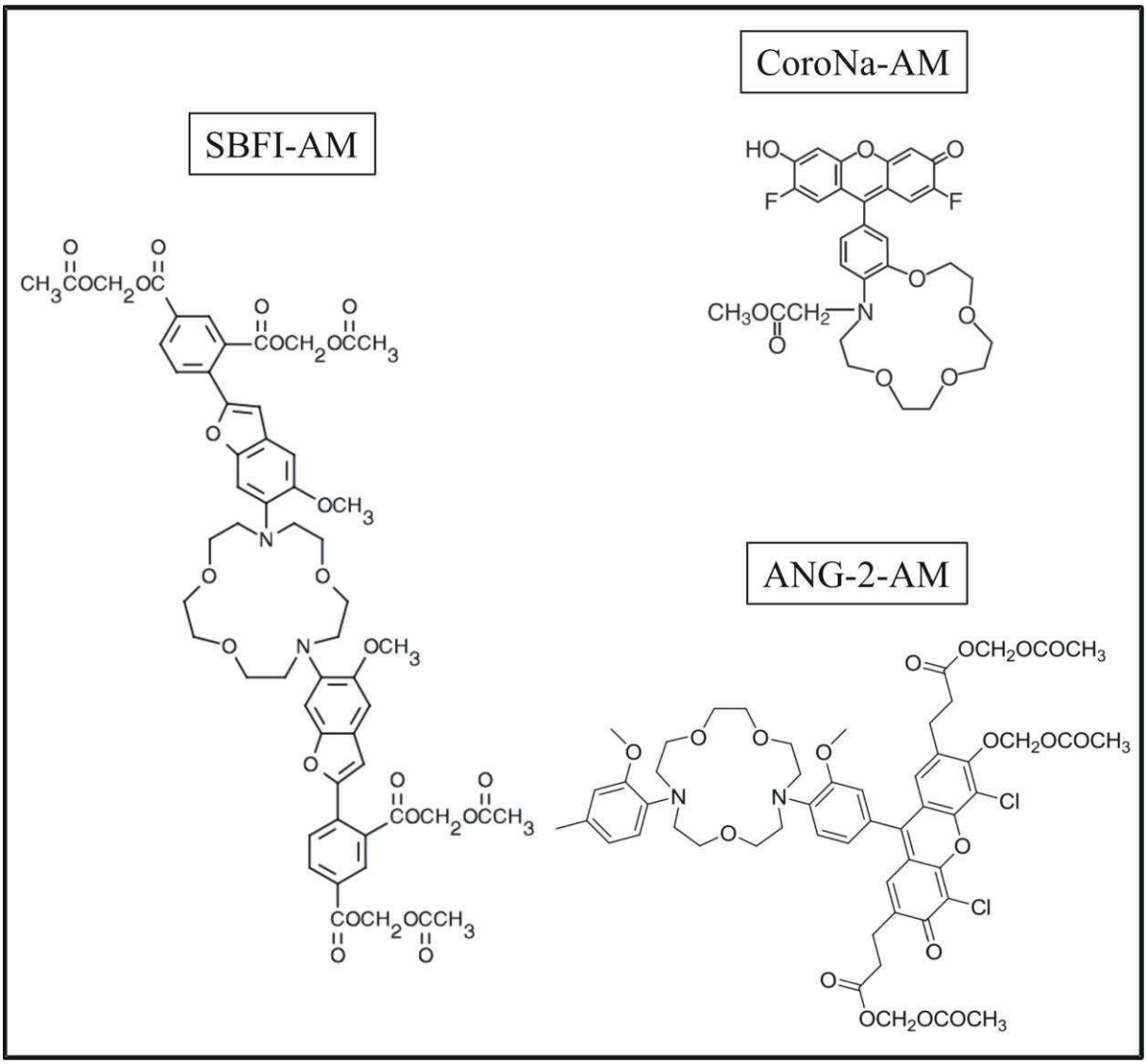

Figure 2

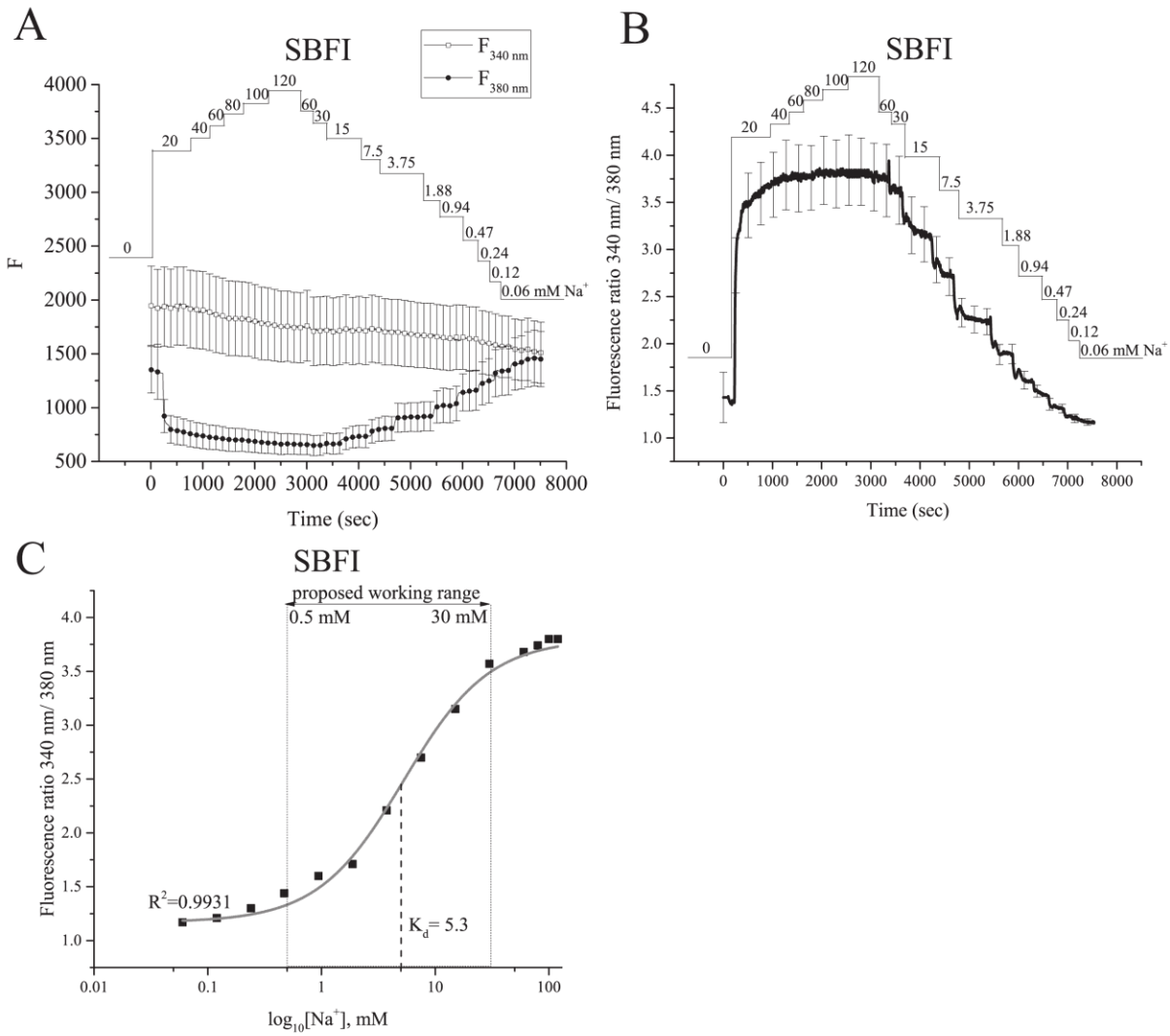

Figure 3

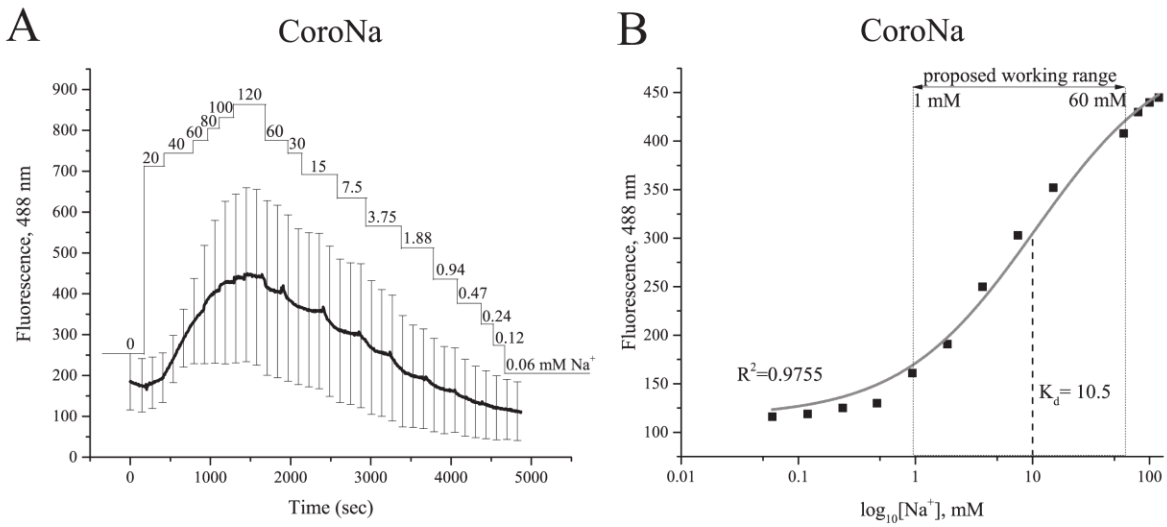

Figure 4

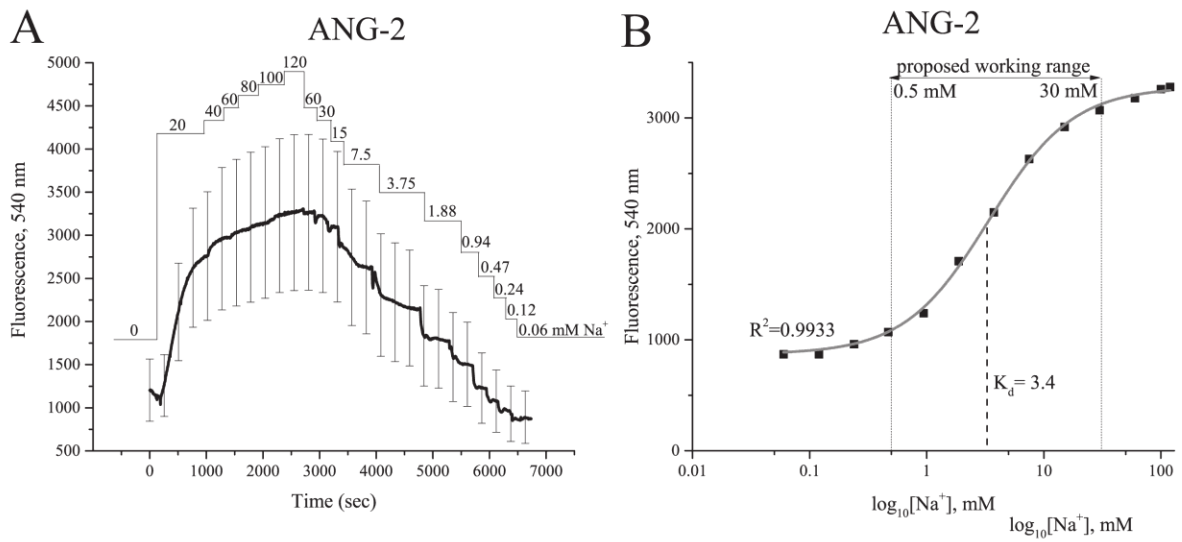

Figure 5

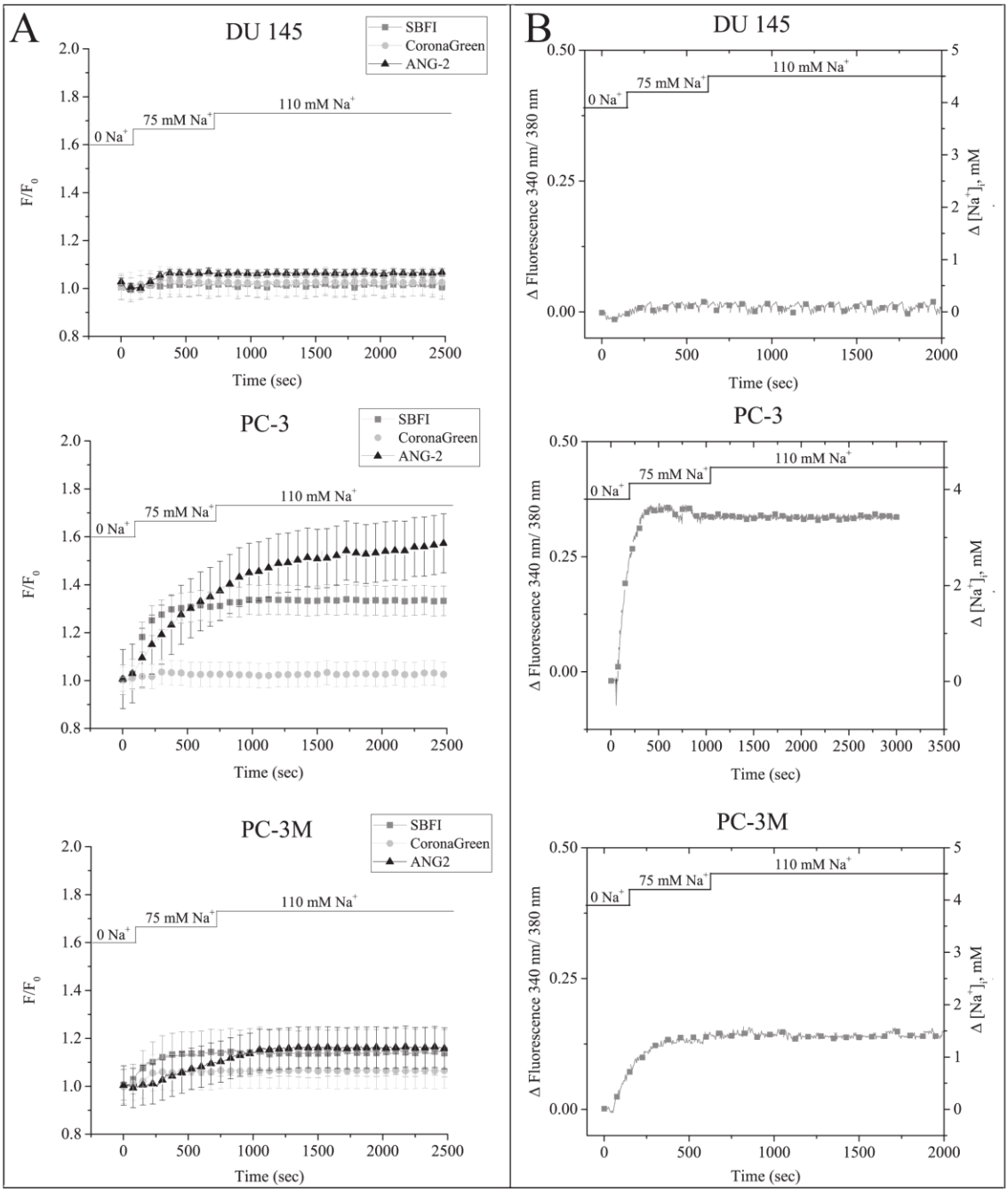

Figure 6

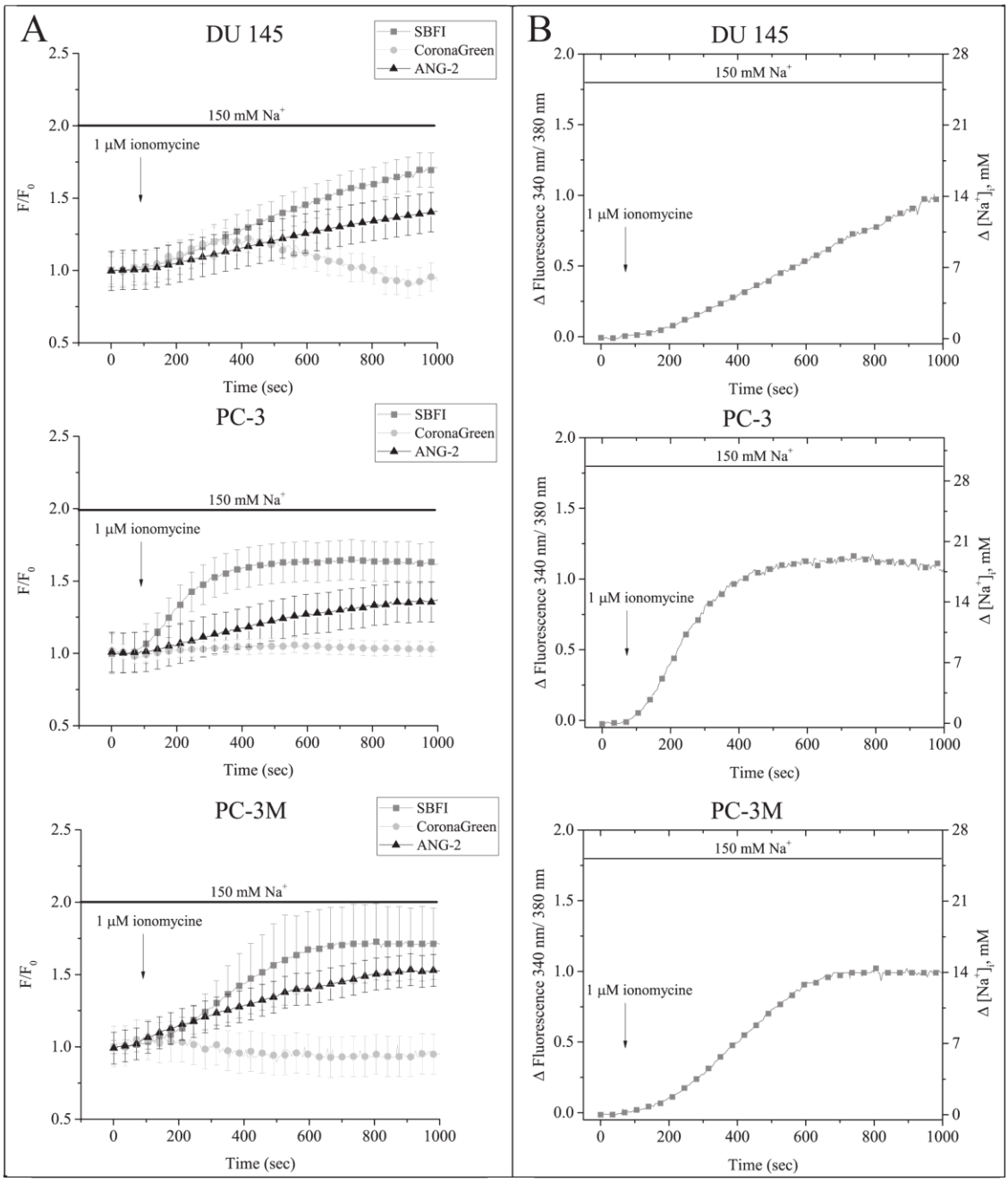

Figure 7

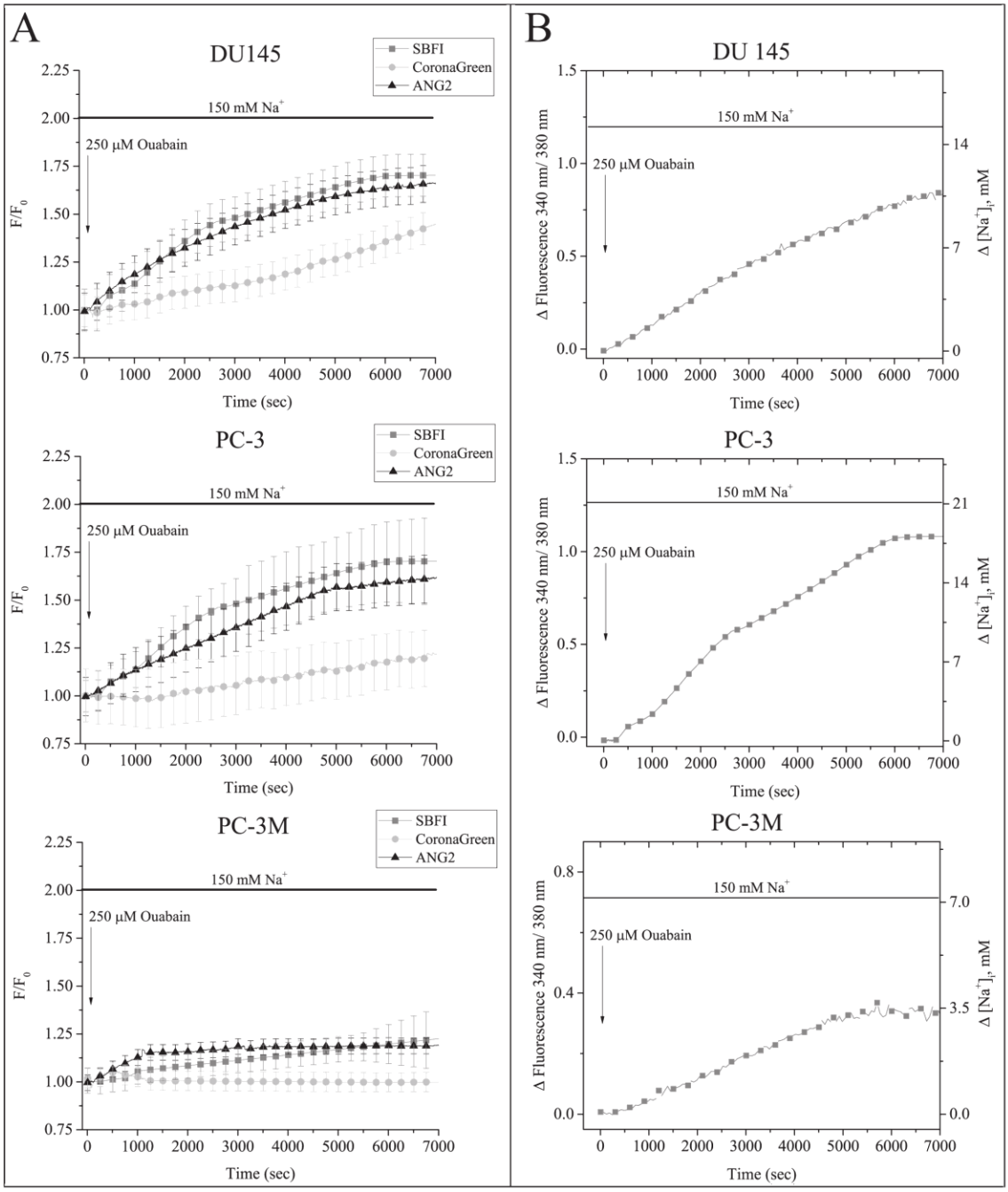

Figure 8

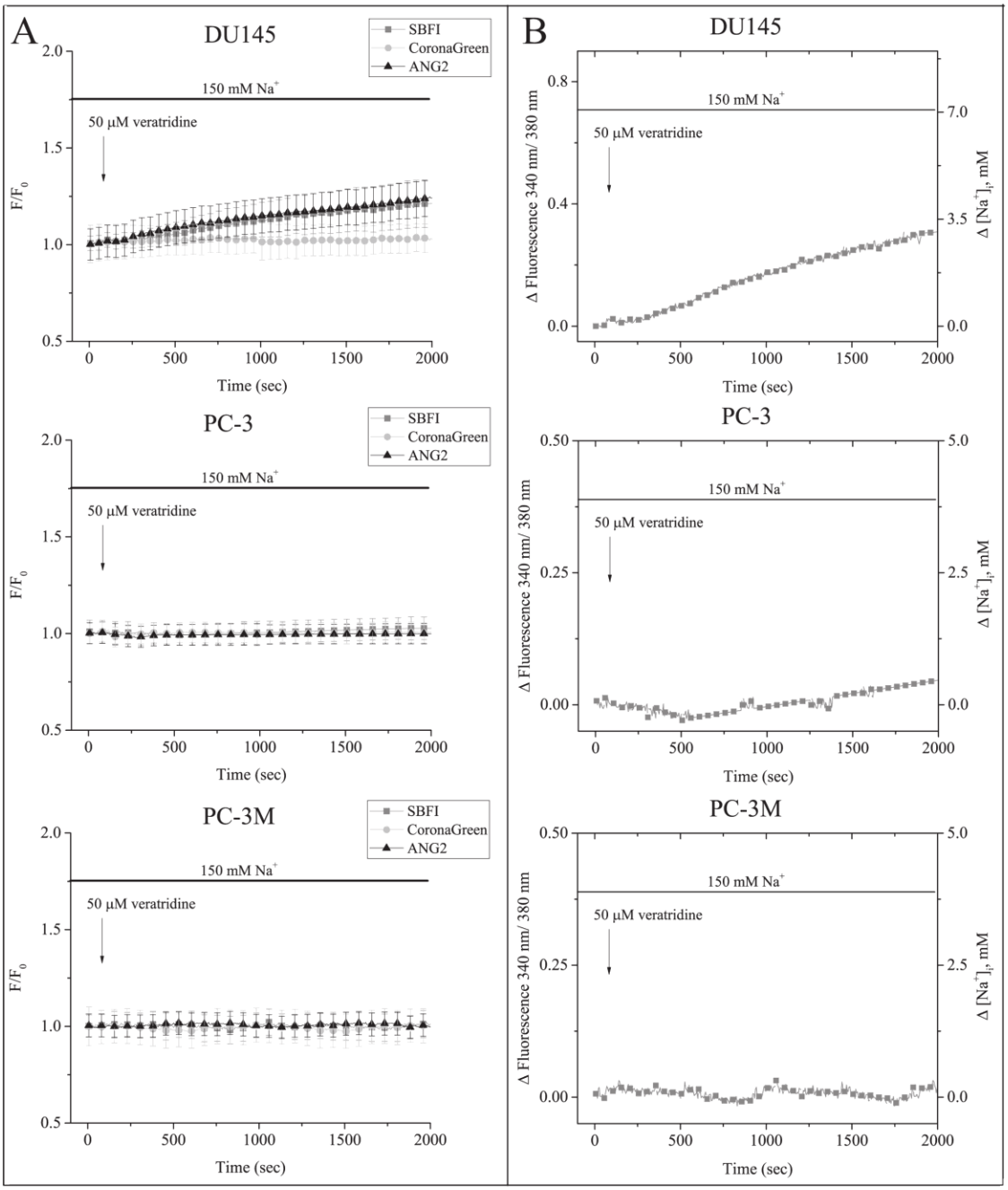

Figure 9

1.5 Aims and scope of the present study

1.5.1 Hypothesis

Amongst carcinomas diagnosed in men, prostate cancer is increasingly the most common and has one of the highest mortality rates. The standard hormone-based therapy works for limited time and most patients then die within months from metastasis – cancer spreading and formation of secondary tumours. Thus, at the present, there is a great unmet need for novel molecular targets (i) to enable early, functional detection of prostate cancer and (ii) to control metastatic disease.

Ion channels are pivotal regulators of cellular homeostasis and offer promising prospects in the field of cancer research. Indeed, membrane potential and various ion channels have been shown to correlate with the main hallmarks of cancer (Prevarskaya *et al.*, 2010; Brackenbury, 2016). Recently, a newly discovered NALCN channel complex, has been found significantly mutated in a number of human cancers (Biankin *et al.*, 2012; De Las Rivas *et al.*, 2012; Lee *et al.*, 2013; Agelopoulos *et al.*, 2015). To date, it is known that due to its resting Na^+ permeability NALCN channelosome plays key role in neuronal excitability, which is linked with molecular clock (Lear *et al.*, 2005, 2013; Lu *et al.*, 2007; Flourakis *et al.*, 2015; Funato *et al.*, 2016; Moose *et al.*, 2017). Of note, altered Na^+ homeostasis has already been implemented in prostate carcinogenesis (Yildirim *et al.*, 2012). Indeed, Na^+ signalling was shown to play a significant role in metastatic cell behaviours such as motility, migration, invasiveness and extracellular matrix remodelling (Besson *et al.*, 2015; Roger *et al.*, 2015). Importantly, elevated total tissue Na^+ concentration was proposed as a highly specific *in vivo* indicator of malignant lesions in human cancer patients (Ouwerkerk *et al.*, 2007; Lupu *et al.*, 2009; Jacobs *et al.*, 2011; Henzler *et al.*, 2012; Schepkin, 2016). However, very little is yet known about the particular mechanistical aspects of how Na^+-dependent signalling regulates cancer progression.

Importantly, the examination of pancreatic cancer genomes by using exome sequencing revealed that genes, including *NALCN*, involved in the axon guidance pathway were significantly mutated (Biankin *et al.*, 2012). Of note, axon guidance molecules were demonstrated being highly involved in migratory potential of normal and tumourigenic tissues, and suggested as potential targets of the anti-cancer therapy (Chédotal *et al.*, 2005). In addition to pancreatic ductal adenocarcinoma, *NALCN* was found significantly mutated in non-small cell lung carcinoma and glioblastoma (Biankin *et al.*, 2012; De Las Rivas *et al.*, 2012; Lee *et al.*, 2013). Furthermore, proto-oncogene Src kinase was reported to be the part of NALCN channel complex (Lu *et al.*, 2009; Wang & Ren, 2009). Na^+ influx is also associated with cancer progression (see section 1.2.6 'Sodium influx in cancer'), and, since primary NALCN function is to provide background Na^+

leak, one can hypothesize on the plausible channel implication in the disease development. However, nothing is yet known about role of NALCN channelosome in tumourigenesis.

Therefore, this PhD project is a pioneer study that would provide first evidence on the role of NALCN in prostate cancer progression and would develop our current knowledge on how Na^+-dependent signalling pathways are involved in the disease advancement. To our knowledge, it is the first study to question the physiological relevance of NALCN in the malignancy development overall (Figure 20).

1.5.2 Main objective and aims

The main objective of this project is to investigate the role of NALCN in the physiopathology of human prostate. Therefore, the specific goals were established as follows:

1) To follow the evolution of NALCN expression in human prostate cancer;

2) To verify the functionality of NALCN channelosome in human prostate cancer cells due to the provided Na^+ leak;

3) To determine the prostate cancer cell behaviours which are regulated by NALCN;

4) To explore molecular mechanisms and signalling pathways involved in NALCN-mediated phenotype of the human prostate cancer cells; and

5) To evaluate the importance of NALCN on prostate carcinogenesis and tumour progression *in vivo*.

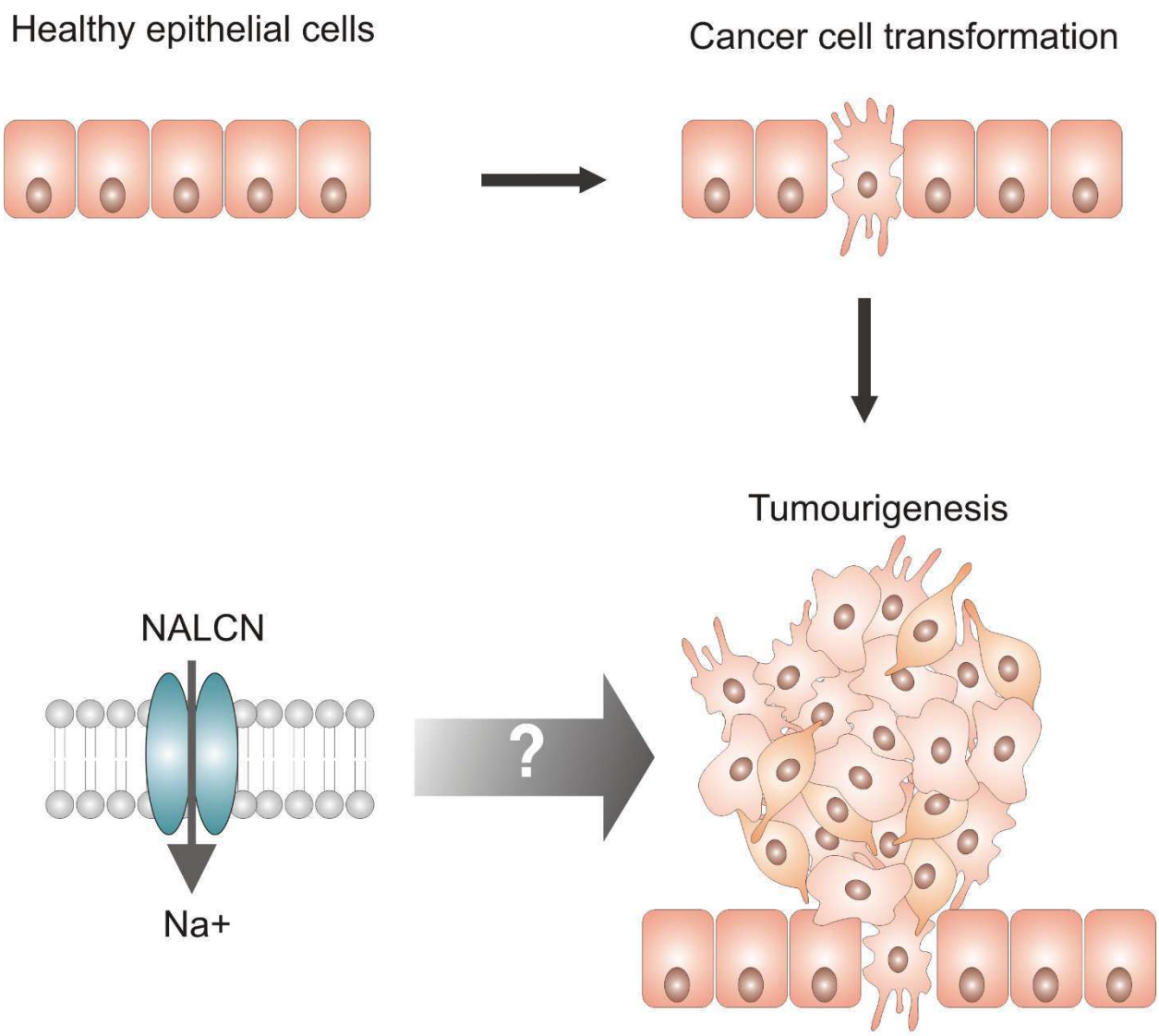

Figure 20. Main hypothesis of this PhD project.
Carcinomas are derived from epithelial cells and represent the most common type of cancer (around 85% of every cancer case). Of note, prostate cancer is nearly always adenocarcinoma, which means that it starts in glandular cells that produce fluids to keep tissues moist. The transformation of healthy cell into cancerous results in tumour outgrowth. Importantly, elevated total tissue Na^+ concentration was proposed as a highly specific *in vivo* indicator of malignant lesions in human cancer patients. Therefore, it is important to investigate whether such Na^+ increase could be conditioned due to the Na^+ leak provided through NALCN channelosome. Our main objective is to understand the role of Na^+ leak (in particular, provided through NALCN) in prostate cancer metastatic behaviours.

2. Materials and methods

2.1 Stock solutions

2.1.1 Buffers and standard solutions

Most chemicals were purchased from Invitrogen Life Technologies and Sigma Aldrich Chemicals unless stated otherwise. Buffers and standard solutions used throughout this study are listed in Table 1. If needed, pH of solutions has been adjusted using combined pH electrode InLab® Flex-Micro (Mettler Toledo). The media and other necessary materials were sterilized by autoclaving at 120ºC. Thermally-labile chemicals were filter-sterilized with 0.2 µm pore polyethersulfone Acrodisc® Supor® membrane filters (514-4126, VWR).

Purchased			
Name		**Reference number, Gibco™**	
Distilled water (dH_2O) DNAse/RNase Free		10977	
Dulbecco's Modified Eagle Medium (DMEM) + GlutaMAX™		31966	
Fetal bovine serum (FBS)		10270	
L-Glutamine		25030	
Dulbecco's Phosphate Buffered Saline (DPBS)		14190	
Phosphate Buffered Saline (PBS)		10010	
Roswell Park Memorial Institute (RPMI) 1640		31870	
0.05% Trypsin-EDTA		25300	
Home-prepared			
Name	**Composition**	**pH; adjusted with**	**Storage**
0 $CaCl_2$ solution	150 mM NaCl; 5 mM KCl; 3 mM $MgCl_2$; 10 mM HEPES; 10 mM Glucose;	7.4; HCl, NaOH	1 month, 4ºC
4 mM $CaCl_2$ solution	150 mM NaCl; 5 mM KCl; 4 mM $CaCl_2$; 1 mM $MgCl_2$; 10 mM HEPES; 10 mM Glucose;	7.4; HCl, NaOH	1 month, 4ºC
8 mM $CaCl_2$ solution	150 mM NaCl; 5 mM KCl; 8mM $CaCl_2$; 10 mM HEPES; 5.6 mM Glucose	7.4; HCl, NaOH	1 month, 4ºC
0 mM NaCl solution	150 mM $CholineCl^-$; 5 mM KCl; 2 mM $CaCl_2$; 1 mM $MgCl_2$; 10 mM HEPES; 5.6 mM Glucose	7.4; HCl, KOH	1 month, 4ºC
150 mM NaCl solution	150 mM NaCl; 5 mM KCl; 2 mM $CaCl_2$; 1 mM $MgCl_2$; 10 mM HEPES; 5.6 mM Glucose	7.4; HCl, NaOH	1 month, 4ºC

Fractionation solution B	250 mM saccharose; 1 mM EDTA; 20 mM HEPES;	7.4; -, NaOH	3 months, 4ºC
Fractionation solution C	250 mM saccharose; 6 mM EDTA; 120 mM HEPES	7.4; -, NaOH	3 months, 4ºC
Fractionation solution D	50% OptiPrep™ in Fractionation solution C	7.4; -,-	3 months, 4ºC
Modified Hank's balanced salt solution (HBSS), without phosphate	150 mM NaCl; 5 mM KCl; 2mM $CaCl_2$; 1 mM $MgCl_2$; 10 mM HEPES; 10 mM Glucose;	7.4; HCl, NaOH	1 month, 4ºC
Mowiol	20% Mowiol® 4-88; 30% glycerol; 100 mM Tris	8.5; -,-	12 months, -20ºC
Laemmli buffer 5x	1 M Tris; 20% SDS; 10% saccharose; 10 mM DTT; 0.25% bromophenol blue	6.8; -, Tris-base	12 months, -20ºC
Loading buffer 6x	10 mM Tris-HCl; 40% glycerol; 0.25% xylene cyanol; 0.25% bromophenol blue	8.0; HCl, Tris-base	3 months, 4ºC
Lysogeny Broth (LB)	1% Tryptone; 0.5% Yeast extract; 1% NaCl	7.0; HCl, Tris-base	3 months, 4ºC
NuPAGE MOPS SDS Running buffer	2.5 mM MOPS; 2.5 mM Tris-base; 0.005% SDS; 0.05 mM EDTA	7.7; -,-	3 months, 4ºC
Phosphate buffer	100 mM KH_2PO_4; 100 mM Na_2HPO_4; 100 mM NaH_2PO_4	7.2; -, -	3 months, 4ºC
Phosphate-buffered saline (PBS)	137 mM NaCl; 2.7 mM KCl; 0.2 mM KH_2PO_4; 1.42 mM $Na_2HPO_4 \cdot 2H_2O$	7.4; HCl, NaOH	3 months, 4ºC
Radioimmunoprecipitation assay (RIPA) buffer	15 mM Phosphate buffer; 150 mM NaCl; 1% Triton x-100; 1% Na^+ deoxycholate;	7.2; HCl, Tris-base	6 months, 4ºC
Solution 1 for chemically competent bacteria	30 mM CH_3COOK; 100 mM $RbCl_2$; 10 mM $CaCl_2$; 50 mM $MgCl_2$;	5.8; Acetic acid, -	3 months, 4ºC
Solution 2 for chemically competent bacteria	10 mM MOPS; 10 mM $RbCl_2$; 75 mM $CaCl_2$; 15% Glycerol	6.5; HCl, -	3 months, 4ºC
Super Optimal Broth with Catabolite repression (SOC)	2% tryptone; 0.5% yeast extract; 10 mM NaCl; 2.5 mM KCl; 10 mM $MgCl_2$; 20 mM Glucose	7.0; -,-	12 months, -20ºC
TBS-Tween (TBS-T)	1.5 mM Tris; 14 mM NaCl; 0.05% Tween20	7.4; HCl, NaOH	3 months, 4ºC

Terrific Broth (TB)	1.2% Tryptone; 2.4% Yeast extract; 0.4% Glycerol; 17 mM KH_2PO_4; 72 mM K_2HPO_4	7.0; HCl; Tris-base	3 months, 4ºC
Tris buffere saline (TBS)	1.5 mM Tris; 14 mM NaCl;	7.4; HCl, NaOH	3 months, 4ºC
Tris-Acetate resolving gel solution	3-8% acrylamide (Merck 100638100); 0.1% SDS (Propure M 112); 0.75 M Tris-base (VWR 103156X)	8.8; acetic acid, NaOH	3 months, 4ºC
Tris-Acetate stacking gel solution	3.2% acrylamide ; 0.1% SDS; 0.5 M Tris-base	8.8; acetic acid, NaOH	3 months, 4ºC
Tris/Acetate/EDTA (TAE) buffer	40 mM Tris-base; 0.1% acetic acid; 1 mM EDTA	8.0; acetic acid, Tris-base	1 month, RT
Tris/Borate/EDTA (TBE) buffer	50 mM boric acid; 50 mM Tris-base; 1 mM EDTA	8.3; HCl,	1 month, RT

Table 1. List of buffers and standard solutions used in this study.

2.1.2 Antibiotics

Antibiotics used throughout this study were prepared at stock solutions in distilled water (dH_2O), stored at -20ºC and used as indicated in Table 2.

Applied for bacterial strains		
Antibiotic	**Working concentration**	**Source**
Carbenicilin (Carb)	30 µg/ml and 100 µg/ml	Gibco™
Kanamycin (Kan)	50 µg/ml	Gibco™
Applied for mammalian cell cultures		
Antibiotic	**Working concentration**	**Source**
Puromycin (Puro)	0.5 µg/ml	Sigma
Geneticin (G418)	700 µg/ml	Sigma

Table 2. List of antibiotics used throughout this study.

2.1.3 Antibodies

Primary antibodies for immunoblotting were prepared in 1% dry milk, 0.02% NaN_3, TBS-T solution, stored at 4ºC and used as indicated in Table 3. Secondary antibodies for immunoblotting were prepared prior to usage at the final concentration of 1:50,000 in 1% dry milk TBS-T solution. In this study anti-mouse refers to peroxidase conjugated affinipure goat, anti-mouse IgG, light chain specific (115-035-174, Jackson Immuno Research), whereas anti-rabbit is peroxidase conjugated IgG fraction monoclonal mouse, anti-rabbit IgG, light chain specific (211-032-171, Jackson Immuno Research).

Primary antibodies for immunocytochemistry were freshly prepared in 5% goat serum in PBS and used at the final concentration of 1:100 (Table 3). Secondary antibodies for immunocytochemistry were freshly prepared 1:2,000 in PBS goat, anti-mouse or anti-rabbit IgG, heavy and light chains, conjugated with Alexa Fluor™ 488 or 546 (Invitrogen).

Antibodies used for immunoblotting and immunocytochemistry				
Primary antibody (ref. number)	Working concentration for immunoblotting	Secondary antibody	Source	Expected band size
β-actin (A5441)	1:1000	anti-mouse	Sigma	42 kDa
Calnexin (MAB3126, C8.B6)	1:1000	anti-mouse	Merck Millipore	100 kDa
Cathepsin-B (sc-6493-R)	1:200	anti-rabbit	Santa-Cruz	37 kDa, 25 kDa
Cathepsin-D (sc-10725)	1:200	anti-rabbit	Santa-Cruz	52 kDa, 46 kDa, 32 kDa
Cortactin (sc-55578)	1:100	anti-mouse	Santa-Cruz	80 kDa
Dynamin-1/2 (MABT188)	0.5 µg/ml	anti-mouse	Merck Millipore	98 kDa
E-Cadherin (sc-21791)	1:200	anti-mouse	Santa-Cruz	135 kDa, 120 kDa, 80 kDa
FAK (BD-610088)	1 µg/ml	anti-mouse	Becton Dickinson Biosciences	125 kDa
Fyn (sc-434)	1:100	anti-mouse	Santa-Cruz	59 kDa
GFP	1:1000	anti-mouse	Clontech	27 kDa
HA (ab9110)	1:2000	anti-rabbit	Abcam	15 kDa
Integrin α5 (ab76609)	1 µg/ml	anti-rabbit	Abcam	128 kDa
Integrin β1 (sc-8978)	1:200	anti-rabbit	Santa-Cruz	140 kDa
Integrin β3 (ab7167)	1 µg/ml	anti-mouse	Abcam	90-110 kDa
Integrin β3 (sc-14009)	1:200	anti-rabbit	Santa-Cruz	90-110 kDa
iPLA$_2$	1:500	anti-rabbit	gift or Prof Bolotina	85 kDa
MT1-MMP (sc-377097)	1:100	anti-rabbit	Santa-Cruz	63 kDa
N-Cadherin (sc-59987)	1:200	anti-mouse	Santa-Cruz	130 kDa
NALCN	1:1000	anti-rabbit	Eurogentec produced by our order	250-300 kDa
p-FAK-Y397 (sc-11765)	1:200	anti-rabbit	Santa-Cruz	125 kDa

p-Src-Y418 (ab40660)	1:1000	anti-rabbit	Abcam	56 kDa
p-Src-Y530 (sc-166860)	1:100	anti-mouse	Santa-Cruz	60 kDa
Pyk2 (ab 16672)	1 µg/ml	anti-rabbit	Abcam	116 kDa
Src-total (ab109381)	1:1000	anti-rabbit	Abcam	60 kDa
Tks5 (sc-736241)	1:200	anti-mouse	Santa-Cruz	140 kDa

Antibodies used for immunohistochemistry		
Antibody	**Working concentration**	**Source**
Ki67	1:50	DakoCytomation
NALCN	1:300	Eurogentec produced by our order
ORAI1 (LS-C94375)	1:4000	Lifespan
SK3 (WPA 017990)	1:300	Sigma
Src-total (ab109381)	1:500	Abcam
STIM1 (710954)	1:1000	Becton Dickinson Biosciences
STIM2 (S85-72)	1:2000	Sigma
TRPC1 (NB 110-74946)	1:4000	Novus Biological

Table 3. List of antibodies used in this study.

2.1.4 Pharmacological agents

Pharmacological agents used in this study are listed in Table 4.

Name	**Mode of action**	**Working concentration**
Acetylcholine (ACh)	Activator of cholinergic receptors	100 µM
Carbachol (CCh)	Cholinomimetic drug, agonist of cholinergic receptors	100 µM
Cisplatin (CS)	Chemotherapeutic drug, inducer of DNA damage	1 µM
Cycloheximide (CHX)	Inhibitor of protein synthesis	1 µM
Cyclopiazonic acid (CPA)	Inhibitor of the sarco/endoplasmic reticulum Ca^{2+} ATPase (SERCA)	50 µM
Epidermal growth factor (EGF)	Stimulator of cell growth and differentiation	100 ng/ml
Neurotensin (NT)	Neuropeptide, suggested being an activator of NALCN	1 µM
PP1	Inhibitor of Src kinase family	10 µM
PP2	Inhibitor of Src kinase family	10 µM
PP3	Negative control for PP1 and PP2	10 µM
Substance P (SP)	Neuropeptide, suggested being an activator of NALCN	1 µM
Thapsigargin (TG)	Inhibitor of SERCA pump	1 µM
Tumour necrosis factor α (TNF-α)	Cytokine	10 ng/ml
KB-R7943 (KB-R)	Inhibitor of reverse mode NCX	1 µM

Table 4. List of pharmacological agents used in this study.

2.2 Oligonucleotides

All oligonucleotides used in this study were purchased from Eurogentec company.

2.2.1 Primers

Primers			
Sequence	**Expected PCR product**	**Usage**	**Reference**
FW-5'- CAGCTTCCGGGAAACCAAAGTC -3' RV-5'- AATTAAGCCGCAGGCTCCACTC -3'	113 bp	18S as a loading control for qPCR	(El Boustany *et al.*, 2008)
FW-5'- ACCCACTCCTCCACCTTTG -3' RV-5'- CTCTTGTGCTCTTGCTGGG -3'	178 bp	GAPDH as a loading control for qPCR	(Borowiec *et al.*, 2013)
FW-5'- GCAAAGCAGAAGAAACCGATAC -3' RV-5'- AACTTAAAAGCTGGTCCTCCTC -3'	584 bp	NALCN screening for cPCR	Dr Arnaud Monteil (IGF, Montpellier, France)
FW-5'- CACAGGTGAAGACTGGAACAAGA -3' RV-5'- CCACAGTCTGTTGCCCAGTATGTA -3'	96 bp	NALCN screening for qPCR	Designed by Oksana Iamshanova for this study
FW-5'- AGCCACTTTTCTCTACGGTCC -3' RV-5'- TACGGAGGCCTCTCCAGTTT -3'	136 bp	NLF-1 screening for qPCR	Designed by Alexandre Bokhobza for this study
FW-5'- CTTGACCTAAAGACCATTGCACTTC -3' RV-5'- AACTTCACATCACAGCTCC -3'	266 bp	TBP as a loading control for cPCR	Designed by Oksana Iamshanova for this study
FW-5'- CTTGACCTAAAGACCATTGCACTTC -3' RV-5'- GTTCTTCACTCTTGGCTCCTGTG -3'	154 bp	TBP as a loading control for qPCR	Designed by Oksana Iamshanova for this study
FW-5'- TATGGTTCTTAGTGAGCCTCTGCAC -3' RV-5'- CAATAGTCCTTCCTCCTGGGTGTC -3'	849 bp	UNC-79 screening for cPCR	Designed by Oksana Iamshanova for this study
FW-5'- GCATCTCGAAGGGTGAGTG -3' RV-5'- CAATAGTCCTTCCTCCTGGGTGTC -3'	163 bp	UNC-79 screening for qPCR	Designed by Oksana Iamshanova for this study
FW-5'- CTGAGGAAGGCACTCAGTGGTC -3' RV-5'- GTTTATGCAGGAGTCTGTGAGGC -3'	854 bp	UNC-80 screening for cPCR	Designed by Oksana Iamshanova for this study
FW-5'- GTCAAGGAAGTGCGATCTCAGATC -3' RV-5'- GTTTATGCAGGAGTCTGTGAGGC -3'	201 bp	UNC-80 screening for qPCR	Designed by Oksana Iamshanova for this study

Table 5. List of primers used in this study.

2.2.2 Small interfering RNA

Small interfering RNA (siRNA)	
Sequence	**Usage**
5'- GGUGAAGACUGGAACAAGAUU -3'	Designed by Oksana Iamshanova for this study
5'- GGAACAAGAUUAUGCAUGACU -3'	Designed by Oksana Iamshanova for this study
5'- AACUGCUGUCAUCAGGGACUU -3'	(Swayne *et al.*, 2009)
5'- AAGAUCGCACAGCCUCUUCAU -3'	(Swayne *et al.*, 2009)
5'- AAUGUAUGACAUAACCCAGCA -3'	(Swayne *et al.*, 2009)

Table 6. List of siRNA used in this study.

2.2.3 Short hairpin RNA

Short interfering RNA (shRNA)	
Sequence	**Usage**
FW 5' – GATCCGGTGAAGACTGGAACAAGATT TTCAAGAGAAATCTTGTTCCAGTCTTCACCTTTTTTGGAAA – 3'	To insert into p*Silencer*™ 4.1-CMV puro plasmid
RV 5' – AGCTTTTCCAAAAAAGGTGAAGACTGGAACAAGATTTCTCTTGAA AATCTTGTTCCAGTCTTCACCG – 3'	

Table 7. List of shRNA used in this study.

2.3 Plasmids

Plasmids used in this study are given in Table 8.

Commercial plasmids		
Plasmid	**Description**	**Source**
pcDNA3	5428 bp; Amp^R; MCS is in the forward (+) orientation (CMV promoter); 5' sequencing primer: CMV-FW; 3' sequencing primer: BGH-RV; Neo^R (SV40 promoter); ColE1 origin	Invitrogen
p*Silencer*™ 4.1-CMV puro	4781 bp; Amp^R; cloning site for siRNA – HindIII(463) and BamHI(516) (CMV promoter); 5' sequencing primer: AGGCGATTAAGTTGGGTA; 3' sequencing primer: CGGTAGGCGTGTACGGTG; $Puro^R$ (SV40 promoter); ColE1 origin	Thermo Fisher Scientific
Constructed plasmids		
Plasmid	**Usage**	**Reference**
pcDNA3-GFP	As control for protein expression with fluorescent tag	Dr Arnaud Monteil (IGF, Montpellier, France)
pcDNA3-hNALCN-GFP	For NALCN overexpression with fluorescent tag	Dr Arnaud Monteil (IGF, Montpellier, France)
p*Silencer*™ 4.1-CMV puro-shNALCN	For establishment of stable NALCN knock-down cell line	Constructed by Oksana Iamshanova for this study

Table 8. List of plasmids used in this study.

2.4 Cell lines, bacterial strains and their growth conditions

2.4.1 Cell lines and their growth conditions

Prostate cancer cell lines, listed in the Table 9, were grown in RPMI 1640 medium (Gibco™, Thermo Fischer Scientific) containing a final concentration of 10% fetal bovine serum (FBS) (Gibco™) and 2 mM L-Glutamine (Gibco™). Primary prostate hTERT-immortalized cell line

Mouse-derived osteoblast precursor cell line MC3T3 E1 was cultured in MEMα medium (Gibco™) containing 10% FBS and 1% Penicillin-Streptomycin (Gibco™).

All cells were routinely cultured at 37ºC in a humidified atmosphere with 5% CO_2. Cultures were split by treatment with 0.25% trypsin-EDTA (Gibco™) for 5 min at 37ºC. All cells used in this study were validated as being mycoplasma free by using Hoechst staining. If needed, the cell lines were amplified and conserved in cryogenic vials (Corning®) at the concentration of 1 million of cells per 1 ml of Recovery Cell Culture Freezing Medium (Gibco™) at -80^{0}C.

2.4.2 Bacterial strains and their growth conditions

E. coli strains (Table 10) were grown in Lysogeny Broth (LB) at 37^{0}C or at 28^{0}C when needed. Colonies were maintained on 1.5% weight/volume (w/v) agar LB plates and stored at 4^{0}C with appropriate antibiotics (Table 2). If needed, the bacteria strains were conserved in 10% DMSO at -80^{0}C.

Prostate cell lines						
Characteristics	**EP156T**	**LNCaP**	**C4-2**	**DU 145**	**PC-3**	**PC-3M**
Origin	hTERT-immortalized EP156 tumour-free tissue culture	Lymph node metastasis in Caucasian male	From C4, LNCaP cultured in castrated mice	Central nervous system metastasis	Lumbar metastasis	Hepatic metastasis of PC-3 cell line, when injected into nude mice.
Metastatic potential (after innoculation into nude mice)	Non-tumourigenic	Poorly tumourigenic until coinoculated with tissue specific mesenchymal or stromal cells or Matrigel. Site-specific metastasis. Osteoblastic phenotype in bone metastasis.	Lymph and bone metastasis. Osteoblastic phenotype in bone metastasis.	Poorly differentiated tumours. Cells maintain phenotype and genotype and metastasize to a variety of organs, including spleen, lung, and liver. Osteolytic phenotype in bone metastasis	Poorly differentiated tumours. Osteolytic phenotype in bone metastasis.	Poorly differentiated tumours.
Androgen sensitivity	n/a	Hormone naïve, AS	Castration resistant, AI (+ mets)?	Castration resistant, AI	Castration resistant, AI	Castration resistant, AI
Androgen receptor (AR)	+	+ (mutated)	+++	-	-	-
Prostate specific antigen (PSA)	+	+	+	-	-	-
Prostate specific membrane antigen (PSMA)	n/a	+	+	-	-	-
5α-reductase	n/a	+	+	-	-	-
Cytokeratin expression	CK-5, CK-7, CK-8, CK-14, CK-18	CK-8, CK-18, CK-20	CK-8	CK-8, CK-18	CK-7, CK-8, CK-18, CK-19,	n/a
Other markers	E-cadherin, p63, ER-β	Vimentin, E-cadherin, a-, b-, g- catenin, PAP, Creb binding protein	Marker chromosome *m1*	TGF-α, IGF-1, EGF, bFGF IGF-I, TGF-β, EGF/TGF-α-R, FGF-R, IGF-I-R, TGF-β-R	E-cadherin, transferrin receptor, TGF-α, EGF-R	n.a
p53/other features	Possibly intact p53	Silent mutation of p53; PTEN inactivation	Low levels of functional p53; PTEN null	Mutated p53: Pro233Leu, Val274Phe; mutated p16 codon 84; heterozygous PTEN	Deletion mutation (Cys138) and nonsense mutation at 169 of p53; PTEN deficient	n/a
Doubling time	~72 hours	60-72 hours	~48 hours	~34 hours	~33 hours	~20 hours
Karyotype	46, XY, dup(20)	33-91, modal of 76-91; highly aneuploid	61-90, modal of 84	46-143, modal of 64; M1, M2, M3, Yq+	55-62, modal of 58; aneuploidy; chromosomes 2, 3, 5, 15, and Y are absent.	Modal of 60-61, similar karyotype pattern as in PC-3
Purchased from	Prof Varda Rotter (Weizmann Institute of Science, Israel)	ATCC, USA	Dr Florence Cabon (Cancer Research Centre of Toulose, France)	ATCC, USA	ATCC, USA	Prof Mustafa Djamgoz (Imperial College London, UK)
Ref.	(Kogan *et al.*, 2006)	(Horoszewicz *et al.*, 1980)	(Wu *et al.*, 1994)	(Stone *et al.*, 1978)	(Kaighn *et al.*, 1979)	(Kozlowski *et al.*, 1984)

Table 9. Prostate cell lines used in this study.

Strain	Genotype description	Source
DH5-α	F-80dlacZ M15 (lacZYA-argF) U169 recA1 endA1hsdR17(rk-, mk+) phoAsupE44 -thi-1 gyrA96 relA1, chemically competent	Thermo Fisher Scientific
OneShot™ Stbl3™	F-mcrB mrrhsdS20(rB-, mB-) recA13 supE44 ara-14 galK2 lacY1 proA2 rpsL20(StrR) xyl-5 λ-leumtl-1, chemically competent	Thermo Fisher Scientific

Table 10. Bacterial strains used throughout this study.

2.5 Cell culture assays

2.5.1 Cell count

Cell count was performed by using hemocytometer, in particular Malassez chamber. A coverslip was placed over the grid surface of the chamber, and then 15 µl of cell suspension were loaded in between. Once the cells settled, they were visualized under transmitted light microscope with 10X objective and were quantified as indicated in the Figure 21A. According to the parameters of the Malassez chamber, 1 square corresponds to the amount of cells in 1 µl of suspension. Therefore, the exact quantity of cells was distinguished as follows:

$$Total\ cells = mean\ from\ the\ squares\ quantified \times suspension\ volume\ (\mu l) \quad (1)$$

2.5.2 Cellular viability

Cellular viability was evaluated by the dye exclusion assay. In brief, cells were plated at $30x10^4$ cells per 35 mm dish and left in the standard growth conditions overnight. The next day, cultures were treated with the potential cytotoxic agents (e.g. siRNA). After the treatment was completed, cells were collected in suspension and stained with 0.4% Trypan Blue Solution (Thermo Fisher Scientific). Necrotic cells would have their plasma membrane ruptured and thus dye would easily stain their intracellular proteins, whereas other cells would stay intact. Afterwards, the dye was substituted with PBS and the proportion of blue cells over total amount of cells was calculated according to the Formula 1. It is generally accepted to have around 5% of necrotic cells within the healthy culture population.

2.5.3 Proliferation

Cell proliferation was investigated due to the direct cell count (as described in section 2.5.1. Cell count) and also by the means of colorimetric assays (Figure 21B, C).

In brief, $1x10^3$ cells were plated in 200 µl of media into 96-well plate and left in the incubator overnight. The next day, treatment would be applied and considered as hour 0. Each subsequent day, 1 plate would be taken for proliferation assay at the required time point. The absorbance was measured at 485 nm wavelength with TriStar^2 Multimodal Reader LB942 (Berthold Technologies). Blank was considered as well without cells and substituted from each data point during analysis.

For MTS/PMS assay the solutions were used as follows: [3-(4,5-dimethylthiazol-2-yl)-5-(3-carboxymethoxyphenyl)-2-(4-sulfophenyl)-2H-tetrazolium (MTS) as an inner salt, phenazine methosulfate (PMS) as an electron coupling reagent. MTS is bioreduced by cells into a formazan

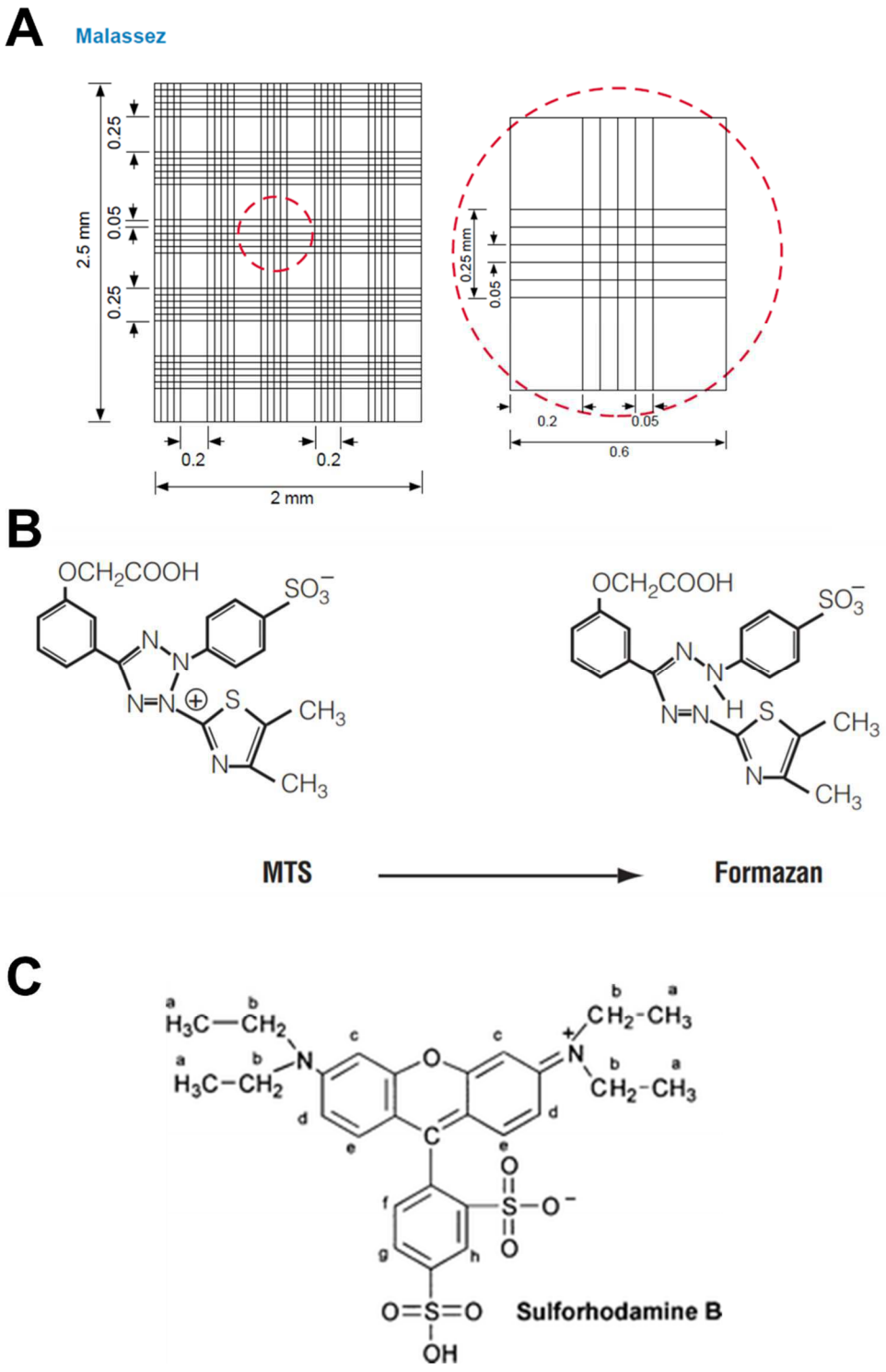

Figure 21. Methods to evaluate cell proliferation used in this study.
A, direct cell count by using the Malassez chanber. **B**, MTS dye, based on metabolic activity of mitochondria. **C**, sulforhodamine B dye, based on general protein synthesis.

product that is soluble in tissue culture medium. The conversion of MTS into aqueous, soluble formazan is accomplished by dehydrogenase enzymes found in metabolically active cells. Therefore, the quantity of formazan product as measured by the amount of 490nm absorbance is directly proportional to the number of living cells in culture. MTS and PMS powders were dissolved in DPBS to a stock concentration of 2 mg/ml and 0.92 mg/ml, respectively. On the day of experiment, solutions were mixed in 20:1 ratio and applied onto living cells during 1 hour in the standard growth conditions.

Another colorimetric assay is based on the fluorescent dye, sulforhodamine B (SFRB), that stains all cellular proteins. The cells were fixed with 10% trichloroacetic acid during 1 hour at 4^0C. Afterwards, all wells were vigorously washed with dH_2O in order to remove fixative and serum proteins. The fixed cells were left to stain for 30 minutes in 0.4% SFRB in 1% acetic acid solution and subsequently washed with 1% acetic acid. The cells were air-dried and the dye was dissolved due to the application of 100 µl 10mM unbuffered Tris base solution, pH 10.5.

2.5.4 Apoptosis assay

The level of apoptosis was estimated from the number of apoptotic nuclei revealed by Hoechst staining. Cells were plated at $30x10^4$ cells per 35 mm dish and left in the standard growth conditions overnight. The next day, cultures were treated with the potential apoptotic agents (e.g. cisplatin). After the treatment was completed, all cells (floating and adherent) were pelleted by centrifugation at 1000 rpm for 5 minutes and resuspended in PBS. Then $5x10^3$ cells from suspension were loaded onto cytospin slides and centrifuged at 2000 rpm for 2 minutes by using Shandon 74000222 Cytospin 3 Centrifuge (Whittemore Entreprises) (Figure 22A). Afterwards, the slides were fixed in ice-cold methanol (MetOH) for 15 minutes at -20^0C and then stained in Hoechst 33258 solution for 30 minutes at the room temperature. The slides were washed in dH_2O, air-dried and assembled with coverslip by using a drop of the Mounting Medium (Sigma). The images were taken with 20x objective visualized at 435 nm wavelength by using the epifluorescent microscope (AxioImager, Zeiss). The apoptotic nuclei were considered as the one exhibiting chromatin condensation or fragmentation (Figure 22B).

2.5.5 Cell cycle analysis

For cell cycle analysis, cells were fixed with ice-cold 70% methanol for 30 minutes, resuspended in 100 µl PBS with 500 µg/ml Ribonuclease A, and stained with 50 µg/ml of propidium iodide for 1 hour at 4^0C. At least 10,000 events per condition were processed by CyAn™ ADP Analyser FACScan flow cytometer (Becton-Dickinson). Data were analysed with CellQuest software.

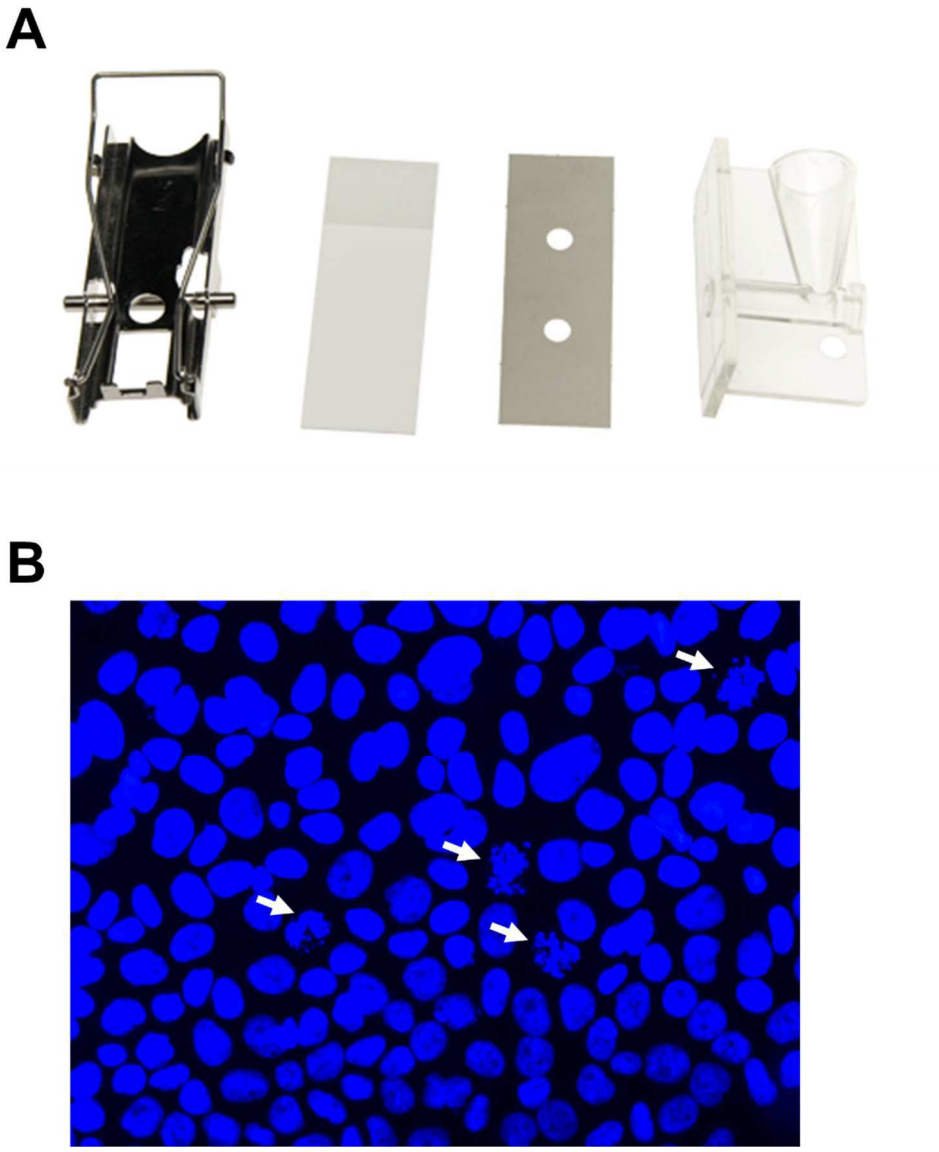

Figure 22. Cell apoptosis assay.
A, representation of the cytospin slide. **B**, representative image of PC-3 cells population with apoptotic nuclei (white arrows).

2.5.6 Time-lapse video microscopy

Cells were kept at 37°C under 5% CO^2 in an incubator chamber for time-lapse video recording. Cell movements were monitored with an inverted microscope (Biostation, Nikon) using a 20x objective lens. To ensure long distance measurement, images mosaic (4 by 4 for tracking, and 8 by 3 for wound healing) were acquired and reconstructed as a single high resolution, high field of view image using FiJi Grid/Collection Stitching Plugin (Schindelin *et al.*, 2012).

2.5.7 Random cell motility

Random motility was analyzed due to the tracking of individual cells. In brief, $1x10^4$ cells were plated into Hi-Q^4 culture dishes (Ibidi) and left in the standard growth conditions overnight. The next day, cells were stained during 30 minutes by using 1:20,000 Hoechst-33342 (H1399, Invitrogen™) staining suitable for living cells. Cells were left in standard growth conditions and images were acquired every 30 minutes for a time lapse of 48 hours. Image stacks were analyzed using trackmate imageJ plugin on the reconstructed mosaic image (Tinevez *et al.*, 2017). For each condition, segmentation was performed on Hoechst stained nucleus. The same optimized tracking parameters were used for each image series. Cells were then automatically tracked using the "simple lap tracker" algorithm and, tracks coordinates and individual tracks mean velocity were measured for each cell. Only cells tracked over a period of more than 5 hours were taken into account and at least 1000 cells tracks were analyzed per condition.

2.5.8 Lateral migration

The wound-healing assay was performed in Culture-Insert 2 Well in μ-Dish 35 mm high, IbiTreat (Ibidi) according to the manufacturer's instructions. $40x10^3$ cells were plated into each compartment of the culture insert and left overnight at the standard growth conditions. The next day, culture insert was removed, dish was filled up with standard growth media and left in the imaging box of video microscope (Biostation, Nikon). Images of the side and wound area were acquired every 30 minutes for a time lapse of 48 hours (Figure 23A,B). Homemade plugin based on (Jonkman *et al.*, 2014) recommendations was developed for ImageJ to automatically detect cells and gap areas.

2.5.9 Chemotaxic migration

Cells at 75 x 10^3 were plated into upper compartment of 8 μm pore Transwell® inserts (Corning™) in a serum-free media, whereas lower compartment was filled with standard growth media, as a chemoattractant (Figure 23C). After 16 hours at 37^0C, 5% CO_2 cells were fixed in ice-cold 100%

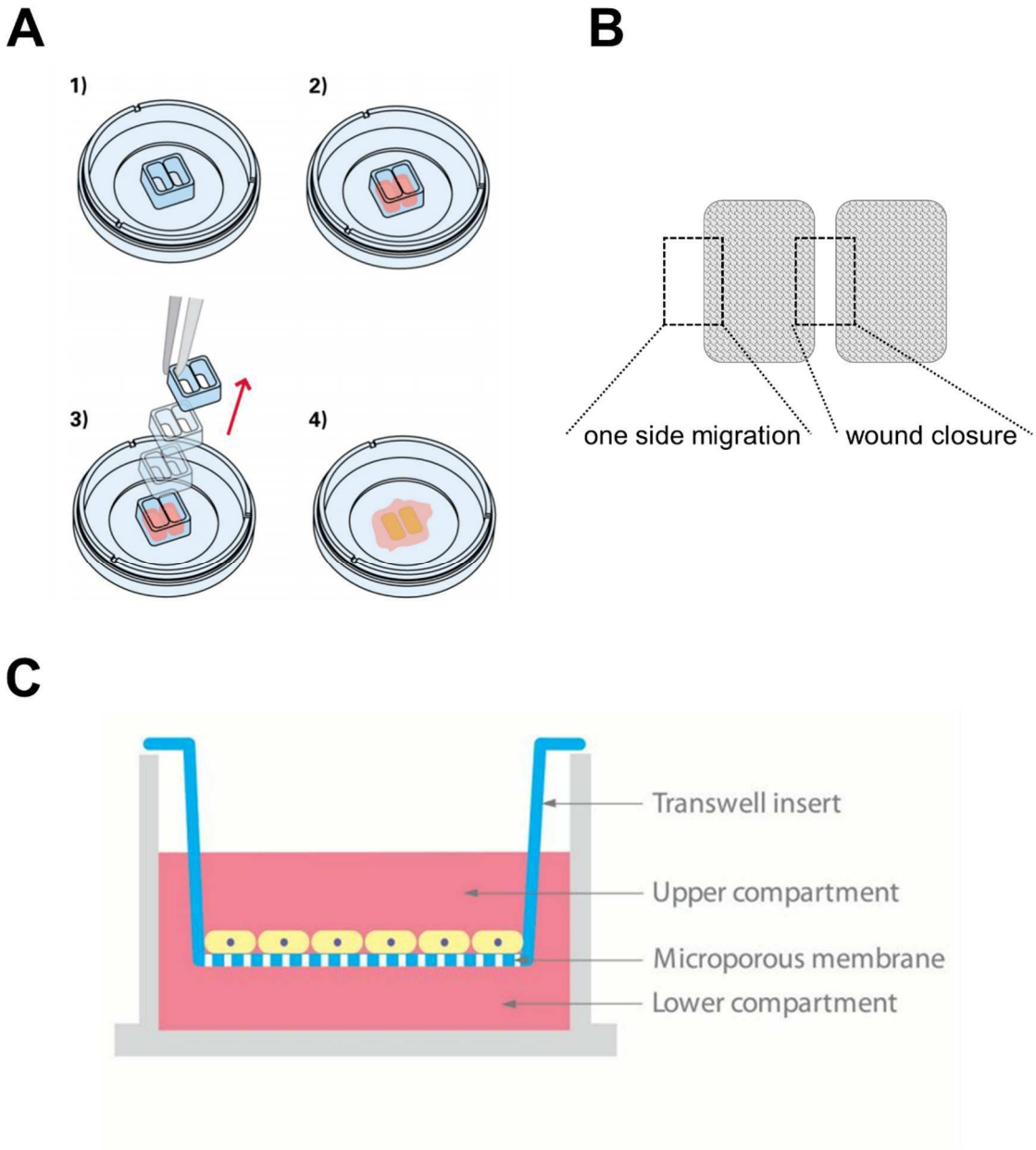

Figure 23. Methods to evaluate cell migration.
A, Principle of the wound-heal assay when using Culture-Insert 2 Well in μ-Dish 35 mm high, IbiTreat (Ibidi). **B**, Analysis of lateral migration based on the cell movement on one side and during the wound closure. **C**, Principle of the Transwell migration assay.

methanol and stained with 1% crystal-violet in 25% methanol. Inserts were washed and the upper area of the filter was rubbed dry to eliminate the non-migrated cells. The data was obtained after counting five random fields of view under an inverted microscope DMIRE2 (Leica) at 5x magnification. At least two inserts for each condition were analysed in each independent experiment.

2.5.10 Chemotaxic invasion

The invasiveness of cells was assessed in a same way as chemotaxic migration. The only difference is that Transwell inserts were pre-coated with 1.25 mg/ml Matrigel™ Basement Membrane Matrix (Becton Dickinson).

2.6 Transfection

In order to introduce various genetic material (e.g. DNA, siRNA, plasmid) different transfection methods were utilized throughout this study. Transient transfection involved temporary incorporation of genetic material into cellular genome, whereas stable transfection was achieved by selecting the cells with corresponding antibiotic resistance (Table 2) and that would exhibit permanent genetic alteration.

2.6.1 Nucleofection

Electroporation-based method, nucleofection, was realized by application of a specific voltage onto cell suspension by using Nucleofector (Amaxa) according to the manufacturer's instructions. In brief, adherent cultures were pelleted and resuspended in 100 µl of nucleofection buffer containing the required amount of genetic material. After suspension was put into special nucleofection cuvette and electroporated, 500 µl of standard growth media were applied and cells were left to recover in the incubator for 5 minutes. Then the whole cell suspension was plated into the dish of interest and left at the standard growth conditions overnight.

2.6.2 Lipofection-like transfection

Lipofection is a method of transfection based on the formation of liposome-embedded genetic material complex, which is transferred through plasma membrane and hence introduced to the cellular genome. To date, different variations of lipofection methods were developed based on the similar principle. In this study, HiPerFect Transfection Reagent (Qiagen) was mostly used for siRNA transfections, whereas X-tremeGENE 9 and X-tremeGENE HP DNA Transfection Reagents (Roche) were used for vector and plasmid introductions.

2.7 Molecular biology techniques

2.7.1 Expression cloning

2.7.1.1 Bacteria transformation

In order to amplify vector or plasmid of interest bacteria were transformed by using heat-shock method. Per each transformation reaction 50 µl of chemically competent bacteria strains (Table 10) were mixed with 50 ng plasmid in 5 µl by gentle swirling and left on ice for 30 minutes. Afterwards, the mixture was incubated in water bath at 42^0C for 45 seconds and left on ice for 2 minutes. In order for bacteria to recover from the heat-shock, 250 µl of Super Optimal Broth with Catabolite repression (SOC) media were added and left shaking at 200 rpm/minutes at 37^0C for 1 hour. Then the mixture was spread onto agar plates and incubated overnight at 28^0C or at 37^0C. In the next days bacteria colonies were checked and inoculated in LB media for further expression cloning manipulations.

2.7.1.2 Plasmid isolation

Plasmid isolation was performed by using Plasmid DNA purification kit (Macherey-Nagel) according to the manufacturer's instructions.

2.7.1.3 Sequencing

In order to verify the cloning results the sequencing procedure was performed by GATC Biotech company.

2.7.1.4 Restriction digest

The restriction digest was performed by using restriction enzymes from NEB according to the manufacturer's instructions.

2.7.1.5 Agarose gel electrophoresis

1% agarose gel was prepared in 0.5x Tris/Borate/EDTA (TBE) or 0.5x Tris/Acetate/EDTA (TAE) buffers by boiling the mixture until it becomes homogenous and transparent. After cooling it down to around 40^0C the DNA gel stain SYBR® Safe (Invitrogen) was added in the ratio of 1:20,000. The gel was left to solidify at the room temperature. Afterwards, samples and 1kb Plus DNA ladder (Invitrogen) were mixed with 6x Loading buffer in the ratio of 5:1 and loaded onto the gel. The gel was let to migrate in 0.5x TBE or 0.5x TAE buffer in RunOne™ Electrophoresis Cell

(EmbiTec) at 100 mV for 20 minutes. The gel visualization was performed by using MiniLumi (Bio-Imaging Systems) machine.

2.7.1.6 DNA extraction from agarose gel

Extractions of DNA from agarose gels was performed by using NucleoSpin® Gel and PCR Clean-up (Macherey-Nagel) according to the manufacturer's instructions.

2.7.1.7 Ligation

Joining of two nucleic acid fragments was done due to the action of a specific enzyme, called ligase. In this study we were using T4 DNA ligase (NEB) according to the manufacturer's instructions.

2.7.2 Polymerase chain reaction (PCR)

2.7.2.1 RNA extraction

Organ tissues and cells were preserved in RNAlaterTM (Sigma). Cellular RNA was purified with the NucleoSpin RNA Plus Kit (Macherey-Nagel). Organ tissues were homogenized with Precellys® Tissue Homogenizer and purified with TRIzol™ Reagent (Invitrogen). The quantity of extracted RNA was measured by BioPhotometer (Eppendorf) and loaded onto agarose gel in order to exclude RNA degradation (Figure 24). If needed, samples were stored at -80^{0}C.

2.7.2.2 DNase treatment

In order to remove DNA concomitant from RNA samples, the DNase treatment was done by using RNase-free DNase I (Ambion) according to the manufacturer's instructions.

2.7.2.3 Reverse transcription

The generation of complement DNA (cDNA) from RNA was performed by reverse transcription (Applied Biosystems). In brief, 2 µg of RNA were annealed with random hexamers at 70^{0}C for 10 minutes. Afterwards, 1x PCR Buffer II, 3 mM MgCl2, 0.5 mM dNTP, 50 units of Moloney Murine Leukemia Virus (M-MuLV) reverse transcriptase and 20 units of RNase inhibitor were used per each reaction. After, mixtures were incubated at room temperature for 15 minutes and then at 42^{0}C for 30 minutes, enzymes were degraded by 70^{0}C for 10 minutes. Samples were stored at -20^{0}C.

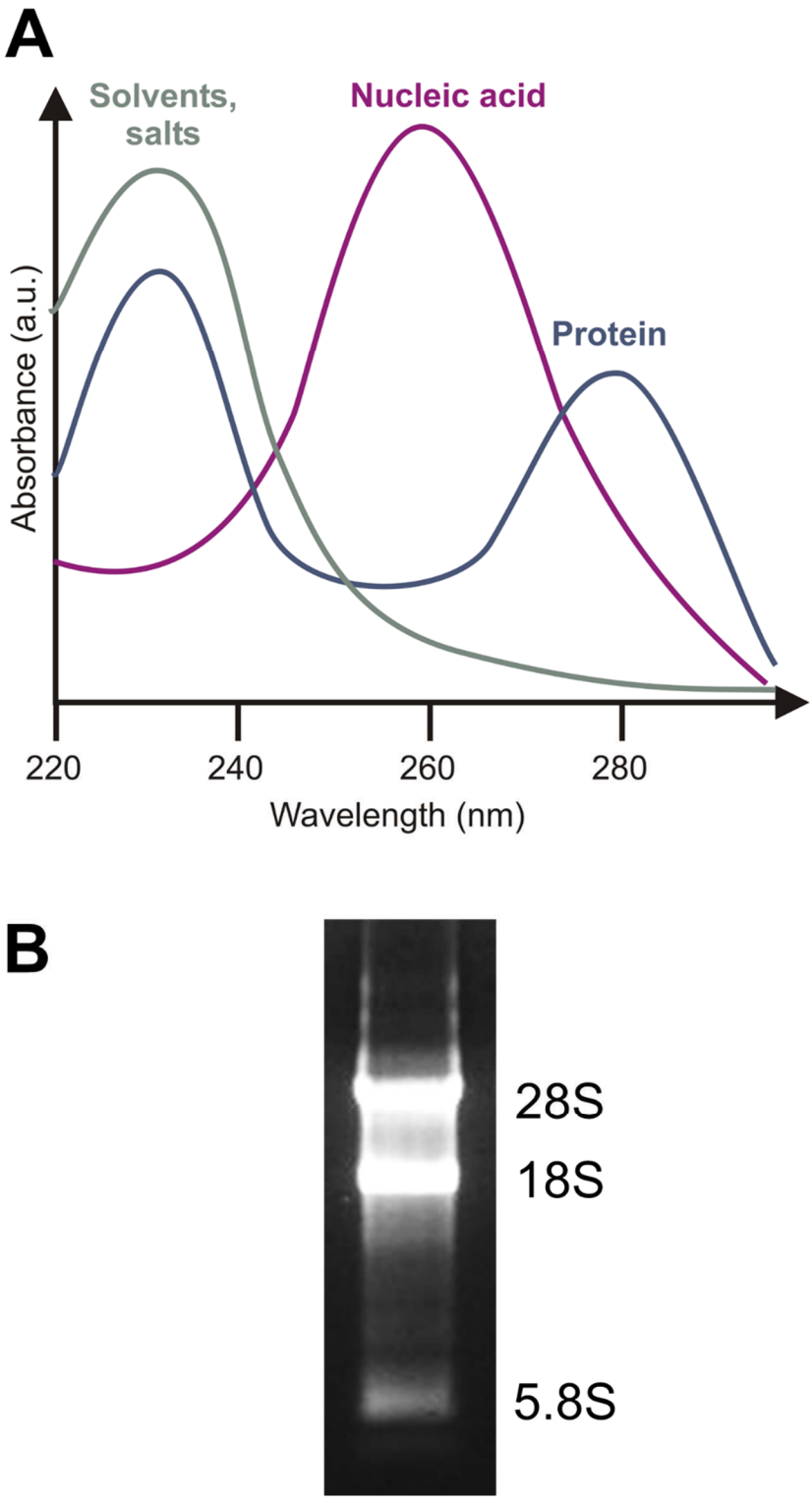

Figure 24. Methods to evaluate integrity of nucleic acids.
A, Typical absorbance spectra of pure nucleic acid, protein samples and other concomitants. Accordingly, absorbance ratio A260/A280<1.8 would likely indicate onto protein contamination, whereas A260/A230<1.8 - onto solvents and salts contamination. **B**, Integral RNA sample on 1% agarose gel. Typical bands of intact ribosomal RNA are indicated. Blurry bands would signify onto RNA degradation.

2.7.2.4 Conventional PCR

In order to amplify DNA segments we have performed conventional polymerase chain reaction (cPCR). Per each reaction 1x PCR Buffer II, 2.5 mM $MgCl_2$, 2 mM dNTP, 500 nM primers (Table 5) and AmpliTaq Gold® DNA polymerase (Applied Biosystems). The detailed protocol is indicated in Table 11. PCR products were loaded onto agarose gel in order to verify the size of expected bands.

2.7.2.5 Quantitative real-time PCR

To assess the variations of gene expression between different samples we have performed quantitave real-time PCR (qPCR) by using SsoFast™ EvaGreen® Supermix on CFX96 Touch™ Real-Time PCR Detection System. The detailed protocol is indicated in Table 11.

Conventional PCR		
Number of cycles	**Conditions**	**Description**
1	94^{0}C – 5:00	Initial cell breakage and DNA denaturation
50	94^{0}C – 0:45	DNA denatures into single strands
	55^{0}C – 0:45	Primers anneal to single stranded DNA template
	72^{0}C – 1:30	Extension/elongation from 3'- end
1	72^{0}C – 10:00	Final extension to make sure all products are full legth
Quantitaitve PCR		
Number of cycles	**Conditions**	**Description**
1	95^{0}C – 0:30	Enzyme activation
45	95^{0}C – 0:05	Denaturation
	60^{0}C – 0:05	Annealing/extension
1	65-95^{0}C (increment 0.5^{0}C) – 0:05/step	Melting curve

Table 11. PCR protocols used throughout this study.

2.7.3 Macromolecule blotting

2.7.3.1 Protein extraction

Organ tissues were homogenized with Precellys® Tissue Homogenizer. The cells were lysed in 1x RIPA buffer with protease and phosphatase inhibitors, sonicated for 10 seconds at 30% intensity and centrifuged at 13000 g for 10 minutes in order to eliminate the nuclei fraction. The concentration of protein lysate was measured with Pierce® BCA Protein Assay (Thermo Fisher Scientific).

2.7.3.2 Sodium dodecyl sulfate polyacrylamide gel electrophoresis (SDS-PAGE)

1xSample Reducing Agent and 1xLDS Sample Buffer (Bolt™, Thermo Fisher Scientific) were added to 50 µg of protein lysate and heated at 95^0C for 5 minutes. Proteins were resolved due to 3-8% Tris-acetate sodium dodecyl sulfate polyacrylamide gel electrophoresis (SDS-PAGE). Stacking gel contained 3.2% polyacrylamide. Thermo Scientific Spectra Multicolor High Range Protein Ladder (Thermo Scientific) was used to verify the size of proteins. Sample were resolved due to migration in 1x NuPAGE MOPS SDS Running buffer (Thermo Fisher Scientific) under constant voltage of 100V.

2.7.3.3 Immunoblotting

Proteins from polyacrylamide gels were transferred onto methanol-activated 0.45 µm PVDF membrane (Immobilon) with Pierce G2 Fast Blotter (Thermo Fisher Scientific). Afterwards, the blots were blocked with 5% milk 1x TBS-T buffer for 1 hour, and then incubated with primary antibodies of interest (Table 3). For HRP-conjugated secondary antibodies blots were developed using SuperSignal™ West Dura Extended Duration Substrate (Thermo Fisher Scientific), and images were captured with Amersham Imager 600 (GE Healthcare Life Sciences). Data was analysed with ImageJ software.

2.7.3.4 Cell fractionation

Cell fractionation was done by using OptiPrep™ Density Gradient Medium (Sigma). Briefly, around $50x10^6$ cells were centrifuged in PBS at 250 g for 10 minutes at 4^0C. Cells were resuspended in 5 ml of Fractionation solution B with protease and phosphatase inhibitors and grinded by using KONTES® DUALL® Tissue Grinder with Glass Pestle (DWK Life Sciences, KIMBLE®). Afterwards, suspension was *quantum satis* in 10 ml of Fractionation solution B and by using Corex® glass tubes centrifuged at 250 g for 10 minutes. The pellet was taken as nulcei fraction, whilst the supernatant fraction was ultracentrifuged at 17,000 g for 20 minutes. Supernantant was recentrifuged at 100,000 g for 2 hours and thus separated into cytosolic and microsomal fractions; whereas pellet was resuspended in 2 ml of Fractionation solution B and due to 10-30% OptiPrep™ gradient resolved into protein fractions of various densities. Each fraction was washed with 6 ml 500 mM HEPES and pelleted by ultracentrifugation at 100,000 g for 1 hour.

2.7.3.5 Invadopodia fractionation

Invadopodia fractionation was performed as previously described in (Busco *et al.*, 2010). As a result, cytoplasmic, plasmalemmal and invadopodia fractions were obtained and further analyzed due to SDS-PAGE and immunoblotting (sections 2.7.3.2-2.7.3.3).

2.7.3.6 Biotinylation

The extraction of plasmalemmal protein fraction was performed by using EZ-Link™ NHS-Biotin (Thermo Fisher Scientific) according to the manufacturer's instructions.

2.7.4 Src kinase activity assay

After extraction of proteins (as described above) without proteinase and phosphatase inhibitors the Src activity was evaluated with ProFluor® Src-Family Kinase Assay (Promega) according to the manufacturer's instructions.

2.7.5 Zymography

Zymography was performed with 1% gelatin 10% SDS-PAGE. The protein samples were extracted (as described above) without addition of reducing agents and boiling. The zymogram were developed with 0.5% Coomassie G-250 in 30% ethanol, 10% acetic acid. Data was analysed with ImageJ software.

2.7.6 Immunostaining

2.7.6.1 Immunocytochemistry

For immunocytochemical analysis $100x10^3$ cells were plated onto 15 mm glass coverslips and left in the standard growth conditions overnight. After coverslips were washed in 1x PBS, they were fixed in ice-cold MetOH or 4% paraformaldehyde (PAF) in PBS for 10 minutes. Then coverslips were blocked in 5% goat serum PBS for 30 minutes, and incubated overnight at 4^0C with primary antibodies (Table 3) that were freshly prepared in 1% goat serum PBS. Afterwards, coverslips were washed with PBS and incubated with fluorophore-conjugated secondary antibodies prepared in 1% goat serum PBS for 1 hour in humidified dark conditions. Afterwards, cellular nuclei were stained with 1:200 DAPI solution in PBS at the room temperature for 10 minutes. Following by washes with PBS, coverslips were mounted on the glass slides by using Mowiol. Visualization was performed with 40x objective on LSM 700 laser scanning confocal microscope (Carl Zeiss).

2.7.6.2 Immunohistochemistry

Slides were deparaffinized, rehydrated, and heated in citrate buffer pH 6 for antigenic retrieval. After blocking for endogenous peroxidase with 3% H_2O_2, the primary antibodies were incubated. The primary antibodies were applied for 1 hour (Table 3). Immunohistochemistry was performed using the streptavidin-biotin-peroxydase method with diaminobenzidine as the chromogen (Kit LSAB, Dakocytomation, Glostrup, Denmark). Slides were finally counterstained with haematoxylin. Negative controls were obtained after omission of the primary antibody or incubation with an irrelevant antibody. Scoring of antibody staining: Staining was scored as follows: -, no stained cells; +, low intensity; ++, high intensity. Ki67 positive cells were expressed as a percentage of total epithelial cells.

2.7.7 Gelatin degradation

The gelatin degradation assay was performed by using QCM™ Gelatin Invadopodia Assay (Red, ECM671, Merck Millipore) according to the manufacturer's instructions. In brief, prior to plating the cells, glass coverslips (15 mm in diameter) were covered with thin layer of fluorescent gelatin-Cy3. After leaving the cells to attach and degrade gelatin at the standard growth conditions, coverslips were washed in PBS and fixed with 4% PAF in PBS. If needed, cells were immunostained with antibodies and 1:200 DAPI dye. Coverslips were mounted onto glass slides by using pre-warmed at 37^0C Mowiol and visualised with 40x objective on LSM 700 laser scanning confocal microscope (Carl Zeiss). The quantity of invadopodia and area of gelatin degradation were calculated and compared within different conditions.

2.7.8 Secretion assay

The vesical secretion was measured with FM® 1-43 dye (Thermo Fisher Scientific) according to the manufacturer's instructions.

2.8 Calcium and sodium imaging

Cytosolic Ca^{2+} concentrations were measured using the ratiometric dye Fura-2-acetoxymethyl ester (AM) (Interchim), whereas cytosolic Na^+ concentrations – with SBFI-AM (Interchim) as previously described in (Iamshanova *et al.*, 2016). Dyes were reconstituted in dimethyl sulfoxide (DMSO) and diluted in HBSS containing 0.02% of Pluronic® F127 to the final concentrations of 1 μM for Fura-2 and 7 μM for SBFI. Fluorescence was excited using an illumination DG4 system (Sutter) fitted with a xenon lamp (300 W). All recordings of Na^+ fluorescence were acquired using objective 20× in the Superfluor Nikon Eclipse Ti- series inverted microscope coupled to an

EMCCD camera Rolera EM-C2 (Qimaging) and processed using Metafluor 7.7.5.0 software (Molecular Devices). The excitation filters represented the following parameters in terms of wavelength and bandwidth: 340 nm/26 nm and 387 nm/11 nm. The emission filters were as follows: 510 nm/84 nm for SBFI.

For the confocal Ca^{2+} imaging, cells were loaded using 5 µM Fluo-4-AM as described previously (Dubois *et al.*, 2014). In brief, experimental chambers containing the cells were placed on the stage of an Axiovert 200M inverted microscope attached to an LSM 510 META laser-scanning unit (Carl Zeiss). x-y confocal images of Fluo-4 fluorescence were acquired at 0.6 Hz using a Plan-Apochromat 40× 1.3 NA objective lens (Carl Zeiss). Fluo-4 fluorescence was excited by the 488 nm line of a 500 mW argon ion laser (Laser-Fertigung) and was captured at wavelengths 505 nm. The illumination intensity was attenuated to 0.6% with an acousto-optical tunable filter (Carl Zeiss). In all experiments, the photomultiplier gain was set at 688. To optimize signal quality, the pinhole was set to provide a confocal optical section <4 µm.

2.9 Data analysis and software

Data were compared using either a 2-tailed Student's t test corrected for multiple comparisons by a Bonferroni adjustment or repeated measures 2-way ANOVA, as indicated. Where necessary, the Shapiro–Wilk test was used to test for normality of the underlying sample distribution. Experimental sample sizes were chosen using power calculations with preliminary experiments or were based on previous experience of variability in similar experiments. Samples that undergone technical failure during processing were excluded from analyses. The Kolmogorov–Smirnov test was used to evaluate the significance between different distributions. For adoptive transfer experiments, recipient mice were randomized prior to cell transfer. The tumor treatment graphs were compared by using the Wilcoxon rank sum test and analysis of animal survival assessed using a log-rank test. In all cases, P values of less than 0.05 were considered significant. Comparison between patient groups was performed using the $\chi 2$ test for categorical data and nonparametric Mann-Whitney U test and Kruskal-Wallis tests for continuous data.

Statistics were calculated using GraphPad Prism 7 software (GraphPad Software Inc.), StatView, version 5.0, software (Abacus Concepts, Berkeley, CA) and OriginPro 2015 Beta3 software (1991–2014 OriginLab Corporation). The figures were created mostly using CorelDRAW 11.633 software (2002 Corel Corporation).

Article 1:

"Comparison of fluorescence probes for intracellular sodium imaging in prostate cancer cell lines."

Iamshanova O, Mariot P, Lehen'kyi V, Prevarskaya N.

Eur Biophys J. 2016 Oct;45(7):765-777. Epub 2016 Sep 22.

3. Results

3.1 Main results

The main results obtained throughout this study are presented as the future manuscript entitled "Na^+ leak governs pacemaking activity of cancer cells required for the metastatic disease development". Results that were not included in this article are described in the separate section afterwards.

Article 2:

"Na^+ leak governs pacemaking activity of cancer cells required for the metastatic disease development".

Article is in preparation

Introduction

Along with the very first functional characterization of NALCN as a Na^+ leak channel that took just 10 years ago, was also discovered its importance in maintaining the resting membrane potential and controlling rhythmic electrical bursts in neurons (Lee et al. 1999, Lu et al. 2007). Indeed, NALCN deletion leads to severe disruption of neuronal activities and knockout mice die within 24 hours of birth (Lu et al. 2007). Thus, NALCN is one of the few channels in the 4x6TM channel family required for neonatal survival (Lu et al. 2007). Today, NALCN is well-recognised as an indispensable component of circadian pacemaker neuronal output (Lu et Feng 2012, Bridget et al. 2013, Flourakis et al. 2015, Lozic et al. 2016). Such rhythmic neuronal activity is required to support repeated firing of action potentials and is established by complex intracellular signalling. Importantly, on molecular level this phenomenon is comprised of various spontaneously active systems including oscillators of circadian nucleus, membrane potential and cytosolic Ca^{2+}. Surprisingly, cytosolic Ca^{2+} oscillations are also a prominent feature of highly aggressive dedifferentiated cancer cells (Iamshanova et al. 2017). In fact, the apparent parallels between tumour and normal, in particular neural, cells generated great interest in the last decades and implies on the possible mirrored traits between these two classes of cells (ref). For example, the neuronal growth cones form protrusions that share molecular, structural and functional characteristics of invadosomes, the sites of attachments with proteolytic activity required by cancer cells to metastasize (Santiago-Medina 2015 Development). In both cases, the release of extracellular matrix degradation enzymes subserves for targeting the nearby tissues. Specifically, Ca^{2+} oscillations, but not the sustained elevated intracellular Ca^{2+} levels, are defined as substantial signalling trigger for the vesicle secretion (Wollman et Meyer 2012). Indeed, abolished Ca^{2+} oscillations revoked fusion of matrix-metalloproteinases-containing vesicles with the plasma membrane and resulted in constrained extracellular matrix degradation (Sun et al. 2010). Noteworthy, the loss of background Na^+

leak is associated with defective rhythmically oscillating activities in neurons and cancer cells, as well as with abrogated secretion especially in cells with fast or continuous vesicle turnover (Lu et al. 2007, Yeh et al. 2008, Bouhours et al. 2011, Jospin et al. 2007, Lear et al. 2005, Pierce-Shimomura et al. 2008, Rizaner et al. 2016). Accordingly, Na^+ signalling was already envisaged as an upstream governor of spontaneous Ca^{2+} oscillations, however, nothing is yet known about its intrinsic mechanisms (Rizaner et al. 2016). In this study, we show for the first time how background Na^+ current provided through 'classically' neuronal pacemaker channel NALCN is employed by highly metastatic cancer cells in their signalling cascade of Ca^{2+} oscillations and its physiological impact on the disease outcome.

Results

NALCN regulates metastasis-associated cancer cell behaviour

To date, being primarily explored in neurons and cardiomyocytes NALCN was reported to be responsible for rhythmic behaviour and was mainly associated with neuronal and muscular channelopathies (Cochet-Bissuel *et al.*, 2014; Bend *et al.*, 2016). Despite its identification in endocrine glands and secretory organs, little is known about role of NALCN in 'non-excitable' cells (Cochet-Bissuel *et al.*, 2014). We found NALCN expression in mammalian prostate (SFig. 1a-c). Although normal prostate has secretory function, secretion may also be engaged in genesis of various pathologies, including carcinogenesis where tumour spread is facilitated by secretion of extracellular matrix (ECM) degrading enzymes. Indeed, our screening of various pancreatic and prostate cancer cell lines, revealed NALCN and its circadian-linked regulator, NLF-1, only in highly aggressive cell lines, but not in those with weak metastatic potential (SFig. 2a-d). Genome sequencing analysis revealed that *NALCN* mutations in prostate cancer cells are unlikely to affect the Na^+ leak channel function (SFig. 2e). Indeed, we demonstrated that in prostate cancer cells from NALCN-positive lines, NALCN is expressed in the plasma membrane (SFig. 3a) and provides pathway for Na^+ influx not observant in NALCN-negative cell lines (SFig. 3b-e). Importantly, cellular viability, cell cycle, apoptosis (neither basal nor induced) and proliferation rate were not affected by the gene silencing, whereas metastasis-associated behaviour, namely, cell motility, migration and invasion were considerably dependent on the level of NALCN expression (SFig. 4a-e, SFig. 5a-m).

In order to assess further the mechanisms promoting cancer cell invasion, we focused on formation of invadopodia, actin-rich membrane protrusions with ECM degradation activity.

Confocal detection of the Cy3-fluorescent gelatine (the ECM component) degradation caused by PC-3 cells revealed that NALCN suppression significantly decreases the number of the

invadopodium formation sites and total area of gelatin degradation (Fig. 1a; SFig. 5k-m). Of note, intracellular pH was not affected by NALCN depletion, whereas intrinsic buffering capacity was significantly augmented (SFig. 5n-o).

Furthermore, confocal mapping of NALCN in PC-3 cells expressing NALCN-GFP revealed that NALCN-enriched dynamic structures ("rosettes") are located at the cell bottom reported by CellMask^{TM} Deep Red plasma membrane stain (SFig. 6a; SVideo1), and that, when these cells co-expressing NALCN-GFP and RCamp (to label the cell body) are placed on gelatine layer, newly-formed invadopodia are appeared to be enriched with NALCN ((Fig. 1b, SFig. 6a; SVideo2). Presence of NALCN in invadopodia was confirmed further by cell fractionation assay (SFig. 6b). Interestingly, NALCN knockdown (NALCN-KD) markedly suppresses expression and activity of the invadopodia marker proto-oncogene Src kinase (SFig. 6b-d). Indeed, previous studies reported that Src kinase is recruited to NALCN channelosome, however, no evidence of direct Src kinase dependence on NALCN expression was then presented (Lu *et al.*, 2009; Wang & Ren, 2009). Our immunocytochemical assay revealed strong co-localisation of NALCN not only with Src kinase but also with other invadopodial proteins, e.g. cortactin, dynamin, matrix metalloproteinase MT1-MMP and Tks5, within specific morphological structures referred to as invadopodia punctae and rosettes (Fig. 1c; SFig.6 e). Recently it was demonstrated that invadopodial precursor assembly in starved melanoma cells can be induced by stimulation with 10% FBS (Sun *et al.*, 2014). We found that FBS-induced invadopodial precursor assembly in starved PC-3 cells reported by actin punctae formation is strongly suppressed by NALCN-KD (Fig. 1d, SFig. 7a). Interestingly, FBS-induced formation of dynamin punctae, reporting invadopodial precursor assembly, occurred at a site of the $[Ca^{2+}]_c$ wave initiation (Fig. 1e, SFig. 7b), which, in turn, coincide with NALCN-enriched rosette (Fig. 1f) forming cap-like structure at the cell bottom (Fig. 1g).

In cancer cells, excretion of ECM-degrading enzymes via vesicle secretion is principal mechanism facilitating invasiveness. Here we report that NALCN bioavailability is an important determinant of the rate of vesicle secretion by PC-3 cells (Fig. 1h) and activity of ECM-degrading enzyme matrix metalloproteinases (Fig. 1i), and that this secretion is controlled by $[Ca^{2+}]_c$ in microdomains, since fast and slow Ca^{2+} chelators suppress this process to different extents (Fig. 1h, 1j, SFig. 8).

Altogether the above results strongly suggest that NALCN provides signalling input to invadopodium formation and cancer cell invasiveness.

NALCN governs Ca^{2+} oscillations

Recently it was demonstrated that in contrast to weakly metastatic human prostate cancer cells (LNCaP), strongly metastatic PC-3M cells are prone to generate Na^+-influx-dependant $[Ca^{2+}]_c$ oscillations (Rizaner *et al.* 2016), and that $[Ca^{2+}]_c$ oscillations are important regulators of secretion (Wollman and Meyer, 2012) and invadopodium formation (Sun *et al.* 2014). We found that FBS-induced initial $[Ca^{2+}]_c$ transient and $[Ca^{2+}]_c$ oscillations are associated with reciprocal changes of $[Ca^{2+}]_{ER}$ (Fig. 2a). Similar pattern of $[Ca^{2+}]_c$ events was recorded in response to stimulations with one of the FBS component – the epidermal growth factor, EGF (Fig. 2b). The initial $[Ca^{2+}]_c$ transient, but not subsequent $[Ca^{2+}]_c$ oscillations, persisted in Ca^{2+}-free solution supplemented with 0.5 mM EGTA, while all $[Ca^{2+}]_c$ response to FBS was abolished following Ca^{2+} store depletion with 50 µM cyclopiazonic acid (CPA) even when the cells were bathed in Ca^{2+}-containing solution (Fig. 2c) We, therefore, concluded that $[Ca^{2+}]_c$ oscillations facilitated by FBS depend on both, repetitive Ca^{2+} influx and Ca^{2+} recycling by the endoplasmic reticulum (ER). To asses possible contribution of NALCN to the genesis of this oscillations we compared spatio-temporal patterns of the FBS-induced $[Ca^{2+}]_c$ response in

starved PC-3 cells pre-treated with control siRNA (siCTL) and siNALCN, using time-laps confocal Ca^{2+} imaging (Fig. 2d-e). This revealed that FBS-induced $[Ca^{2+}]_c$ oscillations are attenuated (reduction in the frequency and signal mass temporal density) by NALCN-KD (Fig. 2f) and that "pacemaker phase" evident in these oscillations is siNALCN-sensitive (Fig. 2d-e). Furthermore, dramatic attenuation of the $[Ca^{2+}]_c$ oscillations following reduction of $[Na^+]_o$ (Fig. 2g) and suppression of FBS-induced inward current by NALCN-KD or $[Na^+]_o$ reduction (Fig. 2h) provide most direct evidence that FBS-induced $[Ca^{2+}]_c$ oscillations are governed by NALCN-mediated Na^+ influx rather than by other signalling pathways not immediately related to the NALCN channel activity.

Moreover, we found that stimulation with 10% FBS of starved PC-3 cells that triggers $[Ca^{2+}]_c$ oscillations promotes Src kinase activity (SFig. 9a), not unlike it was previously reported (Sun *et al.*, 2014). We, therefore, concluded that in these strongly metastatic prostate cancer cells, NALCN facilitates Src kinase activity by promoting $[Ca^{2+}]_c$ oscillations, which depend on (1) NALCN-mediated Na^+ influx (Fig. 2d-h) and (2) repetitive Ca^{2+} influx and Ca^{2+} recycling by the ER (Fig. 2c).

Coupling between NALCN-mediated Na^+ influx and $[Ca^{2+}]_c$ events

Oscillations generally require positive feed-back between elements involved in their genesis. We, therefore, assessed (1) modulation of NALCN-mediated Na^+ influx by $[Ca^{2+}]_e$ and the events leading to $[Ca^{2+}]_c$ elevation and (2) coupling between Na^+ influx and rise of $[Ca^{2+}]_c$. To unravel net effect of $[Ca^{2+}]_c$ elevation on NALCN-mediated Na^+ influx we assessed Na^+ influx induced by $[Na^+]_o$ switch from 0 to 130 mM (Fig. 3a) and Na^+ influx induced by store-operated Ca^{2+} entry, SOCE (Fig. 3c), and compared (Fig. 3d). We found that in PC-3 cells $[Na^+]_o$-switch-induced Na^+ influx (Fig. 3a): (1) is dramatically suppressed by NALCN-KD, (2) is not

modulated by $[Ca^{2+}]_e$, at least within the range of 0 – 4 mM (see also SFig. 9b) in contrast to that previously reported for neurons (Lu *et al.*, 2010; Lu and Feng; 2012), and (3) is not affected by the Ca^{2+} store depletion (see also SFig. 9c). Furthermore, $[Ca^{2+}]_c$ elevation brought about by the ER Ca^{2+} leak following acute block of sarco/endoplasmic reticulum Ca^{2+}-ATPase (SERCA) with thapsigargin (TG) failed to induce Na^+ influx when the cells were bathed in Ca^{2+}-free external solution supplemented by 0.5 mM EGTA (and hence no SOCE was generated) (Fig. 3b). Moreover, we found (Fig. 3c) that: (1) SOCE activation triggers Na^+ influx even at constant $[Na^+]_o$=130 mM in $[Ca^{2+}]_o$-dependent manner (see also SFig. 9d-i), (2) NALCN-KD significantly suppresses not only this Na^+ influx but also SOCE, (3) inhibition of the reverse-mode plasmalemmal Na^+/Ca^{2+} exchanger (RM-NCX) curtails $[Ca^{2+}]_c$ transient caused by SOCE at $[Na^+]_o$=130 mM, does not affect it at $[Na^+]_o$=0 mM and attenuates $[Ca^{2+}]_c$ transient triggered by Na^+ readmission following SOCE activation. Comparison of the effects of NALCN-KD on Na^+ influx caused by the $[Na^+]_o$ switch with that one triggered by SOCE revealed that SOCE significantly augments NALCN-mediated Na^+ influx (Fig. 3d, top). The cell surface *biotinylation assay* revealed that SOCE addresses NALCN to plasma membrane (Fig. 3d, bottom), similarly to that what we have previously reported for TRPV6 (Raphaël *et al.,* 2014). Interestingly, stimulation with 10% FBS also elevates the amount of NALCN protein in the plasma membrane (SFig. 9j).

The above results indicate that Ca^{2+} influx during SOCE, but not Ca^{2+} release from the ER (Fig. 3b) or Ca^{2+} store depletion (Fig. 3a, right panel) *per se*, promote NALCN-mediated Na^+ influx by addressing NALCN protein to the plasma membrane, while enhanced Na^+ influx and/or accumulation, in turn, facilitates Ca^{2+} influx either via RM-NCX (Fig. 3c; SFig. 9k) or by relieving SOCE inactivation. The latter may involve mitochondrial Na^+/Ca^{2+} exchanger (NCLX), the potential of which to modulate ROS production and, hence, SOCE was recently reported (Ben-Kasus Nissim *et al.*, 2017). We found that NCLX silencing notably suppresses

SOCE (Fig. 3c; SFig. 9l), what suggests that in PC-3 cells this exchanger may contribute to signalling chain: NALCN-mediated Na^+ influx – NCLX-mediated Ca^{2+} extrusion from mitochondria – decrease of ROS production – relief of SOCE inactivation. Nevertheless, attenuation of FBS-induced $[Ca^{2+}]_c$ events (both the initial transient and oscillations) by RM-NCX inhibitor KB-R7943 (Fig. 3e), suggests that NALCN-mediated Na^+ influx facilitates RM-NCX-mediated Ca^{2+} entry, while inhibition of FBS-induced inward current by this compound (Fig. 3f) indicates that this Ca^{2+} entry encourages NALCN-mediated Na^+ influx. This positive feed-back between NALCN and RM-NCX may serve to sustain $[Ca^{2+}]_c$ oscillations, modulation of which via the ER Ca^{2+} recycling (Fig. 2a) is also tuned by SOCE and RM-NCX.

NALCN promotes prostate cancer aggressiveness *in vivo*

We found that NALCN is upregulated in cancer prostate biopsies relative to non-cancerous tissues taken from the same patient (Fig. 4a). Furthermore, immunohistochemical analysis revealed that NALCN was negative in non-cancerous prostate glands, with a positive internal control in smooth muscle fibers (Fig. 4b). In human prostate cancer, NALCN staining was observed in 57% of clinically localized hormone-naïve cases, 6% of CRPC (3 cases out of 48) and 62% of metastases (13 cases out of 21). In clinically localized prostate cancer, NALCN expression increased within the ISUP group (ex Gleason score, that reflects the loss of differentiation) ($p=0.0003$), and was also higher in pT3 tumours (with extra-prostatic extension) when compared to pT2 (tumour limited to the prostate gland) ($p=0.0003$). Results are summarized in Table. 4c.

Interestingly, in clinically localized prostate cancer, the expression of NALCN strongly correlated with staining of protooncogenic Src-kinase ($p<0.0001$). Moreover, NALCN expression also correlated with SOCE components - Orai1 ($p<0.0001$), STIM1 ($p=0.005$),

STIM2 ($p=0.007$), and with other plasmalemmal ion channels - SK3 ($p<0.0001$), TRPC1 ($p=0.0006$) (SFig.10a). Importantly, all these proteins were previously reported to be implemented in prostate cancer progression (Chantome *et al.*, 2013; Perrouin Verbe *et al.*, 2016). Yet, no significant correlation between expression of NALCN and expression of either proliferation marker, Ki67, or marker for epithelial-to-mesenchymal transition, Zeb1, was observed (SFig. 10b).

As phosphatase and tensin homologue (PTEN) is one of the most commonly deleted/mutated tumour suppressor genes in human prostate cancer, we utilised PTEN knockout mice model with conditional gene inactivation (floxed allele; L2). Following prolonged tamoxifen administration $PTEN^{-/-}$ mice established prostate adenocarcinoma, whereas $PTEN^{-/-}p53^{-/-}$ developed more aggressive and invasive phenotype of prostate cancer. The *ex vivo* analysis performed on these prostate tumours revealed that NALCN is markedly upregulated during progression of invasive adenocarcinoma, but not during initial tumourigenesis (Fig. 4d).

To study the progression of prostate tumours *in vivo* we utilised PC-3 cells with stable Luciferase activity. Following orthotopic (directly into prostate) injection of these cells into the nude mice the time (12 weeks) was allowed for tumour growth and metastasis. We found that NALCN-KD significantly suppresses tumour growth *in vivo* (Fig. 4e-f, SFig. 11a). This was confirmed further by *ex vivo* analysis (Fig. 4g).

It is well appreciated that primary target of the prostate cancer metastasis is bone tissue. In fact, PC-3 cell line is derived from bone issue of prostate cancer patient. We found that orthotopic (directly into prostate) injection of shNALCN PC-3 cells resulted in markedly decreased level of metastases into mouse skeleton than that caused by orthotopic injection of shCTL PC-3 cells (Fig. 4h). Reduction of metastasis to other organs by NALCN-KD, however less explicit, was also detected (SFig. 11b; SFig. 12). The above observations suggest that NALCN level

determines PC-3 cell invasiveness. To assess this we performed Transwell® invasion assay by using osteoblast conditioned media as a chemoattractant. We found that NALCN-KD significantly reduces invasiveness of PC-3 cells (Fig. 4i). Furthermore, comparison of the effect of the direct injection into tibia of shCTL PC-3 cells with that of the injection of shNALCN PC-3 cells revealed that NALCN-KD significantly reduces bone tissue destruction caused by the prostate cancer cells (Fig. 4j; SFig. 13a-c,).

Altogether the above results indicate that NALCN suppression has profound effect on prostate malignant tumourigenesis and metastasis and, hence, represents novel strategy for prostate cancer therapy.

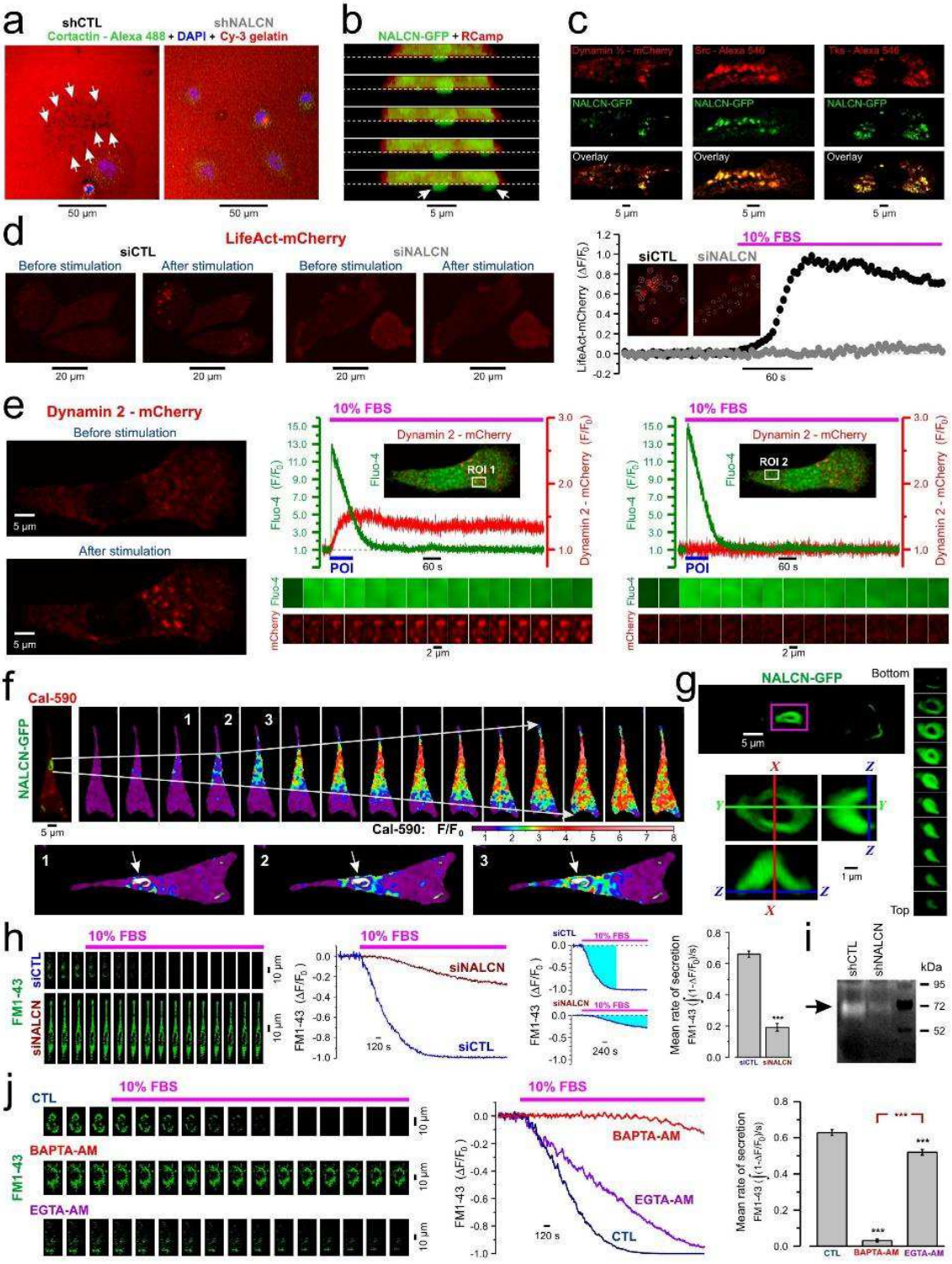

Figure 1. NALCN provides signalling input to invadopodia. a, NALCN-KD suppresses invadopodia formation revealed by Cy3-fluorescent gelatine degradation (arrows). Confocal images of Cy3 (red), DAPI (blue; nuclei) and Alexa 488 (green; anti-cortactin Ab) fluorescence in control (shCTL) and NALCN-KD (shNALCN) 48 h after plating PC-3 cells on gelatine. **b**, Sequential (top to bottom) *z-x* confocal cross-sections of PC-3 cell transfected with NALCN-GFP and RCamp reveal localisation of NALCN in newly-formed invadopodia (arrows). Dashed line: gelatine surface. **c**, Co-localisation of NALCN with invadopodia markers: dynamin (left), Src (middle) and Tks (right), as indicated. **d**, Left: siNALCN suppresses invadopodial precursor assembly in PC-3 cells expressing LifeAct-mCherry. Near-cell-bottom confocal images were captured before and 3 min after stimulation with 10% FBS during *x-y* time-series imaging. Right: corresponding traces of relative changes in mCherry fluorescence averaged at outlined regions (insets). **e**, Left: confocal images of mCherry-dynamin2 fluorescence captured before and 3 min after stimulation with 10% FBS. Middle and right: plots relates the dynamics of $[Ca^{2+}]_c$ changes (fluo-4) to formation of dynamin puncta (mCherry-dynamin2) at two ROIs (insets); the galleries (below) show (left to right) every 40^{th} image (after 90° rotation) during the POI (plots: blue bars), respectively. **f**, Top: the overlay of NALCN-GFP and Cal-590 images (left) is related to the gallery of self-normalised rainbow-coded Cal-590 images showing $[Ca^{2+}]_c$ response to 10% FBS. Bottom: 3 rainbow-coded Cal-590 images are superimposed on grey-coded NALCN-GFP image. Arrows: NALCN-enriched structure. **g**, 3D distribution of NALCN in the region of Ca^{2+} wave initiation: confocal *z*-sections (right) and corresponding *x-y*, *z-y* and *z-x* cross-sections (bottom left). **h**, Left: the galleries of sequential 3D images (left to right: every 25^{th} image) compare FBS-induced degradation of FM1-43-labelled secretory vesicles in PC-3 cells pre-treated with siCTL and siNALCN. Middle: corresponding traces of relative changes in total *z*-stack fluorescence. Right: plot compares mean rate of secretion, calculated as signal mass (cyan, left) per second, in control (siCTL: N=26, n=35) and following NALCN suppression (siNALCN: N=36, n=40). **i**, Zymography compares MMP-2 activity (72 kDa) in control (shCTL) and NALCN-KD (shNALCN) PC-3 cells. **j**, The same as **h**, but for untreated (CTL: N=41, n=45) cells and those pre-loaded with slow (EGTA-AM: N=28, n=35) and fast (BAPTA-AM: N=53, n=62) Ca^{2+} helators. ***P<0.001.

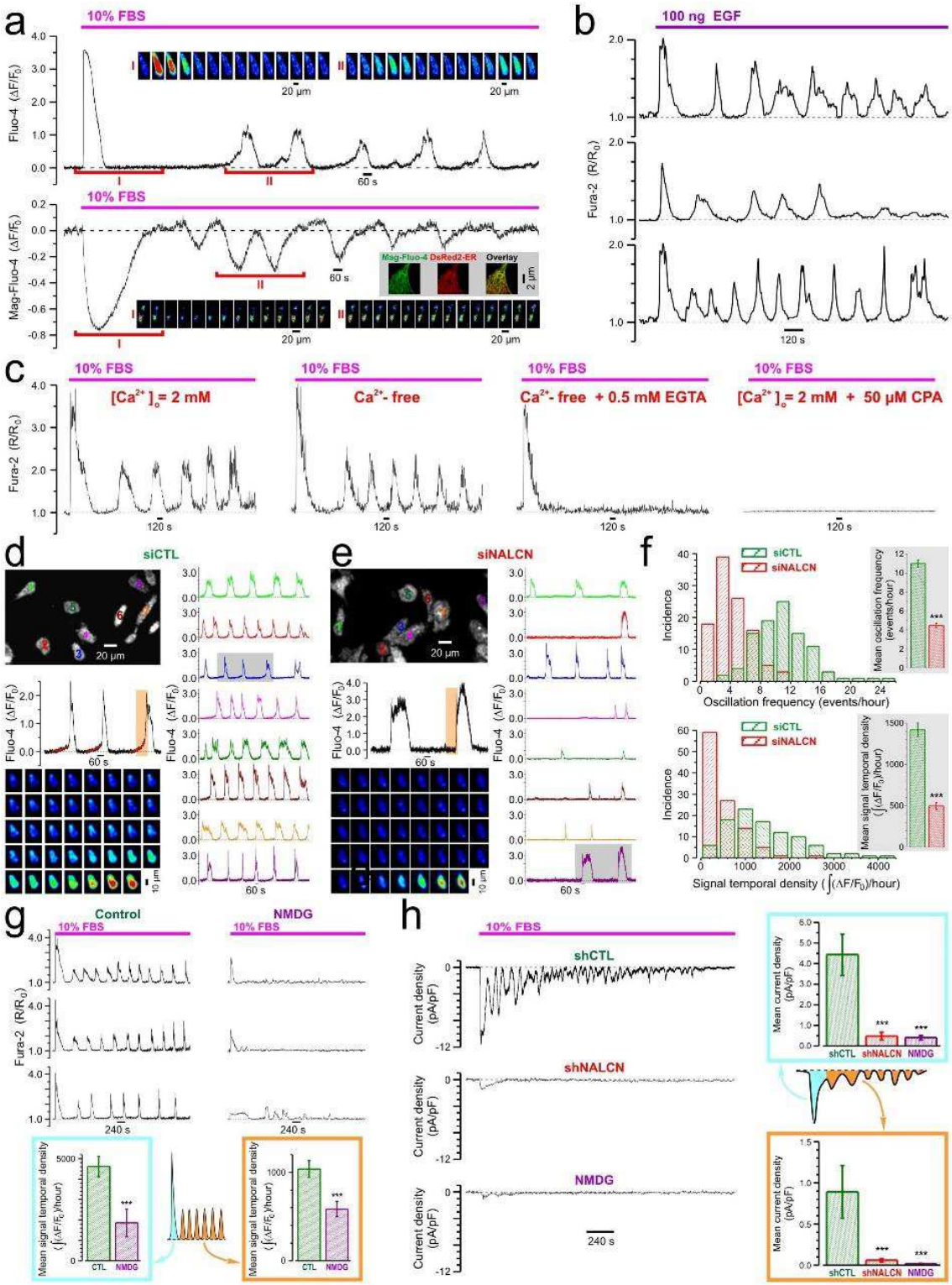

Figure 2. NALCN regulates Ca^{2+} oscillations in PC-3 cells. a, FBS-induced transient $[Ca^{2+}]_c$ elevations (Fluo-4, top) are associated with transient decreases of $[Ca^{2+}]_{ER}$ (Mag-Fluo-4, bottom). The galleries (insets) show every 100th image during the highlighted periods (I and II, respectively). Visualisation of the ER with pDsRed2-ER vector confirms the ER origin of Mag-Fluo-4 signal (grey background inset: confocal images of cell fragment). **b**, Sample traces of EGF-induced $[Ca^{2+}]_c$ responses (Fura-2). **c**, Contribution of Ca^{2+} influx and Ca^{2+} release to FBS-induced $[Ca^{2+}]_c$ response (Fura-2) illustrated by sample traces (left to right): control, nominally Ca^{2+}-free or EGTA-supplemented solutions, and Ca^{2+}-containing solution but depleted Ca^{2+} stores. **d**, **e**, $[Ca^{2+}]_c$ oscillations reported by confocal time-series imaging of fluo-4 fluorescence in FBS-exposed PC-3 cells pre-treated with siCTL (**d**) or siNALCN (**e**). The trace colours (right) correspond to the colour of the cell number (top left). Highlighted (grey background) periods are presented on enlarged plots (left middle) to emphasise that NALCN suppression abolishes "pacemaker events" observed in control (fitted red curves). The galleries (left bottom) show every 3rd image during the highlighted periods (left middle: orange background). **f,** The histograms compare the oscillation frequency (top) and signal temporal density (bottom) distributions for siCTL (n=98) and siNALCN (n=107). Insets: corresponding mean±S.E.M. **g**, FBS-induced $[Ca^{2+}]_c$ response (Fura-2, $\Delta R/R_0$) is attenuated following reduction of $[Na^+]_o$ to 19.5 mM (substitution with NMDG). **h**, FBS-induced inward current (perforated patch, V_h=-80 mV) is suppressed following pre-treatment with shNALCN or reduction of $[Na^+]_o$ to 13 mM (substitution with NMDG). The bar diagram plots: mean signal temporal densities (**g**, n=20-23) and mean current densities (**h**, n=4-6) during initial transient (cyan) and oscillations (orange). Data are mean±S.E.M. ***P<0.001.

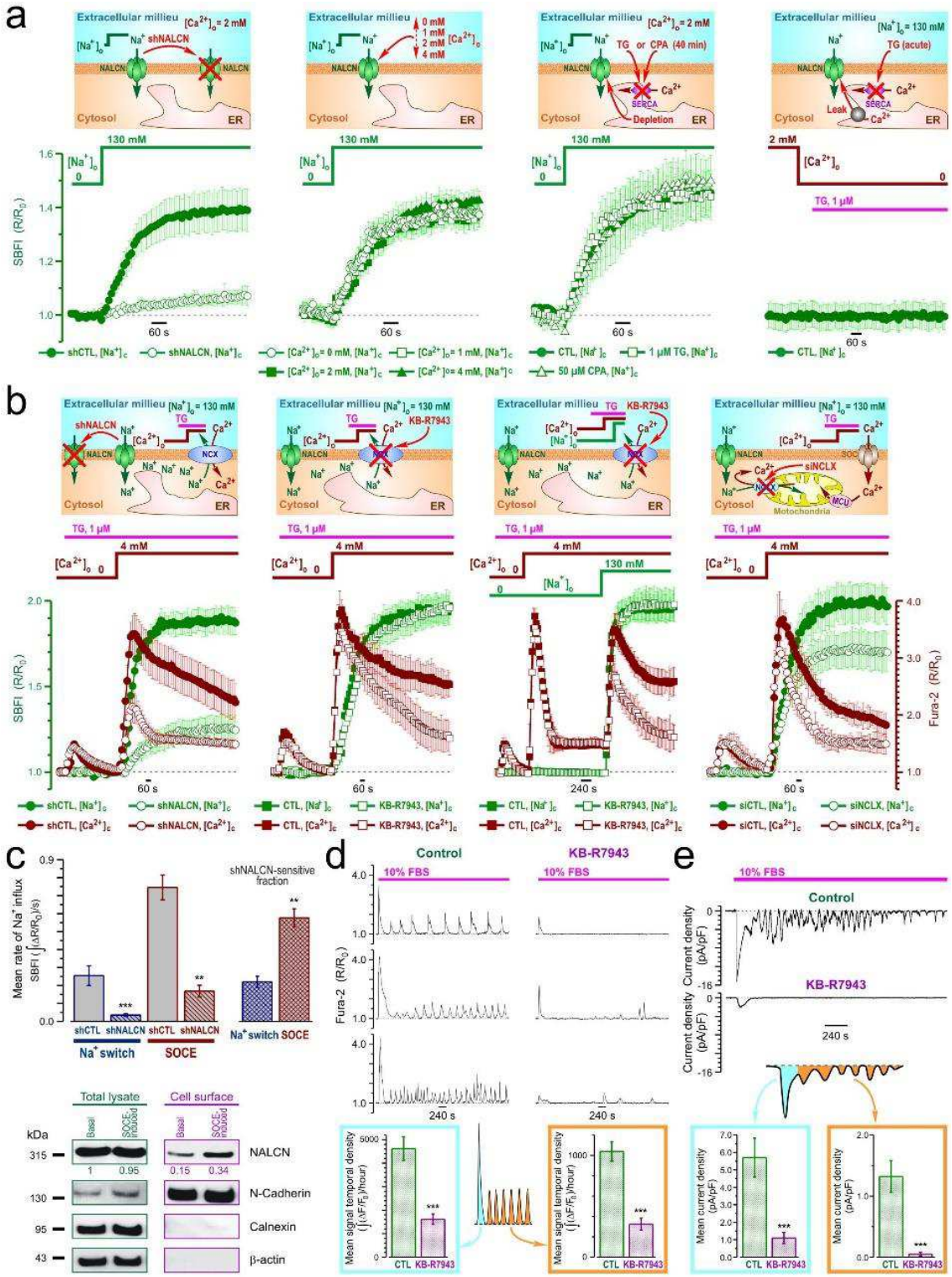

Figure 3. Interplay between SOCE, NALCN and NCX in PC-3 cells. a, $[Na^+]_o$-switch-induced Na^+ influx reported by ratiometric Na^+ indicator SBFI; the effect of (left to right): NALCN-KD, $[Ca^{2+}]_o$, Ca^{2+} store depletion and Ca^{2+} leak from the ER (*n*=45-360). **b**, SOCE-induced changes of $[Na^+]_c$ (SBFI) and $[Ca^{2+}]_c$ (Fura-2); the effect of (left to right): NALCN-KD, the reverse-mode plasmalemmal Na^+/Ca^{2+} exchanger (RM-NCX) inhibitor KB-R7943 (1 μM) at $[Na^+]_o$=130 mM and $[Na^+]_o$ stepped from 0 to 130 mM following SOCE activation, and knockdown of the mitochondrial Na^+/Ca^{2+} exchanger, NCLX-KD (*n*=132-501). In **a** and **b**, cartoons (top) highlight experimental design and plots (bottom) show traces of SBFI (olive) and Fura-2 (wine) fluorescence with the axes (R/R_0) presented in corresponding colour. **c**, SOCE addresses NALCN to plasma membrane. Plots (top) compare mean rates of Na^+ influx induced by $[Na^+]_o$-switch (*n*=283-360) and SOCE (*n*=180-216), and their shNALCN-sensitive fractions. Immunoblotting (bottom) compares NALCN expression in total cell lysates and biotinylated fractions before and following SOCE induction. Numbers show (in corresponding colour) mean values (*n*=3) of NALCN protein levels (band intensity) normalized to N-Cadherin, calnexin and β-actin. KB-R7943 (1 μM) attenuates: (**d**) $[Ca^{2+}]_c$ responses (Fura-2, R/R_0) and (**e**) inward current (perforated patch, V_h=-80 mV) induced by 10% FBS. The bar diagram plots: mean signal temporal densities (**d**, *n*=20) and mean current densities (**e**, *n*=6-8) during initial transient (cyan) and oscillations (orange). Data are mean±S.E.M. ***P*<0.01, ****P*<0.001.

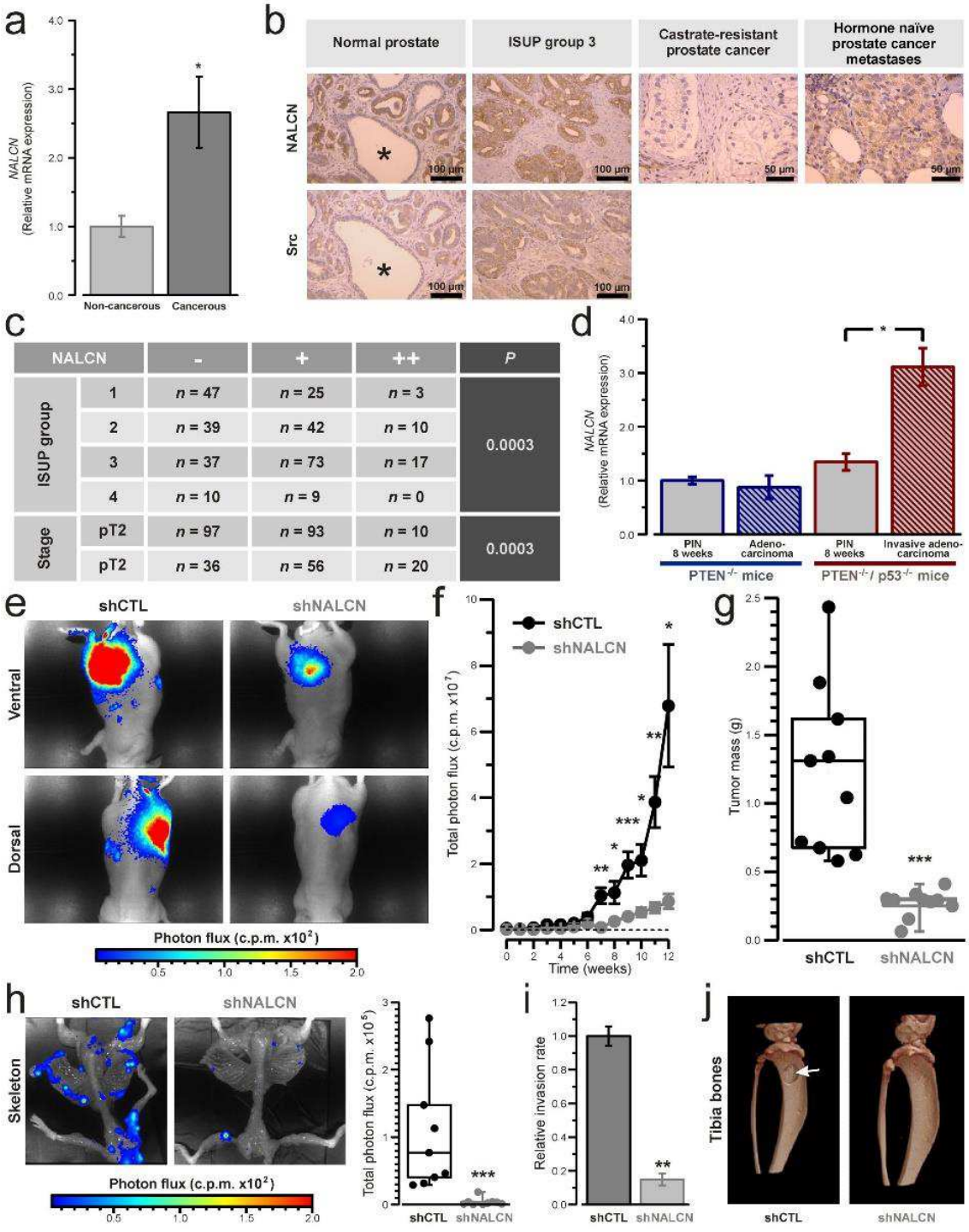

Figure 4. NALCN promotes prostate cancer progression. a, Q-PCR: *NALCN* mRNA level in cancerous vs. non-cancerous prostate biopsies (*n*=28). **b**, Immunohistochemistry: positive staining of NALCN and Src in cancerous, but not in non-cancerous (*****) prostate. **c**, NALCN expression in hormone naïve clinically localized cancer (n=338). **d**, Q-PCR: *NALCN* mRNA levels in adenocarcinoma of $PTEN^{-/-}$ mice, invasive adenocarcinoma or prostatic epithelial neoplasia (PIN) of $PTEN^{-/-}/p53^{-/-}$ mice vs. PIN of $PTEN^{-/-}$ mice (*n*=5). **e**, Bioluminescence images (BLIs) of mice 12 weeks after orthotropic injections of PC-3-Luc-shCTL or PC-3-Luc-shNALCN cells. **f**, BLIs on mice revealed tumour growth suppression by NALCN-KD (*n*=10). **g**, Masses of tumours dissected from mice used in **f** 12 weeks after the injection: box-plots with raw data (*n*=10). **h**, Left: the same as in **e** but BLIs of *ex vivo* skeleton metastases. Right: box-plots with raw data of the BLI bone metastasis assay (*n*=10). **i**, NALCN-KD in PC-3 cells suppresses Transwell® (chemoattractant: conditioned media from osteoblasts) invasion (*n*=3). **j**, X-ray 3D images: osteolysis (arrow) 31 days after intra-tibial injection of PC-3-Luc-shCTL or PC-3-Luc-shNALCN cells. Data are mean±S.E.M. **P*<0.05, ***P*<0.01, ****P*<0.001.

Discussion

In this study we demonstrated that NALCN promotes prostate cancer progression. While many research groups were able to show that Na^+ permeable ion channels indeed potentiated metastatic cancer cell behaviours, the exact mechanism of how Na^+ influx acts on the intracellular signalling remained elusive. According to one of the current hypotheses, it was partially explained due to the changes in membrane potential caused by inward Na^+ current (Yang & Brackenbury, 2013). However, the direct role of its relationship with metastatic cascade was not yet revealed. Moreover, Na^+ influx carried by voltage-gated Na^+ channels was reported to increase H^+ efflux through NHE1, thus enhancing pH-dependent ECM degradation and invasion (Brisson *et al.*, 2011). However, the precise mechanism by which Na^+ current enhances NHE1 is not yet clear. Furthermore, Na^+ influx was proposed to promote migration and invasion of cancer cells due to the regulation of Ca^{2+} signalling. For example, depolarizing Na^+ influx may activate voltage-gated Ca^{2+} channels in the plasma membrane or reverse the mode of NCX mode leading to $[Ca^{2+}]_i$ increase. Additionally, Na^+ uptake by mitochondrial Na^+/Ca^{2+} exchanger, NCLX, may lead to Ca^{2+} liberation from the organelle (Carrithers *et al.*, 2009; Ben-Kasus Nissim *et al.*, 2017). However, the direct link between Na^+ and Ca^{2+} fluxes regulating cancer cell motility and invasiveness was scarcely known and much speculated.

We now display that Na^+ leak indeed potentiates cancer cell aggressiveness due to reversing the mode of NCX and is required to maintain SOCE activity. This in turn, governs cytosolic Ca^{2+} oscillations, which have been reported to initiate invadopodia assembly and its proteolytic activity (Sun *et al.*, 2014). Importantly, current finding uncovers NALCN conductance as a substantial regulator of Ca^{2+} signal rhythmicity in highly dedifferentiated cancer cells, in analogous manner as it establishes spontaneous activity of neurons required for synaptic transmission. Accordingly, in this study we show that NALCN-controlled Ca^{2+} oscillations provide vesicle secretion in cancer cells, needed for extrusion of ECM degrading

enzymes. Of note, exocytosis as a Ca^{2+} dependent process was previously described for other cell types (e.g. insulin production in pancreatic β-cells, neuroendocrine secretion), but for epithelial cells - this is the first time.

Altogether, NALCN-mediated Na^{+} influx is essential for setting up the pacemaking activity of cytosolic Ca^{2+} oscillations required by strongly metastatic cancer cells during disease manifestation. Interestingly, in pacemaker neurons day-night change of NALCN conductance has been linked with its rhythmic translocation driven by ER-residing protein NLF-1 (Flourakis *et al.*, 2015), whereas oscillation of Ca^{2+} signal is defined as intrinsic molecular output of circadian clock. In this regards, our study is in accordance with previous findings pointing on the dysregulated circadian tumour clock that subserves malignancy progression, and thus it provides novel perspectives for the anti-cancer chronotherapeutic strategies.

Supplementary Results

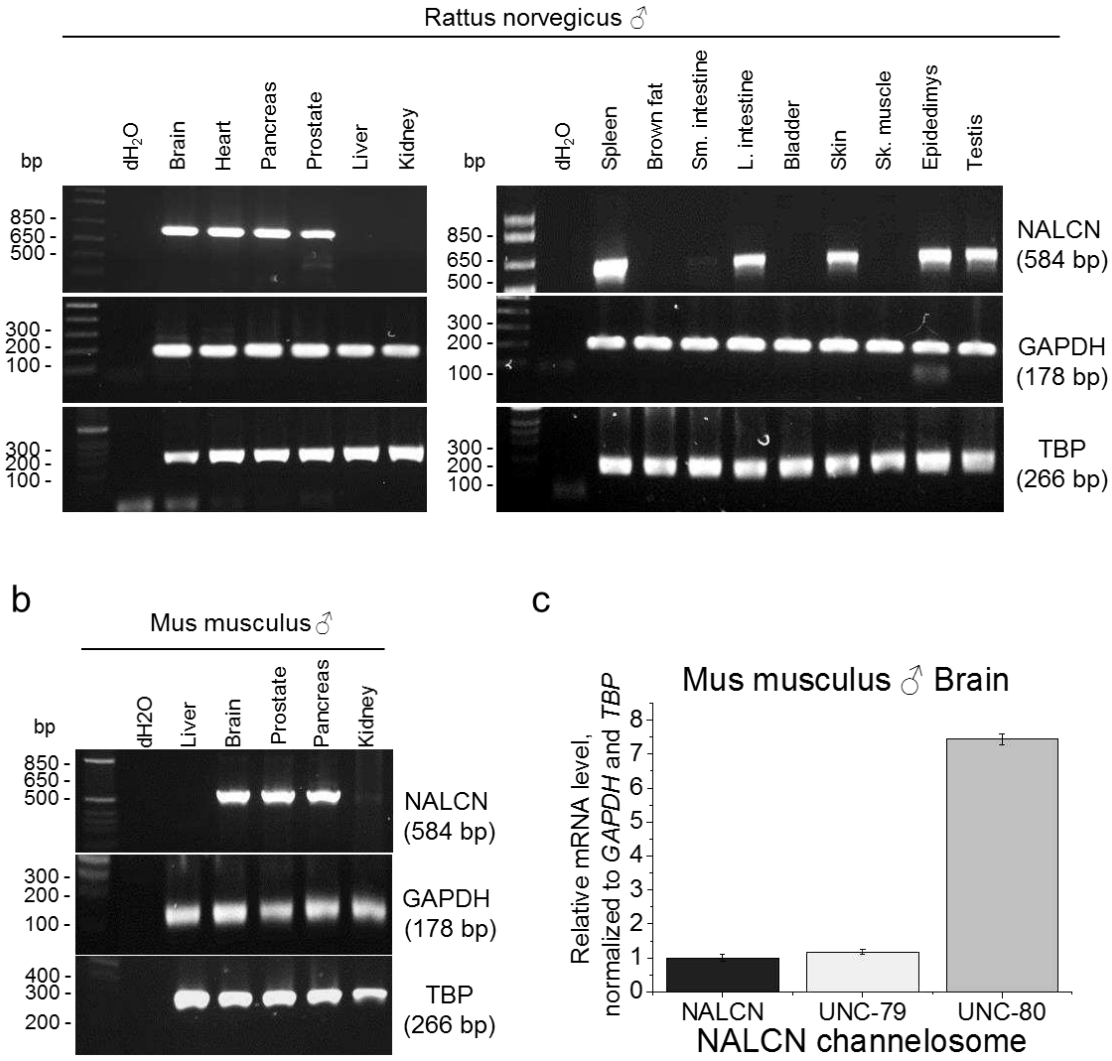

SFigure 1. Screening for *NALCN* in mammalian organs. a, conventional PCR for *NALCN*, *GAPDH* and *TBP* in organs from *Rattus norvegicus* ♂. **b**, conventional PCR for *NALCN*, *GAPDH* and *TBP* in organs from *Mus musculus* ♂. **c**, qRT-PCR for NALCN channelosome genes in brain from *Mus musculus* ♂. Data are normalized to *GAPDH* and *TBP* and are presented as mean values±SEM (n=3).

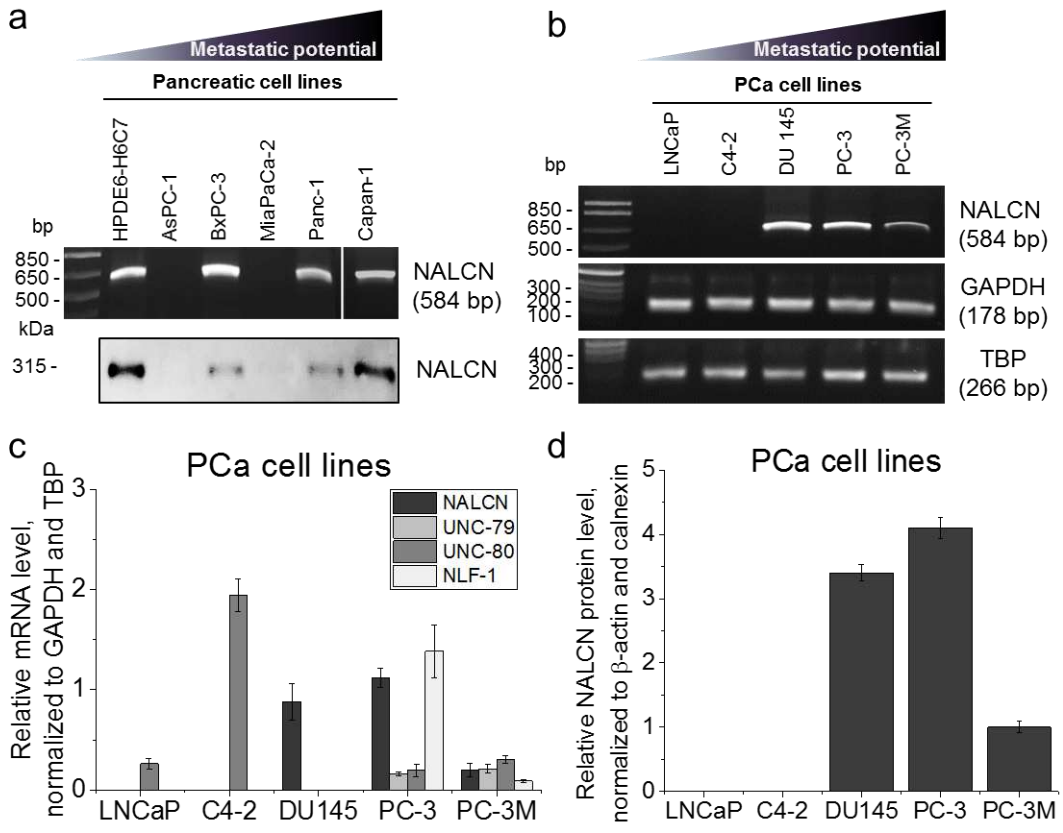

e

Reference	Alternative	Exon	Intron	Position	Aminoacid	DU 145	PC-3	PC-3M
G	A		40/43			0/1	0/1	0/1
G	A	33/44		1238	T	1/1	1/1	1/1
A	G	31/44		1190	L	1/1	1/1	1/1
C	T	31/44		1166	A/T	0/1	-/-	-/-
T	C		27/43			-/-	0/1	-/-
G	T		26/43			1/1	1/1	1/1
C	A	25/44		957	M/I	0/1	-/-	-/-
G	A	20/44		769	H/Y	1/1	-/-	-/-
G	A		18/43			-/-	0/1	0/1
A	G		17/43			1/1	0/1	0/1
G	A	13/44		531	V	-/-	0/1	0/1
ATTATT	A		12/43			-/-	0/1	0/1
T	C		12/43			1/1	0/1	0/1
A	G		12/43			1/1	0/1	0/1

SFigure 2. Screening for *NALCN* channelosome in various human pancreatic and prostate cell lines. a, Screening for *NALCN* mRNA and protein expression in human pancreatic cell lines. **b**, Conventional PCR for *NALCN*, *GAPDH* and *TBP* in human prostate cancer (PCa) cell lines. **c**, QRT-PCR for NALCN channelosome genes in human prostate cancer cell lines. Data are normalized to *GAPDH* and *TBP* and are presented as mean values±SEM (n=5). **d**, NALCN protein level in human prostate cancer cell lines. Data are normalized to β-actin and calnexin and are presented as mean values±SEM (n=3). **e**, Table of genomic mutations corresponding to *NALCN* found in human prostate cancer cell lines endogenously expressing NALCN.

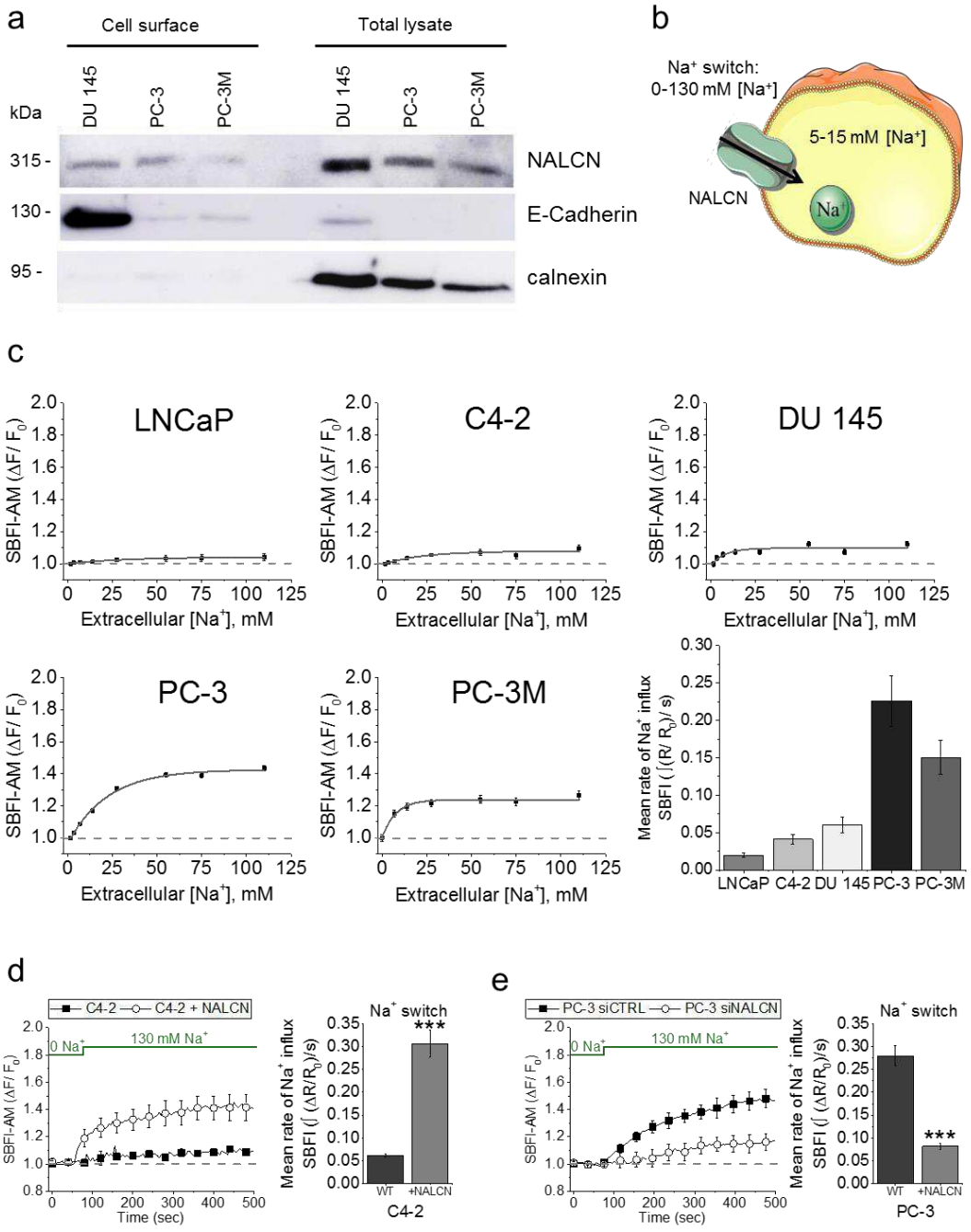

SFigure 3. Evaluation of NALCN channelosome functionality in human prostate cancer cell lines. a, NALCN was found in plasma membrane biotinylated fraction of human prostate cancer cells endogenously expressing the channel. E-Cadherin was used as plasmalemmal marker, whereas ER-residing protein calnexin – as a marker of cytoplasmic fraction. **b**, Illustrative representation of 'Na^+ switch' protocol used to analyse basal Na^+ influx throughout this study. **c**, Background Na^+ influx measured in human prostate cancer cell lines using ratiometric dye SBFI-AM. The bar diagram plots: mean signal temporal densities (n=40-60). **d**, In weakly metastatic C4-2 cells basal Na^+ influx was induced by NALCN overexpression. The bar diagram plots: mean signal temporal densities (n=27-62). **e**, In highly metastatic PC-3 cells transient NALCN silencing (siNALCN) resulted in suppression of basal Na^+ influx. The bar diagram plots: mean signal temporal densities (n=203-241). Data are mean±S.E.M. ***P<0.001.

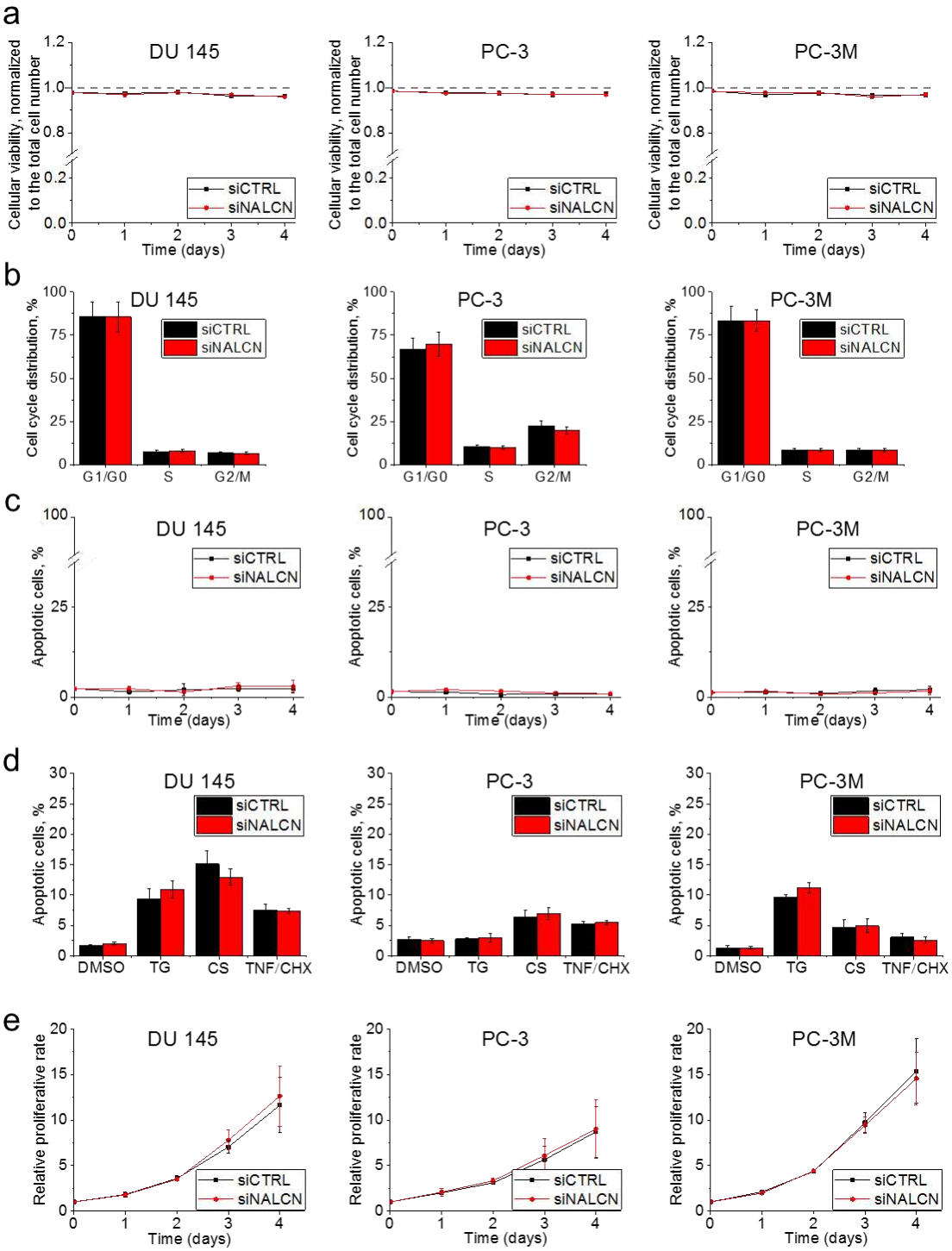

SFigure 4. Effect of NALCN silencing on the cellular growth features of prostate cancer cell lines endogenously expressing the channel. a, Cellular viability assessed by using trypan blue exclusion assay. **b**, Flow cytometry cell cycle analysis using propidium iodide DNA staining. **c**, Basal and **d,** Treatment-induced apoptosis assessed by Hoechst staining. DMSO – 1 µM dimethyl sulfoxide, TG – 1 µM thapsigargin, CS – 1 µM cisplatin, TNF/CHX – 10 ng/ml tumour necrosis factor α in combination with 1 µM cycloheximide. **e**, Cellular proliferation assessed by sulforhodamine B assay. Data are mean±S.E.M (n=3).

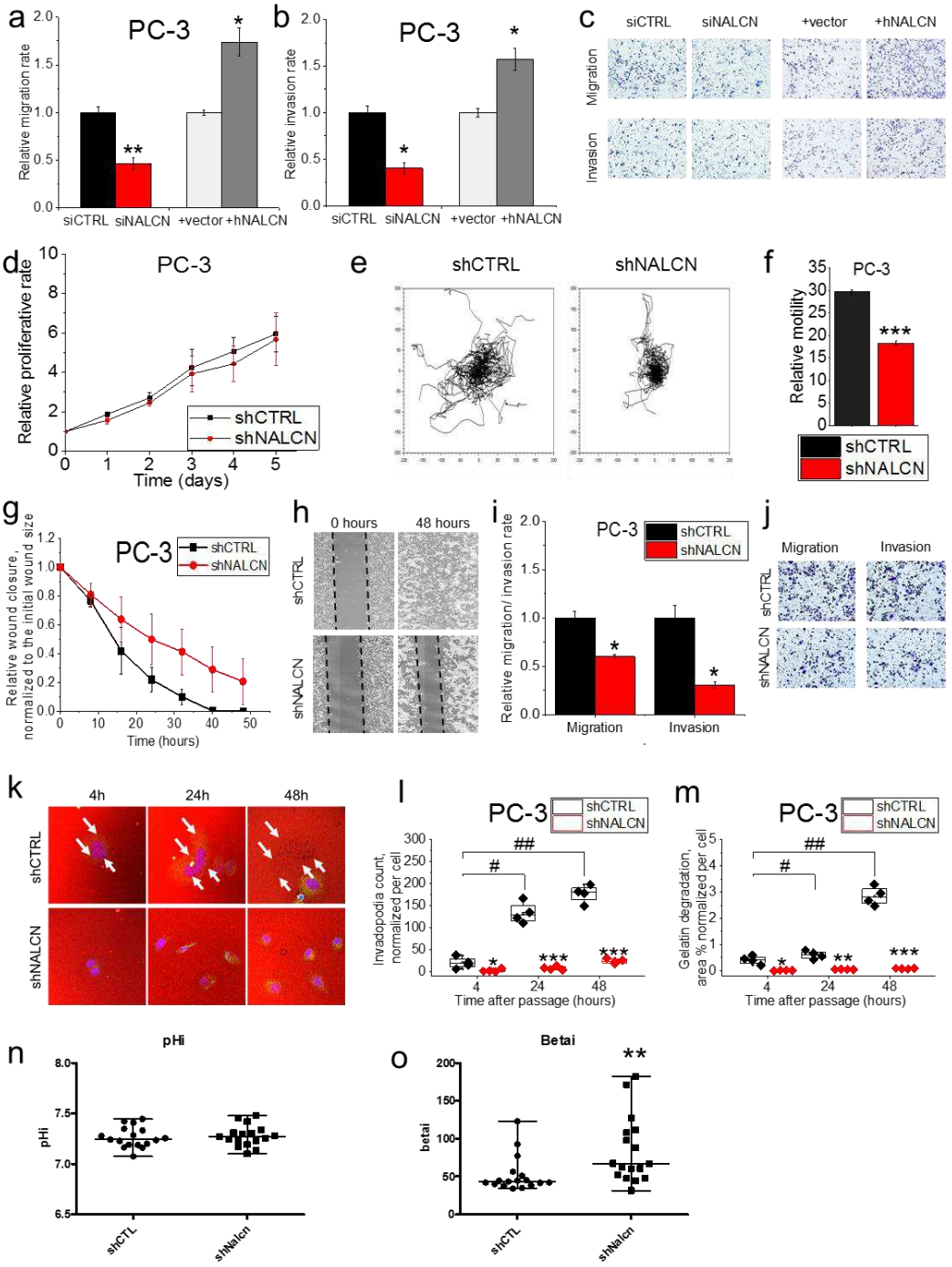

SFigure 5. Role of NALCN in various cancer-associated hallmarks of strongly metastatic PC-3 cells. a, Transwell® migration and **b**, Matrigel invasion assays after transient NALCN suppression and overexpression. Data are presented as mean values mean±S.E.M (n=3). **P*<0.05, ***P*<0.01. **c**, Representative images of boyden chambers analysed for Transwell® migration and Matrigel invasion assays. **d**, Cellular proliferation assessed by sulforhodamine B assay. Data are mean±S.E.M (n=3). **e**, Motility traces of individual control (shCTRL) and NALCN downregulated (shNALCN) cells (*n*=30). **f**, Cellular motility (calculated as μm^2/hour) was remarkably inhibited in NALCN suppressed cells. Data are mean±S.E.M (*n*=838-1629). ****P*<0.001 **g**, Wound-healing is considerably slowed down in NALCN downregulated (shNALCN) cells. Data are mean±S.E.M (n=3). **h**, Representative images of the wound closure process: primary gap at 0 hours and after leaving the cells to migrate for 48 hours. **i**, Transwell® migration and Matrigel invasion assays for control (shCTRL) and cells with stable NALCN downregulation (shNALCN). Data are mean±S.E.M (n=3). **P*<0.05. **k**, Representative images of Cy3-gelatin degradation after cells were plated for 4 hours, 24 hours, and 48 hours. **l**, Invadopodia quantity and **m**, Area of gelatin degradation produced by control (shCTRL) and NALCN knockdown (shNALCN) cells. Data are mean±S.E.M (n=4). **P*<0.05, ***P*<0.01, ****P*<0.001; # *P*<0.05, ## *P*<0.01. **n**, Intracellular pH measured in control (shCTRL) and cells with stable NALCN suppression (shNALCN) (*n*=17). **o**, Intrinsic buffering capacity (β_i, expressed as mM/pH) in control (shCTRL) and cells with stable NALCN suppression (shNALCN) (*n*=17). ***P*<0.01.

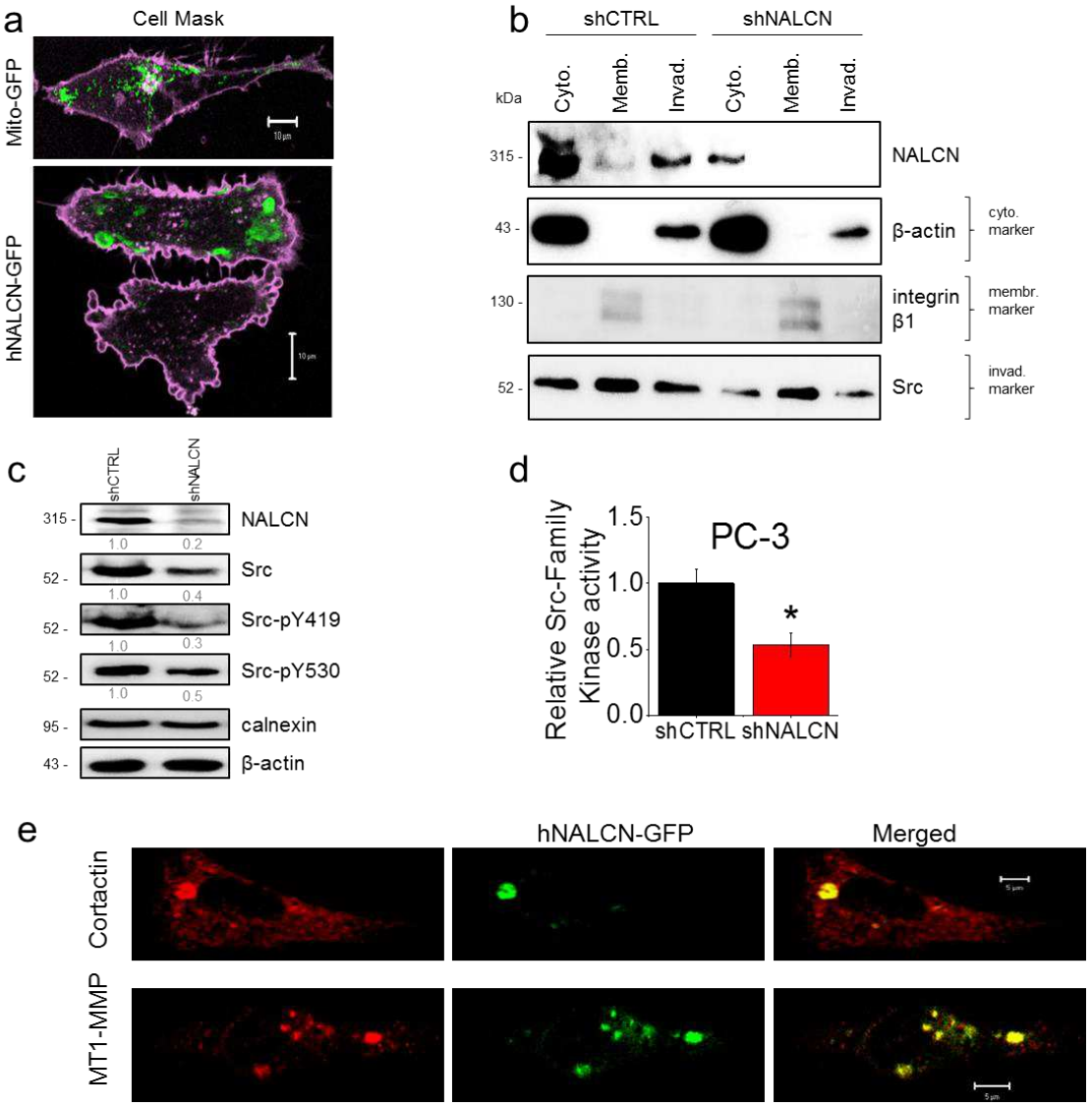

SFigure 6. Role of NALCN in various cancer-associated hallmarks of strongly metastatic PC-3 cells. a, Representative confocal images of PC-3 cells transfected with Mito-GFP and NALCN-GFP plasmids revealing localisation of NALCN-expressing rosettes (GFP, in green) compared to the plasma membrane (Cell mask, in magenta). **b**, Representative immunoblot of NALCN localization in cytoplasmic, membraner and invadopodial fractions of control (shCTRL) and NALCN-downregulated (shNALCN) cells. **c**, Representative immunoblot with band intensities calculated for Src protein level in control (shCTRL) and cells with stable NALCN suppression (shNALCN). Src – total protein level, Src-pY419 – active form of Src, Src-pY530 – nonactive form of Src. **d**, Kinase activity assessed by ProFluor® Src-Family kinase assay. Data are mean±S.E.M (n=3). **P*<0.05. **e**, Representative confocal images of NALCN co-localisation with invadopodia markers: cortactin and MT1-MMP.

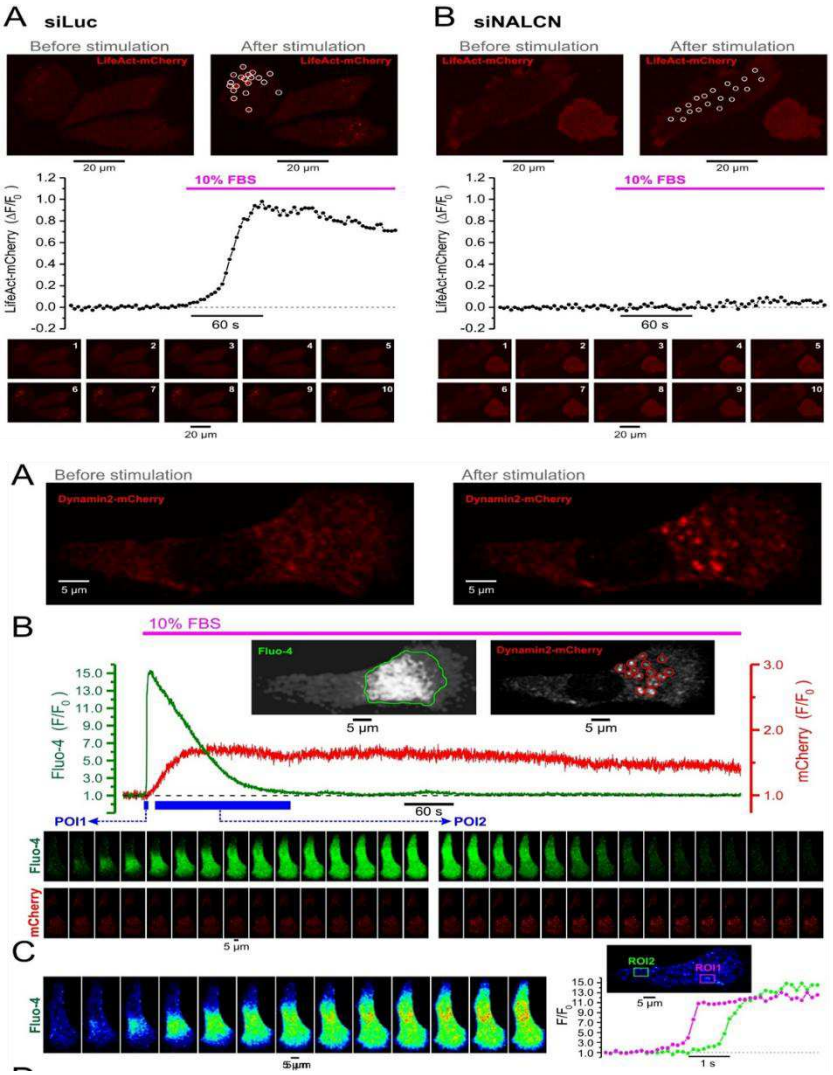

SFigure 7. Spatio-temporal relationship between $[Ca^{2+}]_c$ changes and formation of invadopodia punctae in PC-3 cells.

PC-3 cells expressing LifeAct-mCherry and treated for 48 h with either siLuc (A) or siNALCN (B) were serum starved overnight. Confocal x-y time series imaging (at 0.3 Hz) of mCherry fluorescence from near-cell-bottom optical slice (< 0.6 µm) revealed that stimulation with 10% FBS triggers LifeAct-mCherry puncta formation (A) indicative of invadopodial precursor assembly (Sun *et al.*, 2014). This process was suppressed by siNALCN treatment (B). In A and B, confocal images obtained before and after stimulation (top), the time course of relative changes in mCherry fluorescence intensity (middle; $\Delta F/F_0$) at 19 outlined regions (white circles; top right) and the galleries showing every 10th image during time-series protocol.

A, Fluorescent confocal images of PC-3 cell expressing mCherry-labelled dynamin2 before (left) and 3 min after stimulation with 10% FBS (right). B, Plot (top) shows temporal profiles of self-normalised fluorescence intensity (F/F_0) of fluo-4 (green trace), averaged within outlined region (inset: left, green outline), and mCherry (red trace), averaged within 14 circles (inset: right, red outlines). The galleries (bottom) show confocal images of fluo-4 (top) and mCherry (bottom) fluorescence captured during two periods of interests, POIs (depicted by

blue bars on the plot): POI1 (left gallery: each image) and POI2 (right gallery: every 100th image). Note that increase of the intensity of mCherry fluorescence reflects formation of dynamin puncta. C, The gallery (left) shows rainbow colour-coded images of fluo-4 florescence captured during raising phase of the FBS-induced $[Ca^{2+}]_c$ transient. The plot (right) compares the dynamics of fluo-4 response (F/F0) at the two regions of interest, ROIs: ROI1 – magenta, ROI2 – green (inset: boxed in corresponding colour). Note that the FBS-induced $[Ca^{2+}]_c$ response is initiated at ROI1 and propagates towards ROI2.

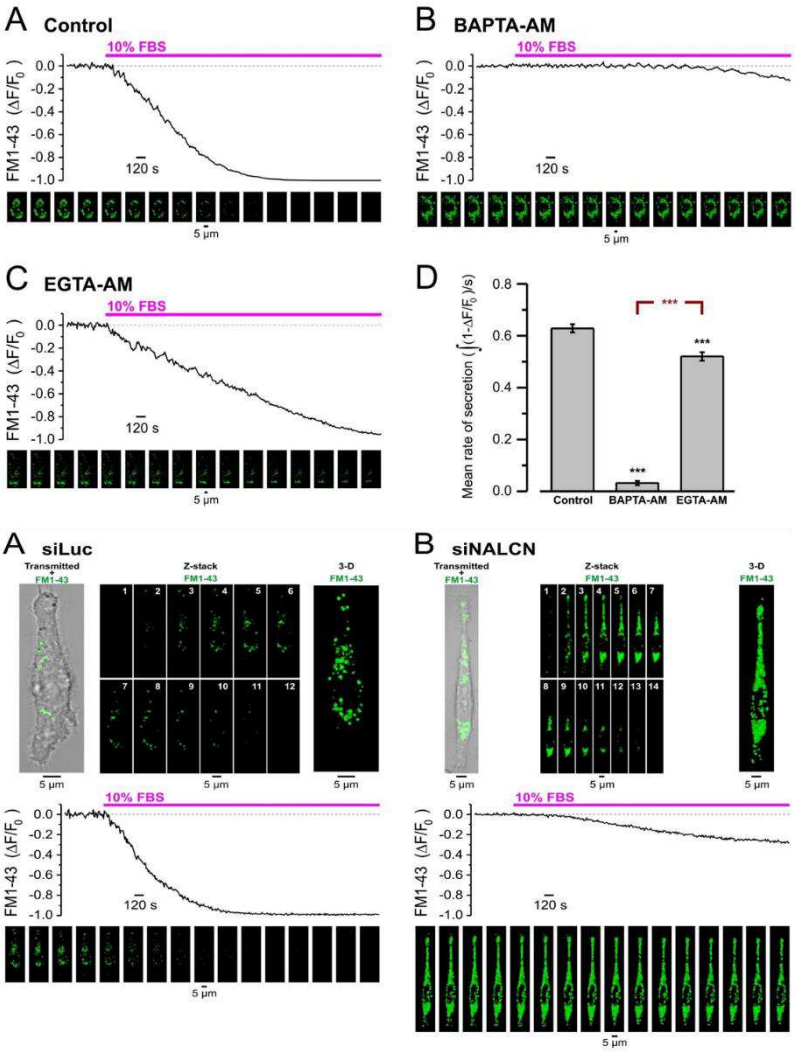

SFigure 8. NALCN facilitates secretion in PC-3 cells.

The secretory vesicles were labelled by 12 h incubation with 5 µM FM1-43 of PC-3 cells. Following FM1-43 washout, the dynamics of secretion induced by 10% FBS was assessed by combining confocal Z-sectioning with time-series imaging of FM1-43 fluorescence: individual Z-stacks were captured 10 s apart. The imaging protocol was performed on the cells untreated with Ca^{2+}-helating agent (A), cells pre-incubated with fast Ca^{2+}-helating agent, 50 µM BAPTA-AM (B) or slow Ca^{2+}-helating agent, 50 µM EGTA-AM (C). Panels A - C show: the plot of relative change in total Z-stack fluorescence ($\Delta F/F_0$) over time (top) and the galleries of corresponding 3-D images (bottom): every 25th image is shown. D, The mean rate of secretion was calculated as signal mass (integrated relative decrease in FM1-43 fluorescence ($\int(1 - \Delta F/F_0)/s$) and compared for untreated (n=45) and BAPTA-AM (n=62) or EGTA-AM (n=35) – treated cells. ***P<0.001. Note that significant difference in the effect of BAPTA-AM and EGTA-AM suggests regulation of secretion by Ca^{2+} influx within functional micro-domains. The secretory vesicles were labelled by 12 h incubation with 5 µM FM1-43 of PC-3 cells pre-treated with either siLuc (A) or siNALCN (B). Following FM1-43 washout, the dynamics of secretion induced by 10% FBS was assessed by combining confocal Z-sectioning with time-series imaging of FM1-43 fluorescence: individual Z-stacks were captured 10 s apart. Panels A and B show: the overlay of transmitted-light and confocal image of FM1-43 fluorescence from single cell (top left), confocal images from individual Z-stack (top middle) and corresponding reconstructed 3-D image (top right), the plot of relative change in total Z-

stack fluorescence ($\Delta F/F_0$) over time (middle) and the galleries of corresponding 3-D images (bottom): every 25th image is shown. C, The mean rate of secretion was calculated as signal mass (integrated relative decrease in FM1-43 fluorescence ($\int(1 - \Delta F/F_0)/s$) (left) and compared for siLuc (n=35) and siNALCN (n=40) -treated cells (right). ***P<0.001.

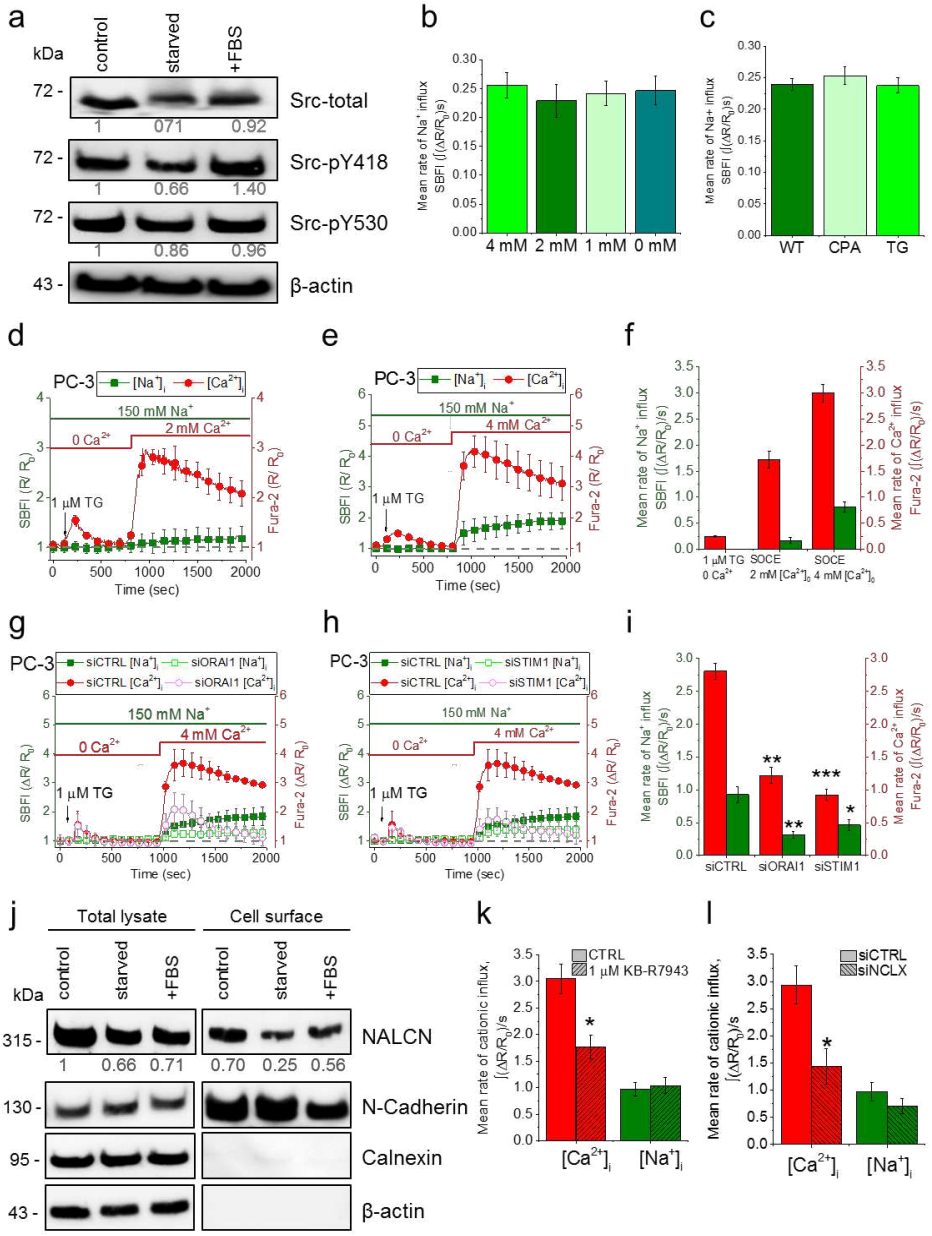

SFigure 9. Interplay between SOCE and NALCN in PC3 cells. a, Representative immunoblot with band intensities calculated for Src protein level in control, starved cells and FBS-stimulated cells after starvation (+FBS). **b**, **c**, Mean rate of Na^+ influx calculated as SBFI-AM signal mass ($\int(\Delta R/R_0)/s$) during different $[Ca^{2+}]_e$ (**b**) and after ER depletion with 50 μM cyclopiazonic acid (CPA) and 1 μM thapsigargin (TG) (**c**). Data are presented as mean values±SEM (*n*=45-360). **d**, **e**, SOCE-induced changes of $[Na^+]_c$ (SBFI) and $[Ca^{2+}]_c$ (Fura-2) using 2 mM $[Ca^{2+}]_e$ (**d**) and 4 mM $[Ca^{2+}]_e$ (e). **f**, Mean rate of Na^+ (SBFI) and Ca^{2+} (Fura-2) influx calculated as signal mass ($\int(\Delta R/R0)/s$) during different SOCE components. Data are presented as mean values±SEM (*n*=283-360). **g**, **h**, SOCE-induced changes of $[Na^+]_c$ (SBFI) and $[Ca^{2+}]_c$ (Fura-2) in control (siCTRL) and after silencing of ORAI1 (siORAI1) (**g**) and STIM1 (siSTIM1) (**h**). **i**, Mean rate of Na^+ (SBFI) and Ca^{2+} (Fura-2) influx calculated as signal mass ($\int(\Delta R/R0)/s$) after silencing of major SOCE players. Data are presented as mean values±SEM (*n*=109-182). **P*<0.05, ***P*<0.01, ****P*<0.001. **j**, Representative immunoblot

with band intensities calculated for NALCN protein level in total cell lysate and biotinylated plasma membrane fraction in control, starved cells and FBS-stimulated cells after starvation (+FBS). N-Cadherin was used as plasmalemmal marker, whereas ER-residing protein calnexin and cytoskeletal β-actin – as markers of cytoplasmic fraction. **k**, **l**, Mean rate of Na^+ (SBFI) and Ca^{2+} (Fura-2) influx calculated as signal mass ($\int(\Delta R/R0)/s$) after pharmacological inhibition of NCX-reverse mode (1 μM KB-R7943) (**k**) and mitochondrial NCLX silencing (siNCLX) (**l**). Data are presented as mean values±SEM (*n*=134-289). **P*<0.05.

SFigure 10. Data are not available yet.

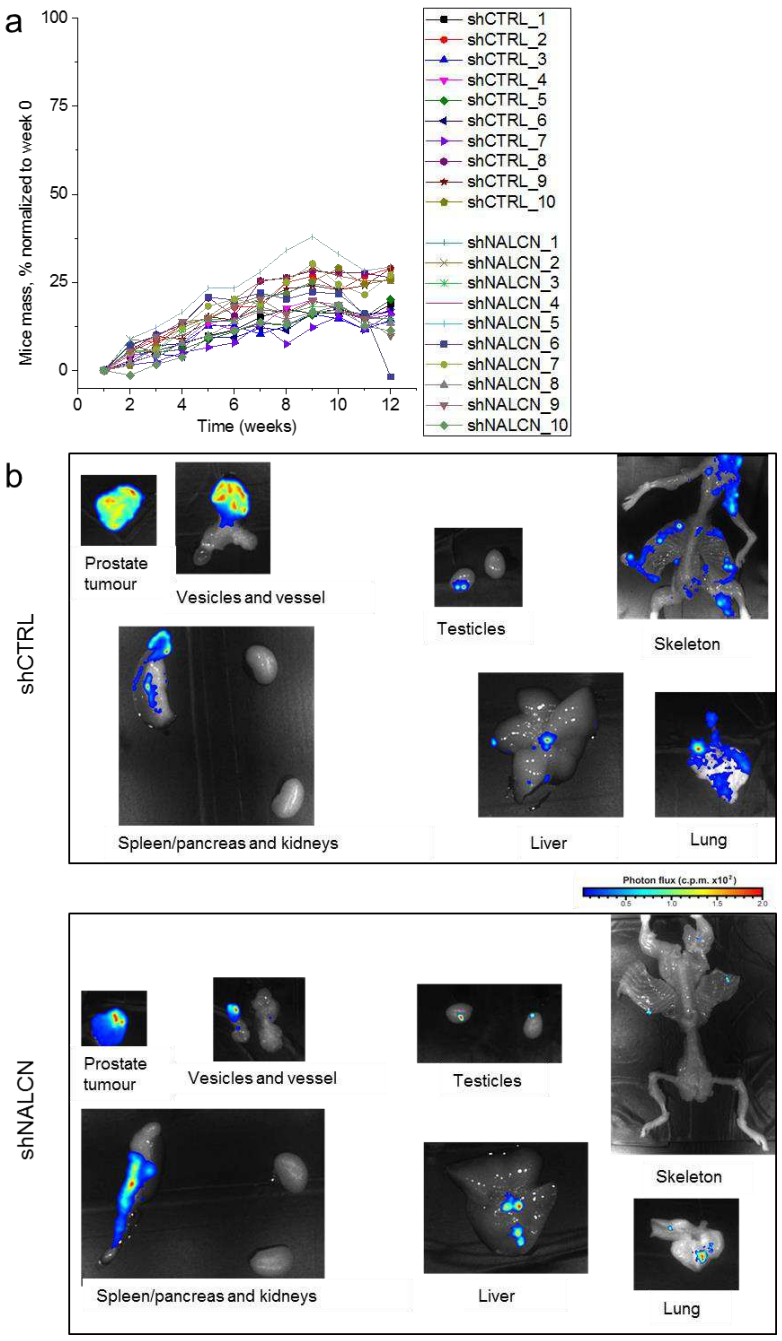

SFigure 11. *In vivo* and *ex vivo* analysis of NALCN tumourigenesis. a, The mass of mice assessed after orthotopic injections of control (shCTRL) and stable NALCN-knockdown (shNALCN) PC-3 cells (n=10). **b**, Representative images of e*x vivo* bioluminescence analysis analysis of various organs with metastatic spread.

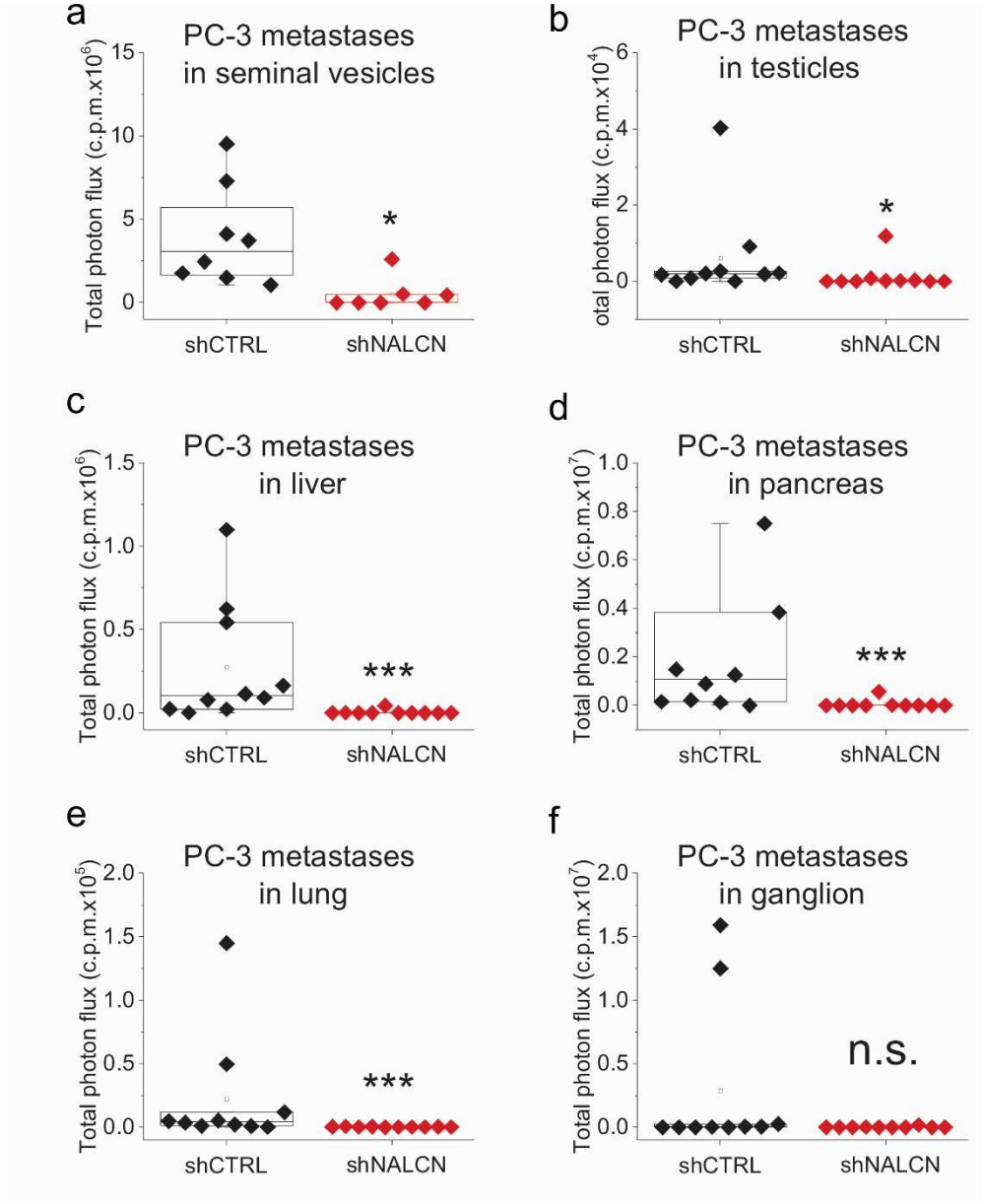

SFigure 12. ***Ex vivo*** **analysis of metastatic spread.** Bioluminescence analysis in mice organs 12 weeks after orthotropic injections of PC-3-Luc-shCTL or PC-3-Luc-shNALCN cells. Counts per minute (c.p.m.) in **a**, seminal vesicles; **b**, testicles; **c**, liver; **d**, pancreas; **e**, lung; **f**, ganglion.

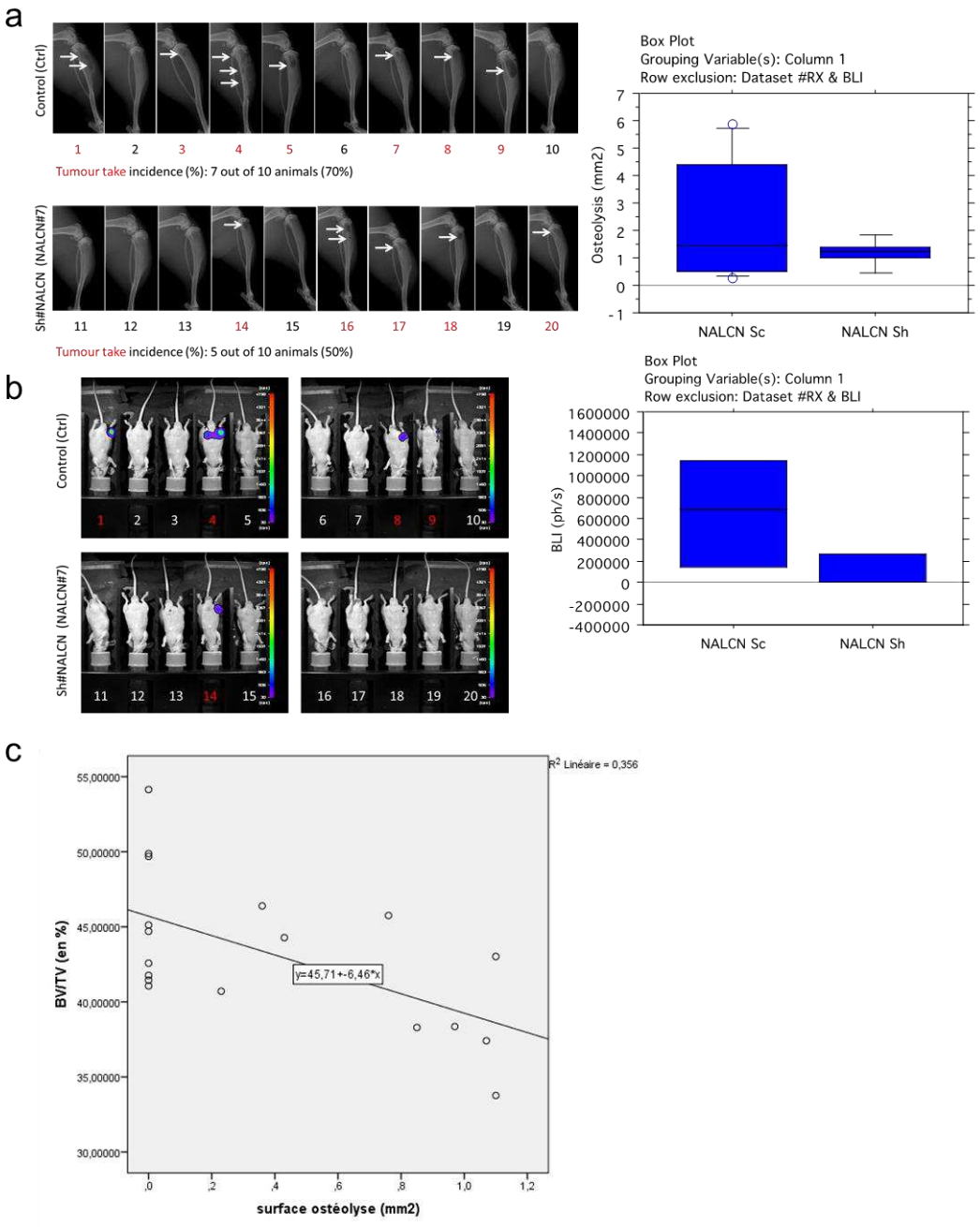

SFigure 13. Analysis of bone tissue desctruction. a, X-ray images: osteolysis (arrow) 31 days after intra-tibial injection of PC-3-Luc-shCTL or PC-3-Luc-shNALCN cells with corresponding area of osteolysis (mm^2). Data are mean±S.E.M. **b**, Bioluminescence of mice 31 days after intra-tibial injection of PC-3-Luc-shCTL or PC-3-Luc-shNALCN cells with corresponding signal analysis (photons/s). Data are mean±S.E.M. **c**, Correlation between osteolysis surface (mm^2) and bone volume/total volume (BV/TV, %). *P* =0,009.

Materials and Methods

1. Study approval

Mice for orthotopic injections of prostate cancer cells were bred and housed at the In Vivo platform of the Cancerop$\hat{o}$le Grand Ouest at Animalerie UTE- IRS1 (Nantes, France) under the animal care license no. C44278. The project was approved by the French national ethical committee (APAFIS #2837-2015112314119496v2).

PTEN null mice were approved by the Institutional Animal Care and Use Committee of the Emory University (Atlanta, GA), which is accredited by the American Association for the Accreditation of Laboratory Animal Care.

Mice for bone metastasis were purchased from Charles River and handled according to the French Ministerial Decree No.87-848 of 19 October 1987. Experimental protocols were approved by the Institutional Animal Care and Use Committee at the Université Lyon-1 (France) (CEEA-55 Comité d'Ethique en Expérimentation Animale DR2014- 32).

2. Cell culture

In this study, human prostate cancer cell lines of epithelial origin have been used. LNCaP, DU 145 and PC-3 have been purchased from the American Type Culture Collection (ATCC®), whereas – C4-2 and PC-3M have been kindly provided by Dr Florence Cabon (Cancer Research Centre of Toulose, France) and Prof. Mustafa Djamgoz (Imperial College London, UK), respectively. These cancer cell lines derive from various metastatic sites and are relatively classified by their tumorigenic potential as follows: LNCaP – issue from lymph node, weakly metastatic (Horoszewicz, et al. 1980); C4-2 – derived from a chimeric tumour induced by co-inoculating castrated mouse with LNCaP-derived subline and bone fibroblasts, weakly metastatic (Wu, et al. 1994); DU 145 – issue from brain, moderately metastatic (Stone, et al.

1978); PC-3 – issue from bone, highly metastatic (Kaighn, et al. 1979); and PC-3M – derived from liver metastases induced by inoculating mouse with PC-3, highly metastatic (Kozlowski, et al. 1984). Cells were routinely cultured at 37ºC in a humidified atmosphere with 5% CO_2 in RPMI 1640 medium (Gibco™, Thermo Fischer Scientific) containing a final concentration of 10% fetal bovine serum (Gibco™) and 2 mM L-Glutamine (Gibco™). Mouse-derived osteoblast precursor cell line MC3T3 E1 was cultured in MEMα medium (Gibco™) containing 10% fetal bovine serum and 1% Penicillin-Streptomycin (Gibco™). Twice a week, cultures were split by treatment with 0.25% trypsin-EDTA (Gibco™, Thermo Fischer Scientific) for 5 min at 37ºC. All cells used in this study were validated as being mycoplasma free by using Hoechst staining.

3. Plasmids

The plasmids were provided by Dr Arnaud Monteil (IGF, Montpellier, France) and listed in the Table S1.

4. Cell transfection

Cells were transfected with 2 µg of each construct or 50 nM of siRNA and 0.2 µg of pmax GFP using either Nucleofector (Amaxa), X-tremeGene 9 DNA Transfection Reagent (Roche) and HiPerFect Transfection Reagent (QIAGEN). Control experiments were performed by transfecting the empty vector or siRNA against Luciferase. Experiments were conducted 3 days after transfection. For establishment of stable cell lines, 700 µg/ml G418 and 2 µg/ml puromycin were used. All siRNAs and shRNAs used in this study listed in the Table S2.

5. Buffers and standard solutions

Most chemicals were purchased from Invitrogen Life Technologies and Sigma Aldrich Chemicals unless stated otherwise. If needed, pH of solutions has been adjusted using

combined pH electrode InLab® Flex-Micro (Mettler Toledo). The media and other necessary materials were sterilized by autoclaving at 120ºC. Thermally-labile chemicals were filter-sterilized with 0.2 μm pore polyethersulfone Acrodisc® Supor® membrane filters (514-4126, VWR).

6. RNA purification, quantitative real-time RT-PCR

Organ tissues and cells were preserved in RNAlater™ (Sigma). Cellular RNA was purified with the NucleoSpin RNA Plus Kit (Macherey-Nagel). Organ tissues were homogenized with Precellys® Tissue Homogenizer and purified with TRIzol™ Reagent (Invitrogen). The generation of cDNA from RNA was performed with reverse transcription (Applied Biosystems) following the DNase treatment (Ambion). Conventional PCR was performed by using AmpliTaq Gold® (Applied Biosystems) on C1000 Touch™ Thermal Cycler (Bio-Rad), whereas quantitative - with SsoFast™ EvaGreen® (Bio-Rad) on CFX96 Touch™ Real-Time PCR Detection System. Primers used in this study are listed in the Table S3.

7. Immunoblotting

Organ tissues were homogenized with Precellys® Tissue Homogenizer. The cells were lysed in 1xRIPA buffer with protease and phosphatase inhibitors, sonicated for 10 seconds at 30% intensity and centrifuged at 13000 g for 10 minutes in order to eliminate the nuclei fraction. The concentration of protein lysate was measured with Pierce® BCA Protein Assay (Thermo Fisher Scientific). 1xSample Reducing Agent and 1xLDS Sample Buffer (Bolt™, Thermo Fisher Scientific) were added to 50 μg of protein lysate and heated at 95^0C for 5 minutes. Proteins were resolved due to 3-8% Tris-acetate SDS-PAGE and transferred onto methanol-activated PVDF membrane with Pierce G2 Fast Blotter (Thermo Fisher Scientific). Afterwards, the blots were blocked with 5% milk TBS-T buffer (15 mM Tris-HCl, 140 mM NaCl, 0.05% Tween20®, pH 7.4) for 1 hour, and then incubated with antibodies. For HRP-conjugated

secondary antibodies blots were developed using SuperSignal™ West Dura Extended Duration Substrate (Thermo Fisher Scientific), and images were captured with Amersham Imager 600 (GE Healthcare Life Sciences). The antibodies used in this study listed in Table S4. Data was analysed with ImageJ software.

8. Cell cycle analysis

For cell cycle analysis, cells were fixed with ice-cold 70 % methanol for 30 minutes, resuspended in 100 µl PBS with 500 µg/ml Ribonuclease A, and stained with 50 µg/ml of propidium iodide for 1 hour at 4^0C. At least 10,000 events per condition were processed by CyAn™ ADP Analyser FACScan flow cytometer (Becton-Dickinson).

9. Cellular viability

Cellular viability was evaluated with Trypan Blue Exclusion assay (Thermo Fisher Scientific).

10. Apoptosis assay

The level of apoptosis was estimated from the number of apoptotic nuclei revealed by Hoechst staining.

11. Proliferation assay

Cells were plated into 96-well plate at 1 x 10^3 cells/well and left overnight at standard growth conditions. At each desired time point, cells were fixed with 50 % Trichloroacetic acid at 4^0C for 1 hour. After removing fixative solution, cells were stained with 0.4 % Sulforhodamine B (Santa Cruz) in 1 % acetic acid. Afterwards, dye up taken by the cells was completely dissolved in 10 mM Tris-base, pH 10.5. The absorbance was measured at 560 nm with TriStar^2 Multimodal Reader LB942 (Berthold Technologies). Blank was considered as well without cells and substituted from each data point during analysis.

12. Time-lapse video microscopy

Cells were seeded at low density, stained with Hoechst and kept at 37°C under 5% CO2 in an incubator chamber for time-lapse video recording. Cell movements were monitored with an inverted microscope (Biostation; Nikon) using a 20× objective lens. To ensure long distance measurement, images mosaic (4 by 4 for tracking, and 8 by 3 for wound healing) were acquired and reconstructed as a single high resolution, high field of view image using FiJi (Schindelin 2012 Nature Methods) Grid/Collection Stitching Plugin.

13. Cellular motility

Images were acquired every 30 minutes for a time lapse of 48 hours. Image stacks were analyzed using trackmate imageJ plugin on se reconstructed mosaic image (Tinevez 2016 Methods). For each condition, segmentation was performed on Hoechst stained nucleus. The same optimized tracking parameters were used for each image series. Cells were then automatically tracked using the “simple lap tracker” algorithm and, tracks coordinates and individual tracks mean velocity were measured for each cells. Only cells tracked over a period of more than 5 hours were taken into account and at least 1000 cells tracks were analyzed per condition.

14. Wound-healing assay

The wound-healing assay was performed in Culture-Insert 2 Well in μ-Dish 35 mm high, IbiTreat (Ibidi) according to the manufacturer’s instructions. Images of the wound area were acquired every 30 minutes for a time lapse of 48 hours. Homemade plugin based on (James 2014 Cell Adhesion and Migration) recommendations was developed for ImageJ to automatically detect cells and wound areas.

15. Transwell® migration and invasion assay

Cells at 75 x 10^3 were plated into upper compartment of 8 µm pore Transwell® inserts (Falcon™) in a serum-free media, whereas lower compartment was filled with standard growth media, as a chemoattractant. For invasion assay inserts were pre-coated with 1.25 mg/ml Matrigel™ Basement Membrane Matrix (Becton Dickinson). After 16 hours at 37^0C, 5 % CO_2 cells were fixed in ice-cold 100% methanol and stained with 1% crystal-violet in 25 % methanol. Inserts were washed and the upper area of the filter was rubbed dry to eliminate the non-migrated cells. The data was obtained after counting five random fields of view under an inverted microscope DMIRE2 (Leica) at ×5 magnification. At least two inserts for each condition were analysed in each independent experiment.

16. Electrophysiological recordings

Sodium currents were recorded in perforated patches made to PC-3 cells at room temperature. Cell-attached patches were formed on control PC-3 cells as well as shScramle or shNALCN PC-3 cells lines, additionally treated with the corresponding siRNA as described above. The gramicidin-containing perforated patch pipette solution contained (in mM) 150 KCl, 1 MgCl2 and 10 HEPES and the extracellular solution contained 140 NaCl, 5 KCl, 1 MgCl2, 2 CaCl2, 5 glucose and 10 Hepes (adjusted to pH 7.3 with KOH or NaOH). Gramicidin was first dissolved in DMSO to a concentration of 50 mg/ml and then diluted in the pipette solution, followed by vortexing at maximal speed and brief sonication, to a final concentration of 100 µg/ml immediately before use. Patch pipettes were made from borosilicate glass capillaries (WPI). The resistance of the pipettes varied between 2 and 4 MΩ. The currents were acquired using an Axopatch 200B amplifier (Molecular Devices), and analyzed offline using pClamp (Molecular Devices) and Origin software (OriginLab Corporation).

17. Calcium and sodium imaging

The Hank's balanced salt solution (HBSS) comprised as follows (in mM): NaCl 150, KCl 5, $MgCl_2$ 1, $CaCl_2$ 2, D-Glucose 10, and HEPES 10, adjusted to pH 7.4 with 1 M NaOH. Na^+-free solution contained the following components (in mM): choline chloride 150, $MgCl_2$ 1, KCl 5, $CaCl_2$ 2, D-Glucose 5.6, and HEPES 10, adjusted to pH 7.4 with 1 M KOH. Extracellular solution with high Na^+ concentration consisted of (in mM): NaCl 150, KCl 5, $MgCl_2$ 1, $CaCl_2$ 2, D-Glucose 5.6, and HEPES 10, adjusted to pH 7.4 with 1 M NaOH. Ca^{2+}-free solution contained the following components (in mM): EGTA-NMDG 5, NaCl 150, $MgCl_2$ 3, KCl 5, D-Glucose 5.6, and HEPES 10, adjusted to pH 7.4 with 1 M NaOH. Extracellular solution with high Ca^{2+} concentration consisted of (in mM): NaCl 150, KCl 5, $CaCl_2$ 8, D-Glucose 5.6, and HEPES 10, adjusted to pH 7.4 with 1 M NaOH.

Cytosolic Ca^{2+} concentrations were measured using the ratiometric dye Fura-2-acetoxymethyl ester (AM) (Interchim), whereas cytosolic Na^+ concentrations – with SBFI-AM (Interchim) as previously described in Iamshanova et al. 2016. Dyes were reconstituted in dimethyl sulfoxide (DMSO) and diluted in HBSS containing 0.02 % of Pluronic® F127 to the final concentrations of 1 μM for Fura-2 and 7 μM for SBFI. Fluorescence was excited using an illumination DG4 system (Sutter) fitted with a xenon lamp (300 W). All recordings of Na^+ fluorescence were acquired using objective 20× in the Superfluor Nikon Eclipse Ti- series inverted microscope coupled to an EMCCD camera Rolera EM-C2 (Qimaging) and processed using Metafluor 7.7.5.0 software (Molecular Devices). The excitation filters represented the following parameters in terms of wavelength and bandwidth: 340 nm/26 nm and 387 nm/11 nm. The emission filters were as follows: 510 nm/84 nm for SBFI.

For the confocal Ca^{2+} imaging, cells were loaded using 5 μM Fluo-4-AM as described previously (Povstyan et al., 2011; Shapovalov et al., 2013a; Dubois Cancer Cell). In brief,

experimental chambers containing the cells were placed on the stage of an Axiovert 200M inverted microscope attached to an LSM 510 META laser-scanning unit (Carl Zeiss). x-y confocal images of Fluo-4 fluorescence were acquired at 0.6 Hz using a Plan-Apochromat 40× 1.3 NA objective lens (Carl Zeiss). Fluo-4 fluorescence was excited by the 488 nm line of a 500 mW argon ion laser (Laser-Fertigung) and was captured at wavelengths 505 nm. The illumination intensity was attenuated to 0.6% with an acousto-optical tunable filter (Carl Zeiss). In all experiments, the photomultiplier gain was set at 688. To optimize signal quality, the pinhole was set to provide a confocal optical section <4 μm.

18. Biotinylation

Protein extraction from cell surface fraction was performed with EZ-Link™ Sulfo-NHS-LC-LC-Biotin (Thermo Fisher Scientific).

19. Invadopodia fractionation

Protein extraction from invadopodia fraction was performed as described earlier in Busco et al. 2010.

20. Src kinase activity assay

After extraction of proteins (as described above) without proteinase and phosphatase inhibitors the Src activity was evaluated with ProFluor® Src-Family Kinase Assay (Promega).

21. Secretion assay

The vesical secretion was measured with FM® 1-43 dye (Thermo Fisher Scientific).

22. Zymography

Zymography was performed with 1 % gelatin 10% SDS-PAGE. The protein samples were extracted (as described above) without addition of reducing agents and boiling. The zymogram

were developed with 0.5 % Coomassie G-250 in 30 % ethanol, 10 % acetic acid. Data was analysed with ImageJ software.

23. Patients and tissue biopsies

Normal prostate tissues (n=58) was obtained from patients treated by cystoprostatectomy for bladder carcinoma, without incidental prostate cancer.

Hormone naïve clinically localized cancer samples (HNCLC) (n=338), were obtained from patients treated by radical prostatectomy for localized PCa.

Forty-eight cases of castration resistant prostate cancers (CRPC) were selected from patients treated with exclusive androgen deprivation therapy (ADT). Tissues were collected by transurethral resection, performed because of lower urinary tract symptoms associated with local tumor progression.

Twenty one cases of metastatic prostate cancer were selected from patients with tissues available for analysis, either lymph nodes (n=14) or bone (n=7). Among these patients, 5 had been previously treated by hormone deprivation (all with bone metastasis) and were castration resistant.

Written informed consents were obtained from patients in accordance with the requirements of the medical ethic committee.

24. Immuno-histochemical analysis

TMA Construction: TMAs were constructed using formalin-fixed paraffin-embedded tissue samples. Original slides stained with hematoxylin-eosin were reviewed using the 2009 TNM classification and the 2014 modified “Gleason” system. For each case, 3 cores 0.6 diameter were transferred from the selected areas to the recipient block, using a TMA workstation

(Manual Tissue Arrayer MTA Booster, Alphelys, France). Serial 3 µm sections of the TMA blocks were used for immunohistochemistry. One section on ten was stained with hematoxylin-eosin to check that the cores adequately represented diagnostic areas.

Immunohistochemistry: Slides were deparaffinized, rehydrated, and heated in citrate buffer pH 6 for antigenic retrieval. After blocking for endogenous peroxidase with 3% hydrogen peroxide, the primary antibodies were incubated. The panel of primary antibodies included NLACN (Eurogentec, dilution 1/300, 1 hour), Src (Abcam, ab109381, dilution 1/500, 1 hour), TRPC1 (Novus Biological, NB 110-74946, dilution 1/4000, 1 hour), Stim1 (BD BioScience 710954, dilution 1/1000, 1 hour), Stim2 (Sigma, S85-72, dilution 1/2000, 1 hour), Orai1 (Lifespan, LS-C94375, dilution 1/4000, 1 hour), SK3 (Sigma, WPA 017990, , dilution 1/300, 1 hour), and the proliferation marker Ki67 (DakoCytomation, dilution 1/50, 30 min). Immunohistochemistry was performed using the streptavidin-biotin-peroxydase method with diaminobenzidine as the chromogen (Kit LSAB, Dakocytomation, Glostrup, Denmark). Slides were finally counterstained with haematoxylin. Negative controls were obtained after omission of the primary antibody or incubation with an irrelevant antibody.

Scoring of antibody staining: Staining for Nalcn, src, TRPC1, ORAI1, Stim1, Stim2 and SK3 was scored as follows: -, no stained cells; +, low intensity; ++, high intensity. Ki67 positive cells were expressed as a percentage of total epithelial cells.

Statistical analyses were carried out with StatView, version 5.0, software (Abacus Concepts, Berkeley, CA). Comparison between groups was performed using the $\chi 2$ test for categorical data and nonparametric Mann-Whitney U test and Kruskal-Wallis tests for continuous data.

25. In vivo xenografts

While under isoflurane anaesthesia, six-week-old male NMRI Nude Mice (Charles River Laboratories) were injected into the prostate gland with two PC-3 Luc cell lines (shCTRL 10 mice, shNALCN 10 mice) suspended in 50µl PBS. Photons emitted by cancer cells were counted by bioluminescent imaging (FimagerTM; BIOSPACE Lab) and expressed in counts per minute (c.p.m.). Tumour growth was monitored by bioluminescence imaging. Animal weight was measured every week. At necropsy, ex vivo BLI measurement for each collected organ was performed within 10 min of D-luciferin intraperitoneal injection (150 mg/kg). Mice were euthanized 12 weeks following implantation of tumour cells and metastatic bioluminescence was measured.

Data were compared using either a 2-tailed Student's t test corrected for multiple comparisons by a Bonferroni adjustment or repeated measures 2-way ANOVA, as indicated. Where necessary, the Shapiro–Wilk test was used to test for normality of the underlying sample distribution. Experimental sample sizes were chosen using power calculations with preliminary experiments or were based on previous experience of variability in similar experiments. Samples that had undergone technical failure during processing were excluded from analyses. The Kolmogorov–Smirnov test was used to evaluate the significance between different distributions. For adoptive transfer experiments, recipient mice were randomized prior to cell transfer. The products of perpendicular tumor diameters were plotted as the mean ± SEM for each data point, and tumor treatment graphs were compared by using the Wilcoxon rank sum test and analysis of animal survival assessed using a log-rank test. In all cases, P values of less than 0.05 were considered significant. Statistics were calculated using GraphPad Prism 7 software (GraphPad Software Inc.).

SCID male mice, 6 weeks of age, were housed in barrier conditions under isolated laminar flow hoods. Mice bearing tumour xenografts were closely monitored for established signs of distress and discomfort and were humanely euthanized. PC-3 cells induce osteolytic lesions, PC-3 cells induce mixed lesions with lytic and osteoblastic regions in the bone marrow cavity (Fradet PLos One 2013). Intra-osseous tumour xenograft experiments were performed as previously described (Fradet PLos One 2013): two PC-3 Luc cell lines (shCTRL 10 mice, shNALCN 10 mice) were suspended as 6 x 10^5 in 15µL PBS and injected in the bone marrow cavity (Fradet PLos One 2013). Mice were sacrificed after 31 days. Radiographs (LifeRay HM Plus, Ferrania) of animals were taken at that time after inoculation using X-ray (MX-20; Faxitron X-ray Corporation). Animals were sacrificed, hind limbs were collected for histology and histomorphometrics analyses. The bone lesion surface, that includes lytic and osteoblastic regions, was measured using the computerized image analysis system MorphoExpert (Exploranova). The extent of bone lesions for each animal was expressed in mm^2. Tibiae were scanned using microcomputed tomography (Skyscan1174, Skyscan) with an 8.1 µM voxel size and an X-ray tube (50 kV; 80 µA) with 0.5 µm aluminum filter. Three-dimensional reconstructions and rendering were performed using the manufacturer's suite (Respectively, NRecon&CTVox, and Skyscan). Bone Volume/Tissue Volume: (%BV/TV) includes residual trabecular and remaining cortical bone. Dissected bones were then processed for histological and histomorphometric analysis (as described in Fradet Cancer Res 2011). Results were plotted as the mean ± SD.

26. Statistical analysis

For tracking experiments, mean and standard error were calculated. Data were also compared using a two-tailed heteroscedastic T-test. While the distribution was not Gaussian, normalized frequency histograms were calculated to represent the overall samples distribution. Statistics were calculated using excel and software.

Statistical analysis was performed using GraphPad Prism software (San Diego,USA). Pairwise comparisons were tested using a non-parametric Mann-Whitney U test for bone metastases. In vitro data were analyzed using ANOVA and Student's t-tests to assess the differences between groups. Results of $P < 0.05$ were considered significant.

Plots were produced using Origin 8.0 (Microcal Software). Results are expressed as mean SE. Statistical analysis was performed using unpaired t tests or ANOVA tests followed by either Dunnett (for multiple control vs. test comparisons) or Student–Newman–Keuls posttests (for multiple comparisons). The Student t test was used for statistical comparison of the differences, and $P < 0.05$ was considered statistically significant

Supplementary Materials

Plasmids used in this study are given in Table S1.

Commercial plasmids		
Plasmid	**Description**	**Source**
pcDNA3	5428 bp; Amp^R; MCS is in the forward (+) orientation (CMV promoter); 5' sequencing primer: CMV-FW; 3' sequencing primer: BGH-RV; Neo^R (SV40 promoter); ColE1 origin	Invitrogen
p*Silencer*™ 4.1-CMV puro	4781 bp; Amp^R; cloning site for siRNA – HindIII(463) and BamHI(516) (CMV promoter); 5' sequencing primer: AGGCGATTAAGTTGGGTA; 3' sequencing primer: CGGTAGGCGTGTACGGTG; $Puro^R$ (SV40 promoter); ColE1 origin	Thermo Fisher Scientific

Constructed plasmids		
Plasmid	**Usage**	**Reference**
pcDNA3-GFP	As control for protein expression with fluorescent tag	Dr Arnaud Monteil (IGF, Montpellier, France)
pcDNA3-hNALCN-GFP	For NALCN overexpression with fluorescent tag	Dr Arnaud Monteil (IGF, Montpellier, France)
p*Silencer*™ 4.1-CMV puro-shNALCN	For establishment of stable NALCN knock-down cell line	Constructed by Oksana Iamshanova for this study

siRNA and shRNA used in this study are given in Table S2.

Small interfering RNA (siRNA)	
Sequence	**Usage**
5'- GGUGAAGACUGGAACAAGAUU -3'	Designed by Oksana Iamshanova for this study

Short interfering RNA (shRNA)	
Sequence	**Usage**
FW 5' – GATCCGGTGAAGACTGGAACAAGATT TTCAAGAGAAATCTTGTTCCAGTCTTCACCTTTTTTGGAAA – 3'	To insert into p*Silencer*™ 4.1-CMV puro plasmid
RV 5' – AGCTTTTCCAAAAAAGGTGAAGACTGGAACAAGATTTCTCTTGAA AATCTTGTTCCAGTCTTCACCG – 3'	

Primers used in this study are given in Table S3.

Primers			
Sequence	**Expected PCR product**	**Usage**	**Reference**
FW-5'- CAGCTTCCGGGAAACCAAAGTC -3' **RV-5'- AATTAAGCCGCAGGCTCCACTC - 3'**	113 bp	18S as a loading control for qPCR	(El Boustany *et al.*, 2008)
FW-5'- ACCCACTCCTCCACCTTTG -3' **RV-5'- CTCTTGTGCTCTTGCTGGG -3'**	178 bp	GAPDH as a loading control for qPCR	Anne-Sophie Borowiec, et al, 2013 Plos One
FW-5'- GCAAAGCAGAAGAAACCGATAC -3' **RV-5'- AACTTAAAAGCTGGTCCTCCTC -3'**	584 bp	NALCN screening for cPCR	Dr Arnaud Monteil (IGF, Montpellier, France)
FW-5'- CACAGGTGAAGACTGGAACAAGA -3' **RV-5'- CCACAGTCTGTTGCCCAGTATGTA -3'**	96 bp	NALCN screening for qPCR	Designed by Oksana Iamshanova for this study
FW-5'- AGCCACTTTTCTCTACGGTCC -3' **RV-5'- TACGGAGGCCTCTCCAGTTT -3'**	136 bp	NLF-1 screening for qPCR	Designed by Alexandre Bokhobza for this study
FW-5'- CTTGACCTAAAGACCATTGCACTTC -3' **RV-5'- AACTTCACATCACAGCTCC -3'**	266 bp	TBP as a loading control for cPCR	Designed by Oksana Iamshanova for this study
FW-5'- CTTGACCTAAAGACCATTGCACTTC -3' **RV-5'- GTTCTTCACTCTTGGCTCCTGTG -3'**	154 bp	TBP as a loading control for qPCR	Designed by Oksana Iamshanova for this study
FW-5'- TATGGTTCTTAGTGAGCCTCTGCAC -3' **RV-5'- CAATAGTCCTTCCTCCTGGGTGTC -3'**	849 bp	UNC79 screening for cPCR	Designed by Oksana Iamshanova for this study
FW-5'- GCATCTCGAAGGGTGAGTG -3' **RV-5'- CAATAGTCCTTCCTCCTGGGTGTC -3'**	163 bp	UNC79 screening for qPCR	Designed by Oksana Iamshanova for this study
FW-5'- CTGAGGAAGGCACTCAGTGGTC -3' **RV-5'- GTTTATGCAGGAGTCTGTGAGGC -3'**	854 bp	UNC80 screening for cPCR	Designed by Oksana Iamshanova for this study
FW-5'- GTCAAGGAAGTGCGATCTCAGATC -3' **RV-5'- GTTTATGCAGGAGTCTGTGAGGC -3'**	201 bp	UNC80 screening for qPCR	Designed by Oksana Iamshanova for this study

Antibodies used in this study are given in Table S4.

Antibodies used for immunoblotting				
Primary antibody (reference number)	**Working concentration**	**Secondary antibody**	**Source**	**Band size**
Calnexin (MAB3126, C8.B6)	1:1000	anti-mouse	Merck Millipore	100 kDa
Cortactin (sc-55578)	1:100	anti-mouse	Santa-Cruz	80 kDa
Dynamin-1/2 (MABT188)	0.5 µg/ml	anti-mouse	Merck Millipore	98 kDa
E-Cadherin (sc-21791)	1:200	anti-mouse	Santa-Cruz	135 kDa, 120 kDa, 80 kDa
MT1-MMP (sc-377097)	1:100	anti-rabbit	Santa-Cruz	63 kDa
N-Cadherin (sc-59987)	1:200	anti-mouse	Santa-Cruz	130 kDa
NALCN	1:1000	anti-rabbit	Eurogentec produced by our order	250-300 kDa
p-Src-Y418 (ab40660)	1:1000	anti-rabbit	Abcam	56 kDa
p-Src-Y530 (sc-166860)	1:100	anti-mouse	Santa-Cruz	60 kDa
Src-total (ab109381)	1:1000	anti-rabbit	Abcam	60 kDa
Tks5 (sc-736241)	1:100	anti-mouse	Santa-Cruz	140 kDa
β-actin (A5441, AC-15)	1:1000	anti-mouse	Sigma	42 kDa

List of references

Bend EG, Si Y, Stevenson DA, Bayrak-Toydemir P, Newcomb TM, Jorgensen EM & Swoboda KJ (2016). NALCN channelopathies. *Neurology*; DOI: 10.1212/WNL.0000000000003095.

Ben-Kasus Nissim T, Zhang X, Elazar A, Roy S, Stolwijk JA, Zhou Y, Motiani RK, Gueguinou M, Hempel N, Hershfinkel M, Gill DL, Trebak M & Sekler I (2017). Mitochondria control store-operated Ca 2+ entry through Na + and redox signals. *EMBO J*; DOI: 10.15252/embj.201592481.

El Boustany C, Bidaux G, Enfissi A, Delcourt P, Prevarskaya N & Capiod T (2008). Capacitative calcium entry and transient receptor potential canonical 6 expression control human hepatoma cell proliferation. *Hepatology*; DOI: 10.1002/hep.22263.

Brisson L, Gillet L, Calaghan S, Besson P, Le Guennec J-Y, Roger S & Gore J (2011). NaV1.5 enhances breast cancer cell invasiveness by increasing NHE1-dependent H+ efflux in caveolae. *Oncogene*; DOI: 10.1038/onc.2010.574.

Carrithers MD, Chatterjee G, Carrithers LM, Offoha R, Iheagwara U, Rahner C, Graham M & Waxman SG (2009). Regulation of podosome formation in macrophages by a splice variant of the sodium channel SCN8A. *J Biol Chem*; DOI: 10.1074/jbc.M801892200.

Chantome A, Potier-Cartereau M, Clarysse L, Fromont G, Marionneau-Lambot S, Gu??guinou M, Pag??s JC, Collin C, Oullier T, Girault A, Arbion F, Haelters JP, Jaffr??s PA, Pinault M, Besson P, Joulin V, Bougnoux P & Vandier C (2013). Pivotal role of the lipid raft SK3-orai1 complex in human cancer cell migration and bone metastases. *Cancer Res*; DOI: 10.1158/0008-5472.CAN-12-4572.

Cochet-Bissuel M, Lory P & Monteil A (2014). The sodium leak channel , NALCN , in health and disease. *Front Cell Neurosci*; DOI: 10.3389/fncel.2014.00132.

Flourakis M, Kula-Eversole E, Hutchison AL, Han TH, Aranda K, Moose DL, White KP, Dinner AR, Lear BC, Ren D, Diekman CO, Raman IM & Allada R (2015). A Conserved Bicycle Model for Circadian Clock Control of Membrane Excitability. *Cell* **162,** 836–848.

Lu B, Su Y, Das S, Wang H, Wang Y, Liu J & Ren D (2009). Peptide neurotransmitters

activate a cation channel complex of NALCN and UNC-80. *Nature* **457,** 741–744.

Perrouin Verbe MA, Bruyere F, Rozet F, Vandier C & Fromont G (2016). Expression of store-operated channel components in prostate cancer: The prognostic paradox. *Hum Pathol*; DOI: 10.1016/j.humpath.2015.09.042.

Sun J, Lu F, He H, Shen J, Messina J, Mathew R, Wang D, Sarnaik AA, Chang WC, Kim M, Cheng H & Yang S (2014). STIM1- and Orai1-mediated Ca2+ oscillation orchestrates invadopodium formation and melanoma invasion. *J Cell Biol*; DOI: 10.1083/jcb.201407082.

Wang H & Ren D (2009). UNC80 functions as a scaffold for Src kinases in NALCN channel function. *Channels (Austin)*; DOI: 10.1038/nature07579.In.

Yang M & Brackenbury WJ (2013). Membrane potential and cancer progression. *Front Physiol*; DOI: 10.3389/fphys.2013.00185.

3.2 Additional results

3.2.1 Screening for NALCN expression

Although previous studies reported on NALCN expression in some mammalian organs (e.g. brain and pancreas), little is yet known on the channel presence in other tissues. Therefore, we have performed qRT-PCR in order to compare the amount of *NALCN* mRNA expressed in different mice organs. For this purpose, we have designed qRT-PCR primers against *NALCN* and TATA box binding protein (*TBP)* genes. TBP was chosen because it was previously described being a suitable housekeeping/reference gene for qRT-PCR analysis within the prostate tissues and cell lines (Ohl *et al.*, 2005; Schulz *et al.*, 2010; Tsaur *et al.*, 2013; Erdmann *et al.*, 2014). Moreover, it was beneficial to use *TBP*, since, as it has appeared, in prostate tissues and cell lines its C_t values were around the same level as for *NALCN*. Prior to analysis, we have verified the efficiency of the designed qRT-PCR primers and optimized the reaction conditions such as the primers concentration, annealing temperature and amount of $MgCl_2$ by using plasmid DNA and mice brain (Annex 7.1-7.7). Glyceraldehyde 3-phosphate dehydrogenase (GAPDH) and ribosomal RNA 18S were already used in our laboratory as the reference genes (Annex 7.8). The result revealed that NALCN is expressed in prostate and pancreas 10 fold less than in brain (Figure 25A).

Furthermore, we have screened for NALCN mRNA in various cell lines by using cPCR. In addition to being expressed in prostate and pancreatic cell lines, we found NALCN mRNA in human fibroblast MRC-5 and IMR-90, human embryonic kidney cells HEK293, immortalized human prostate cells EP156T, cervical cancer cell line HeLa, immortalized human pancreatic stellate cells RLT-PSC and activated pancreatic stellate cells PSC1 (Figure 25B).

3.2.2 Characterization of prostate cancer cell lines

3.2.2.1 By the protein expression profile

Throughout this study human prostate cancer cell lines with different metastatic potential were used: LNCaP and C4-2 are considered being weakly metastatic cell lines, DU 145 – moderate, PC-3 and PC-3M – highly aggressive. Nevertheless, in order to verify our working models, we have performed analysis of the expression level of various proteins commonly referred to as promoters and suppressors of prostate cancer disease (Figure 26; Annex 7.9-7.10). For example, proline-rich kinase Pyk2 was reported to be expressed in healthy prostate epithelial cells and to inversely correlate with prostate tumour aggressiveness (Stanzione *et al.*, 2001). Accordingly, in our cell lines Pyk2 was expressed in cells with low and moderate metastatic potential, but not in highly aggressive phenotype. Overexpression and activation of proto-oncogene Src kinase is often

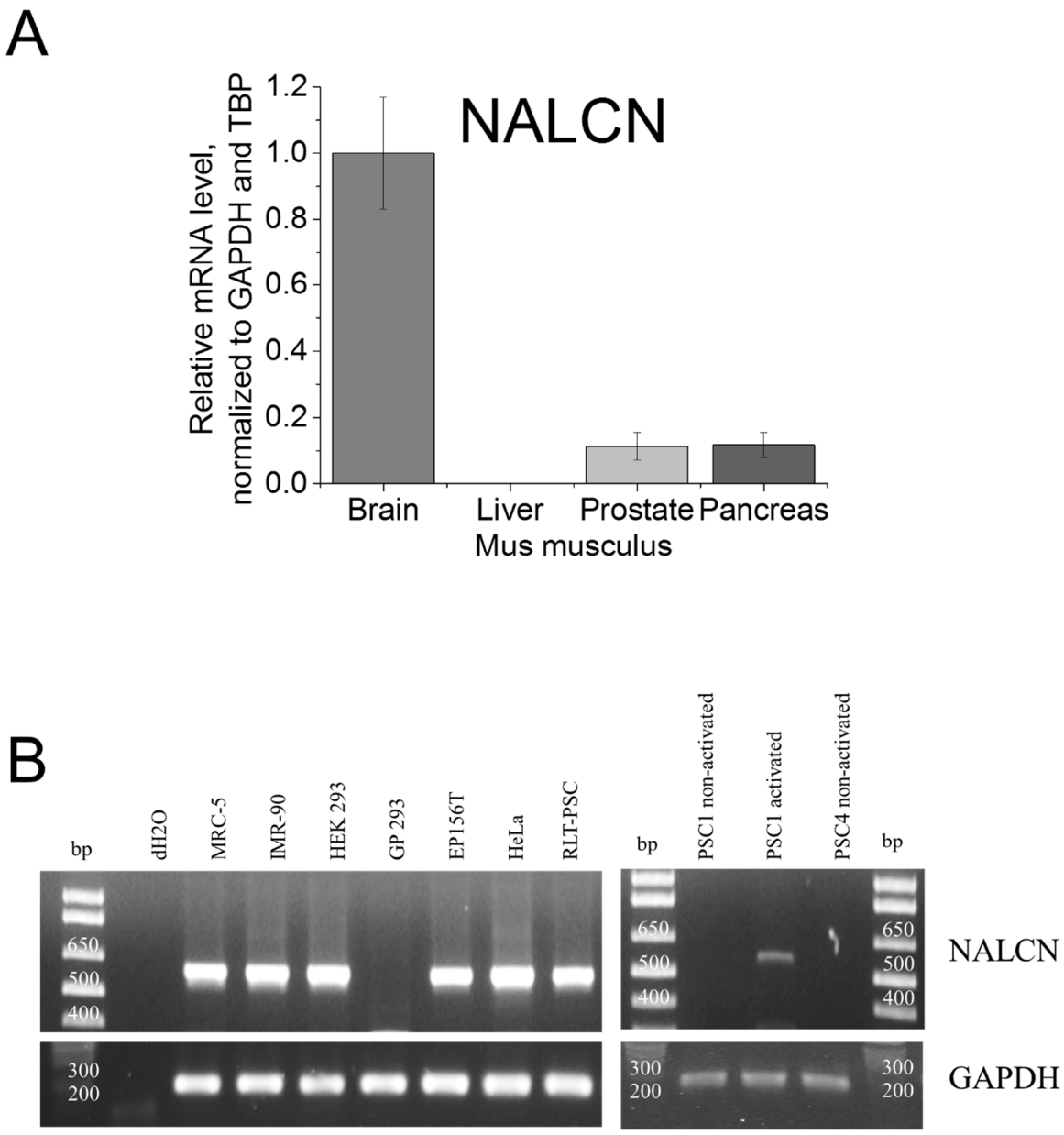

Figure 25. Screening for NALCN mRNA expression. A, qRT-PCR in various organs from Mus ♂ (n=1). B, cPCR against NALCN and GAPDH on various cell lines.

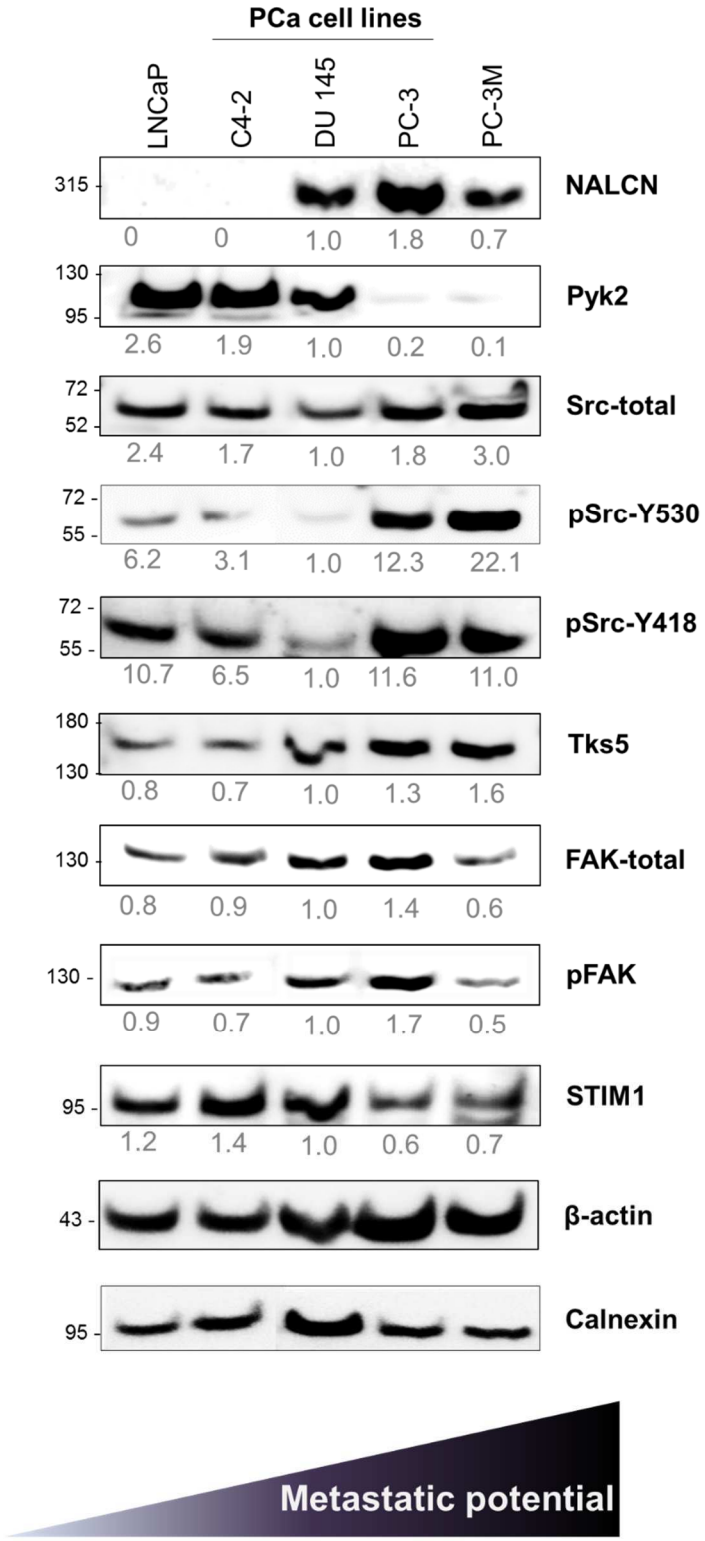

Figure 26. Characterization of human prostate cancer cell lines by the protein expression profile.
The levels of proteins expression were normalized to internal controls, β-actin and calnexin, and relatively compared to DU 145 cell line (n=1).

associated with cancer progression and worst patients' outcome (Fizazi, 2007). Therefore, we have evaluated the level of active form (phosphorylated at Y418), non-active form (phosphorylated at Y530), and the total level of Src expression. One of the downstream target of Src kinase is Tks5, scaffold protein required for podosome formation, ECM degradation and cancer cell invasiveness (Courtneidge *et al.*, 2005; Burger *et al.*, 2014). Indeed, highly metastatic PC-3 and PC-3M were exhibiting the greatest levels of Src kinase and Tks5 within the cell lines tested (Figure 26). During tumourigenesis cancer cells interact with ECM and activate focal adhesion kinase (FAK) signalling pathway that assists in further disease dissemination (Jiang *et al.*, 2015). Accordingly, the level of activated (phosphorylated) FAK and the total level of protein expression were increased in more advanced prostate cancer cell lines, but, surprisingly, not in PC-3M (Figure 26). Interestingly, stromal interaction molecule 1 (STIM1) was shown to possess multiple functions in prostate cancer. On the one hand, STIM1 was found to induce migration and epithelial-to-mesenchymal transition of prostate cancer cells. On the other hand, analysis of human prostate biopsies indicated on the decreased level of STIM1 in malignant lesions when compared with normal tissues (Xu *et al.*, 2015). Our results were in accordance with this findings – STIM1 expression was reduced in human prostate cancer cell lines with the rise of phenotype aggressiveness.

Overall, the protein expression profile verified on the actuality of the previously established model of the relative metastatic potential within the human prostate cancer cell lines tested. However, additional precautions should be taken into account when manipulating with DU 145 and PC-3M cell lines. Since DU 145 expresses the lowest level of proto-oncogene Src kinase and PC-3M possess reduced amount of FAK, the according downstream signalling pathways might be compromised in these cell lines.

3.2.2.2 By store-operated calcium entry

Many studies reported on the importance of SOCE to modulate multiple cellular events, such as gene expression, cell cycle, proliferation, cell motility, migration, and even being associated with various hallmarks of cancer (Prakriya & Lewis, 2015; Fiorio Pla *et al.*, 2016). Interestingly, in addition to allowing substantial Ca^{2+} entry, SOCE signalling was also described to initiate Na^{+} influx due to the activity of non-selective transient receptor potential channels such as TRPM4 for prostate cancer cells (Holzmann *et al.*, 2015). Therefore, we have investigated Ca^{2+} and Na^{+} influx triggered by the activation of SOCE in the number of human prostate cancer cell lines (Figure 27). Interestingly, Ca^{2+} entry was considerably decreased in PC-3 and PC-3M cell lines. However, SOCE-activated Na^{+} influx was the highest in PC-3 cell line.

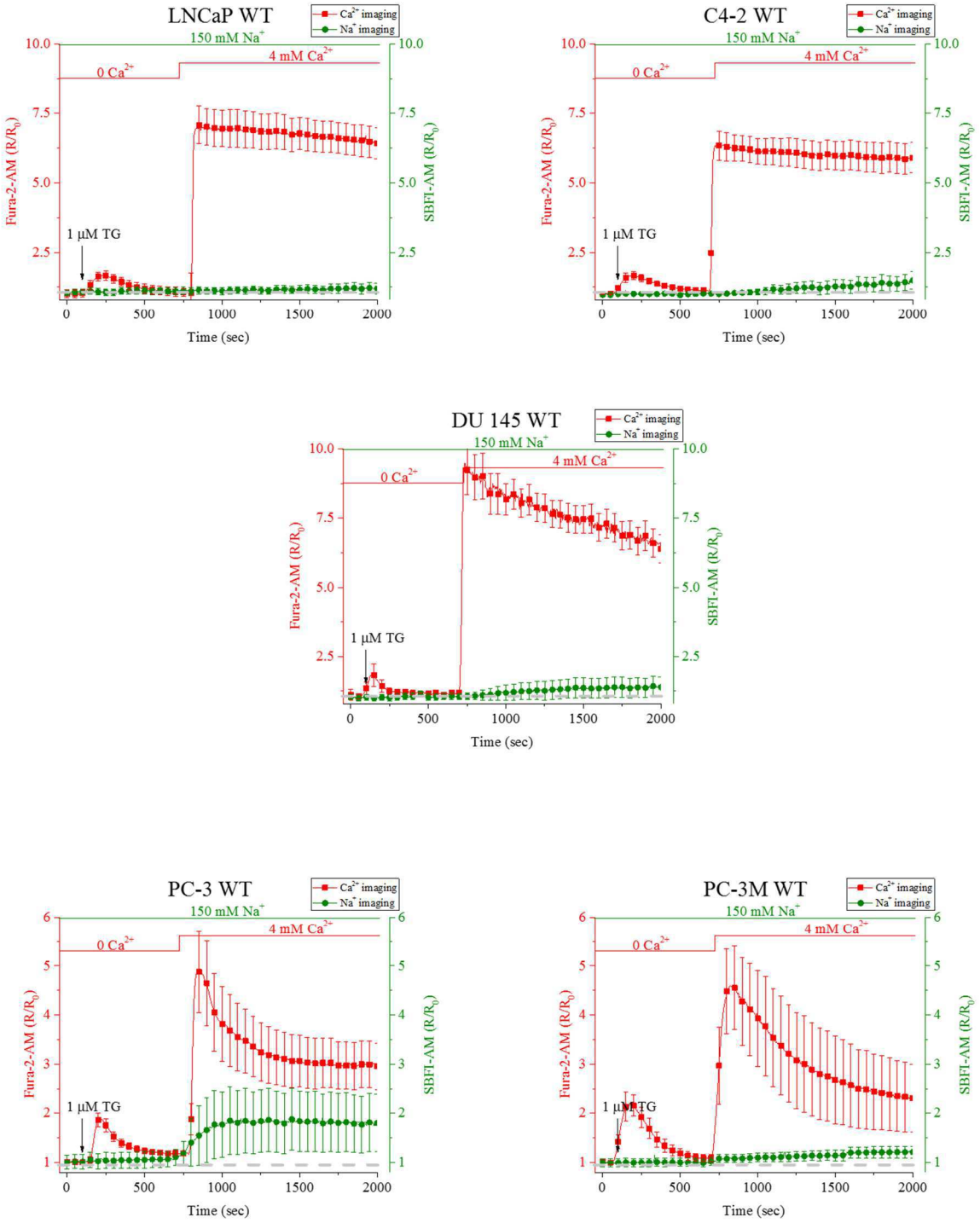

Figure 27. SOCE-induced Ca^{2+} and Na^{+} influxes in human prostate cancer cell lines. Recordings of $[Ca^{2+}]_i$ and $[Na^{+}]_i$ were performed by using Fura-2-AM and SBFI-AM dyes, respectively. The ratios of fluorescence 340 nm/ 380 nm were normalized to the initial ratio values and presented as R/R_0.

These data are in accordance with our previous findings, where the critical component of SOCE machinery that serves as $[Ca^{2+}]_{ER}$-sensing trigger, STIM1, is diminished in prostate cancer cells with the raise of the malignancy profile (Figure 26). Therefore, one can hypothesize that during cancer progression SOCE mechanisms are remodeled in a such way that they would lessen Ca^{2+} influx and promote Na^+ entry instead. Once again, it highlights the importance of Na^+ signalling during establishment of more aggressive phenotype in cancer cells. Nonetheless, in order to determine the functioning of SOCE-induced Na^+ influx more profound analysis is required within the different cancer types and malignancy stages.

3.2.2.3 By cytosolic calcium oscillations

Cytosolic Ca^{2+} oscillations, is a particular feature of intracellular Ca^{2+} signalling, which is frequently present in aggressive cancer cells (Sun *et al.*, 2014; Zhu *et al.*, 2014; Rizaner *et al.*, 2016). Indeed, spontaneous Ca^{2+} oscillations were found in strongly malignant prostate cancer cells PC-3M, and absent in weakly metastatic LNCaP cells (Rizaner *et al.*, 2016). Therefore, we investigated whether other human prostate cancer cell lines used in this study were able to potentiate basal cytosolic Ca^{2+} oscillations. Accordingly, spontaneous Ca^{2+} oscillations were detected in DU 145, PC-3 and PC-3M, but not in immortalized primary prostate cell line EP156T and weakly-metastatic LNCaP and C4-2 cells (Figure 28). Similarly, FBS stimulation evoked cytosolic Ca^{2+} oscillations in strongly metastatic DU 145, PC-3 and PC-3M cells, but not in LNCaP and C4-2 (Figure 29). It indeed implies on the possible attribution of this intracellular signalling to the cancer progression.

3.2.3 Metastatic cancer cell behaviours

In this study our main model of human prostate cancer was mainly represented by PC-3 cell line. However, we have performed additional set of experiments using other cell lines. These results were not included in the main article.

Transient overexpression of NALCN in C4-2 cell line, that does not express the channel endogenously, resulted in increased migration rate, implying on the importance of NALCN to potentiate metastatic cancer cell behaviour (Figure 30; Annex 7.11-7.13). Interestingly, PC-3M was exhibiting similar effects to PC-3 after transient NALCN deregulation, whereas DU 145 – completely opposite (Figure 31A,B; Annex 7.14-7.15). Increased migration and invasion after transient NALCN silencing in DU 145 can be explained by the lack of channelosome proteins in this cell line, or by NALCN mutation found due to the genomic sequencing analysis. Therefore, one can hypothesize that NALCN represent some different function in DU 145 cell line.

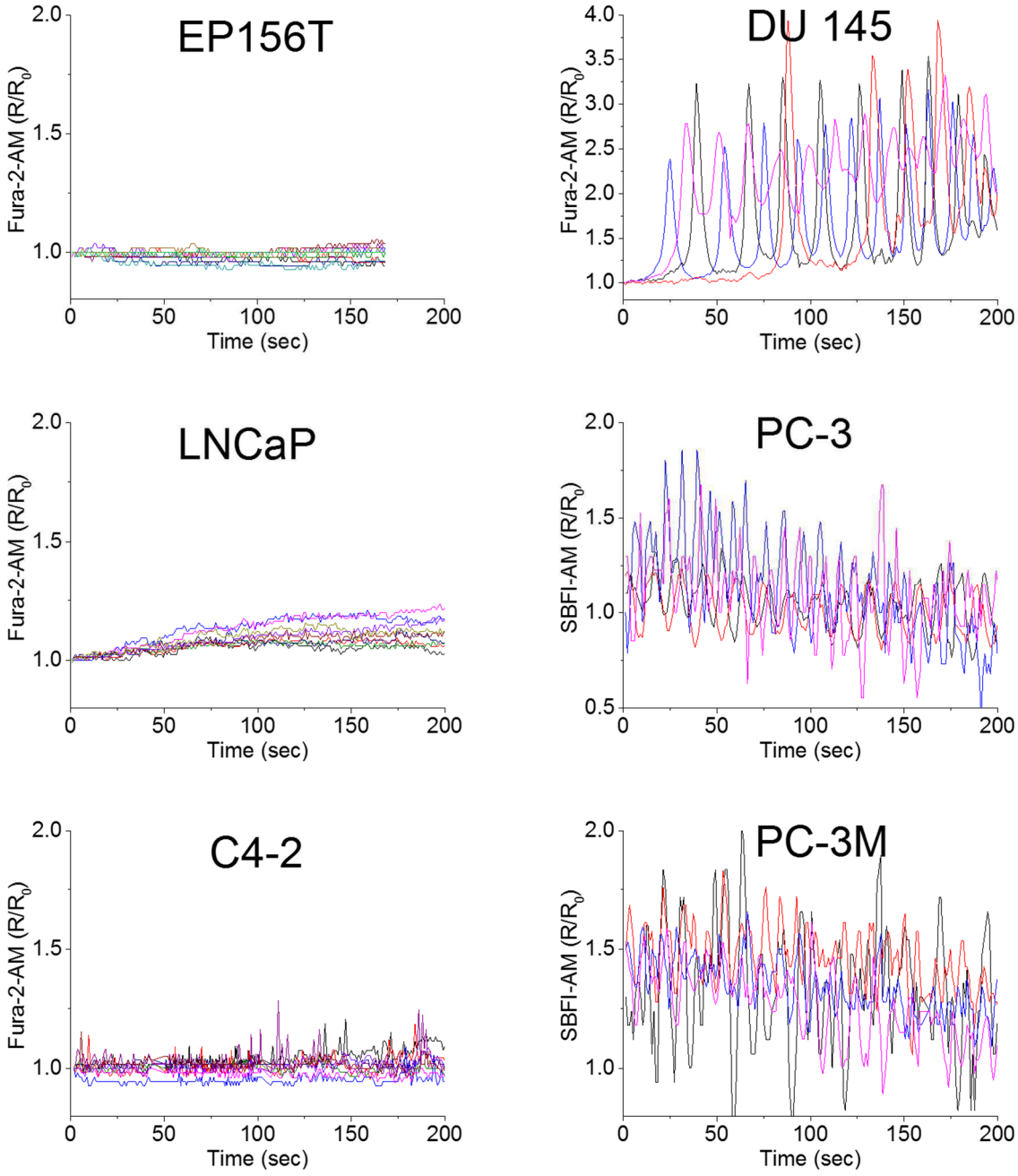

Figure 28. Spontaneous cytosolic Ca^{2+} oscillations in human prostate cell lines. Recordings of $[Ca^{2+}]_i$ were performed by using Fura-2-AM. The ratios of fluorescence 340 nm/ 380 nm were normalized to the initial ratio values and presented as R/R_0.

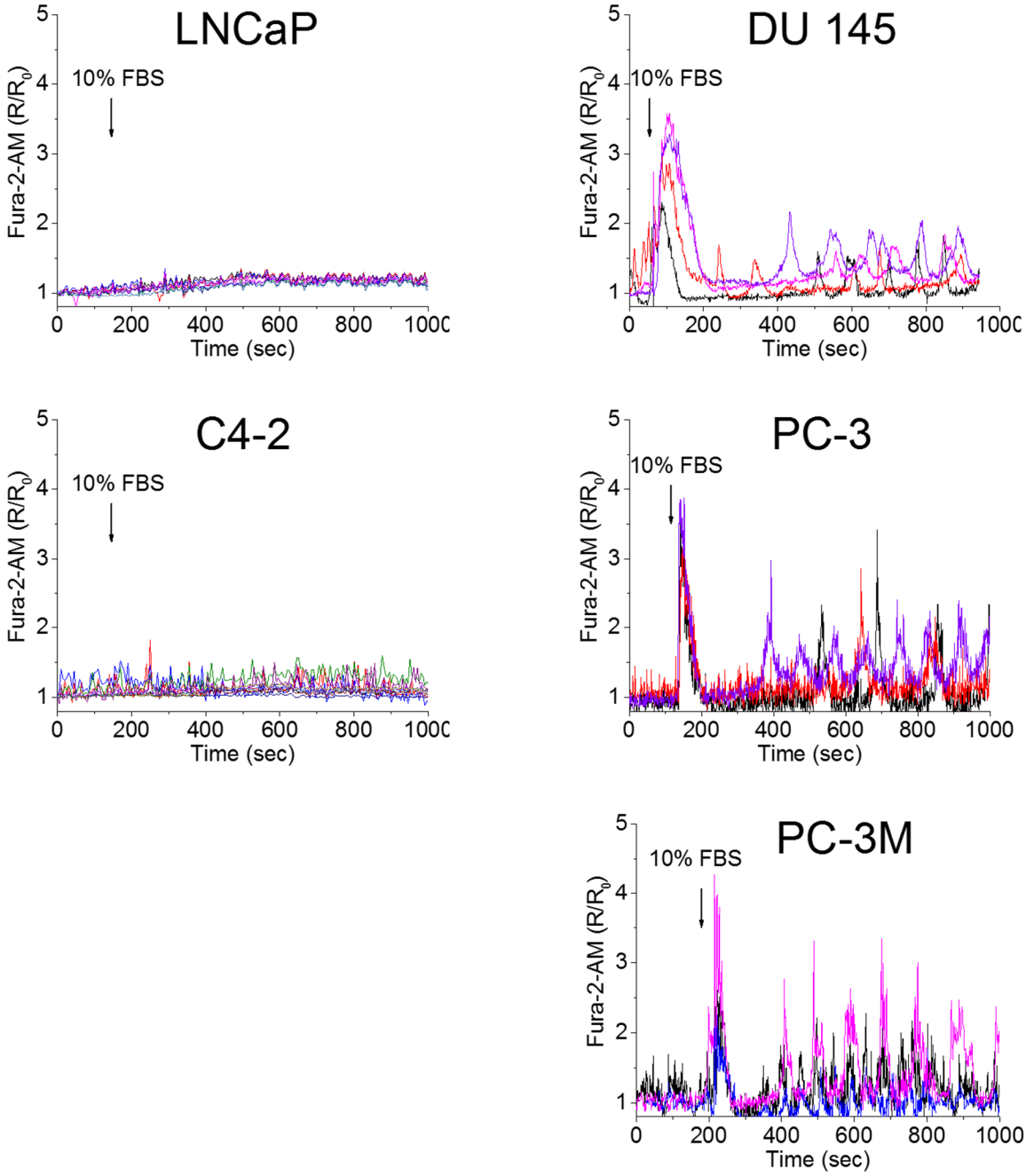

Figure 29. FBS-stimulated cytosolic Ca^{2+} oscillations in human prostate cell lines. Recordings of $[Ca^{2+}]_i$ were performed by using Fura-2-AM. The ratios of fluorescence 340 nm/ 380 nm were normalized to the initial ratio values and presented as R/R_0.

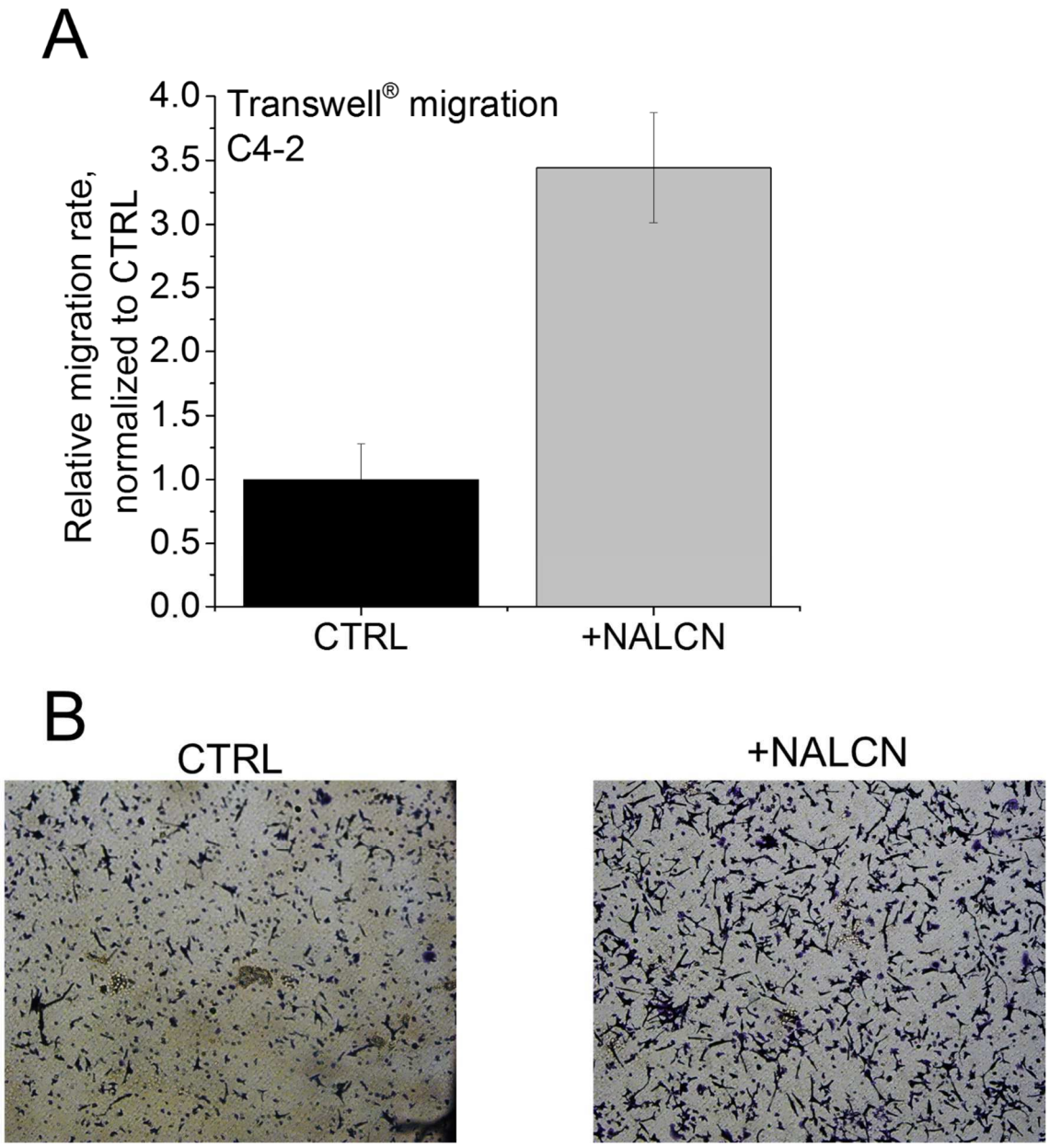

Figure 30. Transwell® migration using C4-2 cells. A, Transwell® migration after transient NALCN overexpression in C4-2 cells, that do not express NALCN endogenously. Data presented as mean values ± SD (n=1). B, representative images of C4-2 migration after mock (CTRL) and NALCN overexpression (+NALCN).

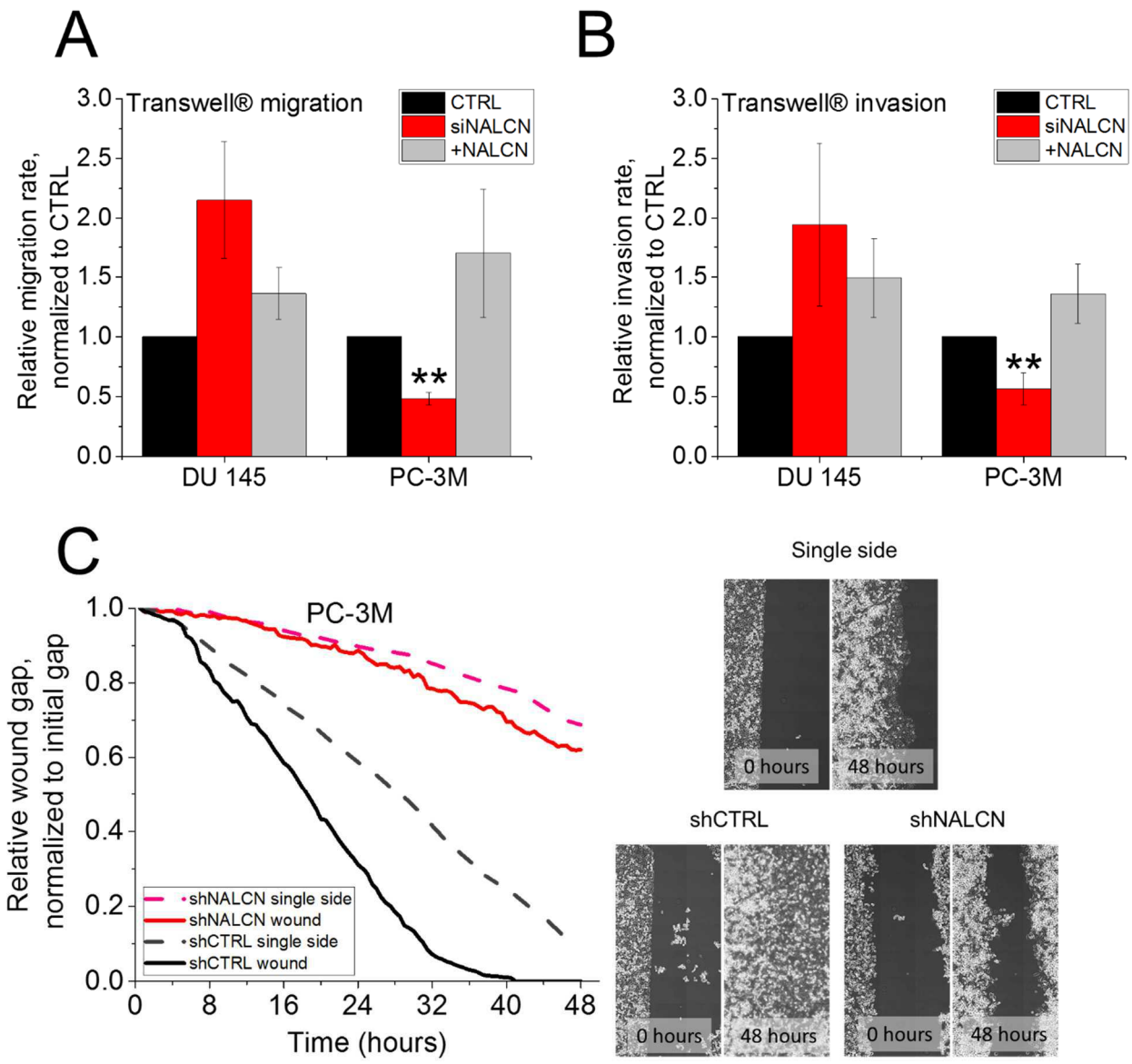

Figure 31. Migration and invasion assay. A, Transwell® migration. Data presented as mean values ± SEM (n=3), **-p<0.01. B, Transwell® invasion. Data presented as mean values ± SEM (n=3), **-p<0.01. C, Wound-healing assay for PC-3M cells with representative images of the wound and single side migration (n=1).

Surprisingly, the stable NALCN knockdown (Annex 7.15) in DU 145 had opposite effect to its transient gene silencing. Accordingly, in all cell lines tested DU 145, PC-3 and PC-3M stable NALCN knockdown resulted in suppressed motility, migration and invasion. It was investigated by using standard conditions as well as by using various pharmacological effectors (Figure 32, 33).

Acidic extracellular pH ($[pH]_e$) is an important feature of tumour microenvironment that subserve dissemination of cancer cells. Indeed, acidic $[pH]_e$ was shown to upregulate the ECM degrading enzyme, cathepsin B, and to increase invasiveness of PC-3 cells (Gao *et al.*, 2015). We have performed similar experiment by using our stable NALCN knockdown cell lines. For this purpose, we have adjusted pH of the media (for both upper and lower compartments of the insert), filter sterilized it and left the cells to migrate as described before. Interestingly, acidic pH promoted migration of DU 145, PC-3, and PC-3M cells, whereas suppressed NALCN efficiently constrained their motility (Figure 34). Indeed, acidic $[pH]_e$ was previously reported to enhance cancer cell migration due to the remodelling of cell-substrate adhesions through regulation of integrin dynamics (Webb *et al.*, 2011). Importantly, throughout this assay we were using RPMI media, which is based on bicarbonate buffer system that enables imitation of the physiological acid-base homeostatic mechanism (e.g. blood system). In brief, pH of the RPMI media is buffered due to the constant presence of 5% CO_2 in the incubator, which is around 100 fold higher than in the air. Therefore, pH value in the incubator and outside would greatly vary. For example, the standard growth RPMI media outside the incubator was having pH 8.4, whereas theoretical pH is expected being around 7.0-7.4. Furthermore, cellular metabolism by itself may also have profound impact on pH of the growth media. Accordingly, we have compared pH values of growth media before and after the experiment and indeed the values were considerably changed: pH 6.4 became pH 7.2, pH 7.4 – pH 7.6, pH 8.4 - pH 7.7, pH 9.4 – pH 7.9, and pH 10.4 – pH 8.1. In order to avoid $[pH]_e$ fluctuation an alternative buffering system, that does not depend on CO_2 presence, could be used. For example, zwitterion buffers like HEPES represent strong buffering system. However, HEPES based buffers lack the nutritional value and are toxic at concentrations over 100 mM. Therefore, if HEPES is used as the primary buffer for stronger buffering capacity, it is still important to maintain sufficient bicarbonate in the medium for nutritional purposes and to avoid toxicity.

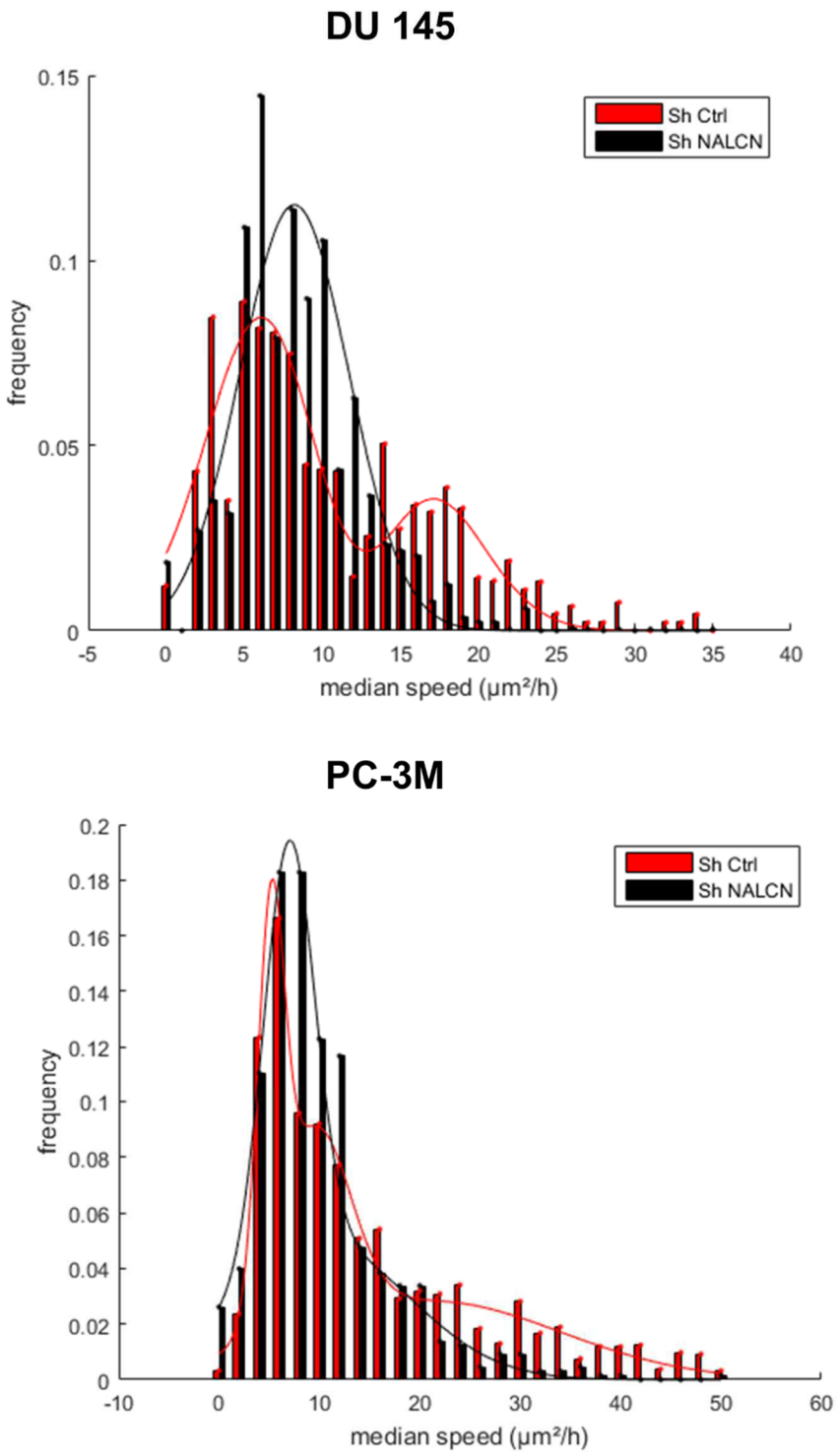

Figure 32. Cellular motility.
Stable NALCN knockdown decreases the median speed of DU 145 and PC-3 cells.
Data presented as mean values ± SD (n=1).

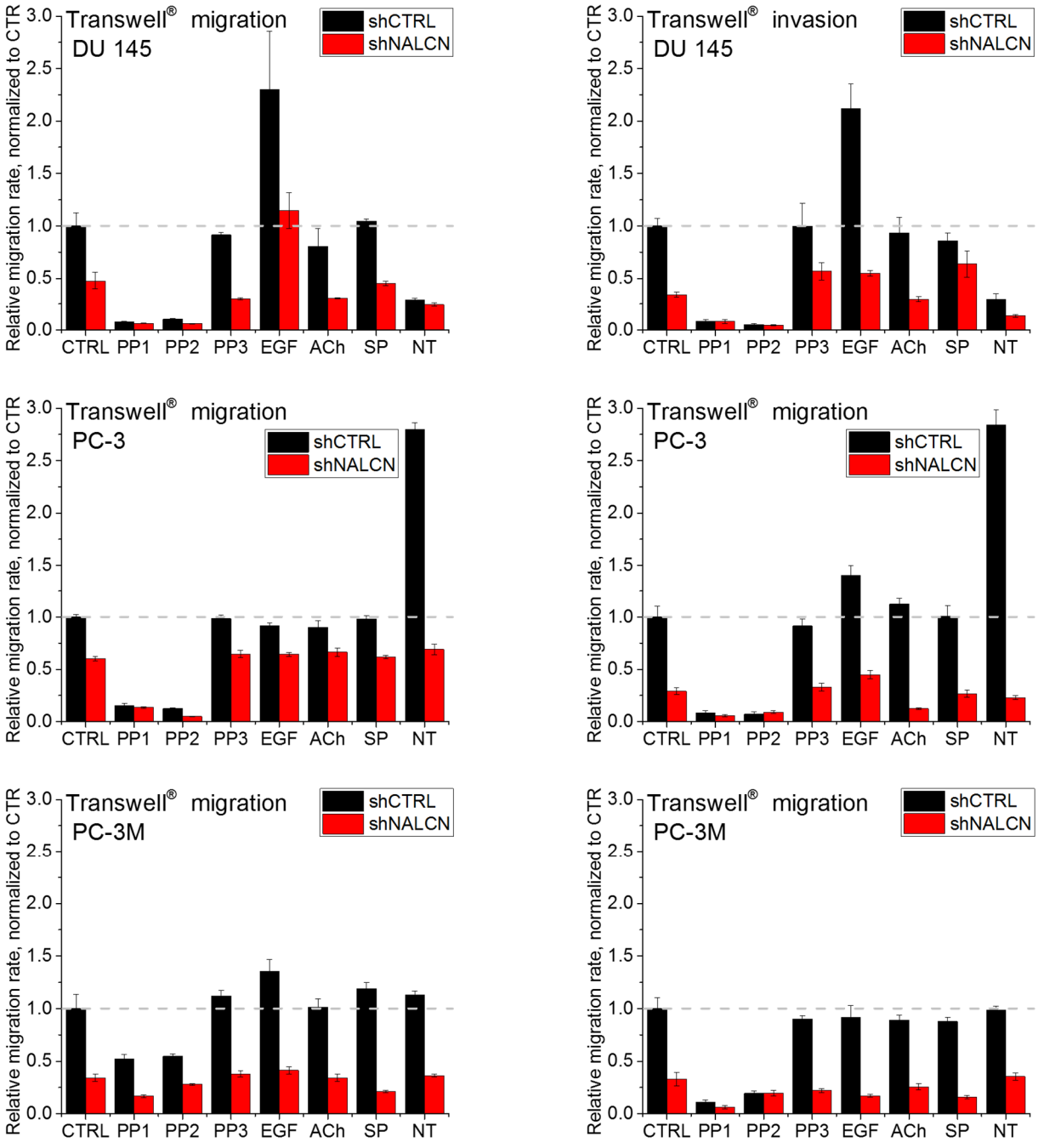

Figure 33. Migration and invasion assay in stable NALCN knockdown cell lines using various pharmacological effectors.
CTRL – control; PP1 and PP2 – 10 μM inhibitors of Src kinase; PP3 – 10 μM negative control for PP1 and PP2; EGF – 100 ng/ml epidermal growth factor; ACh – 100 μM acetylcholine; SP – 1μM substance P; NT – 1 μM neurotensin. Data presented as mean values ± SD (n=1).

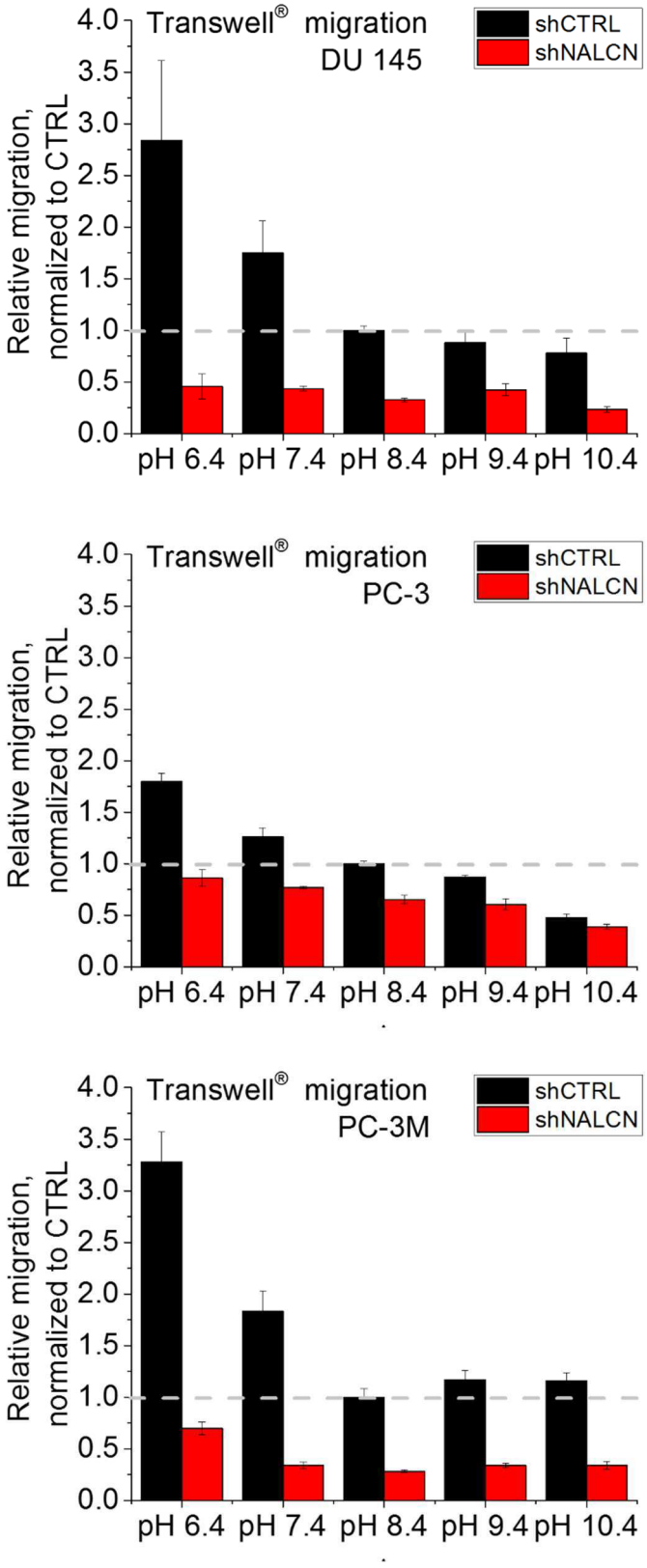

Figure 34. Migration of stable NALCN knockdown cell lines at different extracellular pH. Initial $[pH]_e$ indicated as measured in bicarbonate-based RPMI media at room conditions (0.04% CO_2, 25^0C). NALCN knockdown efficiently constrained acidic pH-evoked migration of DU 145, PC-3 and PC-3M cells. Data presented as mean values ± SD (n=1).

3.2.4 Effect of hypoxia on NALCN expression

During tumourigenesis due to its high proliferative rate cancer cells outgrow their blood supply and hence create microenvironment with low oxygen content, named hypoxia. This phenomenon is very common in malignant tumours and is widely associated with resistance to anticancer therapies as well as with enhanced metastatic potential. Therefore, we have investigated whether hypoxia has any effect on human prostate cancer cells endogenously expressing NALCN (Figure 35A). For this purpose, we have passed the same amount of cells into two separate 10 cm plates and left both of them in the standard growth conditions overnight. Afterwards, one plate was left in standard growth conditions, whereas the other was replaced into hypoxic conditions (incubator with constant humidity, 1.2% O_2, 5% CO_2, 37^0C) for 72 hours. Then the protein extraction was proceeded as usual. For immunoblot analysis we have used primary antibodies that could indicate on the aggressive potential of prostate cancer cells (Figure 35B). For example, Tks5 and Src kinase were found being important promoters of cancer development (Courtneidge *et al.*, 2005; Burger *et al.*, 2014), whereas proline-rich kinase Pyk2 was found being inversely correlated with malignancy progression (Stanzione *et al.*, 2001). Interestingly, DU 145 cells exhibited reduction of cancer cells aggressiveness after growing 72 hours in hypoxic condition, whereas PC-3 and PC-3M - increased their malignant profile (Figure 35B). Accordingly, NALCN protein level in DU 145 was decreased, whilst in PC-3 and PC-3M – elevated. Therefore, short-term hypoxia indeed provokes more aggressive expression pattern together with NALCN upregulation in PC-3 and PC-3M cells, but not in DU 145 cell line.

3.2.5 Intracellular signalling regulated by NALCN

In order to investigate the potential signalling pathways that might be regulated by NALCN expression, we have performed immunoblotting on cells with stable channel suppression. Interestingly, in NALCN knockdown the protein levels of Ca^{2+}-independent phospholipase A2 ($iPLA_2$), cathepsin B, Tks5, FAK, Pyk2 and proto-oncogene Fyn kinase substantially changed, whereas the expression of cathepsin D, integrin α5, integrin β1 and dynamin 1/2 were not changed (Figure 36). The expression profile of cells with stable NALCN downregulation indeed indicates onto reversed malignant profile in these cancer cells.

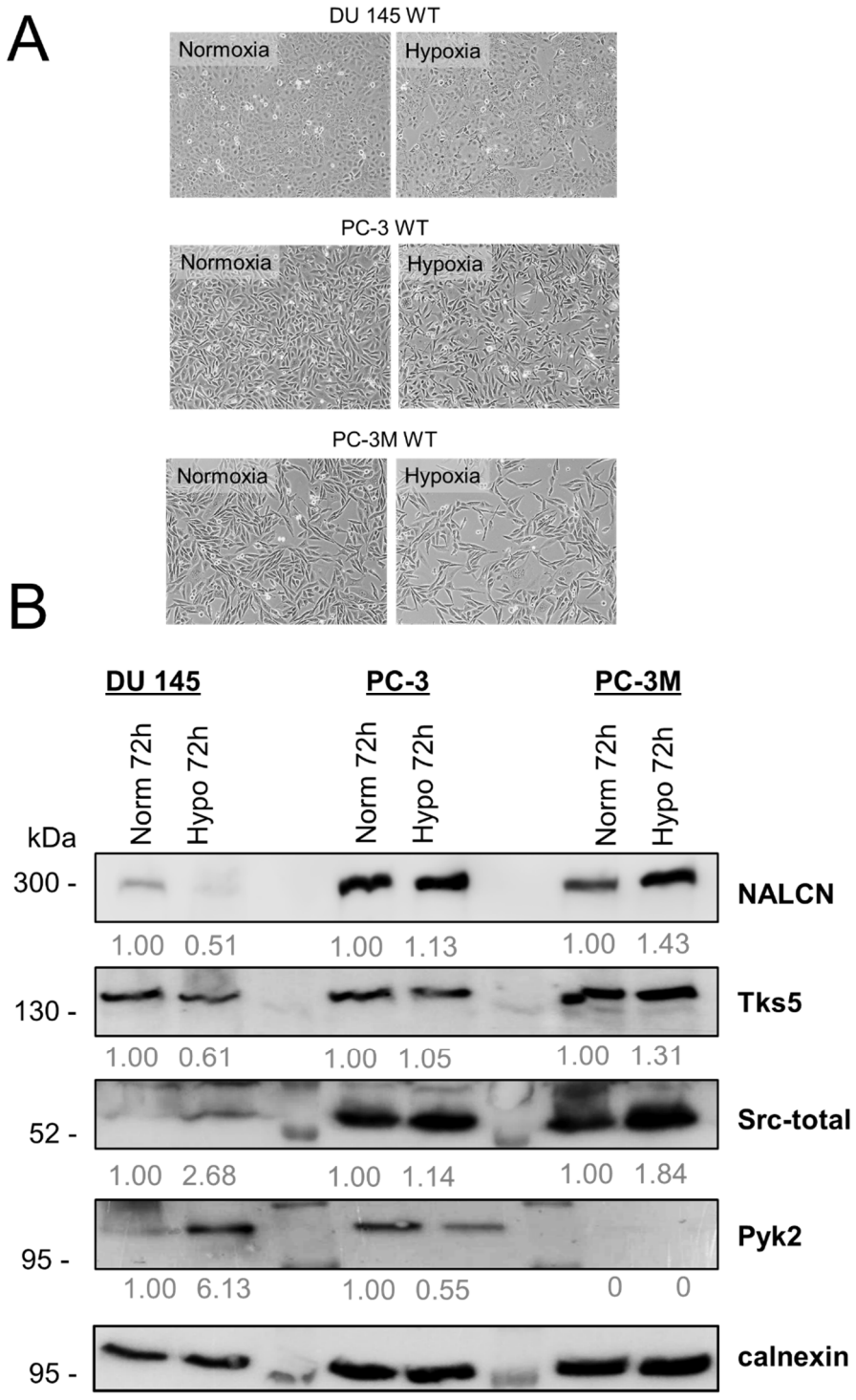

Figure 35. Effect of hypoxia on NALCN expression and other markers of prostate cancer progression.
A, representative images taken with 20x objective of cells grown for 72 hours in standard growth conditions (Normoxia) and at 1,2% O_2 (Hypoxia). **B**, immunoblot revealed with antibodies against various markers of cancer aggressiveness. The values were normalized to the internal reference protein – calnexin (n=1).

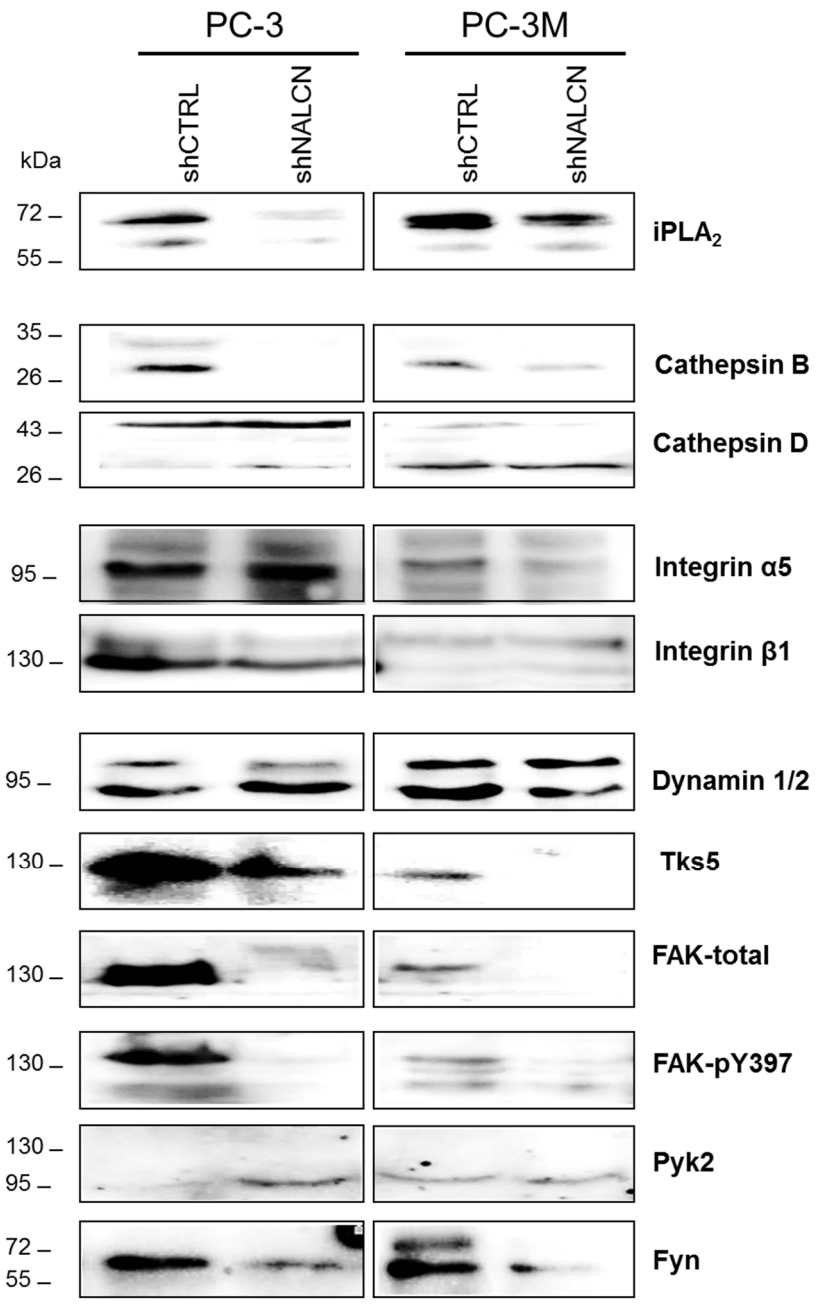

Figure 36. Intracellular signalling regulated by NALCN expression.
Immunoblots were revealed with antibodies against various markers of cancer aggressiveness. (n=1).

3.2.6 Effects of pharmacological agents on basal sodium influx

Neuropeptides such as substance P and neurotensin were reported to activate NALCN channelosome (Lu *et al.*, 2009; Wang & Ren, 2009; Kim *et al.*, 2012; Yeh *et al.*, 2017). Furthermore, Src kinase as the member of the channelosome was also suggested to potentiate its activity (Wang & Ren, 2009). Epidermal growth factor (EGF) evokes cytosolic Ca^{2+} oscillations and is known to be one of the promoters of cancer aggressiveness (Figure 33). Therefore, we have tested whether basal Na^+ leak could be modulated by potential activators and inhibitors of NALCN channelosome. In addition, we have tested mechanosensitivity of channel due to the application of synthetic lipids GS1197. Interestingly, acute application of the activators did not affect basal $[Na^+]_i$, whereas inhibitor of Src kinase, PP2, exhibited no effect on Na^+ influx induced due to the switch of extracellular Na^+ concentration (Figure 37). Nevertheless, long-term pre-incubation with these substances is required in order to verify the scarcity of the effect on Na^+ influx.

3.2.7 NALCN-mediated sodium influx after incubation with working antibody

Ion channel blockage is the biological mechanism of ion flux prevention that may lead to the various intracellular physiological responses. Accordingly, ion channel modulators were suggested being potential substances for treatment of diverse pathological conditions, including cancer disease. Different molecules, such as cations, anions, amino acids, toxins and other chemicals might antagonize activity of ion channels. Additionally, antibodies targeting different channel proteins were found to regulate the ion channel activity by the mean of various mechanisms: direct block of ion permeation, modulation of ion channel gating, internalization and degradation upon surface clustering. To date, the highly specific modulators of NALCN channelosome activity were not yet discovered. Therefore, we have decided to check whether antibody targeting the channel could modulate NALCN-mediated Na^+ influx. Of note, the antibody used throughout this study targets intracellular C-terminal of NALCN protein. Therefore, we have used graphene nanoparticles in order to allow antibody permeation inside of the cell. However, neither 5 minutes, nor 30 minutes incubations with antibody linked to graphene nanoparticles did not affect Na^+ influx in prostate cancer cell line PC-3 (Figure 38). In conclusion, antibody targeting intracellular C-terminus of NALCN fails to modulate activity of the channel. Therefore, another strategy involving antibody targeting extracellular epitope should be considered, in particular designed against extracellular loop within S5 and S6, or so called turret (Xu *et al.*, 2005; Naylor & Beech, 2009).

We have also tried using other type of nanoparticles (lipid nanocapsules) for siRNA transfection, but the toxicity rate was too high (Annex 7.16).

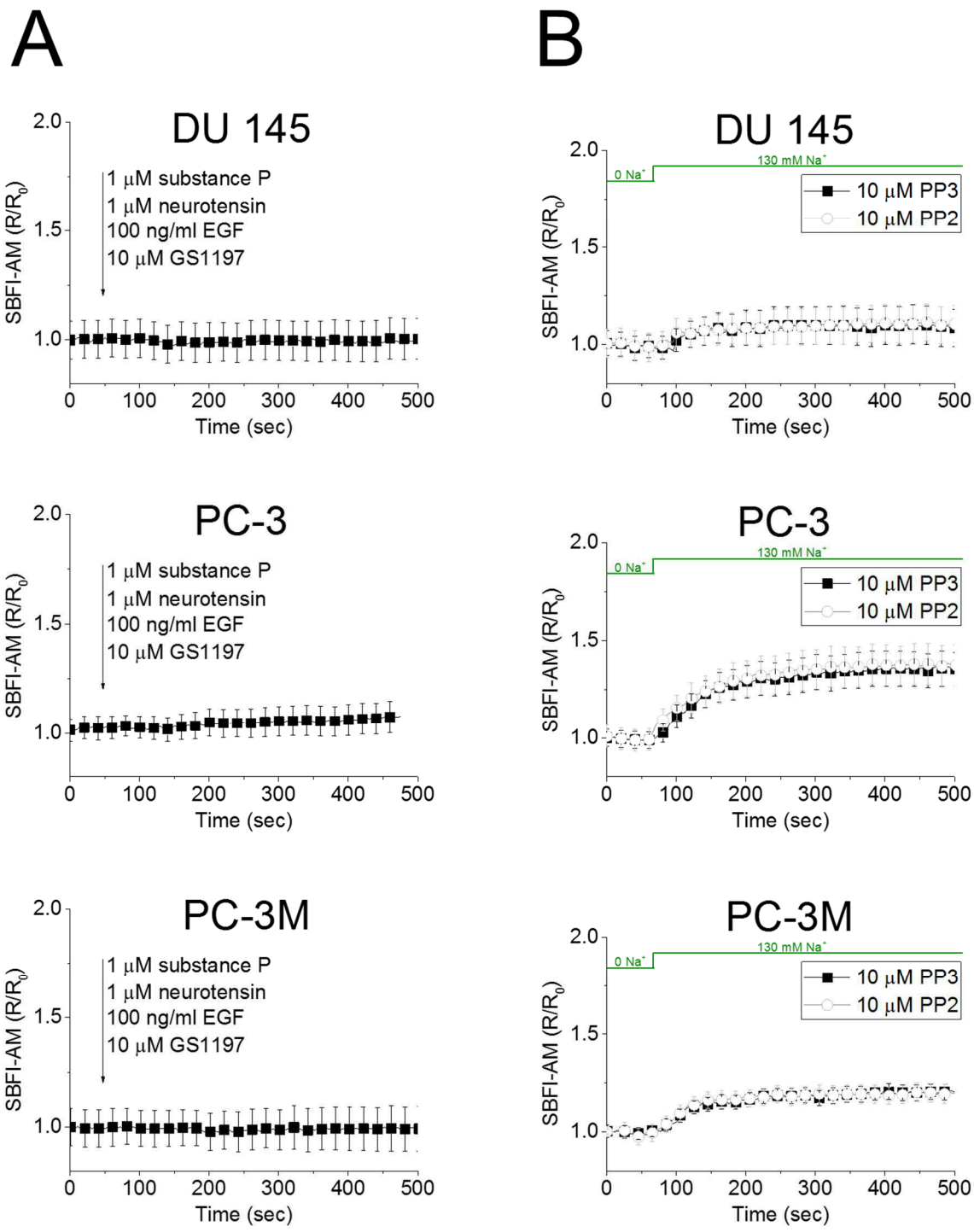

Figure 37. Effect of putative activators and inhibitors of NALCN channelosome on the basal Na^+ leak in human prostate cancer cells.
A, None of the putative activators of NALCN affected $[Na^+]_i$. **B**, inhibitor of Src kinase, PP2, did not change the rate of Na^+ influx evoked by extracellular Na^+ switch, when comparing with its negative control, PP3. Recordings of $[Na^+]_i$ were performed by using SBFI-AM dyes. The ratios of fluorescence 340 nm/ 380 nm were normalized to the initial ratio values and presented as R/R_0. (n=1).

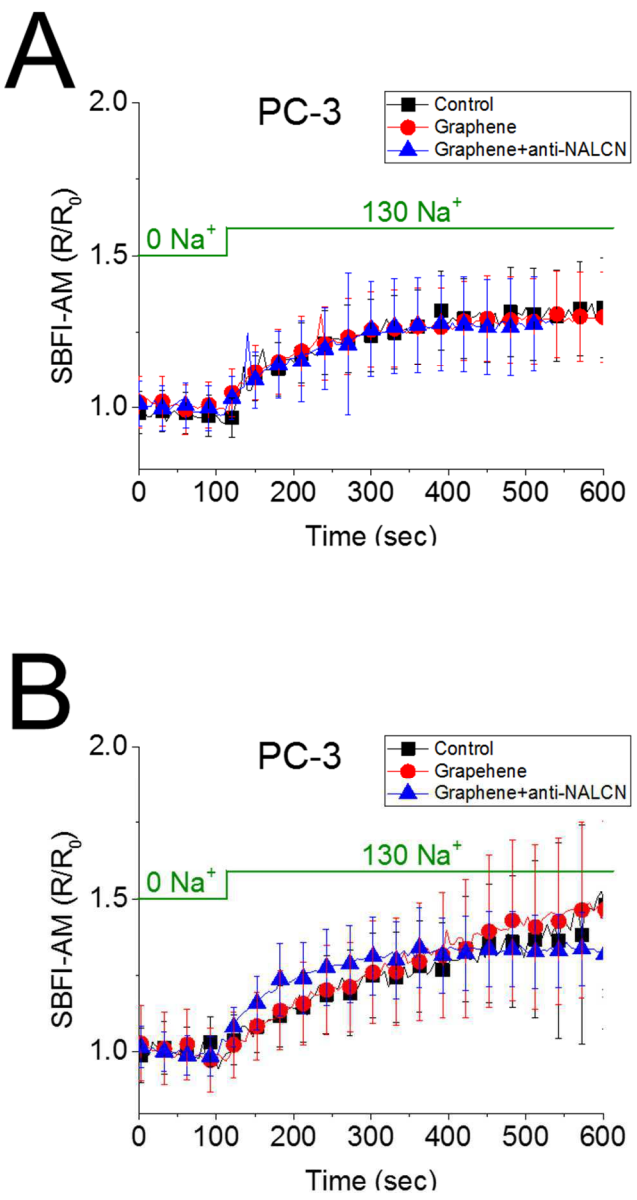

Figure 38. Effect of NALCN-antibody linked to graphene nanoparticles on Na^+ influx. **A**, 5 minutes of preincubation. **B**, 30 minutes of preincubation. Recordings of $[Na^+]_i$ were performed by using SBFI-AM dyes. The ratios of fluorescence 340 nm/ 380 nm were normalized to the initial ratio values and presented as R/R_0. (n=1).

3.2.8 NALCN mutations in human prostate cancer

NALCN mutations were previously reported in various human pathological conditions, including cancer disease (Ding *et al.*, 2010; Biankin *et al.*, 2012; De Las Rivas *et al.*, 2012; Lee *et al.*, 2013). However, nothing was yet known about their implication in prostate tumourigenesis. In our study, we have demonstrated association of NALCN with prostate cancer progression. Therefore, the screening for *NALCN* mutations was performed by Prof Olivier Cussenot (University Pierre et Marie Curie, Paris, France) and Prof Gaelle Fromont-Hankard (University of Tours, Tours, France) on the samples of patients with particularly highly aggressive forms of prostate cancer. Of note, this work was part of ICGC program funded by INCa.

According to the RNA sequencing (RNA-seq) results 3 SNPs were found within 25 patients analysed (Figure 39A). However, all of them were located in the non-coding regions (e.g. introns and 3' flank), and thus theoretically should not affect the protein structure. Nonetheless, non-coding elements might exhibit diverse roles in the regulation of protein-coding genes expression. Accordingly, sequence variants in non-coding regions may lead to gain or loss of DNA motifs that bind with repressors and transcription factors, whereas mutations in micro-RNA binding sites would result in enhanced target gene expression (Khurana *et al.*, 2016). Furthermore, pseudogene deletion would affect the competition for micro-RNA binding with the parent gene, and hence would affect the expression of the latter. For example, pseudogene of phosphatase and tensin homolog (*PTEN*) was found deleted in prostate cancer, and as a result more micro-RNAs were binding to the 3′- untranslated region (UTR) of the parental *PTEN* mRNA, leading to its downregulation (Poliseno *et al.*, 2010). In addition, UTRs were shown to regulate the localization, stability, and translation of their cognate mRNA, and thus mutations occurring in these regions may also affect the protein production. Finally, modifications of intronic sequences can affect the binding of the splice factors, which in turn would lead to differentially spliced or truncated products (Rajan *et al.*, 2009).

Importantly, in one patient *NALCN* was fused with *LUC7L3* gene that encodes cisplatin resistance-associated overexpressed protein (CROP), which is localized in nucleus and could be involved in splicesome formation (Figure 39B) (Nishii *et al.*, 2000). Fusion genes produce proteins with abnormal functions, and hence may contribute to tumour formation. One of the purposes of oncogenic fusion was proposed as follows: a proto-oncogene is fused to a stronger promoter, and thereby the oncogenic function is enhanced. Indeed, in lymphomas oncogene *c-MYC* was found juxtaposed to the promoters of the immunoglobulin heavy chain genes and associated with lymphomagenesis (Gostissa *et al.*, 2009).

A

3 mutations out of 121689 identified in 25 patients with aggressive prostate cancer

Tumour sample	Chromosome	Position	Variant type	Reference allele	Tumour allele	Variant class	HUGO symbol
PR12007	13	102057407	SNP	C	A	Intron	NALCN
PR12011	13	101702212	SNP	G	A	3' Flank	NALCN
PR1200E	13	102063142	SNP	T	A	Intron	NALCN

B

1 fusion out of 763 with high expression of the gene by RNAseq analysis

Tumour sample	HUGO symbol	Chromosome	Position	HUGO symbol	Chromosome	Position
PR12003	LUC7L3	17	48797191	NALCN	13	101910924

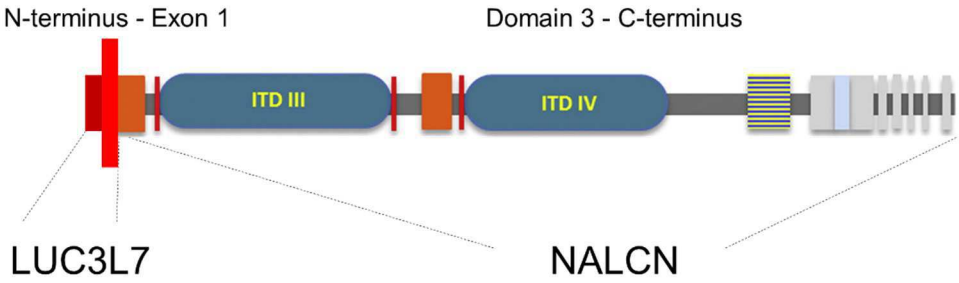

Figure 39. Summary of RNA-Seq for *NALCN* gene performed in 25 patients with aggressive prostate cancer.
A, For *NALCN* gene 3 silent SNP mutations were identified out of 121689. RNA-Seq results did not exhibit significant difference between non-cancerous (n=3) and tumour tissues (n=25) (data not shown). **B**, Interestingly, 1 fusion of *NALCN* with other gene *LUC7L3* that encodes nucleal cisplatin resistance-associated overexpressed protein was discovered. Of note, the nucleotide positions are indicated according to the previous assembly (dated by 2013), since the current assemblies were recently updated (October 2017). Of note, these results were provided by Prof Olivier Cussenot (University Pierre et Marie Curie, Paris, France) and Prof Gaelle Fromont-Hankard (University of Tours, Tours, France) as a part of ICGC program funded by INCa.

4. General conclusions

The main objective of this project was to investigate the role of NALCN in oncogenesis, in particular on the model of prostate cancer disease. Throughout this study we have achieved our established aims as follows:

4.1 Evolution of NALCN expression in human prostate cancer

NALCN was found in human prostate cancer cells lines on both mRNA and protein levels. Specifically, NALCN was expressed in strongly metastatic cancer cells DU 145, PC-3 and PC-3M, but not in the cells with low metastatic potential LNCaP and C4-2. In addition, screening within the pancreatic cells revealed NALCN presence in immortalized normal ductal cells HPDE6-H6C7, and in cancer cells BxPC3, Panc-1, Capan-1, but not in AsPC-1 and MiaPaCa-2. In addition, NALCN was found in healthy rat and mice prostate. Indeed, the results of immunohistochemistry revealed low/none NALCN expression in non-cancerous and early stages of prostate carcinogenesis and high levels of NALCN at more advanced stages of the disease development. Specifically, NALCN was found being overexpressed in the sites of metastases, when comparing with its primary tumours. It supports the hypothesis that NALCN is exclusively required in cancer cells with enhanced migration and invasion.

4.2 Functionality of NALCN channelosome in human prostate cancer cells

NALCN channel complex was reported to provide background Na^+ leak in neurons (Lu *et al.*, 2007), however, nothing was yet known about its function in cancer cells. Therefore, we screened for auxiliary subunits of NALCN channelosome in prostate cancer cells and compared their basal Na^+ influx. Interestingly, only cells expressing NALCN exhibited endogenous plasmalemmal Na^+ leak, whereas NALCN-negative cells were not changing their $[Na^+]_i$ in response to $[Na^+]_e$ switch. Of note, in DU 145 cells lacking UNC-80 subunit Na^+ leak was substantially lower than in PC-3 and PC-3M cells with full channelosome complex. Furthermore, C4-2 cells that possess high endogenous UNC-80 levels acquired remarkable Na^+ leak after NALCN overexpression, whereas NALCN silencing in PC-3 cells considerably inhibited Na^+ leak. Therefore, our results indicate that NALCN indeed represent Na^+ leak channel in human prostate cancer cells.

4.3 Prostate cancer cell behaviours regulated by NALCN

In order to investigate which role NALCN plays in prostate cancer cells, we have performed a number of tissue culture assays. Interestingly, NALCN silencing did not affect cellular viability, basal and induced apoptosis, cell cycle, and proliferation. However, in PC-3 cells NALCN

downregulation significantly suppressed cellular motility, lateral and transverse migration, invasion, invadopodia formation, gelatin degradation, secretion and activity of MMPs. Therefore, due to this study it has been revealed that NALCN potentiates metastatic cancer cell behaviours and is not required for cellular growth of prostate cancer cells *in vitro*.

4.4 Molecular mechanisms and signalling pathways involved in NALCN-mediated phenotype of the human prostate cancer cells

One of the aims of this study was to understand by which means Na^+ leak channel may contribute to the aggressive phenotype of prostate cancer cells. Importantly, previous studies reported on association of proto-oncogene Src kinase with NALCN channelosome (Lu *et al.*, 2009; Swayne *et al.*, 2009; Wang & Ren, 2009). Indeed, NALCN downregulation led to decreased expression and activity of Src kinase, supporting the previous findings that NALCN channelosome acts as a scaffold protein for the kinase. Recently, Ca^{2+} oscillations were demonstrated as an intrinsic molecular mechanism for Src kinase activation and invadopodia formation (Sun *et al.*, 2014). Moreover, Ca^{2+} oscillations were suggested to control secretion process (Wollman & Meyer, 2012). Interestingly, our results indicated that NALCN is an upstream regulator of Ca^{2+} oscillations and vesicle excretion in prostate cancer cells. Therefore, we suggest that NALCN potentiates invasion of cancer cells by the means of following mechanism: Na^+ leak governs Ca^{2+} oscillations that initiate invadopodia assembly through channelosome-guided Src kinase activation and simultaneously provide secretion of ECM-degrading enzymes like MMPs (Figure 40).

4.5 Role of NALCN on prostate carcinogenesis and tumour progression *in vivo*

In order to further assess importance of NALCN in tumourigenesis, the mice were injected with PC-3 cells endogenously expressing NALCN and cells with stable channel downregulation. Interestingly, NALCN suppression constrained tumour growth and metastases spread. Of note, the most frequent site of prostate cancer dissemination is represented by the bones. Importantly, NALCN silencing inhibited skeleton metastases and destruction of the bone tissue. Therefore, our *in vivo* results were in accordance with our *in vitro* results, indicating onto importance of NALCN in prostate tumour progression and metastasis disease.

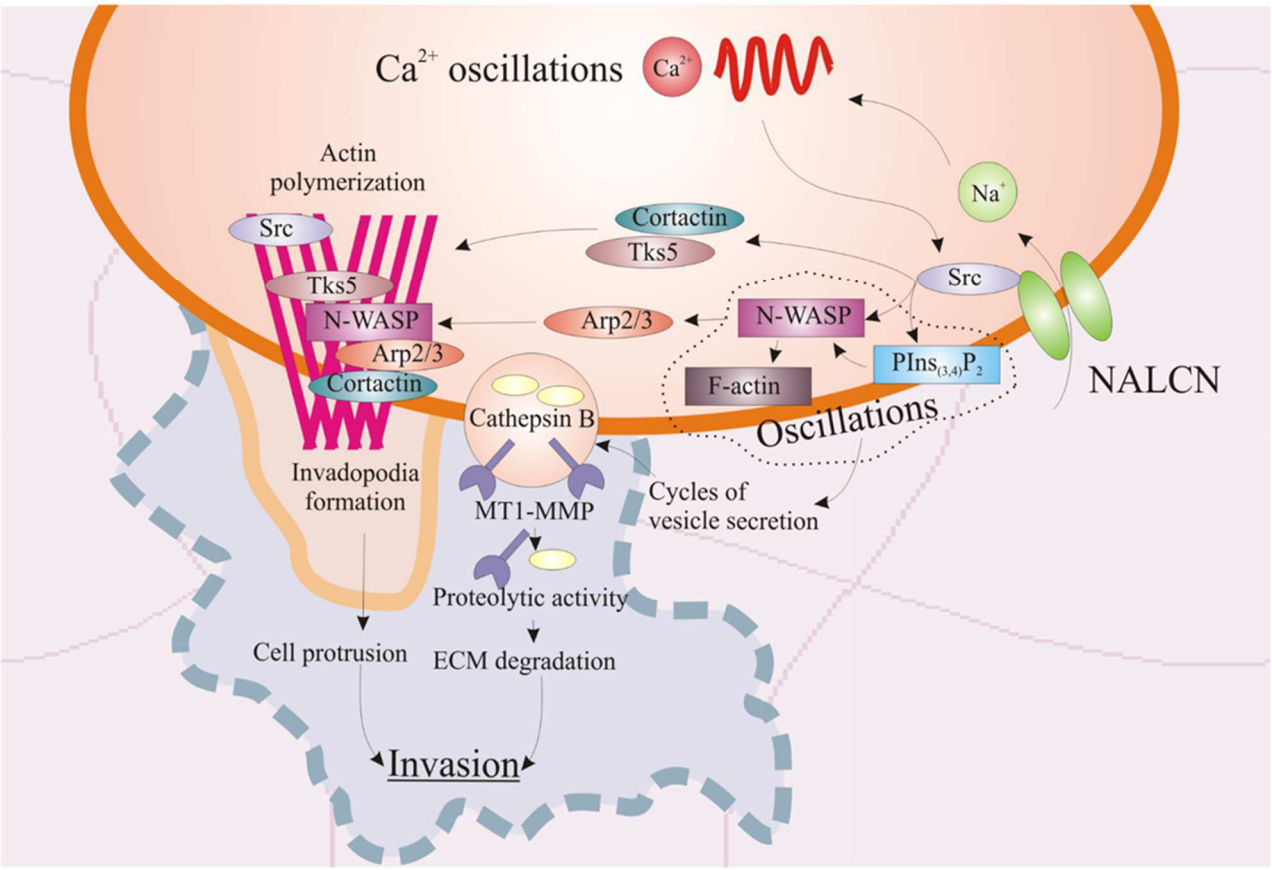

Figure 40. Schematic illustration of NALCN regulated molecular mechanism subserving into cancer cells invasiveness.

5. Perspectives

5.1 Mutations of NALCN channel complex in prostate cancer disease

Until now, the only evidence pointing onto NALCN channelosome implication in cancer disease was due to the results of genomic sequencing analysis. Indeed, NALCN was found within significantly mutated genes in basal-like breast cancer metastases and xenografts, pancreatic ductal adenocarcinoma, advanced non-small cell lung carcinoma, and glioblastoma (Ding *et al.*, 2010; Biankin *et al.*, 2012; De Las Rivas *et al.*, 2012; Lee *et al.*, 2013). In this study, the role of NALCN in tumourigenesis was shown for the first time by using the model of prostate cancer. Our preliminary results revealed several NALCN mutations in coding and non-coding regions within human prostate cancer patients (n=25) and cell lines DU 145, PC-3 and PC-3M. Therefore, it might be useful to expand the number of cancer patients in order to proceed with identification of cancer-associated *NALCN* mutations and its oncogenic potential. Moreover, analysis of other channelosome members might provide additional information.

5.2 Function of NALCN pore

In this study, we significantly affected prostate cancer cells aggressiveness due to the changes in NALCN expression. However, there is still an open question: whether NALCN promotes prostate cancer progression due to its function as a leak channel or rather due to some ion-independent down-stream signalling? In order to investigate this question, different pore mutants could be utilized. When being first functionally characterized, NALCN was reported being a non-selective cation channel possessing not only Na^+, but also K^+ and Ca^{2+} permeability (Lu *et al.*, 2007). The selectivity sequence was proposed as follows: P_{Na} (1.3) > P_K (1.2) > P_{Cs} (1.0) > P_{Ca} (0.5) (Lu *et al.*, 2007). Since Ca^{2+} represents ubiquitous intracellular second messenger and expression of K^+ leak channels decreases in prostate cancer, NALCN contribution into Ca^{2+} and K^+ signalling should be evaluated in human prostate cancer cells (Williams *et al.*, 2013). Interestingly, due to site-directed mutagenesis EEKE pore of NALCN channel was mutated onto EEKA and reported to provide gadolinium (Gd^{3+})-resistant current with decreased Ca^{2+} permeability: P_{Na} (1.3) = P_K (1.3) > P_{Cs} (1.0) > P_{Ca} (0.1) (Lu *et al.*, 2007). Furthermore, NALCN-EEEE mutant resembling the pore of voltage-gated Ca^{2+} channels (Cav1-2) was created, but it did not generate measurable currents in HEK293 cells and neurons (Lu *et al.*, 2007). Similarly, in *D. melanogaster* EEEE mutant did not restore the phenotype of wild-type EEKE channel (Lear *et al.*, 2005). Therefore, NALCN-EEKA and NALCN-EEEE overexpression in prostate cancer cells could be compared with the wild-type

NALCN-EEKE and assessed by Na^+ imaging, Ca^{2+} imaging, K^+ imaging, patch-clamp and tissue culture assays.

5.3 Implication of auxiliary subunits in prostate cancer progression

NALCN interacting proteins were shown being involved in the folding, stabilization, cellular localization, and to some extent activation of the channel. Therefore, investigation of the channelosome auxiliary subunits would provide more understanding in the mechanism of NALCN regulation during prostate carcinogenesis. Thus, UNC-80, UNC-79 and NLF-1 should be screened in healthy and non-cancerous prostate tissues. Furthermore, basal Na^+ leak and cancer-associated behaviours could be investigated after overexpression and silencing of the auxiliary subunits in human prostate cancer cell lines (e.g. PC-3 and PC-3M cells with full channel complex). Importantly, our immunohistochemical analysis already exhibited high correlation between NALCN and proto-oncogene Src kinase in prostate tumour biopsies. Moreover, in PC-3 cells stable NALCN suppression resulted in decreased Src kinase levels. However, it was not tested whether NALCN overexpression would enable Src kinase upregulation. Furthermore, *vice versa* effect of Src silencing or constant activation on the level of NALCN expression and intracellular localization was not investigated yet in prostate cancer cells. Moreover, recent study in *C. elegans* revealed that NCA-1/NCA-2, orthologues of mammalian NALCN, are downstream targets of G_q/Rho kinase pathway, which is known to be implemented in cancer progression (Sahai & Marshall, 2002; Topalidou *et al.*, 2017). Therefore, another axis of future studies could be focused on the investigation of NALCN regulation by Rho proteins during carcinogenesis. In addition, Rho proteins are known to be controlled by GPCRs and indeed NALCN has been reported to depend on functioning of the latter (Lu *et al.*, 2009, 2010; Swayne *et al.*, 2009). For example, M3R was shown to activate NALCN-current in pancreatic cells and to promote prostate cancer progression, which is in accordance with our current findings on NALCN (Swayne *et al.*, 2009; Magnon *et al.*, 2013). Therefore, M3R receptor might provide additional pathway for NALCN upregulation during prostate carcinogenesis. Interestingly, CaSR was shown to potentiate prostate cancer aggressiveness, and to inhibit NALCN-mediated background current in neurons (Lu *et al.*, 2010; Ahearn *et al.*, 2016). However, in our model of prostate cancer cells NALCN basal Na^+ leak was insensitive to $[Ca^{2+}]_e$. Therefore, it would be useful to investigate whether in prostate cancer cells CaSR affects NALCN in a similar manner as it was reported for neuronal cells or whether their relationship involves additional tissue-dependent mechanisms.

5.4 Store-operated calcium entry and NALCN

In this study we show for the first time that NALCN is substantial contributor into SOCE mechanism. Interestingly, relationship between SOCE and Na^+ influx was recently described on the model of HEK293T cells (Ben-Kasus Nissim *et al.*, 2017). Specifically, Ben-Kasus Nissim and colleagues pointed on the importance of mitochondrial Na^+/Ca^{2+} exchanger, NCLX, during SOCE activation. Accordingly, NCLX prevents toxicity of mitochondrial Ca^{2+} overload due to the sequestration of Ca^{2+} in exchange for Na^+ uptake and thus maintains SOCE activity. It highlights the significance of plasmalemmal Na^+ influx during SOCE as an additional source of cytosolic Na^+ required for cell survival. Indeed, our results revealed that during SOCE activation the presence of NALCN in plasma membrane as well as NALCN-mediated Na^+ influx are enhanced. However, the mechanism of SOCE-induced NALCN trafficking remains elusive. Therefore, several research strategies could be utilized in order to clarify this subject.

Furthermore, the major SOCE players, ORAI and STIM proteins, were reported to interact with other channels and hence to activate supplementary pathways for plasmalemmal ion influx. For example, TRPC1 channel, was reported to contribute into SOCE and to regulate various functions in many cell types (Ambudkar *et al.*, 2017). Indeed, STIM1 was shown to activate TRPC1 via its C-terminal polybasic domain, which is distinct from the STIM1-ORAI activating region. In addition, TRPC1 function critically depends on ORAI1-mediated Ca^{2+} entry which triggers recruitment of TRPC1 into the plasma membrane where it is then activated by STIM1 (Ambudkar *et al.*, 2017). Of note, staining for NALCN in human prostate biopsies significantly correlated with ORAI1, STIM1, and STIM2. Therefore, in order to investigate whether analogous to TRPC1 recruitment might be exploited during SOCE-induced NALCN trafficking, coimmunoprecipitation analysis between NALCN and major SOCE proteins, ORAI1-3 and STIM1-2, should be compared before and after ER store depletion in human prostate cancer cells.

5.5 NALCN-mediated molecular mechanisms and intracellular signalling

Although in our study we suggest NALCN-mediated molecular mechanism and intracellular signalling pathway that promotes prostate cancer aggressiveness, some principal questions remain unaddressed.

For example, in this study we suggested the link between NALCN and mitochondrial NCLX. Previously, NCLX was reported to regulate SOCE due to its role in preventing the production of ROS and subsequent ORAI inactivation (Ben-Kasus Nissim *et al.*, 2017). However, it was not confirmed in our model of prostate cancer cells. Therefore, it would be useful to verify whether indeed silencing of NCLX and NALCN leads to increased ROS levels in PC-3 cells.

Furthermore, previous studies reported that Na^+ influx provided by voltage-gated sodium channels, Nav, increases activity NHE1, which in turn increases H^+ efflux and hence activates acidic-dependent ECM-degrading enzymes, cathepsins (Brisson *et al.*, 2011). Thus, Na^+ influx was suggested to potentiate cancer cell invasiveness due to the upregulation of NHE1. However, nothing is yet known about relationship between basal Na^+ leak provided by NALCN and functioning of NHE1 during carcinogenesis.

In addition, we provided evidence that short-term hypoxia enhanced NALCN expression in strongly metastatic prostate cancer cells. However, the particular mechanism of this upregulation was not investigated.

Moreover, in our stable NALCN knockdown cells we observed some striking differences in the protein level of iPLA2, cathepsin B, src kinase, Fyn, Tks5, FAK, and Pyk2. Therefore, it should be investigated whether such changes in expression are conditioned by impaired transcription or by dysregulated protein degradation.

Interestingly, FAK and Pyk2 are both focal adhesion kinases. Importantly, NALCN suppression led to FAK inhibition and Pyk2 upregulation, which is consistent with less aggressive profile of prostate cancer (Stanzione *et al.*, 2001). Therefore, attachment and detachment properties of prostate cancer cells should be changed upon NALCN downregulation. It could provide additional insights into NALCN-associated metastatic cancer cell behaviours, and should be determined in the further studies.

6. List of references

Abruzzi KC, Rodriguez J, Menet JS, Desrochers J, Zadina A, Luo W, Tkachev S & Rosbash M (2011). Drosophila CLOCK target gene characterization: Implications for circadian tissue-specific gene expression. *Genes Dev* **25,** 2374–2386.

Adeyemo A, Gerry N, Chen G, Herbert A, Doumatey A, Huang H, Zhou J, Lashley K, Chen Y, Christman M & Rotimi C (2009). A genome-wide association study of hypertension and blood pressure in African Americans. *PLoS Genet* **5,** e1000564.

Agelopoulos K et al. (2015). Deep sequencing in conjunction with expression and functional analyses reveals activation of FGFR1 in Ewing sarcoma. *Clin Cancer Res* **21,** 4935–4946.

Ahearn TU, Tchrakian N, Wilson KM, Lis R, Nuttall E, Sesso HD, Loda M, Giovannucci E, Mucci LA, Finn S & Shui IM (2016). Calcium-sensing receptor tumor expression and lethal prostate cancer progression. *J Clin Endocrinol Metab* **101,** 2520–2527.

Ahern CA, Zhang JF, Wookalis MJ & Horn R (2005). Modulation of the cardiac sodium channel Nav1.5 by Fyn, a Src family tyrosine kinase. *Circ Res* **96,** 991–998.

Al-Sayed MD, Al-Zaidan H, Albakheet A, Hakami H, Kenana R, Al-Yafee Y, Al-Dosary M, Qari A, Al-Sheddi T, Al-Muheiza M, Al-Qubbaj W, Lakmache Y, Al-Hindi H, Ghaziuddin M, Colak D & Kaya N (2013). Mutations in NALCN cause an autosomal-recessive syndrome with severe hypotonia, speech impairment, and cognitive delay. *Am J Hum Genet* **93,** 721–726.

Ambudkar IS, de Souza LB & Ong HL (2017). TRPC1, Orai1, and STIM1 in SOCE: Friends in tight spaces. *Cell Calcium* **63,** 33–39.

Andrikopoulos P, Baba A, Matsuda T, Djamgoz MBA, Yaqoob MM & Eccles SA (2011). Ca2+ influx through reverse mode Na+/Ca2+ exchange is critical for vascular endothelial growth factor-mediated extracellular signal-regulated kinase (ERK) 1/2 activation and angiogenic functions of human endothelial cells. *J Biol Chem* **286,** 37919–37931.

Anney RJL et al. (2008). Conduct disorder and ADHD: Evaluation of conduct problems as a categorical and quantitative trait in the international multicentre ADHD genetics study. *Am J Med Genet Part B Neuropsychiatr Genet* **147,** 1369–1378.

Aoyagi K, Rossignol E, Hamdan FF, Mulcahy B, Xie L, Nagamatsu S, Rouleau GA, Zhen M & Michaud JL (2015). A Gain-of-Function Mutation in NALCN in a Child with Intellectual Disability, Ataxia, and Arthrogryposis. *Hum Mutat* **36,** 753–757.

Askland K, Read C & Moore J (2009). Pathways-based analyses of whole-genome association study data in bipolar disorder reveal genes mediating ion channel activity and synaptic neurotransmission. *Hum Genet* **125,** 63–79.

Balaban H, Bayrakli F, Kartal U, Pinarbasi E, Topaktas S & Kars HZ (2012). A novel locus for restless legs syndrome on chromosome 13q. *Eur Neurol* **68,** 111–116.

Balasubramaniam SL, Gopalakrishnapillai A, Gangadharan V, Duncan RL & Barwe SP (2015). Sodium-calcium exchanger 1 regulates epithelial cell migration via calcium-dependent extracellular signal-regulated kinase signaling. *J Biol Chem* **290,** 12463–12473.

Baum AE et al. (2008). A genome-wide association study implicates diacylglycerol kinase eta (DGKH) and several other genes in the etiology of bipolar disorder. *Mol Psychiatry* **13,** 197–207.

Ben-Kasus Nissim T, Zhang X, Elazar A, Roy S, Stolwijk JA, Zhou Y, Motiani RK, Gueguinou M, Hempel N, Hershfinkel M, Gill DL, Trebak M & Sekler I (2017). Mitochondria control store-operated Ca2+ entry through Na+ and redox signals. *EMBO J* **36,** 797–815.

Bend EG, Si Y, Stevenson DA, Bayrak-Toydemir P, Newcomb TM, Jorgensen EM & Swoboda KJ (2016). NALCN channelopathies. *Neurology* **87,** 1131–1139.

Besson P, Driffort V, Bon É, Gradek F, Chevalier S & Roger S (2015). How do voltage-gated sodium channels enhance migration and invasiveness in cancer cells? *Biochim Biophys Acta - Biomembr* **1848,** 2493–2501.

Biankin A V. et al. (2012). Pancreatic cancer genomes reveal aberrations in axon guidance pathway genes. *Nature* **491,** 399–405.

Borowiec AS, Delcourt P, Dewailly E & Bidaux G (2013). Optimal Differentiation of In Vitro Keratinocytes Requires Multifactorial External Control. *PLoS One*; DOI: 10.1371/journal.pone.0077507.

Bouhours M, Po MD, Gao S, Hung W, Li H, Georgiou J, Roder JC & Zhen M (2011). A co-operative regulation of neuronal excitability by UNC-7 innexin and NCA/NALCN leak channel. *Mol Brain*; DOI: 10.1186/1756-6606-4-16.

El Boustany C, Bidaux G, Enfissi A, Delcourt P, Prevarskaya N & Capiod T (2008). Capacitative calcium entry and transient receptor potential canonical 6 expression control human hepatoma cell proliferation. *Hepatology* **47,** 2068–2077.

Brackenbury WJ (2016). Ion Channels in Cancer. In *Ion Channels in Health and Disease*, pp. 131–163.

Brisson L, Driffort V, Benoist L, Poet M, Counillon L, Antelmi E, Rubino R, Besson P, Labbal F, Chevalier S, Reshkin SJ, Gore J & Roger S (2013). NaV1.5 Na+ channels allosterically regulate the NHE-1 exchanger and promote the activity of breast cancer cell invadopodia. *J Cell Sci* **126,** 4835–4842.

Brisson L, Gillet L, Calaghan S, Besson P, Le Guennec JY, Roger S & Gore J (2011). Nav1.5

enhances breast cancer cell invasiveness by increasing NHE1-dependent H+ efflux in caveolae. *Oncogene* **30,** 2070–2076.

Burg ED, Langan ST & Nash HA (2013). Drosophila social clustering is disrupted by anesthetics and in narrow abdomen ion channel mutants. *Genes, Brain Behav* **12,** 338–347.

Burger KL, Learman BS, Boucherle AK, Sirintrapun SJ, Isom S, Díaz B, Courtneidge SA & Seals DF (2014). Src-dependent Tks5 phosphorylation regulates invadopodia-associated invasion in prostate cancer cells. *Prostate* **74,** 134–148.

Busco G, Cardone RA, Greco MR, Bellizzi A, Colella M, Antelmi E, Mancini MT, Dell'Aquila ME, Casavola V, Paradiso A & Reshkin SJ (2010). NHE1 promotes invadopodial ECM proteolysis through acidification of the peri-invadopodial space. *FASEB J* **24,** 3903–3915.

Campbell DB & Nash H a (1994). Use of Drosophila mutants to distinguish among volatile general anesthetics. *Proc Natl Acad Sci U S A* **91,** 2135–2139.

Cardone RA, Casavola V & Reshkin SJ (2005). The role of disturbed pH dynamics and the Na+/H+ exchanger in metastasis. *Nat Rev Cancer*; DOI: 10.1038/nrc1713.

Carrithers MD, Chatterjee G, Carrithers LM, Offoha R, Iheagwara U, Rahner C, Graham M & Waxman SG (2009). Regulation of podosome formation in macrophages by a splice variant of the sodium channel SCN8A. *J Biol Chem* **284,** 8114–8126.

Catterall W a (2012). Voltage-gated sodium channels at 60: structure, function and pathophysiology. *J Physiol*; DOI: 10.1113/jphysiol.2011.224204.

Chédotal A, Kerjan G & Moreau-Fauvarque C (2005). The brain within the tumor: New roles for axon guidance molecules in cancers. *Cell Death Differ* **12,** 1044–1056.

Chong JX et al. (2015). De novo mutations in NALCN cause a syndrome characterized by congenital contractures of the limbs and face, hypotonia, and developmental delay. *Am J Hum Genet* **96,** 462–473.

Cochet-Bissuel M, Lory P & Monteil A (2014). The sodium leak channel, NALCN, in health and disease. *Front Cell Neurosci*; DOI: 10.3389/fncel.2014.00132.

Courtneidge SA, Azucena EF, Pass I, Seals DF & Tesfay L (2005). The Src substrate Tks5, podosomes (Invadopodia), and cancer cell invasion. In *Cold Spring Harbor Symposia on Quantitative Biology*, pp. 167–171.

Davies AG, Friedberg RI, Gupta H, Chan CL, Shelton KL & Bettinger JC (2012). Different genes influence toluene- and ethanol-induced locomotor impairment in C. elegans. *Drug Alcohol Depend* **122,** 47–54.

Detera-Wadleigh SD & McMahon FJ (2006). G72/G30 in Schizophrenia and Bipolar Disorder: Review and Meta-analysis. *Biol Psychiatry* **60,** 106–114.

Ding L et al. (2010). Genome remodelling in a basal-like breast cancer metastasis and xenograft. *Nature* **464,** 999–1005.

Djamgoz MB a & Onkal R (2013). Persistent current blockers of voltage-gated sodium channels: a clinical opportunity for controlling metastatic disease. *Recent Pat Anticancer Drug Discov* **8,** 66–84.

Dong H, Shim K-N, Li JMJ, Estrema C, Ornelas T a, Nguyen F, Liu S, Ramamoorthy SL, Ho S, Carethers JM & Chow JYC (2010). Molecular mechanisms underlying Ca2+-mediated motility of human pancreatic duct cells. *Am J Physiol Cell Physiol*; DOI: 10.1152/ajpcell.00242.2010.

Dubois C, Vanden Abeele F, Lehen'kyi V, Gkika D, Guarmit B, Lepage G, Slomianny C, Borowiec A, Bidaux G, Benahmed M, Shuba Y & Prevarskaya N (2014). Remodeling of Channel-Forming ORAI Proteins Determines an Oncogenic Switch in Prostate Cancer. *Cancer Cell* **26,** 19–32.

Dudev T & Lim C (2014). Evolution of eukaryotic ion channels: Principles Underlying the conversion of Ca2+-selective to Na+-selective channels. *J Am Chem Soc* **136,** 3553–3559.

Erdmann K, Kaulke K, Thomae C, Huebner D, Sergon M, Froehner M, Wirth MP & Fuessel S (2014). Elevated expression of prostate cancer-associated genes is linked to down-regulation of microRNAs. *BMC Cancer*; DOI: 10.1186/1471-2407-14-82.

Farfariello V, Iamshanova O, Germain E, Fliniaux I & Prevarskaya N (2015). Calcium homeostasis in cancer: A focus on senescence. *Biochim Biophys Acta*; DOI: 10.1016/j.bbamcr.2015.03.005.

Fiorio Pla A, Kondratska K & Prevarskaya N (2016). STIM and ORAI proteins: crucial roles in hallmarks of cancer. *Am J Physiol Physiol* **310,** C509–C519.

Fizazi K (2007). The role of Src in prostate cancer. *Ann Oncol* **18,** 1765–1773.

Flourakis M, Kula-Eversole E, Hutchison AL, Han TH, Aranda K, Moose DL, White KP, Dinner AR, Lear BC, Ren D, Diekman CO, Raman IM & Allada R (2015). A Conserved Bicycle Model for Circadian Clock Control of Membrane Excitability. *Cell* **162,** 836–848.

Franciolini F & Petris a (1989). Evolution of ionic channels of biological membranes. *Mol Biol Evol*.

Fridlyand LE, Jacobson DA & Philipson LH (2013). Ion channels and regulation of insulin secretion in human β-cells :A computational systems analysis. *Islets* **5,** 1–15.

Fukai R, Saitsu H, Okamoto N, Sakai Y, Fattal-Valevski A, Masaaki S, Kitai Y, Torio M, Kojima-Ishii K, Ihara K, Chernuha V, Nakashima M, Miyatake S, Tanaka F, Miyake N & Matsumoto N (2016). De novo missense mutations in NALCN cause developmental and intellectual

impairment with hypotonia. *J Hum Genet* **61,** 451–455.

Funato H et al. (2016). Forward-genetics analysis of sleep in randomly mutagenized mice. *Nature*; DOI: 10.1038/nature20142.

Furukawa H, Singh SK, Mancusso R & Gouaux E (2005). Subunit arrangement and function in NMDA receptors. *Nature* **438,** 185–192.

Gal M, Magen D, Zahran Y, Eran A, Khayat M, Gafni C, Levanon EY, Mandel H & Ravidi S (2016). A novel homozygous splice site mutation in NALCN identified in siblings with cachexia, strabismus, severe intellectual disability, epilepsy and abnormal respiratory rhythm. *Eur J Med Genet* **59,** 204–209.

Gao L, Fang YQ, Zhang TY, Ge B, Tang RJ, Huang JF, Jiang LM & Tan N (2015). Acidic extracellular microenvironment promotes the invasion and cathepsin B secretion of PC-3 cells. *Int J Clin Exp Med* **8,** 7367–7373.

Ghezzi A, Liebeskind BJ, Thompson A, Atkinson NS & Zakon HH (2014). Ancient association between cation leak channels and Mid1 proteins is conserved in fungi and animals. *Front Mol Neurosci*; DOI: 10.3389/fnmol.2014.00015.

Gillet L, Roger S, Besson P, Lecaille F, Gore J, Bougnoux P, Lalmanach G & Le Guennec J-Y (2009). Voltage-gated Sodium Channel Activity Promotes Cysteine Cathepsin-dependent Invasiveness and Colony Growth of Human Cancer Cells. *J Biol Chem* **284,** 8680–8691.

Gómez-Garre P et al. (2014). Lack of validation of variants associated with cervical dystonia risk: A GWAS replication study. *Mov Disord* **29,** 1825–1828.

Gonzalez MJ, Miranda-Massari JR, Berdiel MJ, Duconge J, Rodríguez-López JL, Hunninghake R & Cobas-Rosario VJ (2014). High dose intraveneous Vitamin C and chikungunya fever: A case report. *J Orthomol Med* **29,** 154–156.

Gostissa M, Yan CT, Bianco JM, Cogné M, Pinaud E & Alt FW (2009). Long-range oncogenic activation of Igh-c-myc translocations by the Igh 3′ regulatory region. *Nature* **462,** 803–807.

Grupe A et al. (2007). Evidence for novel susceptibility genes for late-onset Alzheimer's disease from a genome-wide association study of putative functional variants. *Hum Mol Genet* **16,** 865–873.

Guan Z, Scott RL & Nash H a (2000). A new assay for the genetic study of general anesthesia in Drosophila melanogaster: Use in analysis of mutations in the X-chromosomal 12E region. *J Neurogenet* **14,** 25–42.

Gudermann T & Roelle S (2006). Calcium-dependent growth regulation of small cell lung cancer cells by neuropeptides. *Endocr Relat Cancer* **13,** 1069–1084.

Henzler T, Konstandin S, Schmid-Bindert G, Apfaltrer P, Haneder S, Wenz F, Schad L, Manegold

C, Schoenberg SO & Fink C (2012). Imaging of tumor viability in lung cancer: initial results using 23Na-MRI. *RöFo - Fortschritte auf dem Gebiet der Röntgenstrahlen und der Bildgeb Verfahren* **184,** 340–344.

Hirschfield GM et al. (2009). Primary biliary cirrhosis associated with HLA, IL12A, and IL12RB2 variants. *N Engl J Med* **360,** 2544–2555.

Holzmann C et al. (2015). Transient receptor potential melastatin 4 channel contributes to migration of androgen-insensitive prostate cancer cells. *Oncotarget* **6,** 41783–41793.

Horoszewicz JS, Leong SS, Chu TM, Wajsman ZL, Friedman M, Papsidero L, Kim U, Chai LS, Kakati S, Arya SK & Sandberg AA (1980). The LNCaP cell line - a new model for studies on human prostatic carcinoma. *Prog Clin Biol Res* **37,** 115–132.

Huang C, Yang YF, Yin N, Chen JL, Wang J, Zhang H & Tan ZP (2012). Congenital heart defect and mental retardation in a patient with a 13q33.1-34 deletion. *Gene* **498,** 308–310.

Humphrey JA, Hamming KS, Thacker CMM, Scott RL, Sedensky MMM, Snutch TP, Morgan PGG & Nash HA (2007). A Putative Cation Channel and Its Novel Regulator: Cross-Species Conservation of Effects on General Anesthesia. *Curr Biol* **17,** 624–629.

Iamshanova O, Fiorio Pla A & Prevarskaya N (2017). Molecular mechanisms of tumour invasion: regulation by calcium signals. *J Physiol* **595,** 3063–3075.

Iamshanova O, Mariot P, Lehen'kyi V & Prevarskaya N (2016). Comparison of fluorescence probes for intracellular sodium imaging in prostate cancer cell lines. *Eur Biophys J* **45,** 765–777.

Ifuku M, Farber K, Okuno Y, Yamakawa Y, Miyamoto T, Nolte C, Merrino VF, Kita S, Iwamoto T, Komuro I, Wang B, Cheung G, Ishikawa E, Ooboshi H, Bader M, Wada K, Kettenmann H & Noda M (2007). Bradykinin-Induced Microglial Migration Mediated by B1-Bradykinin Receptors Depends on Ca2+ Influx via Reverse-Mode Activity of the Na+/Ca2+ Exchanger. *J Neurosci* **27,** 13065–13073.

Iossifov I et al. (2012). De Novo Gene Disruptions in Children on the Autistic Spectrum. *Neuron* **74,** 285–299.

Jacobs MA, Ouwerkerk R, Wolff AC, Gabrielson E, Warzecha H, Jeter S, Bluemke DA, Wahl R & Stearns V (2011). Monitoring of neoadjuvant chemotherapy using multiparametric, 23Na sodium MR, and multimodality (PET/CT/MRI) imaging in locally advanced breast cancer. *Breast Cancer Res Treat* **128,** 119–126.

Jang DH, Chae H & Kim M (2015). Autistic and Rett-like features associated with 2q33.3-q34 interstitial deletion. *Am J Med Genet Part A* **167,** 2213–2218.

Jelassi B, Chantme A, Alcaraz-Pérez F, Baroja-Mazo A, Cayuela ML, Pelegrin P, Surprenant A

& Roger S (2011). P2X 7 receptor activation enhances SK3 channels- and cystein cathepsin-dependent cancer cells invasiveness. *Oncogene* **30,** 2108–2122.

Jentsch TJ (2016). VRACs and other ion channels and transporters in the regulation of cell volume and beyond. *Nat Rev Mol Cell Biol*; DOI: 10.1038/nrm.2016.29.

Jiang WG et al. (2015). Tissue invasion and metastasis: Molecular, biological and clinical perspectives. *Semin Cancer Biol* **35,** S244–S275.

Jonkman JEN, Cathcart JA, Xu F, Bartolini ME, Amon JE, Stevens KM & Colarusso P (2014). An introduction to the wound healing assay using live-cell microscopy. *Cell Adhes Migr* **8,** 440–451.

Jospin M, Watanabe S, Joshi D, Young S, Hamming K, Thacker C, Snutch TP, Jorgensen EM & Schuske K (2007). UNC-80 and the NCA Ion Channels Contribute to Endocytosis Defects in Synaptojanin Mutants. *Curr Biol*; DOI: 10.1016/j.cub.2007.08.036.

Kaighn ME, Narayan KS, Ohnuki Y, Lechner JF & Jones LW (1979). Establishment and characterization of a human prostatic carcinoma cell line (PC-3). *Invest Urol* **17,** 16–23.

Kang HJ et al. (2011). Spatio-temporal transcriptome of the human brain. *Nature* **478,** 483–489.

Kapoor A, Auer DR, Lee D, Chatterjee S & Chakravarti A (2017). Testing the Ret and Sema3d genetic interaction in mouse enteric nervous system development. *Hum Mol Genet* **26,** 1811–1820.

Kapoor N, Bartoszewski R, Qadri YJ, Bebok Z, Bublen JK, Fuller CM & Benos DJ (2009). Knockdown of ASIC1 and epithelial sodium channel subunits inhibits glioblastoma whole cell current and cell migration. *J Biol Chem* **284,** 24526–24541.

Karakaya M, Heller R, Kunde V, Zimmer KP, Chao CM, Nürnberg P & Cirak S (2016). Novel Mutations in the Nonselective Sodium Leak Channel (NALCN) Lead to Distal Arthrogryposis with Increased Muscle Tone. *Neuropediatrics* **47,** 273–277.

Kasap M, Bonnett K, Aamodt EJ & Dwyer DS (2017). Akinesia and freezing caused by Na+ leak-current channel (NALCN) deficiency corrected by pharmacological inhibition of K+ channels and gap junctions. *J Comp Neurol* **525,** 1109–1121.

Khurana E, Fu Y, Chakravarty D, Demichelis F, Rubin MA & Gerstein M (2016). Role of non-coding sequence variants in cancer. *Nat Rev Genet* **17,** 93–108.

Kim BJ, Chang IY, Choi S, Jun JY, Jeon JH, Xu WX, Kwon YK, Ren D & So I (2012). Involvement of Na +-leak channel in substance P-induced depolarization of pacemaking activity in interstitial cells of Cajal. *Cell Physiol Biochem* **29,** 501–510.

Kirchhoff M, Bisgaard AM, Stoeva R, Dimitrov B, Gillessen-Kaesbach G, Fryns JP, Rose H, Grozdanova L, Ivanov I, Keymolen K, Fagerberg C, Tranebjaerg L, Skovby F & Stefanova

M (2009). Phenotype and 244k array-cgh characterization of chromosome 13q deletions: An update of the phenotypic map of 13q21.1-qter. *Am J Med Genet Part A* **149,** 894–905.

Kiss T (2008). Persistent Na-channels: Origin and function. *Acta Biol Hung* **59,** 1–12.

Kogan I, Goldfinger N, Milyavsky M, Cohen M, Shats I, Dobler G, Klocker H, Wasylyk B, Voller M, Aalders T, Schalken JA, Oren M & Rotter V (2006). hTERT-immortalized prostate epithelial and stromal-derived cells: An authentic in vitro model for differentiation and carcinogenesis. *Cancer Res* **66,** 3531–3540.

Köroğlu Ç, Seven M & Tolun A (2013). Recessive truncating NALCN mutation in infantile neuroaxonal dystrophy with facial dysmorphism. *J Med Genet* **50,** 515–520.

Kozlowski JM, Fidler IJ, Campbell D, Xu ZL, Kaighn ME & Hart IR (1984). Metastatic behavior of human tumor cell lines grown in the nude mouse. *Cancer Res* **44,** 3522–3529.

Krishnan KS & Nash HA (1990). A genetic study of the anesthetic response: Mutants of Drosophila melanogaster altered in sensitivity to halothane. *Genetics* **87,** 8632–8636.

Lalani SR et al. (2013). Rare DNA copy number variants in cardiovascular malformations with extracardiac abnormalities. *Eur J Hum Genet*; DOI: 10.1038/ejhg.2012.155.

De Las Rivas J, Fontanillo C, Aibar S & Sanchez-Santos JM (2012). Combined analysis of genome-wide expression and copy number profiles to identify key altered genomic regions in cancer. *BMC Genomics* **13 Suppl 5,** S5.

Lear BC, Darrah EJ, Aldrich BT, Gebre S, Scott RL, Nash HA & Allada R (2013). UNC79 and UNC80, putative auxiliary subunits of the NARROW ABDOMEN ion channel, are indispensable for robust circadian locomotor rhythms in Drosophila. *PLoS One*; DOI: 10.1371/journal.pone.0078147.

Lear BC, Lin JM, Keath JR, McGill JJ, Raman IM & Allada R (2005). The ion channel narrow abdomen is critical for neural output of the Drosophila circadian pacemaker. *Neuron* **48,** 965–976.

Lee JH, Barral S, Cheng R, Chacon I, Santana V, Williamson J, Lantigua R, Medrano M, Jimenez-Velazquez IZ, Stern Y, Tycko B, Rogaeva E, Wakutani Y, Kawarai T, St George-Hyslop P & Mayeux R (2008). Age-at-onset linkage analysis in Caribbean Hispanics with familial late-onset Alzheimer's disease. *Neurogenetics* **9,** 51–60.

Lee JH, Cribbs LL & Perez-Reyes E (1999). Cloning of a novel four repeat protein related to voltage-gated sodium and calcium channels. *FEBS Lett*; DOI: 10.1016/S0014-5793(99)00082-4.

Lee Y, Yoon K-A, Joo J, Lee D, Bae K, Han J-Y & Lee JS (2013). Prognostic implications of genetic variants in advanced non-small cell lung cancer: a genome-wide association study.

Carcinogenesis **34,** 307–313.

LELE KP, PENROSE LS & STALLARD HB (1963). Chromosome deletion in a case of retinoblastoma. *Ann Hum Genet* **27,** 171–174.

Li M et al. (2014). Whole-exome and targeted gene sequencing of gallbladder carcinoma identifies recurrent mutations in the ErbB pathway. *Nat Genet* **46,** 872–876.

Li Z & Xie Z (2009). The Na/K-ATPase/Src complex and cardiotonic steroid-activated protein kinase cascades. *Pflugers Arch Eur J Physiol* **457,** 635–644.

Liebeskind BJ, Hillis DM & Zakon HH (2012). Phylogeny unites animal sodium leak channels with fungal calcium channels in an ancient, voltage-insensitive clade. In *Molecular Biology and Evolution*.

Lind PA, Macgregor S, Vink JM, Pergadia ML, Hansell NK, De Moor MHM, Smit AB, Hottenga J-JJ, Richter MM, Heath AC, Martin NG, Willemsen G, De Geus EJC, Vogelzangs N, Penninx BW, Whitfield JB, Montgomery GW, Boomsma DI & Madden PAF (2010). A genomewide association study of nicotine and alcohol dependence in Australian and Dutch populations. *Twin Res Hum Genet* **13,** 10–29.

Liu J & Xie ZJ (2010). The sodium pump and cardiotonic steroids-induced signal transduction protein kinases and calcium-signaling microdomain in regulation of transporter trafficking. *Biochim Biophys Acta - Mol Basis Dis* **1802,** 1237–1245.

Livak KJ & Schmittgen TD (2001). Analysis of relative gene expression data using real-time quantitative PCR and the 2-ΔΔCT method. *Methods* **25,** 402–408.

Lozic B, Johansson S, Lovric Kojundzic S, Markic J, Knappskog PM, Hahn AF & Boman H (2016). Novel NALCN variant: altered respiratory and circadian rhythm, anesthetic sensitivity. *Ann Clin Transl Neurol* **3,** 876–883.

Lu B, Su Y, Das S, Liu J, Xia J & Ren D (2007). The Neuronal Channel NALCN Contributes Resting Sodium Permeability and Is Required for Normal Respiratory Rhythm. *Cell* **129,** 371–383.

Lu B, Su Y, Das S, Wang H, Wang Y, Liu J & Ren D (2009). Peptide neurotransmitters activate a cation channel complex of NALCN and UNC-80. *Nature* **457,** 741–744.

Lu B, Zhang Q, Wang H, Wang Y, Nakayama M & Ren D (2010). Extracellular Calcium Controls Background Current and Neuronal Excitability via an UNC79-UNC80-NALCN Cation Channel Complex. *Neuron* **68,** 488–499.

Lu TZ & Feng ZP (2011). A sodium leak current regulates pacemaker activity of adult central pattern generator neurons in lymnaea stagnalis. *PLoS One*; DOI: 10.1371/journal.pone.0018745.

Lu TZ & Feng ZP (2012). NALCN: A regulator of pacemaker activity. *Mol Neurobiol* **45,** 415–423.

Lupu M, Thomas CD, Maillard P, Loock B, Chauvin B, Aerts I, Croisy A, Belloir E, Volk A & Mispelter J (2009). 23Na MRI longitudinal follow-up of PDT in a xenograft model of human retinoblastoma. *Photodiagnosis Photodyn Ther*; DOI: 10.1016/j.pdpdt.2009.10.009.

Lutas A, Lahmann C, Soumillon M & Yellen G (2016). The leak channel NALCN controls tonic firing and glycolytic sensitivity of substantia nigra pars reticulata neurons. *Elife* **5,** e15271.

Magnon C, Hall SJ, Lin J, Xue X, Gerber L, Freedland SJ & Frenette PS (2013). Autonomic Nerve Development Cancer Progression. *Science* **341,** 1–10.

Mason WS, Gill US, Litwin S, Zhou Y, Peri S, Pop O, Hong MLW, Naik S, Quaglia A, Bertoletti A & Kennedy PTF (2016). HBV DNA Integration and Clonal Hepatocyte Expansion in Chronic Hepatitis B Patients Considered Immune Tolerant. *Gastroenterology* **151,** 986–998.e4.

Matkovich SJ, Van Booven DJ, Youker KA, Torre-Amione G, Diwan A, Eschenbacher WH, Dorn LE, Watson MA, Margulies KB & Dorn GW (2009). Reciprocal regulation of myocardial microRNAs and messenger RNA in human cardiomyopathy and reversal of the microRNA signature by biomechanical support. *Circulation* **119,** 1263–1271.

Mayfield RD, Harris RA & Schuckit MA (2008). Genetic factors influencing alcohol dependence. *Br J Pharmacol* **154,** 275–287.

McGuire TF, Sajithlal GB, Lu J, Nicholls RD & Prochownik E V. (2012). In vivo evolution of tumor-derived endothelial cells. *PLoS One*; DOI: 10.1371/journal.pone.0037138.

Mead CLR, Kuzyk MA, Moradian A, Wilson GM, Holt RA & Morin GB (2010). Cytosolic protein interactions of the schizophrenia susceptibility gene dysbindin. *J Neurochem* **113,** 1491–1503.

Minto CF, Schnider TW & Shafer SL (1997). Pharmacokinetics and pharmacodynamics of remifentanil. II. Model application. *Anesthesiology* **86,** 24–33.

Mir B, Iyer S, Ramaswami M & Krishnan KS (1997). A genetic and mosaic analysis of a locus involved in the anesthesia response of Drosophila melanogaster. *Genetics* **147,** 701–712.

Mok KY, Schneider SA, Trabzuni D, Stamelou M, Edwards M, Kasperaviciute D, Pickering-Brown S, Silverdale M, Hardy J & Bhatia KP (2014). Genomewide association study in cervical dystonia demonstrates possible association with sodium leak channel. *Mov Disord* **29,** 245–251.

Monteith GR, Prevarskaya N & Roberts-Thomson SJ (2017). The calcium-cancer signalling nexus. *Nat Rev Cancer* **17,** 367–380.

Moose DL, Haase SJ, Aldrich BT & Lear BC (2017). The Narrow Abdomen Ion Channel Complex Is Highly Stable and Persists from Development into Adult Stages to Promote Behavioral Rhythmicity. *Front Cell Neurosci*; DOI: 10.3389/fncel.2017.00159.

Morgan PG, Radke GW & Sedensky MM (2000). Effects of nonimmobilizers and halothane on Caenorhabditis elegans. *Anesth Analg* **91,** 1007–1012.

Morgan PG, Sedensky M & Meneely PM (1990). Multiple sites of action of volatile anesthetics in Caenorhabditis elegans. *Proc Natl Acad Sci U S A* **87,** 2965–2969.

Morgan PG & Sedensky MM (1995). Mutations Affecting Sensitivity to Ethanol in the Nematode, Caenorhabditis elegans. *Alcohol Clin Exp Res* **19,** 1423–1429.

Morgan PG, Sedensky MM, Meneely PM & Cascorbi HF (1988). The effect of two genes on anesthetic response in the nematode Caenorhabditis elegans. *Anesthesiology* **69,** 246–251.

Morozova T V, Goldman D, Mackay TF & Anholt RR (2012). The genetic basis of alcoholism: Multiple phenotypes, many genes, complex networks. *Genome Biol* **13,** 239.

Moylan CA, Pang H, Dellinger A, Suzuki A, Garrett ME, Guy CD, Murphy SK, Ashley-Koch AE, Choi SS, Michelotti GA, Hampton DD, Chen Y, Tillmann HL, Hauser MA, Abdelmalek MF & Diehl AM (2014). Hepatic gene expression profiles differentiate presymptomatic patients with mild versus severe nonalcoholic fatty liver disease. *Hepatology* **59,** 471–482.

Nagase T, Kikuno R & Ohara O (2001). Prediction of the coding sequences of unidentified human genes. XXII. The complete sequences of 50 new cDNA clones which code for large proteins. *DNA Res* **8,** 319–327.

Nakayama M, Iida M, Koseki H & Ohara O (2006). A gene-targeting approach for functional characterization of KIAA genes encoding extremely large proteins. *FASEB J* **20,** 1718–1720.

NASH HA, CAMPBELL DB & KRISHNAN KS (1991). New Mutants of Drosophila That Are Resistant to the Anesthetic Effects of Halothane. *Ann N Y Acad Sci* **625,** 540–544.

Nash HA, Scott RL, Lear BC & Allada R (2002). An unusual cation channel mediates photic control of locomotion in Drosophila. *Curr Biol*; DOI: 10.1016/S0960-9822(02)01358-1.

Naylor J & Beech DJ (2009). Extracellular Ion Channel Inhibitor Antibodies. *Open Drug Discov J* **1,** 36–42.

Nishii Y, Morishima M, Kakehi Y, Umehara K, Kioka N, Terano Y, Amachi T & Ueda K (2000). CROP/Luc7A, a novel serine/arginine-rich nuclear protein, isolated from cisplatin-resistant cell line. *FEBS Lett* **465,** 153–156.

Nishikawa KI & Kidokoro Y (1999). Halothane presynaptically depresses synaptic transmission in wild-type Drosophila larvae but not in halothane-resistant (har) mutants. *Anesthesiology* **90,** 1691–1697.

Nurnberger JI, Foroud T, Flury L, Su J, Meyer ET, Hu K, Crowe R, Edenberg H, Goate A, Bierut L, Reich T, Schuckit M & Reich W (2001). Evidence for a locus on chromosome 1 that influences vulnerability to alcoholism and affective disorder. *Am J Psychiatry* **158,** 718–724.

Ohl F, Jung M, Xu C, Stephan C, Rabien A, Burkhardt M, Nitsche A, Kristiansen G, Loening SA, Radonić A & Jung K (2005). Gene expression studies in prostate cancer tissue: Which reference gene should be selected for normalization? *J Mol Med* **83,** 1014–1024.

Ollila HM, Soronen P, Silander K, Palo OM, Kieseppä T, Kaunisto MA, Lönnqvist J, Peltonen L, Partonen T & Paunio T (2009). Findings from bipolar disorder genome-wide association studies replicate in a Finnish bipolar family-cohort. *Mol Psychiatry* **14,** 351–353.

Onkal R, Mattis JH, Fraser SP, Diss JKJ, Shao D, Okuse K & Djamgoz MBA (2008). Alternative splicing of Nav1.5: An electrophysiological comparison of "neonatal" and "adult" isoforms and critical involvement of a lysine residue. *J Cell Physiol* **216,** 716–726.

Orlov SN, Klimanova EA, Tverskoi AM, Vladychenskaya EA, Smolyaninova L V. & Lopina OD (2017). Na+i,K+i-Dependent and -Independent signaling triggered by cardiotonic steroids: Facts and artifacts. *Molecules*; DOI: 10.3390/molecules22040635.

Ouwerkerk R, Jacobs MA, Macura KJ, Wolff AC, Stearns V, Mezban SD, Khouri NF, Bluemke DA & Bottomley PA (2007). Elevated tissue sodium concentration in malignant breast lesions detected with non-invasive Na-23 MRI. *Breast Cancer Res Treat*; DOI: 10.1007/s10549-006-9485-4.

Patel AJ, Honoré E, Maingret F, Lesage F, Fink M, Duprat F & Lazdunski M (1998). A mammalian two pore domain mechano-gated S-like K+ channel. *EMBO J* **17,** 4283–4290.

Pei J & Grishin N V. (2012). Cysteine-rich domains related to Frizzled receptors and Hedgehog-interacting proteins. *Protein Sci*; DOI: 10.1002/pro.2105.

Perez Y, Kadir R, Volodarsky M, Noyman I, Flusser H, Shorer Z, Gradstein L, Birnbaum RY & Birk OS (2016). UNC80 mutation causes a syndrome of hypotonia, severe intellectual disability, dyskinesia and dysmorphism, similar to that caused by mutations in its interacting cation channel NALCN. *J Med Genet* **53,** 397–402.

Pierce-Shimomura JT, Chen BL, Mun JJ, Ho R, Sarkis R & McIntire SL (2008). Genetic analysis of crawling and swimming locomotory patterns in C. elegans. *Proc Natl Acad Sci* **105,** 20982–20987.

Poliseno L, Salmena L, Zhang J, Carver B, Haveman WJ & Pandolfi PP (2010). A coding-independent function of gene and pseudogene mRNAs regulates tumour biology. *Nature* **465,** 1033–1038.

Pollard TD & Earnshaw WC (2008). *Cell biology*.

Prakriya M & Lewis RS (2015). Store-Operated Calcium Channels. *Physiol Rev* **95,** 1383–1436.

Prevarskaya N, Skryma R & Shuba Y (2010). Ion channels and the hallmarks of cancer. *Trends Mol Med*; DOI: 10.1016/j.molmed.2010.01.005.

Raizman JE, Komljenovic J, Chang R, Deng C, Bedosky KM, Rattan SG, Cunnington RH, Freed DH & Dixon IMC (2007). The participation of the Na+–Ca2+ exchanger in primary cardiac myofibroblast migration, contraction, and proliferation. *J Cell Physiol* **213,** 540–551.

Rajan P, Elliott DJ, Robson CN & Leung HY (2009). Alternative splicing and biological heterogeneity in prostate cancer. *Nat Rev Urol* **6,** 454–460.

Rajaram S, Spangler TL, Sedensky MM & Morgan PG (1999). A stomatin and a degenerin interact to control anesthetic sensitivity in Caenorhabditis elegans. *Genetics* **153,** 1673–1682.

Ratnapriya R, Vijai J, Kadandale JS, Iyer RS, Radhakrishnan K & Anand A (2010). A locus for juvenile myoclonic epilepsy maps to 2q33-q36. *Hum Genet* **128,** 123–130.

Ren D (2011). Sodium leak channels in neuronal excitability and rhythmic behaviors. *Neuron* **72,** 899–911.

Renigunta V, Schlichthörl G & Daut J (2015). Much more than a leak: structure and function of K2P-channels. *Pflügers Arch - Eur J Physiol* **467,** 867–894.

Rizaner N, Onkal R, Fraser SP, Pristerá A, Okuse K & Djamgoz MBA (2016). Intracellular calcium oscillations in strongly metastatic human breast and prostate cancer cells: control by voltage-gated sodium channel activity. *Eur Biophys J* **45,** 735–748.

Roger S, Besson P & Le Guennec JY (2003). Involvement of a novel fast inward sodium current in the invasion capacity of a breast cancer cell line. *Biochim Biophys Acta - Biomembr* **1616,** 107–111.

Roger S, Gillet L, Le Guennec JY & Besson P (2015). Voltage-gated sodium channels and cancer: Is excitability their primary role? *Front Pharmacol*; DOI: 10.3389/fphar.2015.00152.

Sahai E & Marshall CJ (2002). RHO–GTPASES AND CANCER. *Nat Rev Cancer* **2,** 133–142.

Sárközy M, Szucs G, Pipicz M, Zvara Á, Éder K, Fekete V, Szucs C, Bárkányi J, Csonka C, Puskás LG, Kónya C, Ferdinandy P & Csont T (2015). The effect of a preparation of minerals, vitamins and trace elements on the cardiac gene expression pattern in male diabetic rats. *Cardiovasc Diabetol*; DOI: 10.1186/s12933-015-0248-6.

Schepkin VD (2016). Sodium MRI of glioma in animal models at ultrahigh magnetic fields. *NMR Biomed* **29,** 175–186.

Scheuer T (2011). Regulation of sodium channel activity by phosphorylation. *Semin Cell Dev Biol* **22,** 160–165.

Schindelin J, Arganda-Carreras I, Frise E, Kaynig V, Longair M, Pietzsch T, Preibisch S, Rueden

C, Saalfeld S, Schmid B, Tinevez J-Y, White DJ, Hartenstein V, Eliceiri K, Tomancak P & Cardona A (2012). Fiji: an open-source platform for biological-image analysis. *Nat Methods*; DOI: 10.1038/nmeth.2019.

Schuckit MA, Edenberg HJ, Kalmijn J, Flury L, Smith TL, Reich T, Bierut L, Goate A & Foroud T (2001). A genome-wide search for genes that relate to a low level of response to alcohol. *Alcohol Clin Exp Res* **25,** 323–329.

Schulz W a, Ingenwerth M, Djuidje CE, Hader C, Rahnenführer J & Engers R (2010). Changes in cortical cytoskeletal and extracellular matrix gene expression in prostate cancer are related to oncogenic ERG deregulation. *BMC Cancer*; DOI: 10.1186/1471-2407-10-505.

Scott WK, Hauser ER, Schmechel DE, Welsh-Bohmer KA, Small GW, Roses AD, Saunders AM, Gilbert JR, Vance JM, Haines JL & Pericak-Vance MA (2003). Odered-Subsets Linkage Analysis Detects Novel Alzheimer Disease Loci on Chromosomes 2q34 and 15q22. *Am J Hum Genet* **73,** 1041–1051.

Sedensky MM & Meneely PM (1987). Genetic analysis of halothane sensitivity in Caenorhabditis elegans. *Science* **236,** 952–954.

Senatore A, Monteil A, van Minnen J, Smit AB & Spafford JD (2013). NALCN Ion Channels Have Alternative Selectivity Filters Resembling Calcium Channels or Sodium Channels. *PLoS One*; DOI: 10.1371/journal.pone.0055088.

Senatore A & Spafford JD (2013). A uniquely adaptable pore is consistent with NALCN being an ion sensor. *Channels* **7,** 60–68.

Shamseldin HE, Faqeih E, Alasmari A, Zaki MS, Gleeson JG & Alkuraya FS (2016). Mutations in UNC80, Encoding Part of the UNC79-UNC80-NALCN Channel Complex, Cause Autosomal-Recessive Severe Infantile Encephalopathy. *Am J Hum Genet* **98,** 210–215.

Shi Y, Abe C, Holloway BB, Shu S, Kumar NN, Weaver JL, Sen J, Perez-Reyes E, Stornetta RL, Guyenet PG & Bayliss DA (2016). Nalcn Is a “Leak” Sodium Channel That Regulates Excitability of Brainstem Chemosensory Neurons and Breathing. *J Neurosci* **36,** 8174–8187.

Singaram VK, Somerlot BH, Falk SA, Falk MJ, Sedensky MM & Morgan PG (2011). Optical reversal of halothane-induced immobility in C. elegans. *Curr Biol* **21,** 2070–2076.

Sinke AP, Caputo C, Tsaih S-W, Yuan R, Ren D, Deen PMT & Korstanje R (2011). Genetic analysis of mouse strains with variable serum sodium concentrations identifies the Nalcn sodium channel as a novel player in osmoregulation. *Physiol Genomics*; DOI: 10.1152/physiolgenomics.00188.2010.

Sinke AP & Deen PMT (2011). The physiological implication of novel proteins in systemic osmoregulation. *FASEB J* **25,** 3279–3289.

Sivaraman I, Friedman NR & Prayson RA (2016). Muscle biopsy findings in a child with NALCN gene mutation. *J Clin Neurosci* **34,** 222–223.

Snutch TP & Monteil A (2007). The Sodium "Leak" Has Finally Been Plugged. *Neuron* **54,** 505–507.

Sottoriva A, Kang H, Ma Z, Graham TA, Salomon MP, Zhao J, Marjoram P, Siegmund K, Press MF, Shibata D & Curtis C (2015). A big bang model of human colorectal tumor growth. *Nat Genet* **47,** 209–216.

Souza RP, Rosa DVF, Romano-Silva MA, Zhen M, Meltzer HY, Lieberman JA, Remington G, Kennedy JL & Wong AHC (2011). Lack of association of NALCN genetic variants with schizophrenia. *Psychiatry Res* **185,** 450–452.

Speca DJ, Chihara D, Ashique AM, Bowers MS, Pierce-Shimomura JT, Lee J, Rabbee N, Speed TP, Gularte RJ, Chitwood J, Medrano JF, Liao M, Sonner JM, Eger EI, Peterson AS & Mcintire SL (2010). Conserved role of unc-79 in ethanol responses in lightweight mutant mice. *PLoS Genet*; DOI: 10.1371/journal.pgen.1001057.

Stanzione R, Picascia A, Chieffi P, Imbimbo C, Palmieri A, Mirone V, Staibano S, Franco R, De Rosa G, Schlessinger J & Tramontano D (2001). Variations of proline-rich kinase Pyk2 expression correlate with prostate cancer progression. *Lab Investig* **81,** 51–59.

Stone KR, Mickey DD, Wunderli H, Mickey GH & Paulson DF (1978). Isolation of a human prostate carcinoma cell line (DU 145). *Int J Cancer* **21,** 274–281.

Stray-Pedersen A et al. (2016). Biallelic Mutations in UNC80 Cause Persistent Hypotonia, Encephalopathy, Growth Retardation, and Severe Intellectual Disability. *Am J Hum Genet* **98,** 202–209.

Strohl KP (2003). Periodic breathing and genetics. *Respir Physiol Neurobiol* **135,** 179–185.

Sun J, Lu F, He H, Shen J, Messina J, Mathew R, Wang D, Sarnaik AA, Chang WC, Kim M, Cheng H & Yang S (2014). STIM1- and Orai1-mediated Ca2+oscillation orchestrates invadopodium formation and melanoma invasion. *J Cell Biol* **207,** 535–548.

Swayne LA, Mezghrani A, Lory P, Nargeot J & Monteil A (2010). The NALCN ion channel is a new actor in pancreatic β-cell physiology. *Islets*; DOI: 10.4161/isl.2.1.10522.

Swayne LA, Mezghrani A, Varrault A, Chemin J, Bertrand G, Dalle S, Bourinet E, Lory P, Miller RJ, Nargeot J & Monteil A (2009). The NALCN ion channel is activated by M3 muscarinic receptors in a pancreatic beta-cell line. *EMBO Rep* **10,** 873–880.

Van Swinderen B (2006). A succession of anesthetic endpoints in the Drosophila brain. *J Neurobiol* **66,** 1195–1211.

Taguchi K, Hamamoto S, Okada A, Unno R, Kamisawa H, Naiki T, Ando R, Mizuno K, Kawai

N, Tozawa K, Kohri K & Yasui T (2017). Genome-Wide Gene Expression Profiling of Randall's Plaques in Calcium Oxalate Stone Formers. *J Am Soc Nephrol* **28,** 333–347.

Teo C, Zai C, Borlido C, Tomasetti C, Strauss J, Shinkai T, Le Foll B, Wong A, Kennedy JL & De Luca V (2012). Analysis of treatment-resistant schizophrenia and 384 markers from candidate genes. *Pharmacogenet Genomics* **22,** 807–811.

Terracciano A, Tanaka T, Sutin AR, Sanna S, Deiana B, Lai S, Uda M, Schlessinger D, Abecasis GR, Ferrucci L & Costa PT (2010). Genome-wide association scan of trait depression. *Biol Psychiatry* **68,** 811–817.

Tinevez JY, Perry N, Schindelin J, Hoopes GM, Reynolds GD, Laplantine E, Bednarek SY, Shorte SL & Eliceiri KW (2017). TrackMate: An open and extensible platform for single-particle tracking. *Methods* **115,** 80–90.

Topalidou I, Chen PA, Cooper K, Watanabe S, Jorgensen EM & Ailion M (2017). The NCA-1 and NCA-2 Ion channels function downstream of Gq and Rho to regulate locomotion in Caenorhabditis elegans. *Genetics*; DOI: 10.1534/genetics.116.198820.

Tsaur I, Renninger M, Hennenlotter J, Oppermann E, Munz M, Kuehs U, Stenzl A & Schilling D (2013). Reliable housekeeping gene combination for quantitative PCR of lymph nodes in patients with prostate cancer. *Anticancer Res* **33,** 5243–5248.

Valkanas E, Schaffer K, Dunham C, Maduro V, du Souich C, Rupps R, Adams DR, Baradaran-Heravi A, Flynn E, Malicdan MC, Gahl WA, Toro C & Boerkoel CF (2016). Phenotypic evolution of UNC80 loss of function. *Am J Med Genet Part A* **170,** 3106–3114.

Valle JW, Lamarca A, Goyal L, Barriuso J & Zhu AX (2017). New horizons for precision medicine in biliary tract cancers. *Cancer Discov* **7,** 943–962.

Vivero M, Cho MT, Begtrup A, Wentzensen IM, Walsh L, Payne K, Zarate YA, Bosanko K, Schaefer GB, DeBrosse S, Pollack L, Mason K, Retterer K, DeWard S, Juusola J & Chung WK (2017). Additional de novo missense genetic variants in NALCN associated with CLIFAHDD syndrome. *Clin Genet* **91,** 929–931.

Vlaeminck-Guillem V, Gillet G & Rimokh R (2014). Src: Marker or Actor in Prostate Cancer Aggressiveness. *Front Oncol*; DOI: 10.3389/fonc.2014.00222.

Wang H & Ren D (2009). UNC80 functions as a scaffold for Src kinases in NALCN channel function. *Channels (Austin)* **3,** 161–163.

Wang KS, Liu XF & Aragam N (2010). A genome-wide meta-analysis identifies novel loci associated with schizophrenia and bipolar disorder. *Schizophr Res* **124,** 192–199.

Wang Y, Koh K, Ichinose Y, Yasumura M, Ohtsuka T & Takiyama Y (2016). A de novo mutation in the NALCN gene in an adult patient with cerebellar ataxia associated with intellectual

disability and arthrogryposis. *Clin Genet* **90,** 556–557.

Webb BA, Chimenti M, Jacobson MP & Barber DL (2011). Dysregulated pH: A perfect storm for cancer progression. *Nat Rev Cancer* **11,** 671–677.

Wen J, Pang Y, Zhou T, Qi X, Zhao M & Xuan B (2016). Essential role of Na + / Ca2 + exchanger 1 in smoking-induced growth and migration of esophageal squamous cell carcinoma. *Oncotarget*.

Wetherill L, Kapoor M, Agrawal A, Bucholz K, Koller D, Bertelsen SE, Le N, Wang JC, Almasy L, Hesselbrock V, Kramer J, Nurnberger JI, Schuckit M, Tischfield JA, Xuei X, Porjesz B, Edenberg HJ, Goate AM & Foroud T (2014). Family-Based Association Analysis of Alcohol Dependence Criteria and Severity. *Alcohol Clin Exp Res* **38,** 354–366.

Whan V, Hobbs M, McWilliam S, Lynn DJ, Lutzow YS, Khatkar M, Barendse W, Raadsma H & Tellam RL (2010). Bovine proteins containing poly-glutamine repeats are often polymorphic and enriched for components of transcriptional regulatory complexes. *BMC Genomics*; DOI: 10.1186/1471-2164-11-654.

Williams S, Bateman A & O'Kelly I (2013). Altered Expression of Two-Pore Domain Potassium (K2P) Channels in Cancer. *PLoS One*; DOI: 10.1371/journal.pone.0074589.

Wollman R & Meyer T (2012). Coordinated oscillations in cortical actin and Ca2+ correlate with cycles of vesicle secretion. *Nat Cell Biol* **14,** 1261–1269.

Wu H ???C, Hsieh J ???T, Gleave ME, Brown NM, Pathak S & Chung LWK (1994). Derivation of androgen-independent human LNCaP prostatic cancer cell sublines: Role of bone stromal cells. *Int J Cancer* **57,** 406–412.

Xia J, Huang N, Huang H, Sun L, Dong S, Su J, Zhang J, Wang L, Lin L, Shi M, Bin J, Liao Y, Li N & Liao W (2016). Voltage-gated sodium channel Nav1.7 promotes gastric cancer progression through MACC1-mediated upregulation of NHE1. *Int J Cancer* **139,** 2553–2569.

Xie L, Gao S, Alcaire SM, Aoyagi K, Wang Y, Griffin JK, Stagljar I, Nagamatsu S & Zhen M (2013). NLF-1 Delivers a Sodium Leak Channel to Regulate Neuronal Excitability and Modulate Rhythmic Locomotion. *Neuron* **77,** 1069–1082.

Xie Z & Askari A (2002). Na+/K+-ATPase as a signal transducer. *Eur J Biochem* **269,** 2434–2439.

Xu SZ, Zeng F, Lei M, Li J, Gao B, Xiong C, Sivaprasadarao A & Beech DJ (2005). Generation of functional ion-channel tools by E3 targeting. *Nat Biotechnol* **23,** 1289–1293.

Xu Y, Zhang S, Niu H, Ye Y, Hu F, Chen S, Li X, Luo X, Jiang S, Liu Y, Chen Y, Li J, Xiang R & Li N (2015). STIM1 accelerates cell senescence in a remodeled microenvironment but enhances the epithelial-to-mesenchymal transition in prostate cancer. *Sci Rep*; DOI: 10.1038/srep11754.

Ye Q, Li Z, Tian J, Xie JX, Liu L & Xie Z (2011). Identification of a potential receptor that couples ion transport to protein kinase activity. *J Biol Chem* **286,** 6225–6232.

Yeh E, Ng S, Zhang M, Bouhours M, Wang Y, Wang M, Hung W, Aoyagi K, Melnik-Martinez K, Li M, Liu F, Schafer WR & Zhen M (2008). A putative cation channel, NCA-1, and a novel protein, UNC-80, transmit neuronal activity in C. elegans. *PLoS Biol* **6,** 0552–0567.

Yeh SY, Huang WH, Wang W, Ward CS, Chao ES, Wu Z, Tang B, Tang J, Sun JJ, Esther van der Heijden M, Gray PA, Xue M, Ray RS, Ren D & Zoghbi HY (2017). Respiratory Network Stability and Modulatory Response to Substance P Require Nalcn. *Neuron* **94,** 294–303.e4.

Yi YH, Ho PY, Chen TW, Lin WJ, Gukassyan V, Tsai TH, Wang DW, Lew TS, Tang CY, Lo SJ, Chen TY, Kao FJ & Lin CH (2009). Membrane targeting and coupling of NHE1-integrin αIIbβ-NCX1 by lipid rafts following integrin-ligand interactions trigger Ca2+oscillations. *J Biol Chem* **284,** 3855–3864.

Yildirim S, Altun S, Gumushan H, Patel A & Djamgoz MBA (2012). Voltage-gated sodium channel activity promotes prostate cancer metastasis in vivo. *Cancer Lett*; DOI: 10.1016/j.canlet.2012.03.036.

Yu FH & Catterall WA (2004). The VGL-Chanome: A Protein Superfamily Specialized for Electrical Signaling and Ionic Homeostasis. *Sci Signal*; DOI: 10.1126/stke.2532004re15.

Zhou Q, Yang J, Cao B, Chen Y, Wei Q, Ou R, Song W, Zhao B, Wu Y & Shang H (2016). Association Analysis of NALCN Polymorphisms rs1338041 and rs61973742 in a Chinese Population with Isolated Cervical Dystonia. *Parkinsons Dis*; DOI: 10.1155/2016/9281790.

Zhu H, Zhang H, Jin F, Fang M, Huang M, Yang CS, Chen T, Fu L & Pan Z (2014). Elevated Orai1 expression mediates tumor-promoting intracellular Ca2+ oscillations in human esophageal squamous cell carcinoma. *Oncotarget* **5,** 3455–3471.

7. Annexes

7.1 Mycoplasma test

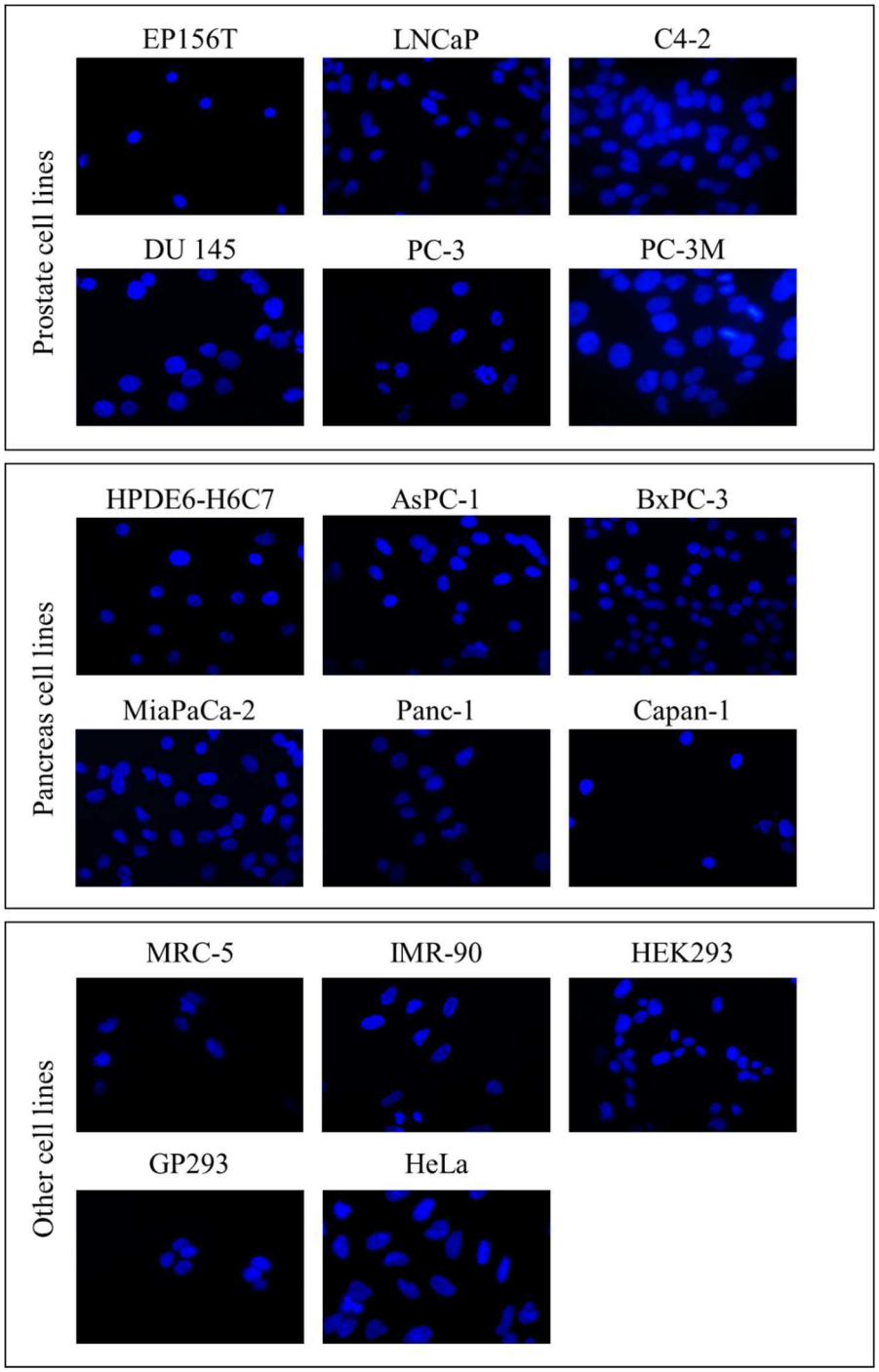

Figure 41. Mycoplasma test by using Hoechst staining.
None of cell lines tested exhibit any mycoplasma-like staining by using Hoechst dye.

7.2 Optimization of cPCR efficiency for *NALCN*

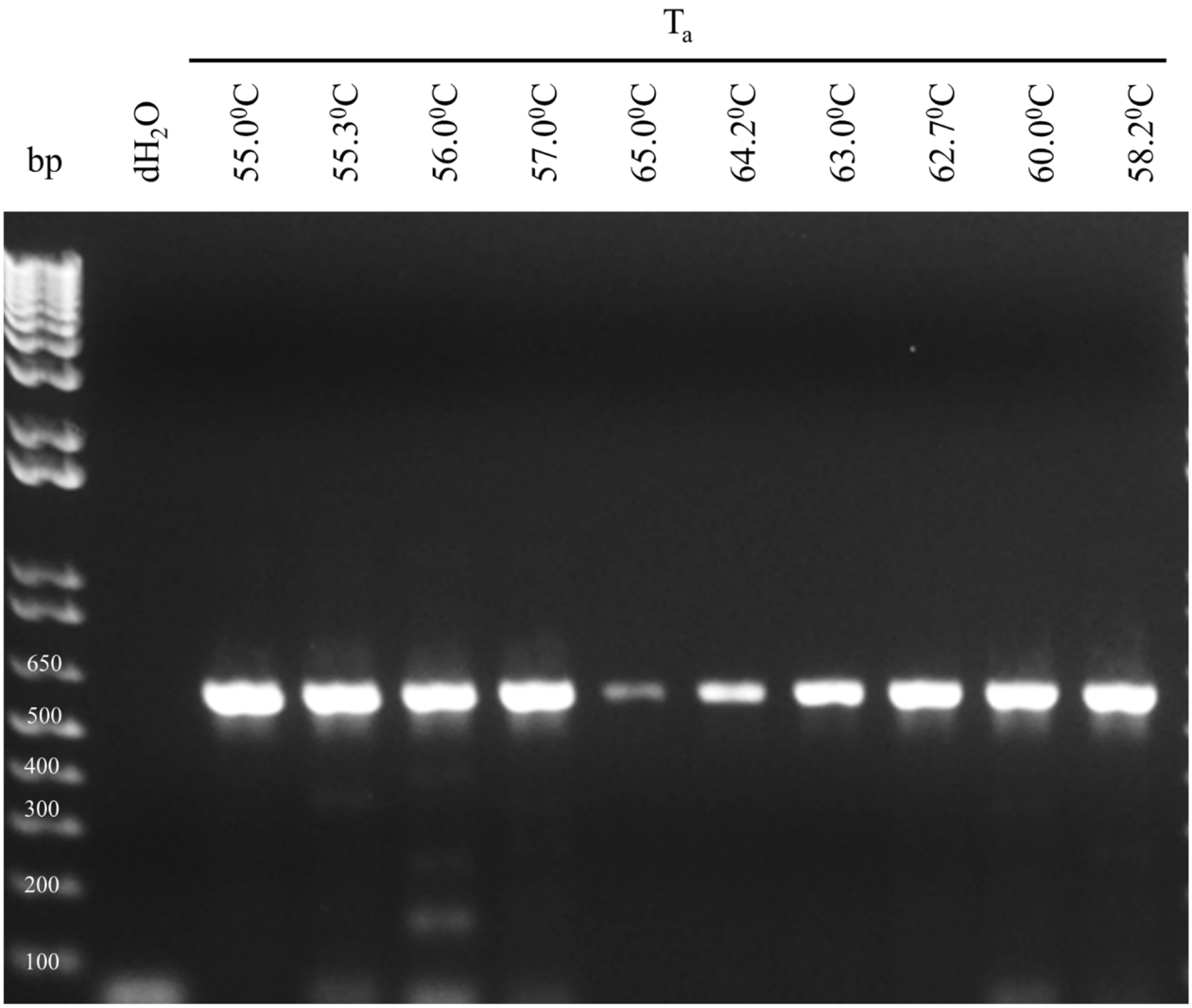

Figure 42. Temperature gradient cPCR against *NALCN* on cDNA from Mus ♂ brain. Temperature gradient (55-65^{0}C) was performed by cDNA from Mus ♂ brain. Each reaction was performed by using 1.25 ng of cDNA. Annealing temperature T_a=60^{0}C was chosen as the most optimal within the tested range.

7.3 Optimization of cPCR efficiency for *TBP*

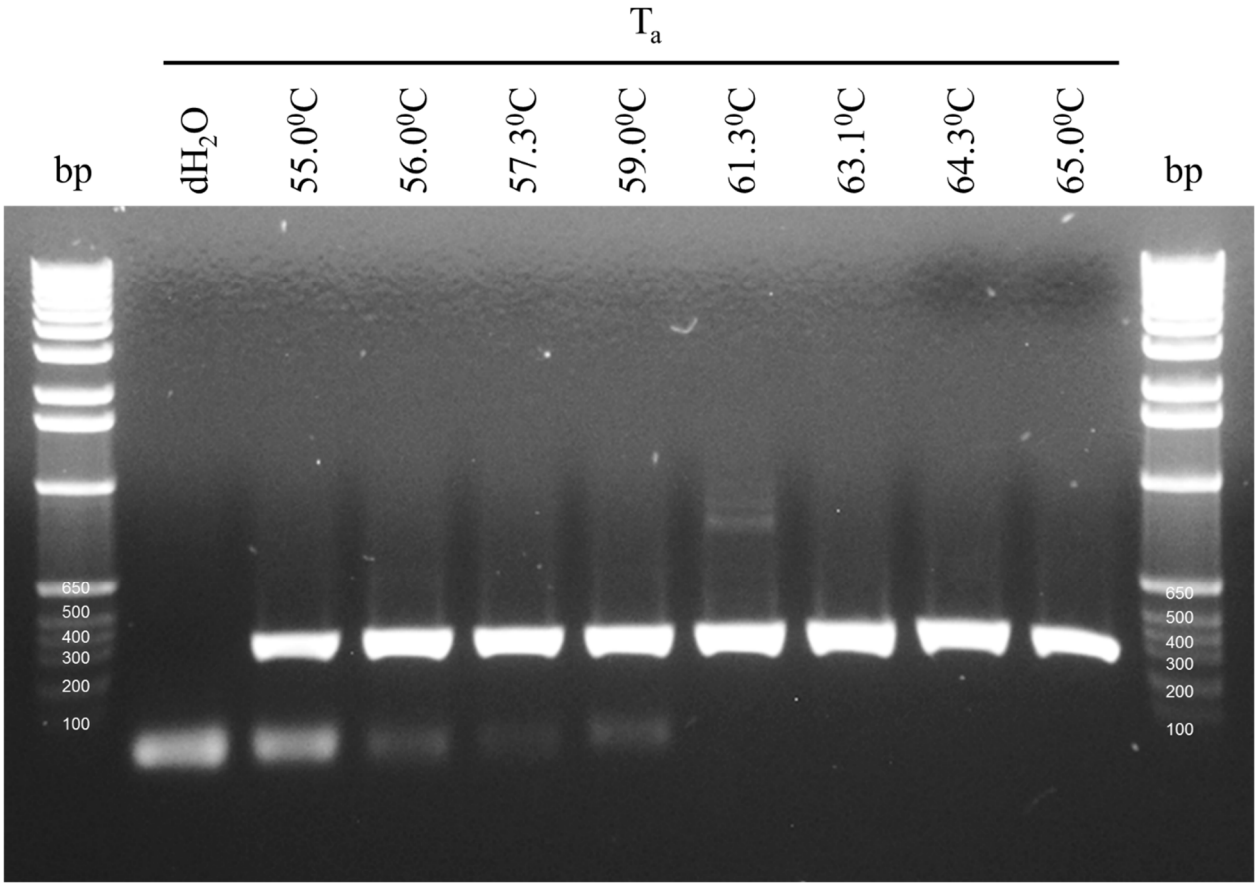

Figure 43. Temperature gradient cRT-PCR against *TBP* on cDNA from Mus ♂ brain. Temperature gradient (55-65^{0}C) was performed by cDNA from Mus ♂ brain. Each reaction was performed by using 1.25 ng of cDNA. Annealing temperature T_a=60^{0}C was chosen as the most optimal within the tested range.

7.4 Optimization of qRT-PCR efficiency for *NALCN*

T_a	Efficiency, %	R^2
60°C	104.9	0.999
59.7°C	97.8	0.991
59.2°C	97.4	0.994
58.2°C	112.6	0.981
57.0°C	99.4	0.997
56.0°C	97.4	0.992
55.3°C	103.9	0.999
55.0°C	108.7	0.997

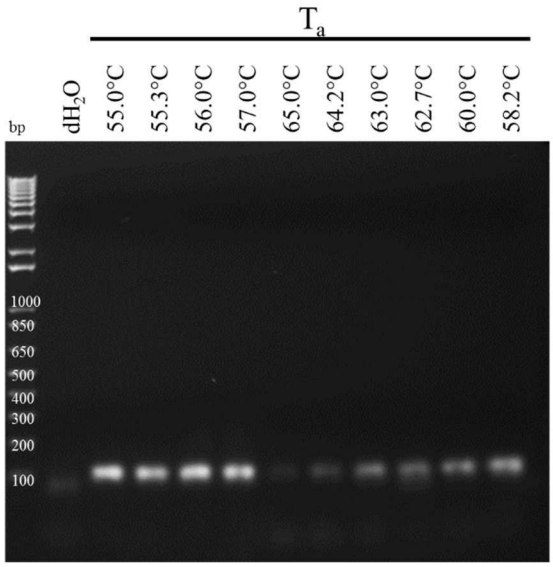

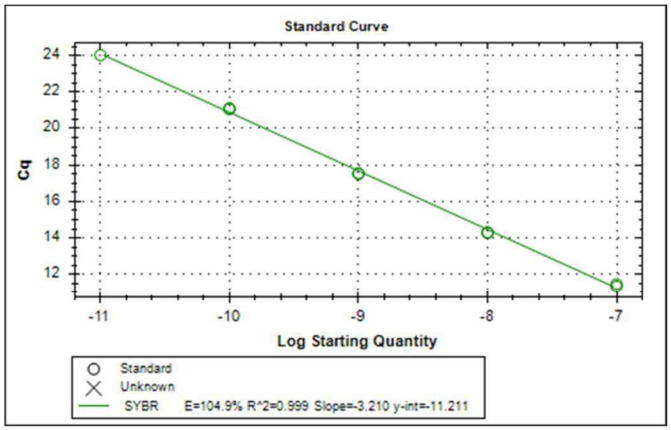

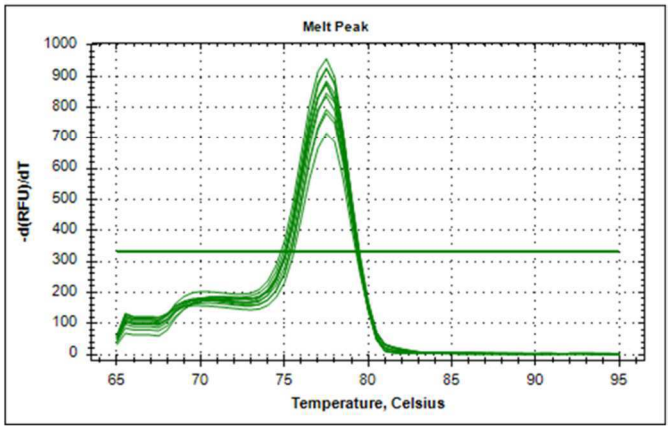

Figure 44. Temperature gradient qRT-PCR against *NALCN* on plasmid DNA.
Temperature gradient (55-60^{0}C) was performed by using plasmid pcDNA5-FRT-hNALCN. Each reaction contained 300 nM of primers against *NALCN* and 4 mM $MgCl_2$. Melting peak for each amplicon was yielding at the same temperature - T_m = 77.5^{0}C. Annealing temperature T_a=60^{0}C was chosen as the most optimal within the tested range.

T_a	Efficiency, %	R^2
60°C	98.5	0.988
59.7°C	109,3	0.998
59.2°C	125,9	0.992
58.2°C	124,7	0.933
57.0°C	120,7	0.962
56.0°C	122,7	0.993
55.3°C	126,4	0.996
55.0°C	117,2	0.996

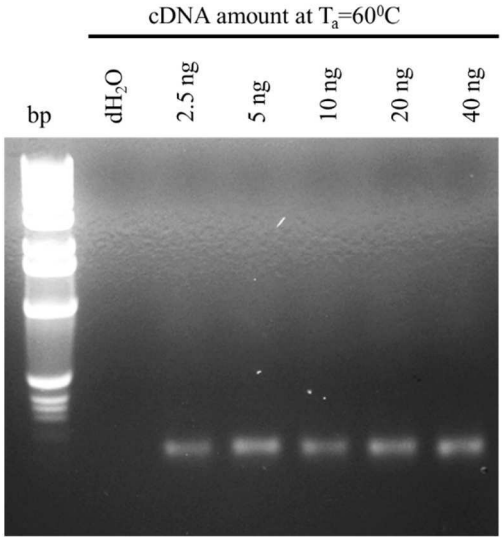

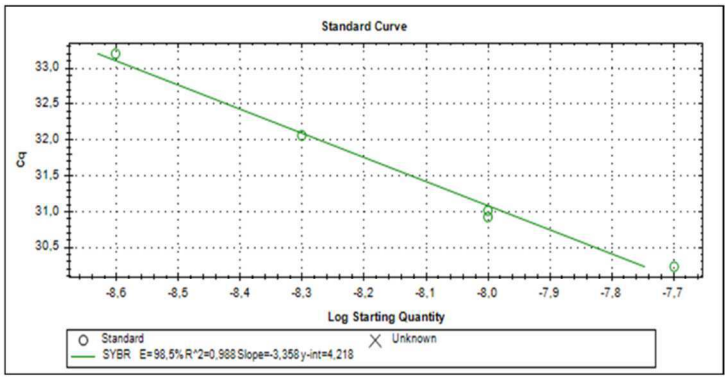

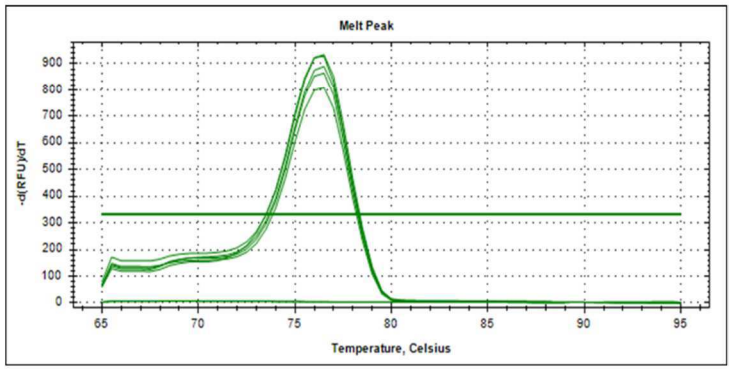

Figure 45. Temperature gradient qRT-PCR against *NALCN* on cDNA from Mus ♂ brain. Temperature gradient (55-60^{0}C) was performed by using cDNA from Mus ♂ brain. Each reaction contained 300 nM of primers against *NALCN* and 4 mM $MgCl_2$. Melting peak for each amplicon was yielding at the same temperature - T_m = 76.5^{0}C. Annealing temperature T_a=60^{0}C was chosen as the most optimal within the tested range.

Primer concentration (nM) FW/RV	Efficiency, %	R^2
200/200	127.3	0.975
200/300	103.8	0.991
200/400	135.8	0.984
200/500	124.7	0.966
300/200	116.9	0.982
300/300	104.8	0.997
300/400	130.9	0.991
300/500	123.6	0.989
400/200	104,1	0.997
400/300	109.9	0.978
400/400	107.1	0.978
400/500	121.4	0.985
500/200	111.8	0.986
500/300	121.1	0.988
500/400	137,2	0.984
500/500	119.7	0.982

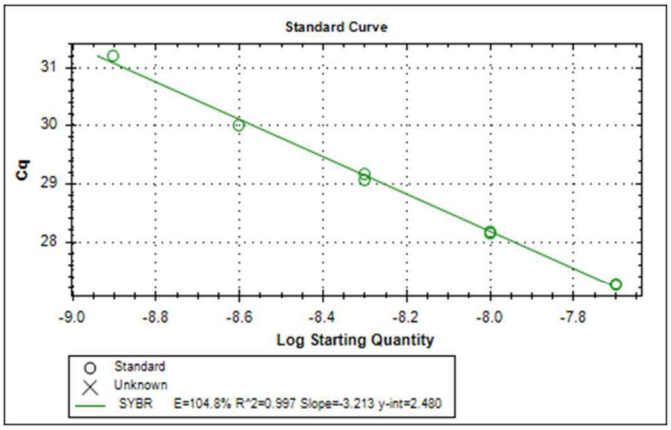

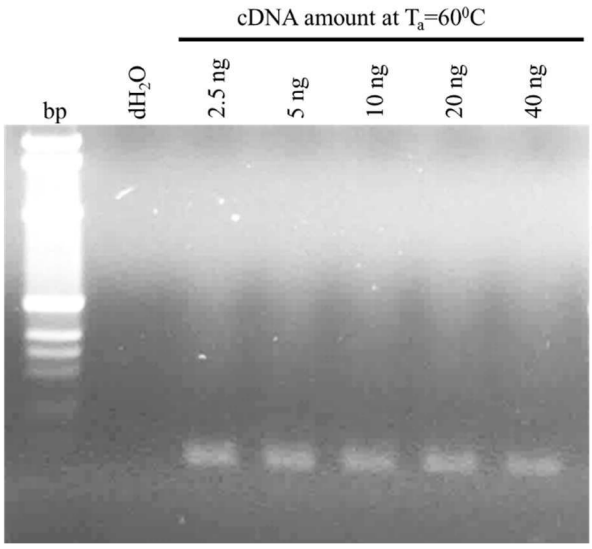

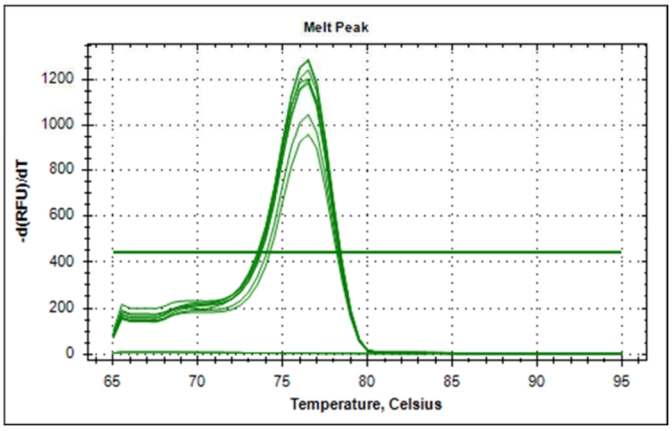

Figure 46. Optimization of primer concentration for qRT-PCR against *NALCN* on cDNA from Mus ♂ brain.
qRT-PCR was performed by using cDNA from Mus ♂ brain. Each reaction was performed at T_a=60^{0}C and contained different primers concentration (as indicated) and 4 mM $MgCl_2$. Melting peak for each amplicon was yielding at the same temperature - T_m = 76.5^{0}C. For each primer (FW and RV) the final concentration of 300 nM was chosen as the most optimal within the tested range.

$MgCl_2$	Efficiency, %	R^2
4 mM	112.7	0.995
5 mM	133.2	0.988

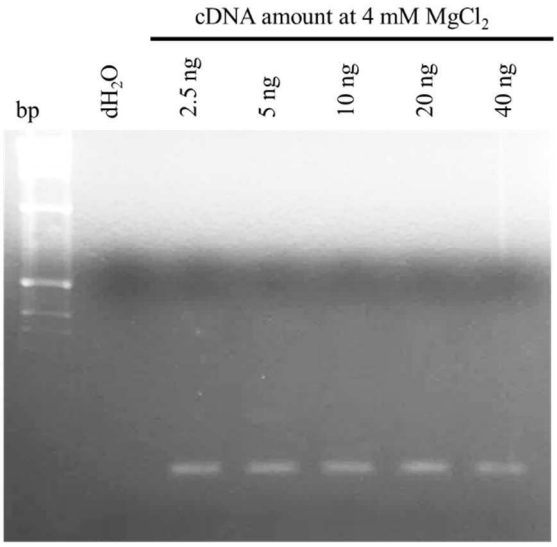

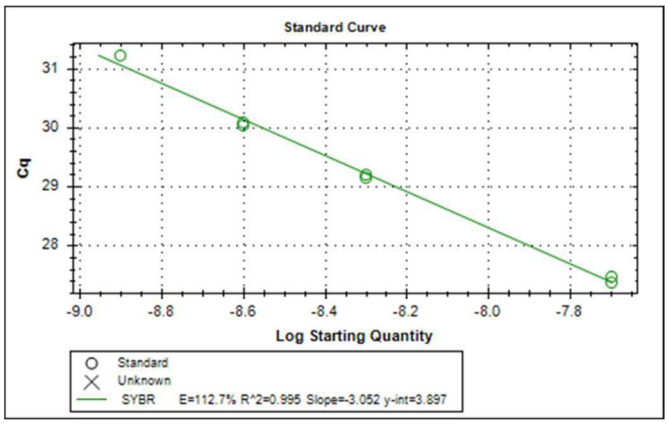

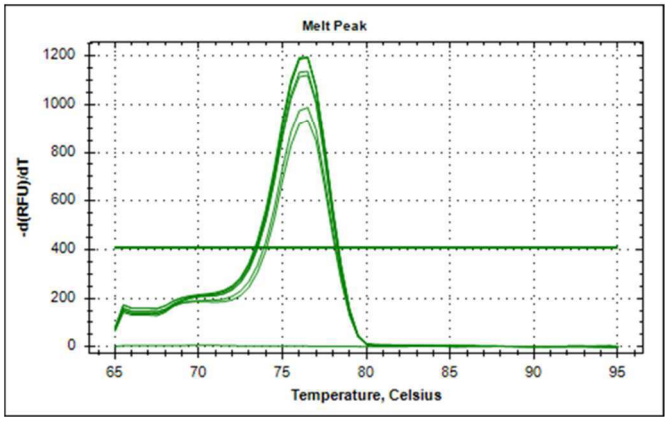

Figure 47. Optimization of $MgCl_2$ concentration for qRT-PCR against *NALCN* on cDNA from Mus ♂ brain.
qRT-PCR was performed by using cDNA from Mus ♂ brain. Each reaction was performed at T_a=60^{0}C and 300 nM primers concentration with 4 mM and 5 mM $MgCl_2$. Melting peak for each amplicon was yielding at the same temperature - T_m = 76.5^{0}C. Concentration of $MgCl_2$ of 4 mM was chosen as the most optimal within the tested range.

T_a	Efficiency, %	R^2
60°C	103.8	0.989
59.7°C	97.5	0.974
59.2°C	91.9	0.937
58.2°C	114.3	0.930
57.0°C	134.3	0.978
56.0°C	101.9	0.988
55.3°C	123.7	0.987
55.0°C	113.9	0.978

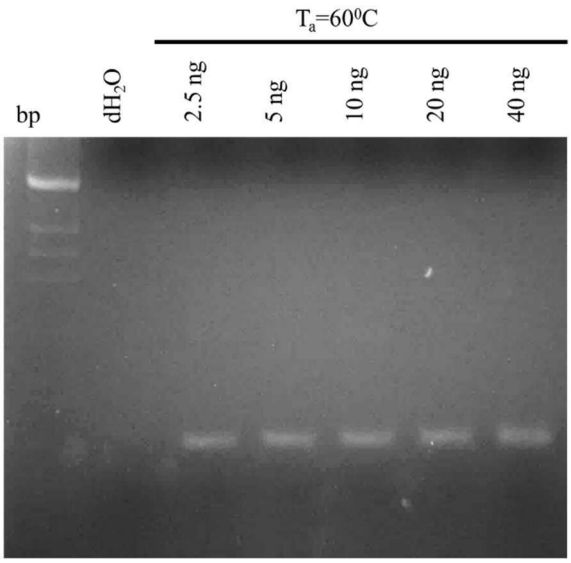

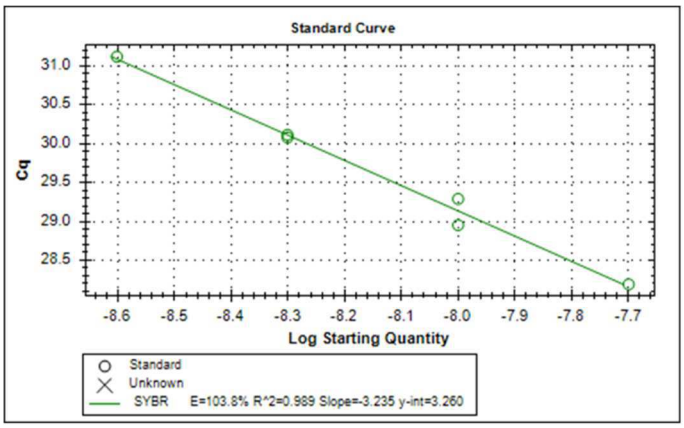

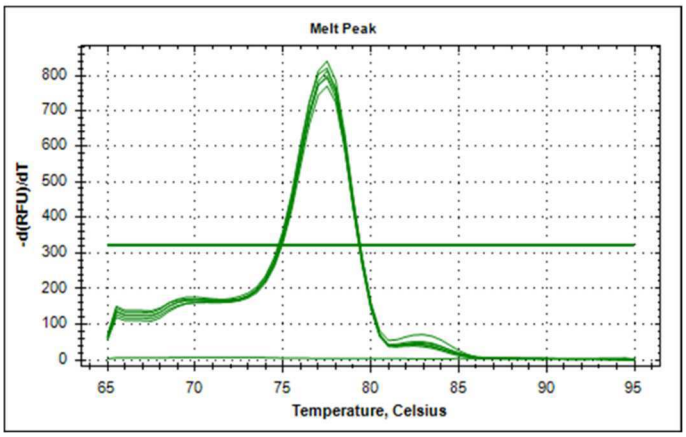

Figure 48. Temperature gradient qRT-PCR against *NALCN* on cDNA from PC-3. Temperature gradient (55-60^{0}C) was performed by using cDNA from PC-3 cell line. Each reaction contained 300 nM of primers against *NALCN* and 4 mM $MgCl_2$. Melting peak for each amplicon was yielding at the same temperature - T_m = 77.5^{0}C. Annealing temperature T_a=60^{0}C was chosen as the most optimal within the tested range.

Primer concentration (nM) FW/RV	Efficiency, %	R^2
200/200	103.3	0.985
200/300	95.6	0.994
200/400	121.8	0.983
200/500	104.5	0.962
300/200	117.3	0.977
300/300	97.0	0.996
300/400	103.5	0.954
300/500	88.5	0.933
400/200	108.1	0.976
400/300	93.8	0.971
400/400	123.6	0.967
400/500	107.2	0.970
500/200	122.5	0.972
500/300	98.2	0.982
500/400	94.1	0.971
500/500	112.7	0.925

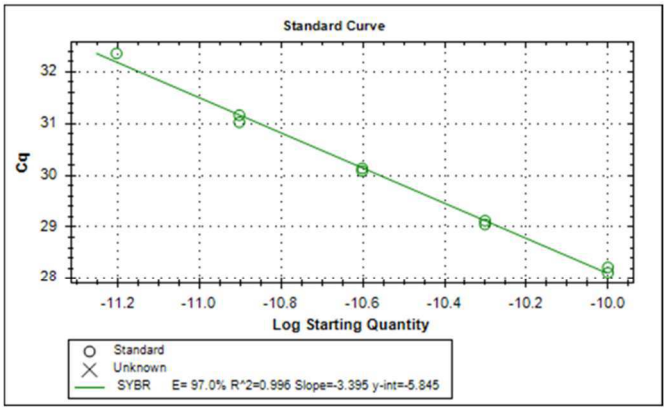

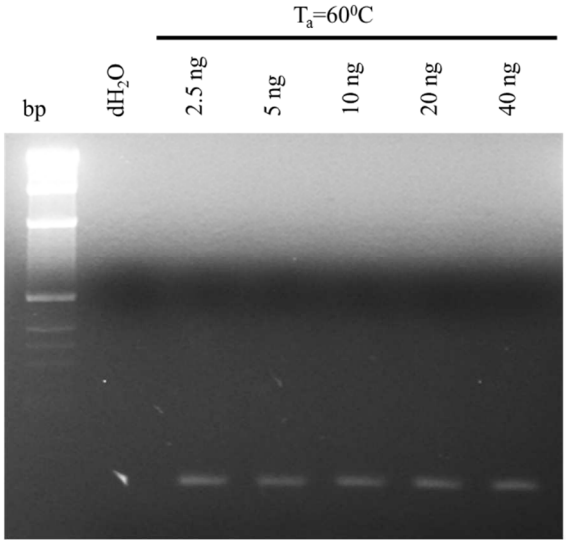

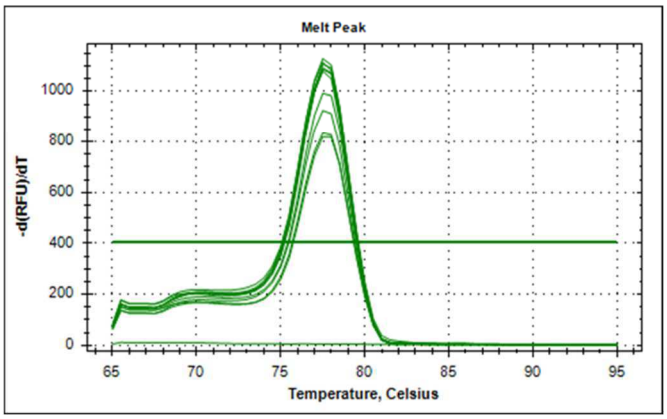

Figure 49. Optimization of primer concentration for qRT-PCR against *NALCN* on cDNA from PC-3.
qRT-PCR was performed by using cDNA from PC-3 cell line. Each reaction was performed at Ta=60^0C and contained different primers concentration (as indicated) and 4 mM $MgCl_2$. Melting peak for each amplicon was yielding at the same temperature - T_m = 77.5^0C. For each primer (FW and RV) the final concentration of 300 nM was chosen as the most optimal within the tested range.

$MgCl_2$	Efficiency, %	R^2
4 mM	112.8	0.996
5 mM	133.7	0.972

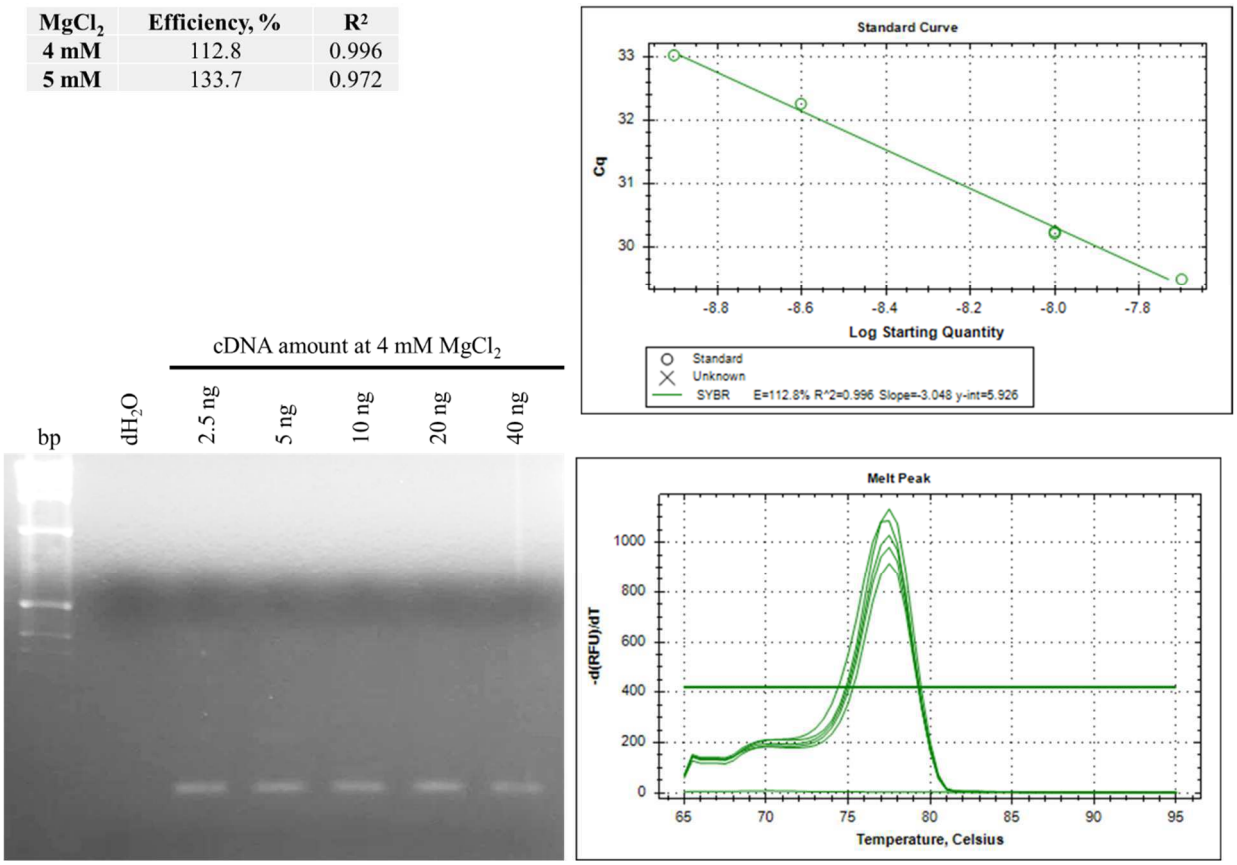

Figure 50. Optimization of $MgCl_2$ concentration for qRT-PCR against *NALCN* on cDNA from PC-3.
qRT-PCR was performed by using cDNA from PC-3 cell line. Each reaction was performed at T_a=60^{0}C and 300 nM primers concentration with 4 mM and 5 mM $MgCl_2$. Melting peak for each amplicon was yielding at the same temperature - T_m = 77.5^{0}C. Concentration of $MgCl_2$ of 4 mM was chosen as the most optimal within the tested range.

7.5 Optimization of qRT-PCR efficiency for *UNC-80*

T_a	Efficiency, %	R^2
63.6°C	108.3	0.976
63.3°C	105.2	0.981
62.6°C	105.7	0.978
61.4°C	103.4	0.983
60.0°C	101.4	0.994
58.8°C	105.4	0.982
58.0°C	100.8	0.984
57.6°C	111.1	0.989

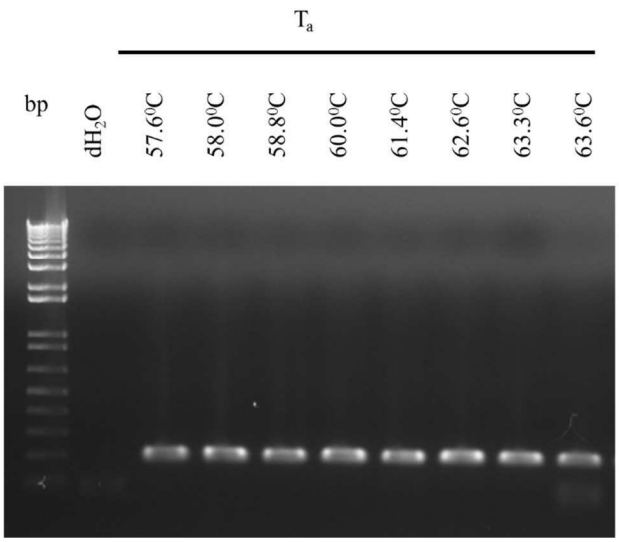

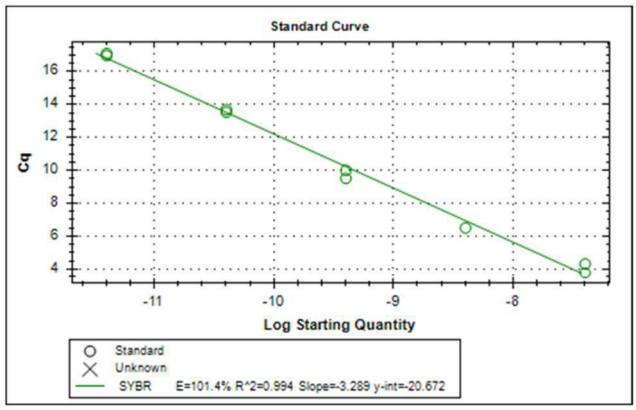

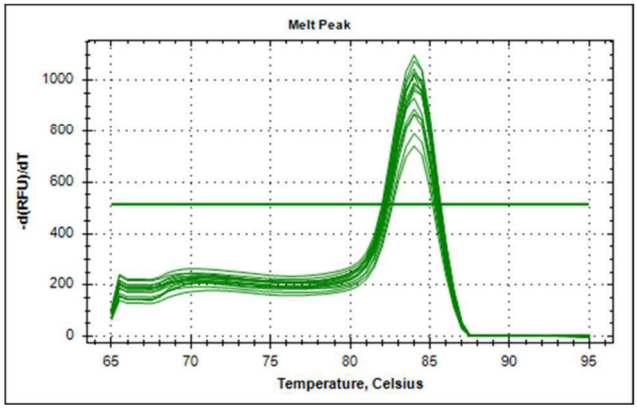

Figure 51. Temperature gradient qRT-PCR against *UNC-80* on plasmid DNA.
Temperature gradient (57.6-63.6^{0}C) was performed by using hUNC80irese2eGFP plasmid. Each reaction contained 300 nM of primers against *UNC-80* and 4 mM $MgCl_2$. Melting peak for each amplicon was yielding at the same temperature - T_m = 84.0^{0}C. Of note, amplicons from Mus ♂ brain and prostate cancer cell lines were having their melting peaks at T_m = 84.0^{0}C. Annealing temperature T_a=60^{0}C was chosen as the most optimal within the tested range.

7.6 Optimization of qRT-PCR efficiency for *UNC-79*

T_a	Efficiency, %	R^2
63.6°C	148.3	0.930
63.3°C	140.8	0.927
62.6°C	135.8	0.807
61.4°C	127.1	0.839
60.0°C	104.1	0.938
58.8°C	137.5	0.898
58.0°C	139.1	0.894
57.6°C	91.6	0.958

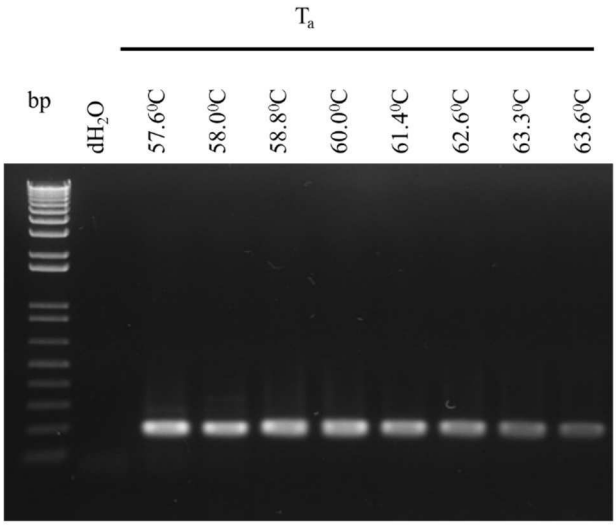

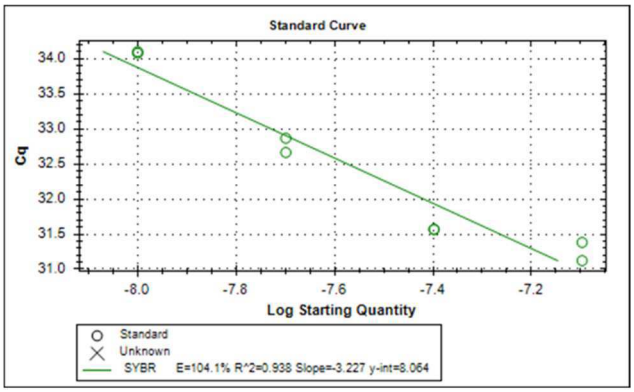

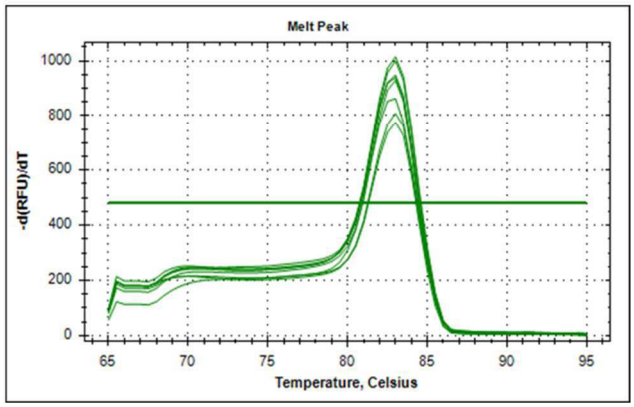

Figure 52. Temperature gradient qRT-PCR against *UNC-79* on cDNA from PC-3. Temperature gradient (57.6-63.6^{0}C) was performed by using cDNA frpm PC-3 cell line. Each reaction contained 300 nM of primers against *UNC-80* and 4 mM $MgCl_2$. Melting peak for each amplicon was yielding at the same temperature - T_m = 83.0^{0}C. Annealing temperature T_a=60^{0}C was chosen as the most optimal within the tested range.

7.7 Optimization of qRT-PCR efficiency for *TBP*

T_a	Efficiency, %	R^2
60°C	101.0	0.990
59.7°C	102.9	0.979
59.2°C	114.5	0.990
58.2°C	110.7	0.993
57.0°C	111.5	0.980
56.0°C	106.1	0.981
55.3°C	110.7	0.991
55.0°C	101.5	0.970

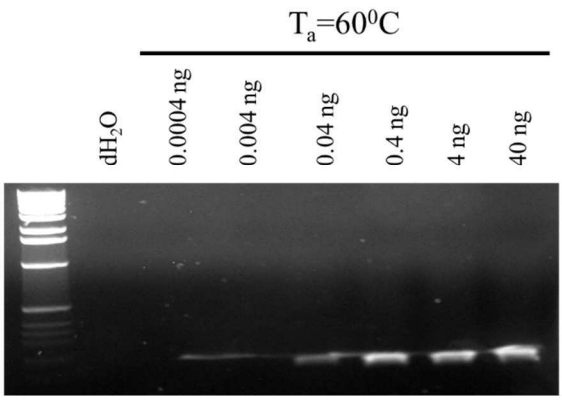

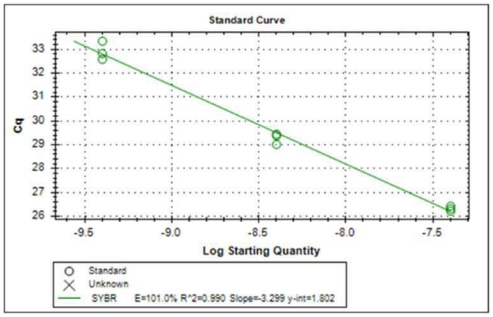

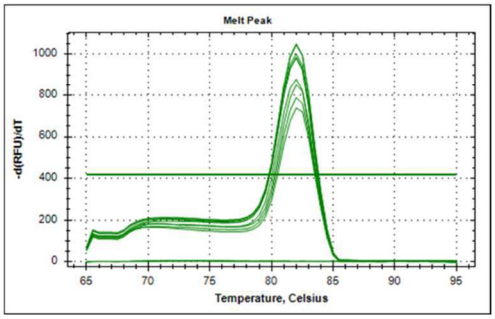

Figure 53. Temperature gradient qRT-PCR against *TBP* on cDNA from PC-3.
Temperature gradient (55-60^{0}C) was performed by cDNA from PC-3 cell line. Melting peak for each amplicon was yielding at the same temperature - T_m = 82.0^{0}C. Annealing temperature T_a=60^{0}C was chosen as the most optimal within the tested range.

7.8 Verification of internal control genes

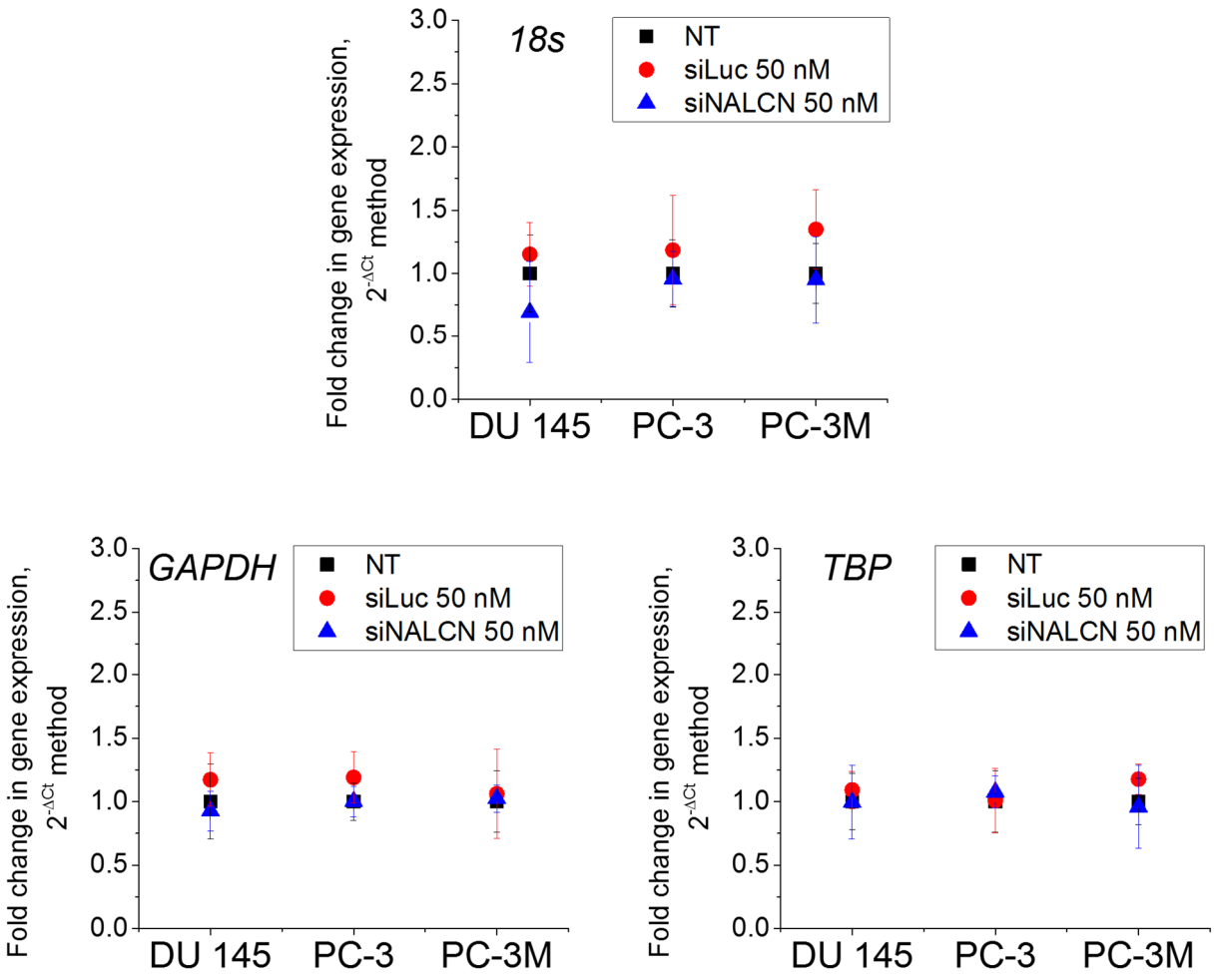

Figure 54. Validation of housekeeping/reference genes as suitable internal controls for qRT-PCR.
The following experiment was conducted to validate the effect of transfection on the expression of *18S*, *GAPDH* and *TBP* genes as standard candidates for internal control genes. DU 145, PC-3 and PC-3M cell lines were mock transfected (NT) and transfected with 50 nM siRNA against *Luciferase* (siLuc), gene which is not expressed in mammals, and 50 nM siRNA against *NALCN* (siNALCN). Samples were collected after 48 hours of transfection, mRNA extracted, converted into cDNA and subjected to qRT-PCR. The fold change in gene expression was calculated by using $2^{-\Delta Ct}$ method, where $\Delta Ct = (Ct_{(siRNA)} - Ct_{(NT)})$ as described by (Livak & Schmittgen, 2001).

7.9 Protein standard curve

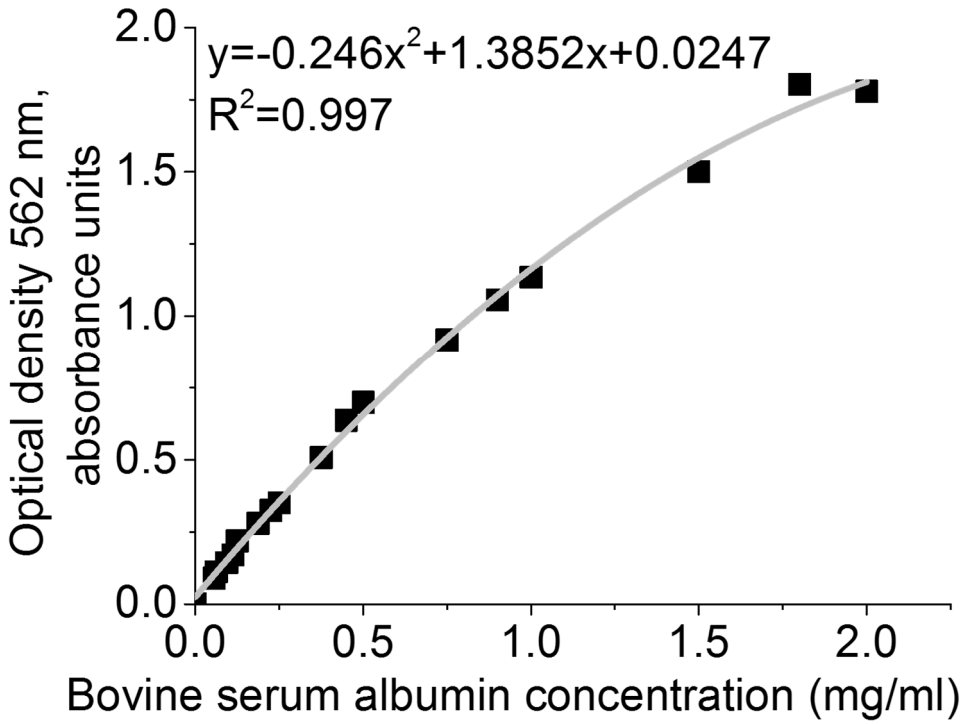

Figure 55. Protein standard curve according to Pierce™ BCA Protein Assay Kit.
The protein standard curve was done using albumin standards provided with the assay kit according to the manufacturer's instructions.

7.10 Optimization of immunoblotting conditions

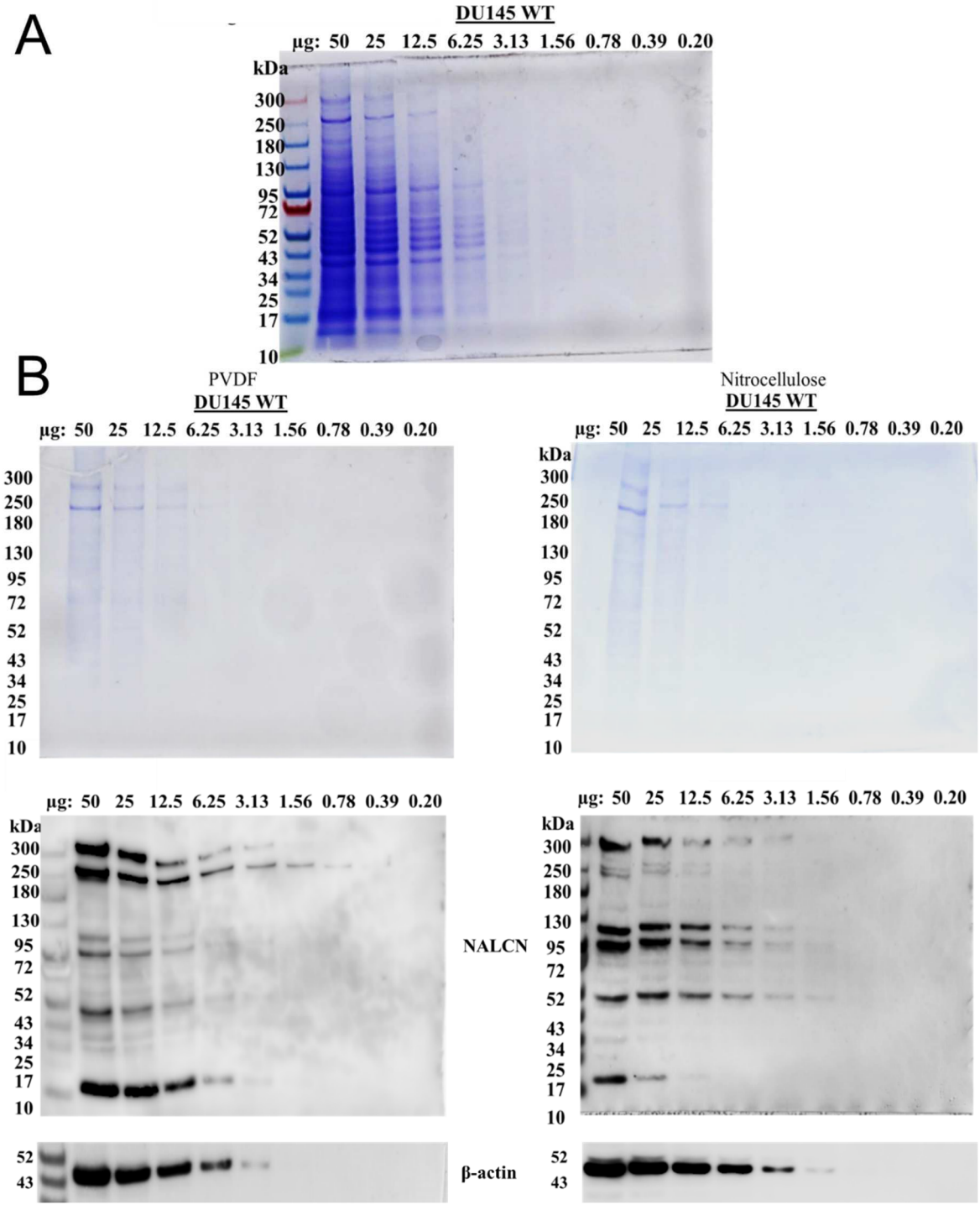

Figure 56. Optimization of protein transfer from SDS-PAGE onto membrane.
A, 3-8% SDS-PAGE loaded with different amount of protein extract from DU 145 cells and stained with Coomasie Brilliant Blue R-250. B, Semi-dry transfer was performed on the PVDF and nitrocellulose membranes. SDS-PAGE gels were stained with Coomasie Brilliant Blue R-250 in order to visualize the excess of proteins that were not transferred. The blots were revealed using antibody against NALCN and β-actin. Since the expected size of NALCN bands (200-300 kDa) appeared more efficiently transferred onto PVDF, this membrane was used in further experimental procedures. The optimal protein amount for an assay was determined as 25 µg.

7.11 Transfection efficiency of nucleofection

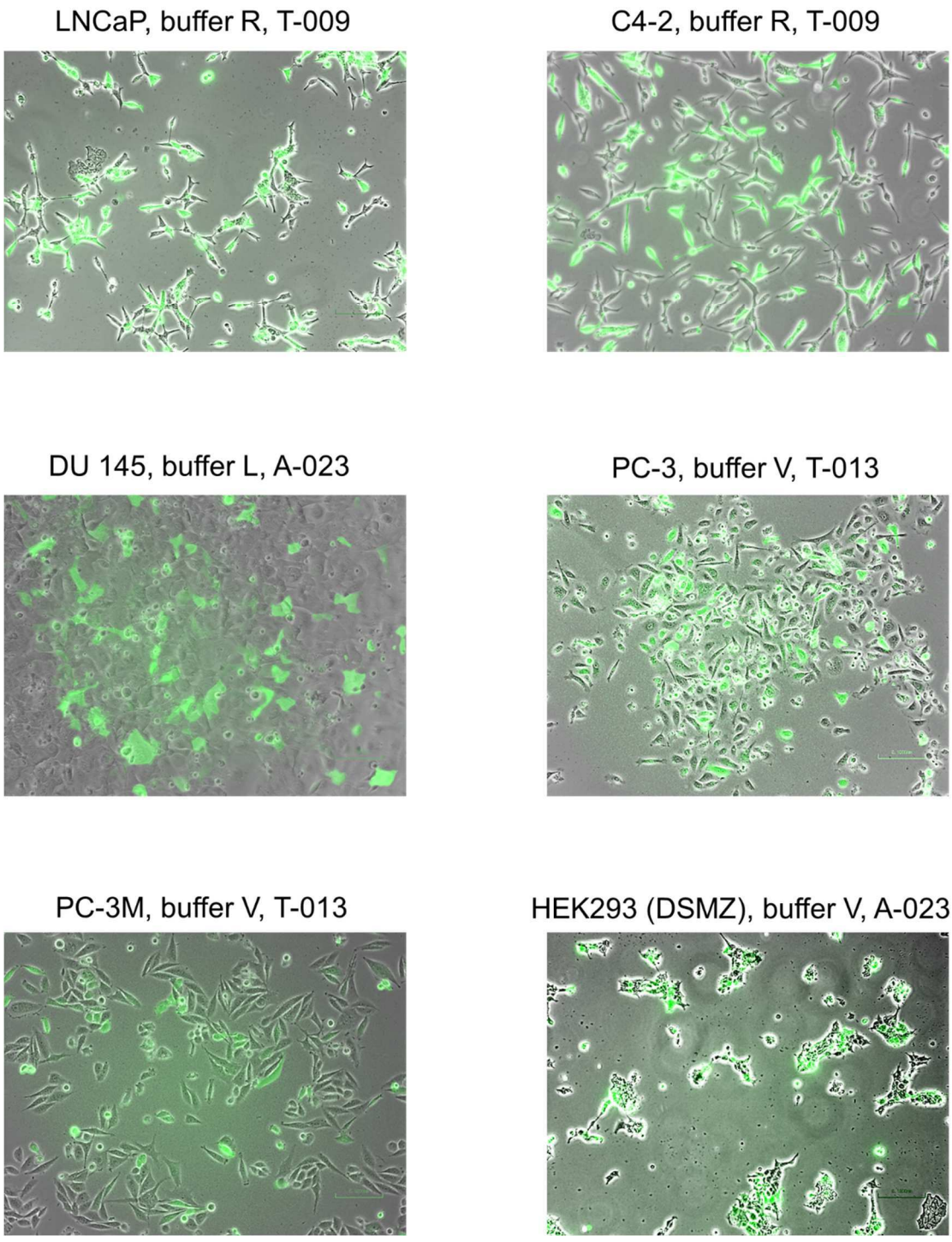

Figure 57. Transfection efficiency by using nucleofection method in various cell lines. Buffer and program conditions are indicated for each cell line and resulted in following level of transfection: LNCaP – 49%, C4-2 – 48%, DU-145 – 8%, PC-3 – 19%, PC-3M – 10%, and HEK293 – 22%. The images were taken 48 hours after nucleofecting 1 µg of pmax-GFP plasmid.

7.12 Pattern of NALCN overexpression

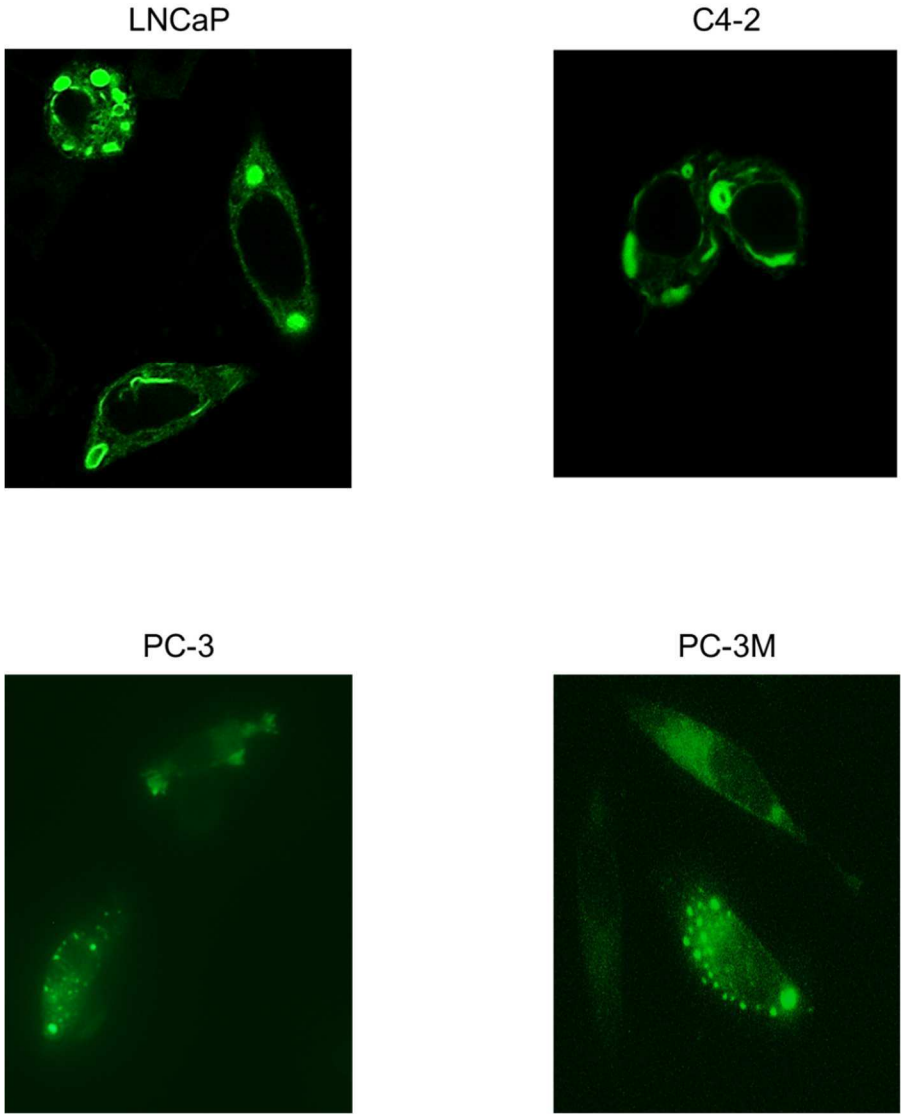

Figure 58. Representative images of NALCN-GFP overexpression in human prostate cancer cell lines.
Overexpression of NALCN is represented by some special structures, or so called punctae and rosettes.

7.13 Optimization of siRNA knock-down

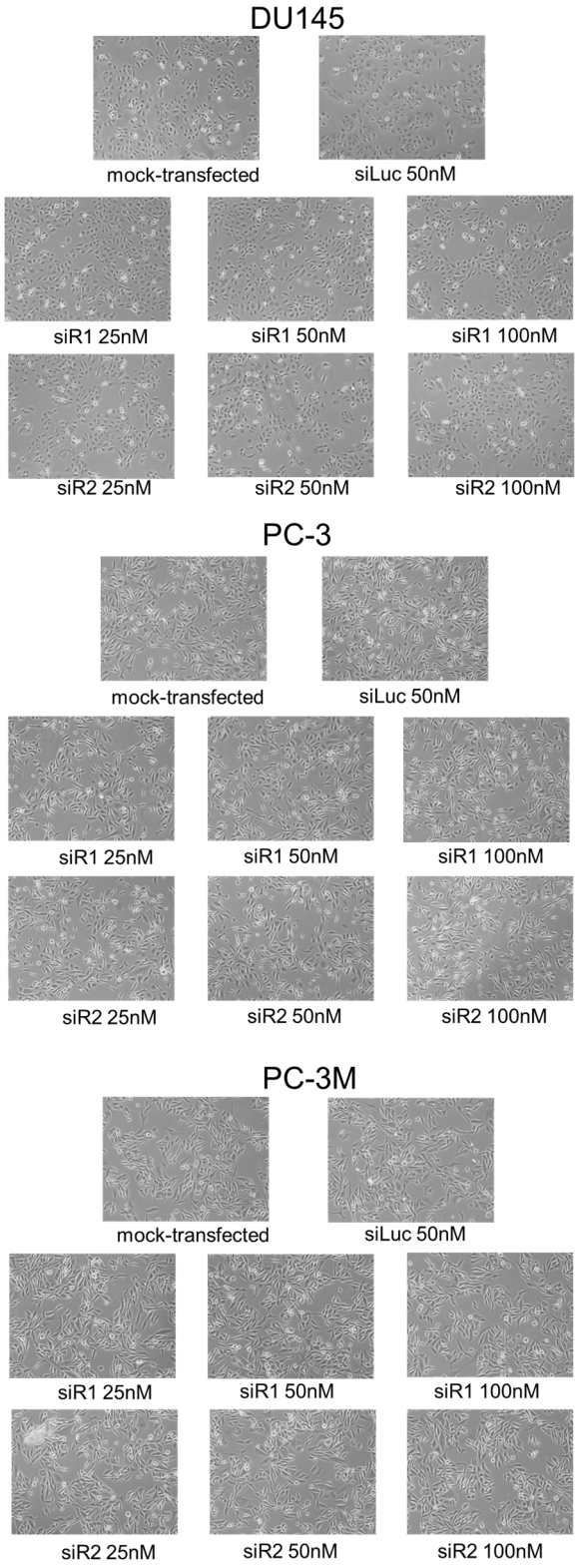

Figure 59. Representative images of human prostate cancer cells after transient NALCN knockdown.
The images were taken after 48 hours of transfection with 20x objective.

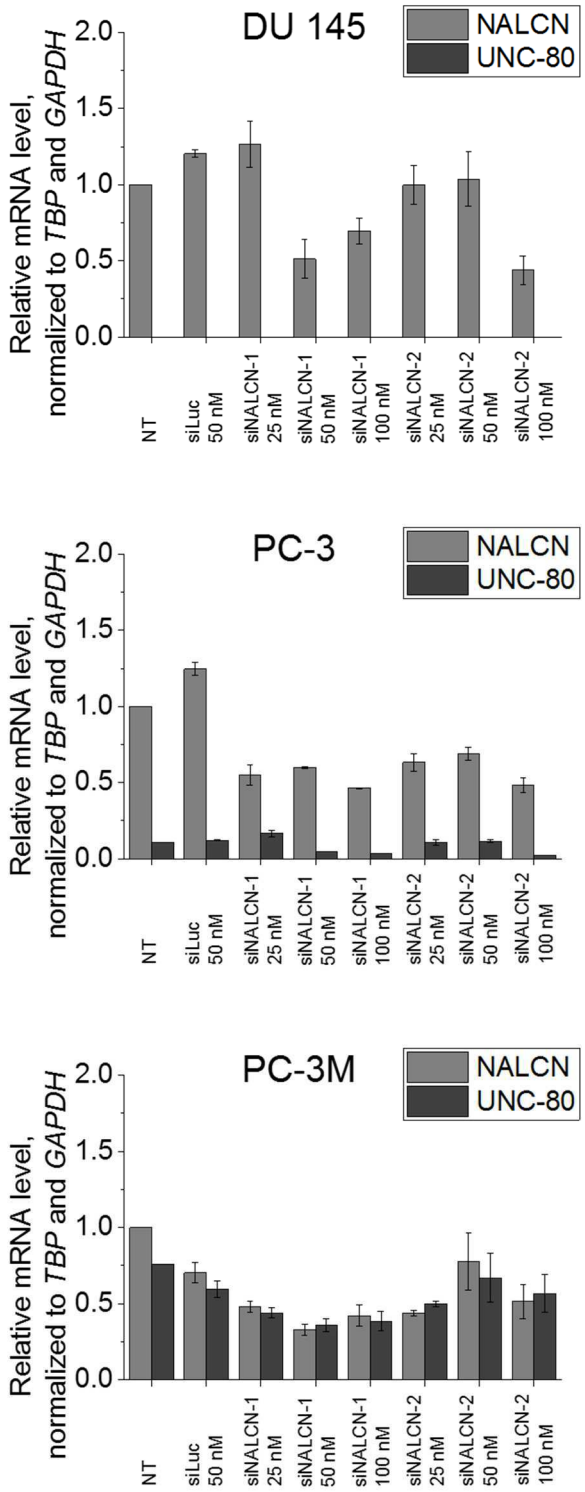

Figure 60. Validation of siRNA quantity sufficient to create NALCN knockdown in human prostate cancer cell lines.
The level of NALCN knockdown was verified by qRT-PCR after 48 hours of mock (NT) and HiPerfect siRNA transfection. Interestingly, the level of *UNC-80* mRNA was dependent on *NALCN* expression (n=1). The quantity of 50 nM siRNA against *NALCN* was considered as optimal within all cell lines tested to create NALCN knockdown.

7.14 Verification of transient NALCN knockdown

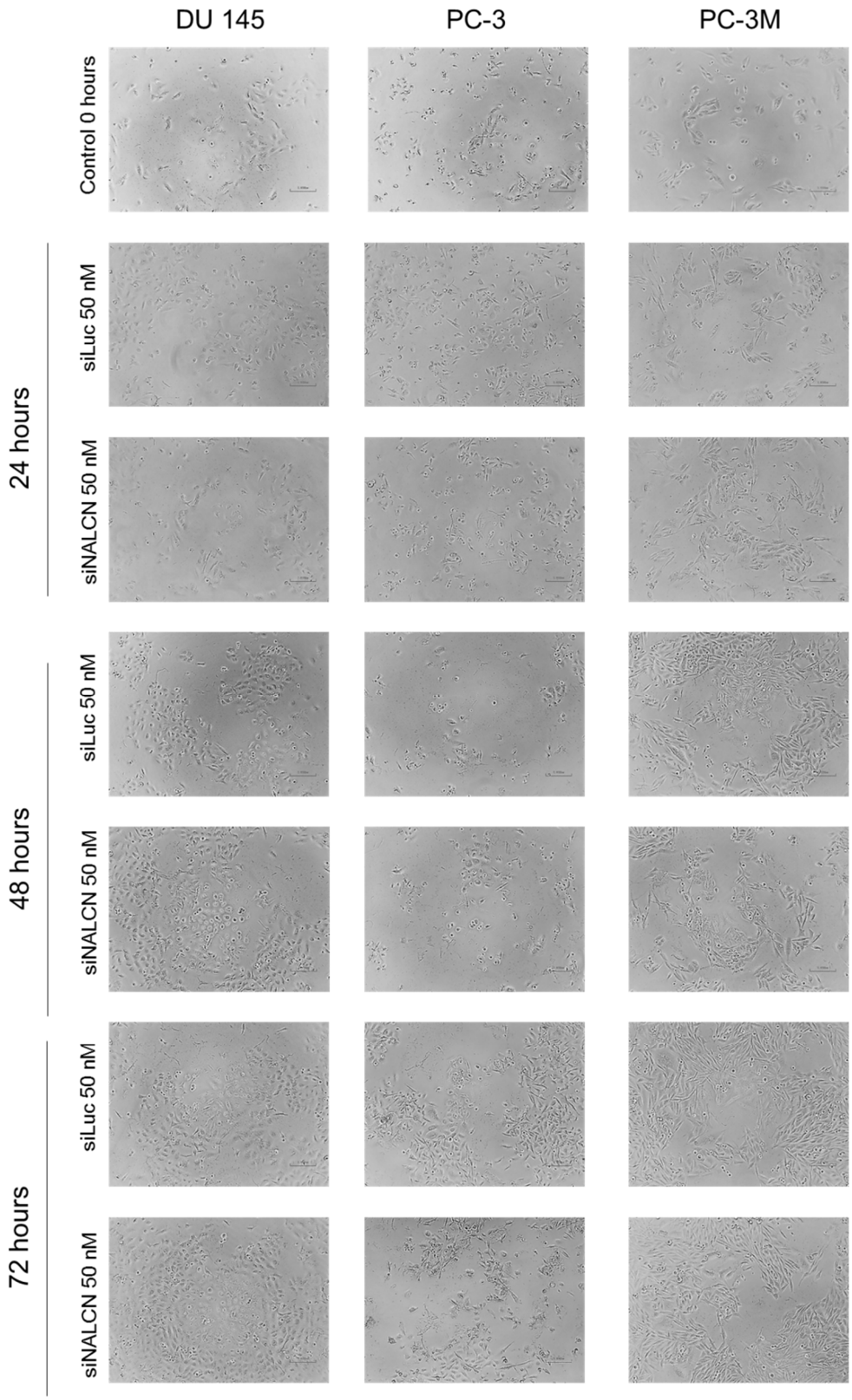

Figure 61. Representative images of human prostate cancer cells after transient NALCN knockdown with siNALCN-1.
The images were taken with 20x objective.

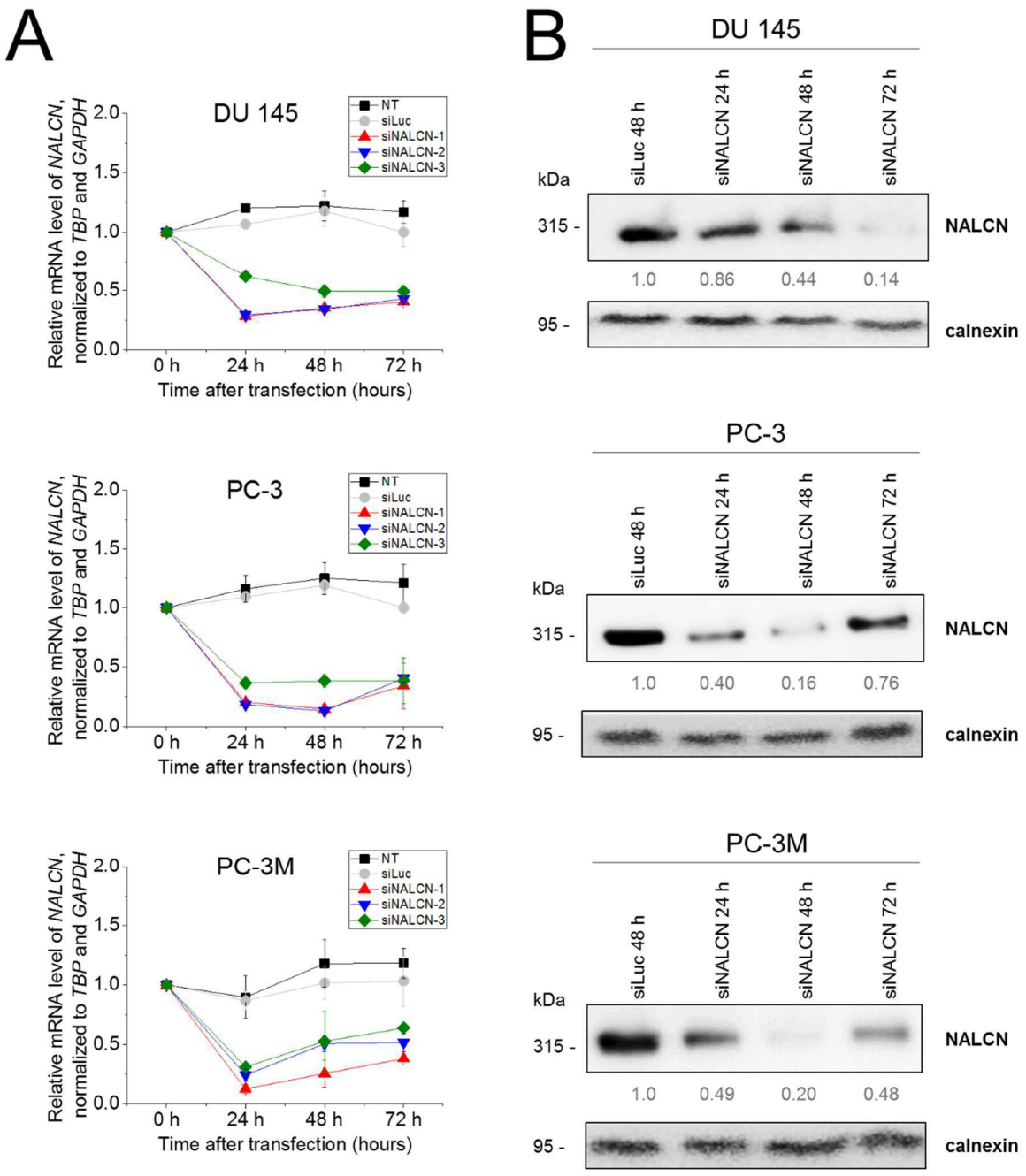

Figure 62. Verification of transient NALCN knockdown in human prostate cancer cell lines.
A, on mRNA level by using qRT-PCR. Data presented as mean values ± SEM (n=3). B, on protein level by using immublotting technique. Representative images of immnuoblots are shown (n=3).

7.15 Verification of stable NALCN knockdown

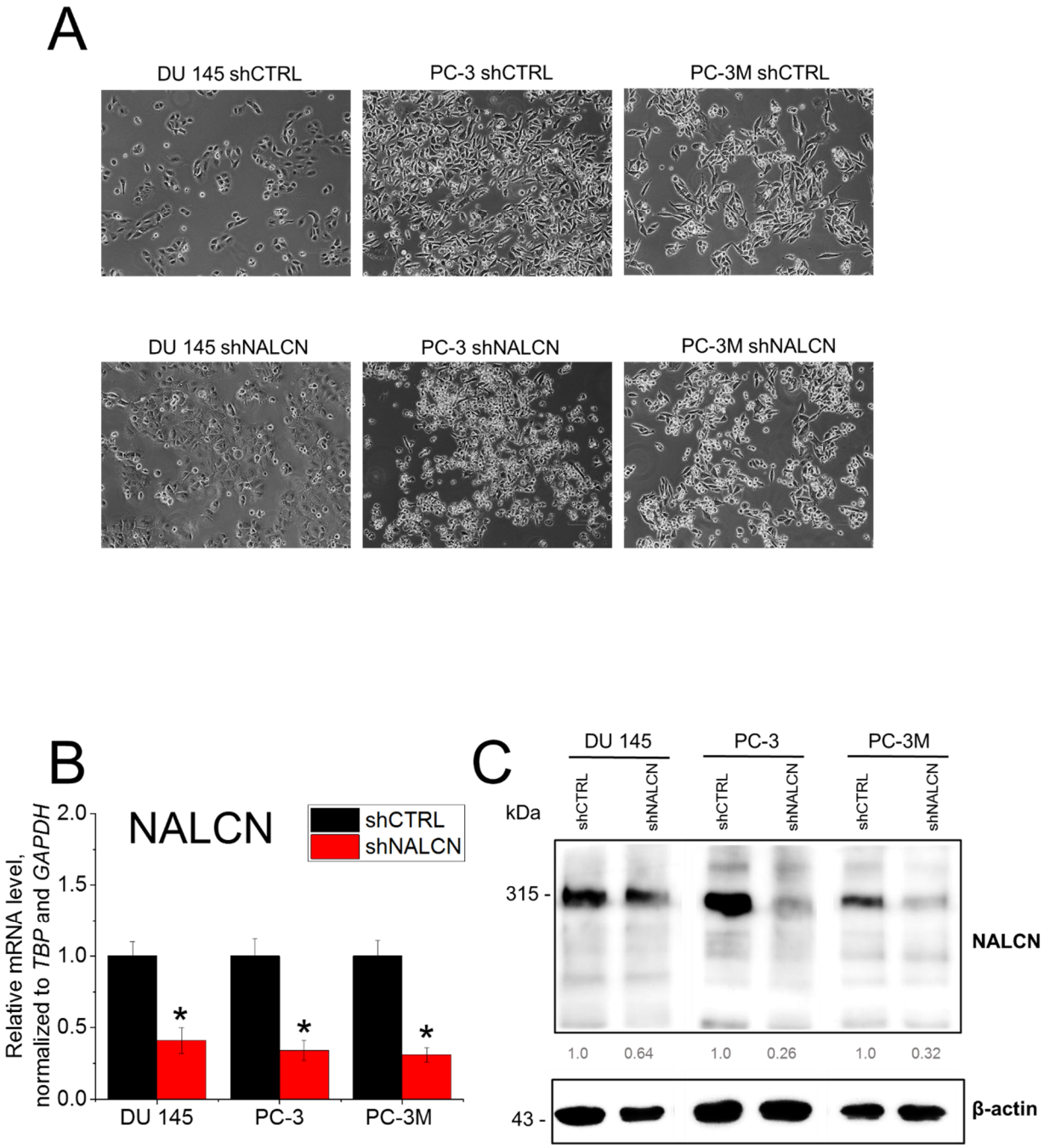

Figure 63. Verification of stable NALCN knockdown in human prostate cancer cell lines. A, representative cell images taken with 20x objective. B, on mRNA level by using qRT-PCR. *-$p<0.05$ (n=3). B, on protein level by using immunoblotting.

7.16 siRNA transfection by using nanoparticles

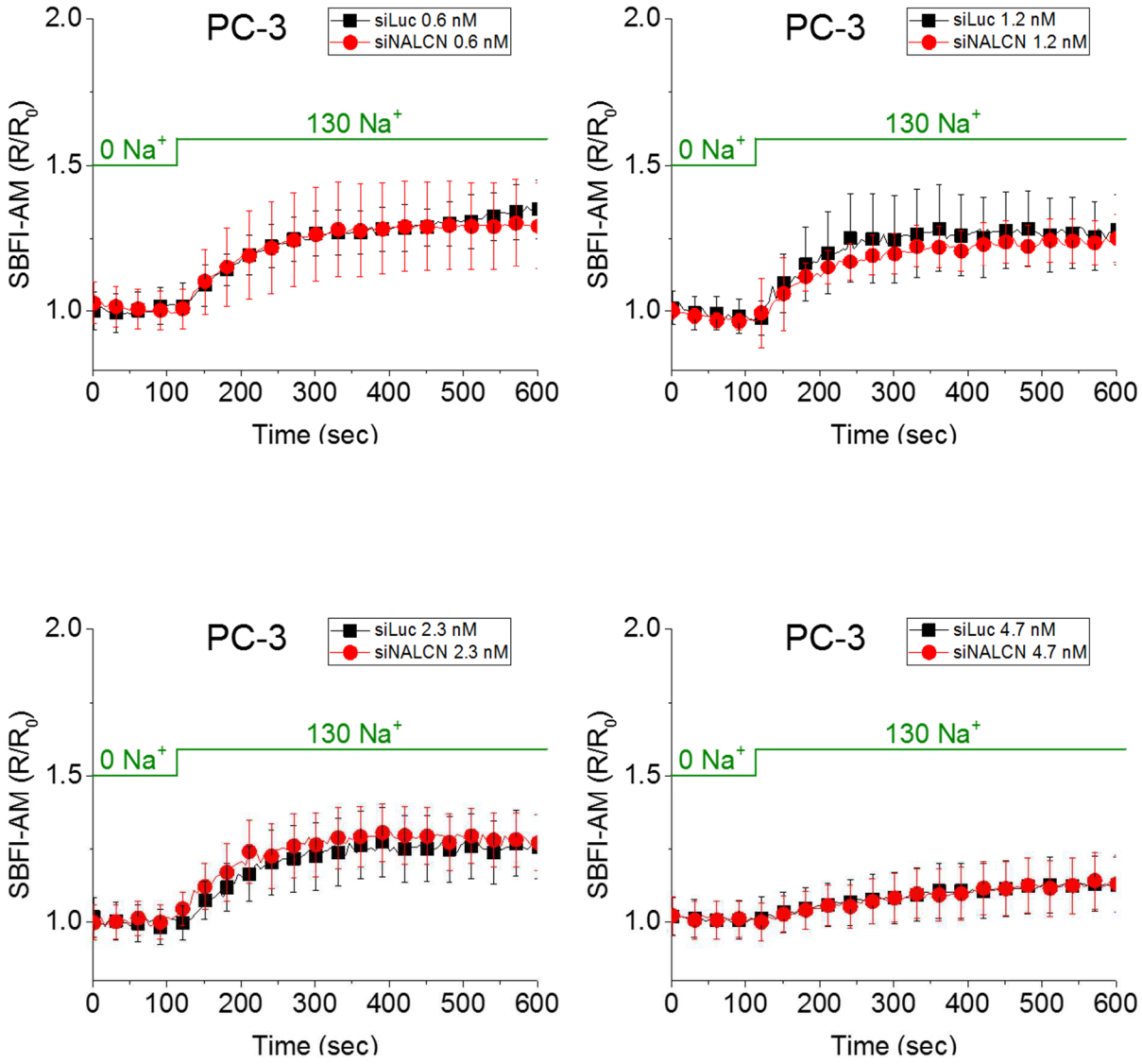

Figure 64. Na^+ influx in PC-3 cells after transfection with siRNA linked to lipid nanocapsules LNC25.
At the low doses there is no difference between Na^+ influx produced in control cells (siLuc) or cells treated with siRNA against NALCN (siNALCN). However, the higher doses inhibited Na^+ influx more likely due to the toxicity of the nanocapsules themselves.

7.17 Apoptosis induction in human prostate cancer cell lines

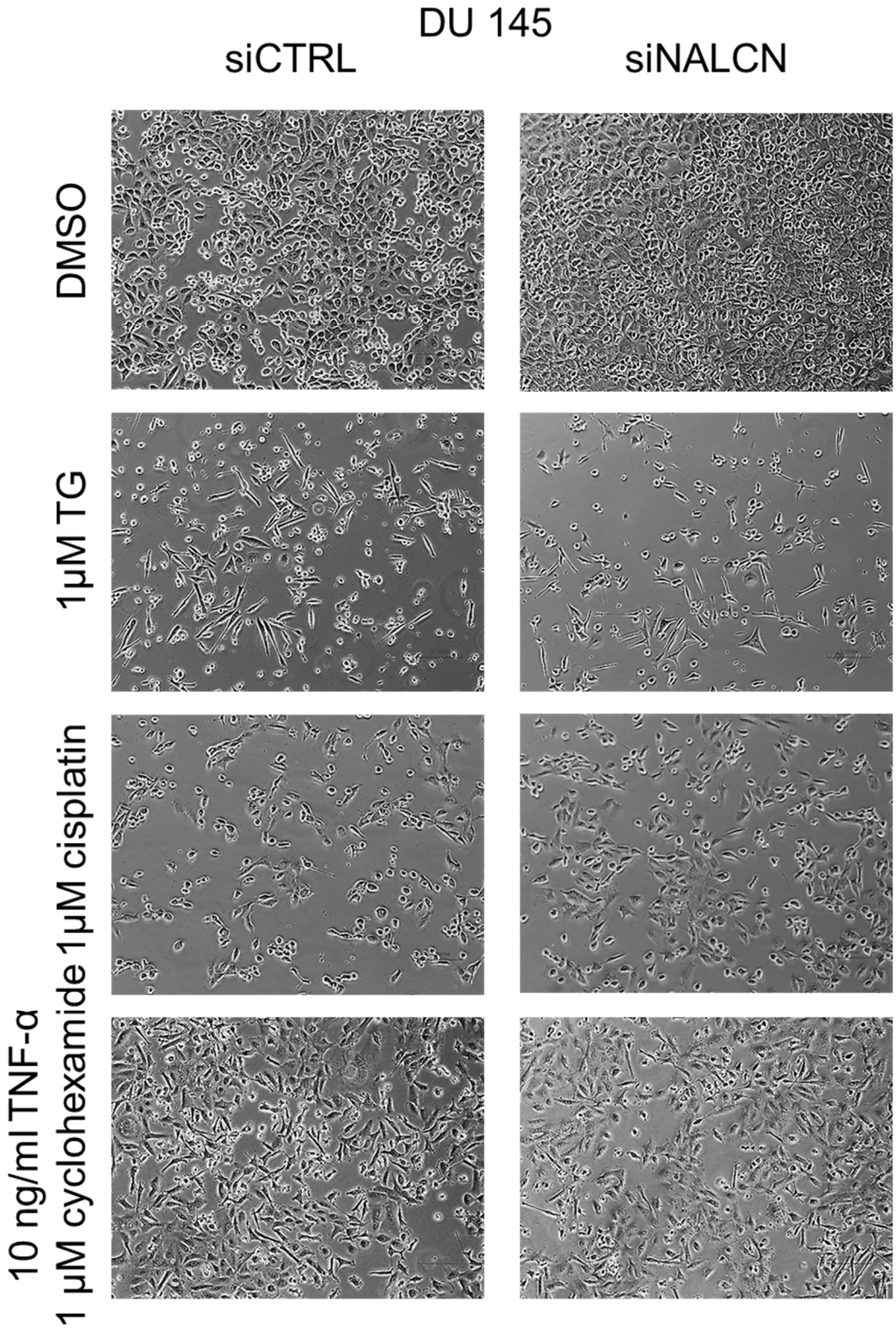

Figure 65. Representative images of DU 145 cells after apoptosis induction.
Images were taken after 72 hours of transfection with siRNA and 48 hours after apoptosis induction with 20x objective.

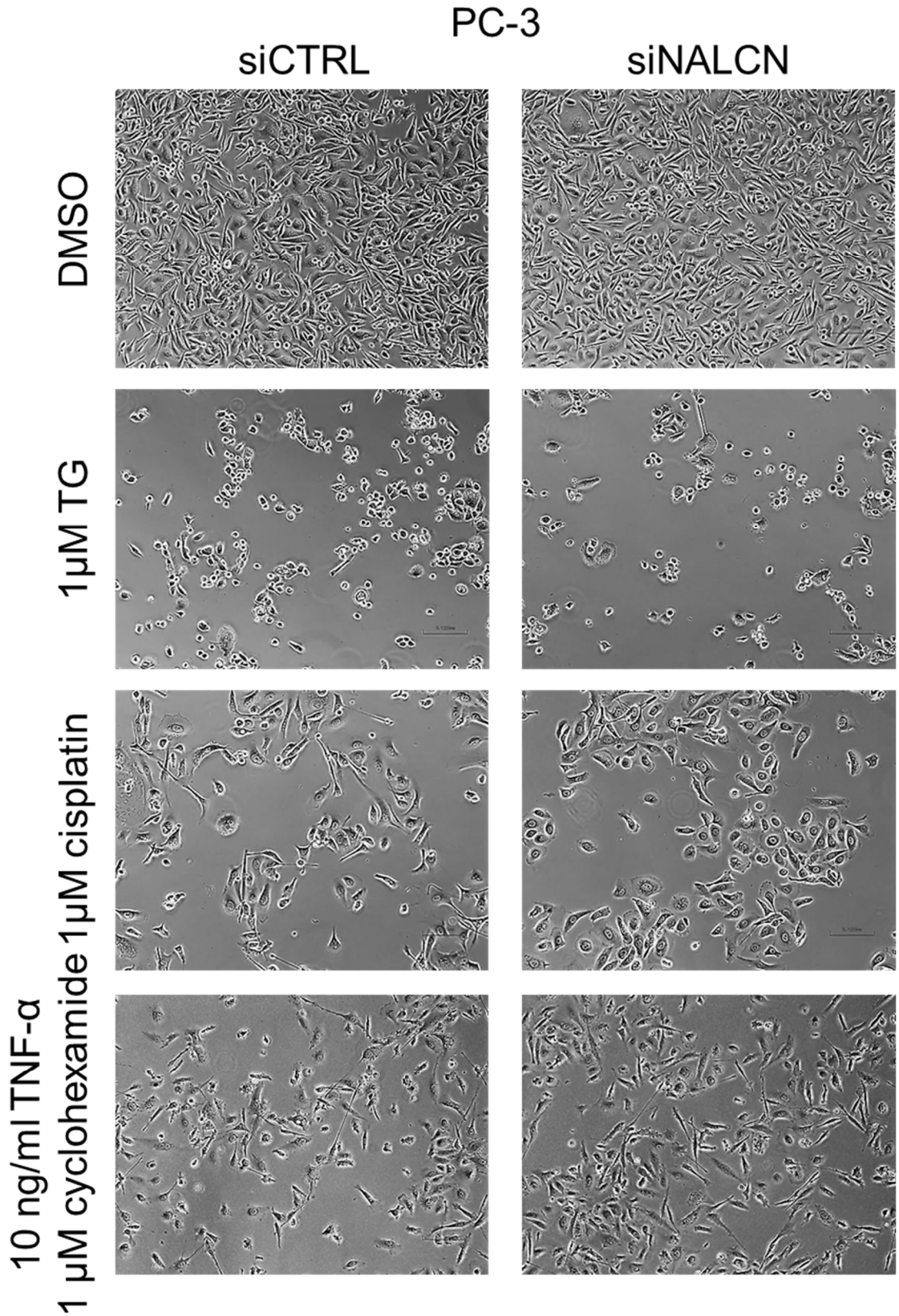

Figure 66. Representative images of PC-3 cells after apoptosis induction.
Images were taken after 72 hours of transfection with siRNA and 48 hours after apoptosis induction with 20x objective.

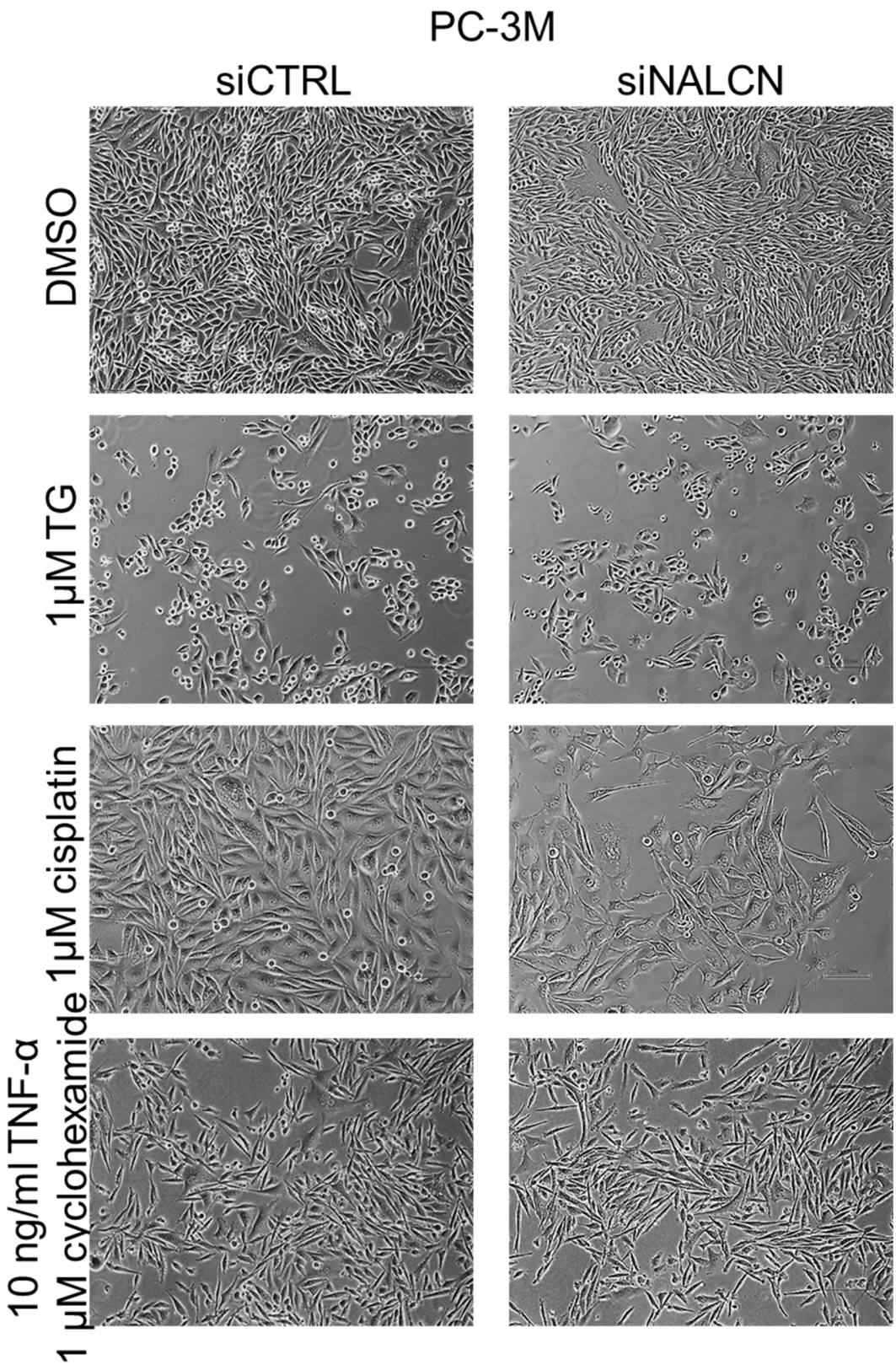

Figure 67. Representative images of PC-3M cells after apoptosis induction.
Images were taken after 72 hours of transfection with siRNA and 48 hours after apoptosis induction with 20x objective.

7.18 Calibration of ProFluor® Src-Family Kinase assay

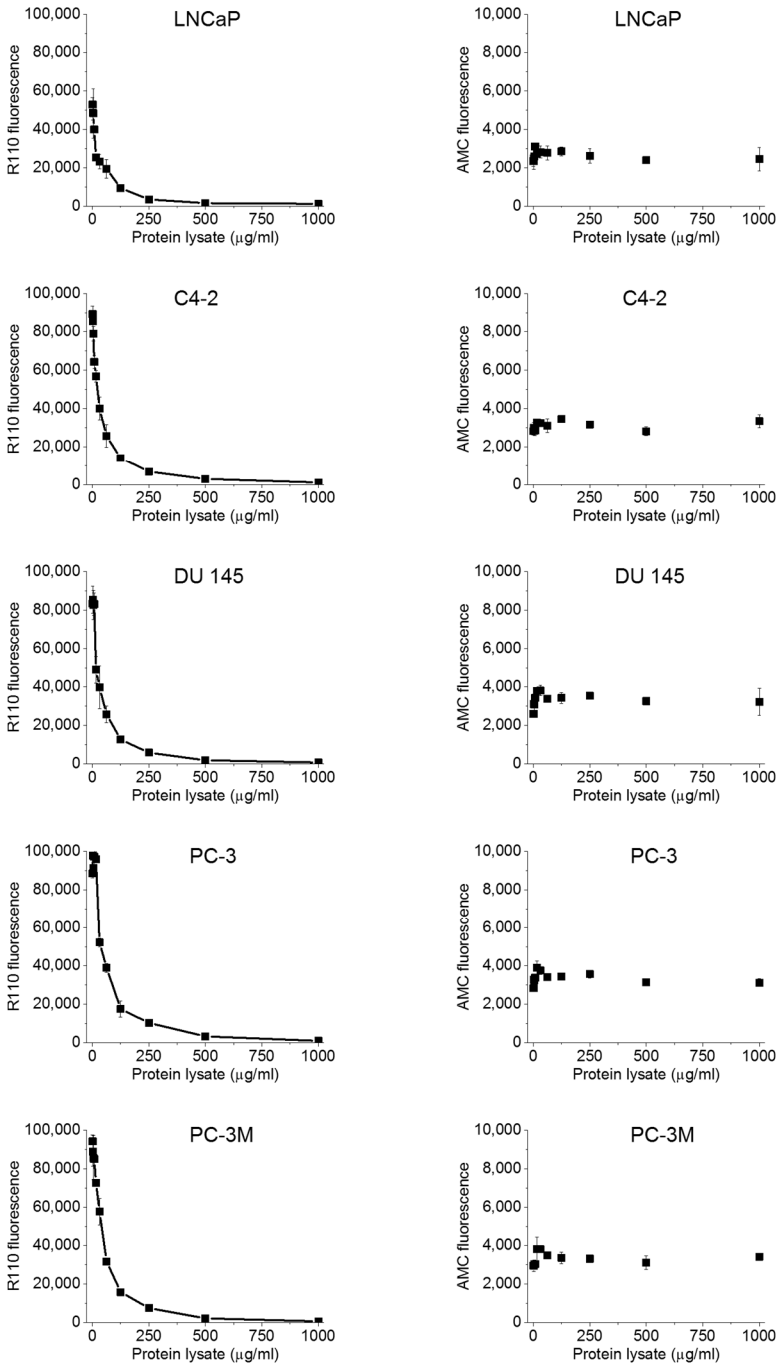

Figure 68. Calibration curves using protein lysates from different human prostate cancer cell lines for ProFluor® Src-Family Kinase assay.
Rhodamine 110 (R110) is essentially nonfluorescent in the bisamide form. When R110 peptide substrate is not phosphorylated, it is cleaved due to the protease acitvity, subsequently amino acid residues are removed and R110 becomes fluorescent. When this substrate is phosphorylated (presumably by Src-Family kinase activity), protease activity is blocked, and R110 is left in nonfluorescent form. Thus, the measured R110 fluorescence intensity is inversely correlated with kinase activity. The control AMC substrate (alanine-alanine-phenylalanine linked to 7-amino-4-methylcoumarin) has different excitation and emission wavelength than the R110 substrate, and will identify any false negatives in the assay. AMC substrate contains no phosphorylation site, and thus its cleavage is independent of kinase activity.

7.19 Invadopodia fractionation

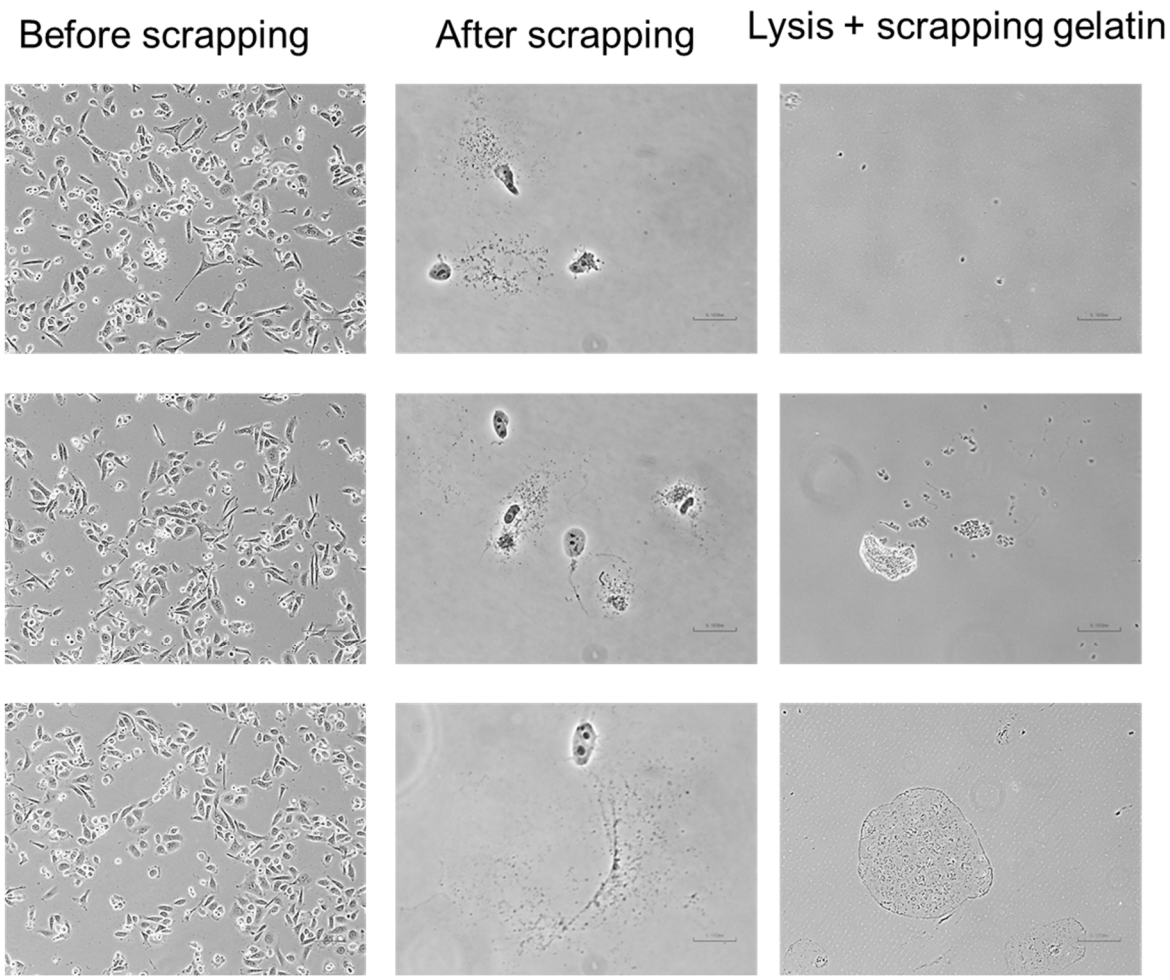

Figure 69. Representative images of different steps within invadopodia fractionation assay.
All images were taken with 20x objective.